



HAL
open science

Investigating knock in an industrial spark-ignition engine by Large-Eddy Simulation

Matthieu Leguille

► **To cite this version:**

Matthieu Leguille. Investigating knock in an industrial spark-ignition engine by Large-Eddy Simulation. Thermics [physics.class-ph]. Université Paris Saclay (COmUE), 2018. English. NNT : 2018SACLC081 . tel-02053428

HAL Id: tel-02053428

<https://theses.hal.science/tel-02053428>

Submitted on 1 Mar 2019

HAL is a multi-disciplinary open access archive for the deposit and dissemination of scientific research documents, whether they are published or not. The documents may come from teaching and research institutions in France or abroad, or from public or private research centers.

L'archive ouverte pluridisciplinaire **HAL**, est destinée au dépôt et à la diffusion de documents scientifiques de niveau recherche, publiés ou non, émanant des établissements d'enseignement et de recherche français ou étrangers, des laboratoires publics ou privés.

Investigating knock in an industrial spark-ignition engine by Large-Eddy Simulation

Thèse de doctorat de l'Université Paris-Saclay
préparée à CentraleSupélec

Ecole doctorale n°579
Sciences mécaniques et énergétiques, matériaux et
géosciences (SMEMaG)
Spécialité de doctorat: Combustion

Thèse soutenue à Rueil-Malmaison, le 28 Novembre 2018, par

Matthieu Leguille

Composition du jury:

Christine Rousselle Professeur, Université d'Orléans (PRISME)	Présidente
Luc Vervisch Professeur, INSA Rouen - CORIA	Rapporteur
Stefano Fontanesi Professeur, Università degli studi di Modena e Reggio Emilia	Rapporteur
Denis Veynante Directeur de recherche, CentraleSupélec (EM2C)	Examineur
Christian Angelberger Docteur, IFP Energies nouvelles	Directeur de thèse
Olivier Colin Docteur, IFP Energies nouvelles	Promoteur de thèse
Frédéric Ravet Expert combustion, Renault SA	Promoteur de thèse

Remerciements

Mes premiers remerciements vont aux membres de mon jury de thèse, le Professeur Christine Rousselle, présidente du jury, le Professeur Luc Vervisch et le Professeur Stefano Fontanesi qui m'ont fait l'honneur d'être rapporteurs, et le Docteur Denis Veynante pour sa participation en tant qu'examineur. Je les remercie pour l'intérêt qu'ils ont porté à mon travail, et pour l'expertise apportée à son évaluation.

Je tiens à remercier chaleureusement mon directeur de thèse, Christian Angelberger, et mes encadrants, Frédéric Ravet, Olivier Colin et Karine Truffin. Je leur suis énormément reconnaissant pour tout ce qu'ils m'ont appris durant ces trois années. Ils m'ont toujours témoigné leur confiance, apporté leur riche expérience en combustion, accordé le degré de liberté suffisant pour que je puisse m'exprimer pleinement dans mes recherches. Je n'oublie pas toutes les répétitions orales et les corrections minutieuses du manuscrit qui m'ont parfois fait "tirer la langue", mais sans aucun doute m'ont toujours tiré vers le haut.

J'ai eu le plaisir de partager de nombreux bons moments avec mes collègues permanents de l'IFP Energies nouvelles. Je les remercie pour leur disponibilité à mes questions, et les solutions qu'ils m'ont apportées parfois au prix de quelques sucreries. Je voudrais également remercier vivement mes collègues Renault de Lardy. Ils m'ont fait profiter de leur expertise de motoriste à chacune de mes visites, donnant ainsi tout son sens à cette thèse Cifre. Je souhaite enfin exprimer ma gratitude à toute l'équipe de Convergent Science pour leur aide précieuse dans la mise en place de mes simulations. Je remercie en particulier les trois présidents que j'ai cotoyé et qui m'ont accueilli avec enthousiasme dans leurs locaux de Madison (WI, USA): le Docteur Eric Pomraning, le Docteur Peter Kelly Senecal et le Docteur Keith Richards.

J'ai eu le très grand plaisir de partager ces trois années de thèse avec "mon doudou" Antoine. Un collègue de bureau à l'insatiable curiosité scientifique et oenologique, à l'humour subtile et le sifflement toujours bien accordé. J'ai également une pensée particulière pour tous mes collègues thésards: Edouard, Gorka, Lefteris, Fabien, Edouard, Alexis, Julien, Benoît, Maxime, Hassan, Louise et Andreas. C'est avec joie que je m'étais fait un devoir de les battre quotidiennement aux fléchettes.

Je voudrais aussi remercier Jérôme ("Djérôme" pour les américains) et Alie ("ma maître de stage"), avec qui je me suis lié d'amitié au fur et à mesure de nos échanges professionnels. Un grand merci à mes deux incroyables "roommates" Laurel et Jen. Elles m'ont ouvert les portes de leur quotidien, leurs amis, et m'ont permis d'apprécier leur splendide ville. Je n'oublie pas mes potes de Paname, qui malgré cette remarque angoissante dans la dernière ligne droite, "Ah ouais c'est bientôt la fin d'ta thèse!", m'ont permis de conserver mon équilibre de vie.

Mes derniers remerciements vont à ma petite soeur qui porte continuellement de l'attention à son grand frère, à mes parents qui ont toujours soutenu les choix vers lesquels je m'engageais pleinement, et enfin à ma compagne, Clémentine, qui m'a encouragé tous les jours dans cette aventure d'une vie, et sans qui je n'aurais probablement pas vu la ligne d'arrivée.

Abstract

The rising concerns about the environment have led car manufacturers to come up with new engine technologies, in order to reduce the impact of internal combustion engines on CO_2 emissions. In this context, downsizing of turbocharged spark-ignition engines has become a commonly used technology, the advantage of which is to operate the engine under thermally more efficient high loads. However, these high loads favour the appearance of potentially damaging knock phenomena, which prevent the engine to fully exploit its potential. Because of cyclic combustion variability (CCV) in the engine, knock, which depends on the local conditions inside the combustion chamber, can appear at different locations and timings and not in all engine cycles. In this thesis, a Large-Eddy Simulation (LES) approach was selected to investigate and further improve our understanding of the appearance of knock. The study is based on the LES of a production engine, the RENAULT 1.2 TCe 115. For this engine, a set of 30 cycles was initially simulated at a single operating point, corresponding to a knocking point in the test bench database from RENAULT. The results were compared to experimental findings, both in terms of CCV and knock. Subsequently, a spark-timing sweep was simulated in order to enlarge the LES database to also include weaker and stronger knock levels. The resulting LES, which consists of 150 combustion cycles, was used to develop methodologies and tools with the objective to better characterize and understand knock. The computational access to any quantity inside the combustion chamber, together with the separate description with the present LES approach, between the spark-triggered premixed flame propagation and auto-ignition, were exploited to characterize knock focusing on its source: auto-ignition in the fresh gases. Then, the developed methodologies and tools supported a detailed analysis of the mechanisms that control the knock onset. In particular, its link with CCV was explored. The results point out the impact of the cyclic variability in the premixed flame propagation speed and shape on knock.

Résumé

Les préoccupations environnementales actuelles ont conduit les constructeurs automobiles à proposer de nouvelles technologies dans le but de réduire les émissions de CO_2 . Parmi ces technologies, le downsizing appliqué aux moteurs turbocompressés à allumage commandé est une des solutions privilégiées, car permettant d'atteindre des points de fonctionnement fortement chargés, avec un meilleur rendement thermique. Cependant, les fortes charges favorisent l'apparition de cliquetis, un phénomène potentiellement dommageable pour le moteur et qui l'empêche d'exploiter tout son potentiel. Du fait des variabilités cycliques de combustion dans le moteur, le cliquetis, qui dépend des conditions locales dans la chambre de combustion, peut apparaître uniquement sur quelques cycles, à différents endroits et instants. Dans cette thèse, une approche par Simulation aux Grandes Echelles (SGE) a été choisie, dans le but d'étudier et d'améliorer notre compréhension du cliquetis. L'étude se base sur la SGE d'un moteur industriel, le RENAULT 1.2 TCe 115. Un premier ensemble de 30 cycles a été simulé sur un point de fonctionnement de référence, correspondant à un point cliquetant dans la base de données banc d'essais fournie par RENAULT. Les résultats de simulation ont été comparés aux résultats expérimentaux, aussi bien en termes de variabilités cycliques de combustion que de cliquetis. A la suite, un balayage d'avance à l'allumage a été simulé pour étendre la base de données LES à des points plus faiblement et plus fortement cliquetants. La base de données résultante se compose de 150 cycles de combustion, utilisés pour développer des méthodologies et outils, dans le but de mieux caractériser le cliquetis et d'approfondir sa compréhension. L'accès numérique à toute grandeur dans la chambre de combustion, combiné à la description séparée dans cette simulation entre la flamme de pré-mélange initiée par la bougie et l'auto-inflammation dans les gaz frais, ont permis de caractériser le cliquetis en se focalisant sur son origine: l'auto-inflammation. A la suite, les méthodologies et outils développés ont soutenu une analyse détaillée des mécanismes qui contrôlent l'apparition du cliquetis. En particulier, le lien entre le cliquetis et les variabilités cycliques de combustion a été exploré. Les résultats mettent notamment en évidence l'impact des variabilités cycliques, aussi bien de la vitesse de propagation que de la forme de la flamme de pré-mélange, sur le cliquetis.

Contents

1	Introduction	13
1.1	Environmental context	13
1.2	Basic operation of a modern spark-ignition engine	14
1.3	Introduction to engine knock	17
1.4	Objective of the thesis	20
1.5	Structure of the manuscript	21
1.6	Congress and publications	21
I	Auto-ignition and Engine Knock Modelling	23
2	A literature review on engine knock	25
2.1	Auto-ignition of a premixed air-fuel mixture	26
2.1.1	Rating of fuels propensity to knock: the Octane Number	26
2.1.2	Auto-ignition chemistry fundamentals	27
2.1.3	Auto-ignition chemistry modelling	29
2.1.4	Theory of auto-ignition propagation in the surrounding fresh gases . .	31

2.2	Knock in spark-ignition engines	33
2.2.1	Optical diagnostics of knock in engines	33
2.2.2	Knock detection based on pressure oscillations analysis	35
2.2.3	Key parameters influencing knock	36
2.2.4	Knock and cyclic combustion variability	38
2.2.5	Knock control in the automotive industry	39
2.3	Summary of the literature review	40
3	LES modelling approach	43
3.1	Principle of the LES	44
3.1.1	Concept of the LES	44
3.1.2	LES system of equations	45
3.2	Description of the used LES modelling approach	47
3.2.1	Modelling of the unresolved convective fluxes	48
3.2.2	Turbulent premixed combustion modelling	49
3.2.2.1	Combustion regime in a spark-ignition engine.	49
3.2.2.2	The Extended Coherent Flame Model for LES	50
3.2.3	Spark-ignition modelling	58
3.2.3.1	Modelling of the initial burned gases kernel	60
3.2.3.2	Laminar flame kernel growth and transition towards a prop- agating turbulent premixed flame	61
3.2.4	Auto-ignition modelling	62
II	LES of an Industrial Direct-injection Spark-ignition Engine	65
4	The RENAULT 1.2 TCe 115 engine	67
4.1	Engine characteristics and geometry	68
4.2	Choice of the reference operating point	70
5	Wall Temperature Distribution by CHT Simulation	75

5.1	CHT methodology	76
5.2	Computational domain for the CHT simulation	77
5.3	Computational set-up	79
5.3.1	Computational mesh	79
5.3.2	RANS approach for the combustion simulation	80
5.3.3	Boundary conditions	81
5.3.4	Material properties	82
5.4	Results and Validation	83
5.4.1	Validation of the RANS simulation	83
5.4.2	Validation of the CHT predictions	84
5.5	Conclusion	86
6	LES of the RENAULT 1.2 TCe 115 Engine	89
6.1	Numerical set-up	90
6.1.1	Computational meshes	90
6.1.2	Inlet and outlet boundary conditions	92
6.1.3	Direct fuel injection	93
6.1.4	Numerical parameters and combustion modelling	94
6.1.5	Wall boundary condition	95
6.2	Validation of the LES at ROP	96
6.2.1	Check on actual and target boundary conditions	96
6.2.2	Quality of the LES	97
6.2.3	Comparison between LES and experimental results	98
6.2.3.1	Cyclic combustion variability at ROP	99
6.2.3.2	Knock at ROP	102
6.3	Spark-timing sweep	104
6.4	Summary of Part II	108

III	LES analysis of Engine Knock	109
7	Characterization of Engine Knock	111
7.1	Limits of pressure oscillations-based indicators	112
7.1.1	Impact of the probe location	112
7.1.2	Impact of the method of analysis	113
7.2	A CFD-based indicator to quantify auto-ignition	114
7.2.1	Definition of the Computational Knock Index	115
7.2.2	Removing cool flame impact in the CKI calculation	115
7.3	Computational Knock Index vs. Knock Intensity	120
7.3.1	Definition of a knocking cycle	120
7.3.2	Correlation between CKI and KI	121
7.4	Conclusion	123
8	Investigations of Engine Knock	125
8.1	Knock and combustion speed	126
8.1.1	Correlation between CKI and combustion speed	126
8.1.2	Exploring the origins of the combustion speed variability at ROP . . .	128
8.1.2.1	Timing of appearance of the combustion speed variability . .	129
8.1.2.2	Specific characteristics of the fast and slow combustion cycles	129
8.1.3	CKI as a function of \mathbf{CA}_{50} for the 150 simulated cycles	140
8.2	Knock and premixed flame shape	141
8.2.1	Correlation between CKI and the remaining proportion of fuel mass .	141
8.2.2	Characterizing the flame shape	145
8.2.3	Analysis of individual cycles	147
8.2.3.1	Exploring the distribution of end-gas	148
8.2.3.2	Exploring the first auto-ignition spots	152
8.2.3.3	Characterizing the secondary auto-ignition spots	154
8.2.3.4	Summary of the analysis on individual cycles	159

8.2.4	Statistical analysis	161
8.3	Summary of Part III	164
Conclusions and Perspectives		167

CHAPTER

1

Introduction

1.1 Environmental context

Over the past decades, the rising concern about the environment has led legislators to impose more and more stringent environmental standards, in order to limit the level of greenhouse gas (GHG) emissions. Between 1990 and 2015, GHG emissions in the European Union (EU) were down by 22% (*Eurostat source*), and already surpasses the 2020 target. Figure 1.1 shows the relative contribution of the main source sectors in terms of GHG emissions. Within the positive evolution, transport is the only domain to increase its contribution, from 15% in 1990 to 23% in 2015. This is explained by the impressive increase of international flight number, and also by the tremendous growth of the world's vehicle fleet, the amount of which has already exceeded 1 billion units in 2010.

Considering the population growth and the subsequent increasing demand in vehicles, this trend will not be reversed in the next decades. The OECD¹ forecasts that the number of vehicles registered worldwide would reach between 2 billion and 3.2 billion by 2050, depending on the considered scenario. As a consequence, the level of acceptable CO_2 emissions (identified as the main GHG) is highly restricted and regularly lowered by the EU, with an average limit for each car manufacturer decreasing gradually, see Figure 1.2.

In this context, electric cars appear as a promising alternative to Internal Combustion Engines (ICE). However, even if the market share of electric vehicles is in constant expansion, it only represented 1.5% of the new vehicles registrations in 2016. In response to today's consensus on pollutant emissions in a global context of growing demand, car manufacturers have no choice but to improve the overall efficiency of ICE.

¹Organisation for Economic Co-operation and Development

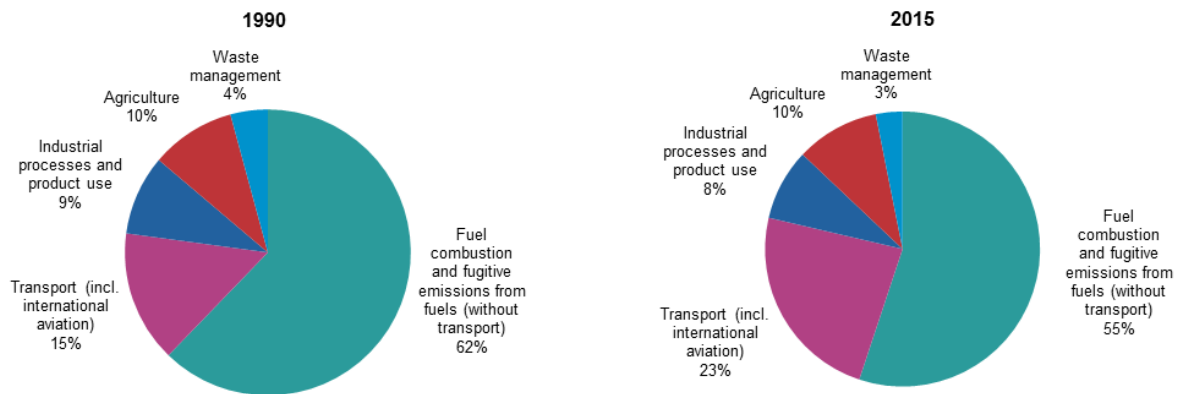


Figure 1.1: Contribution of each source sector to GHG emissions (source Eurostat).

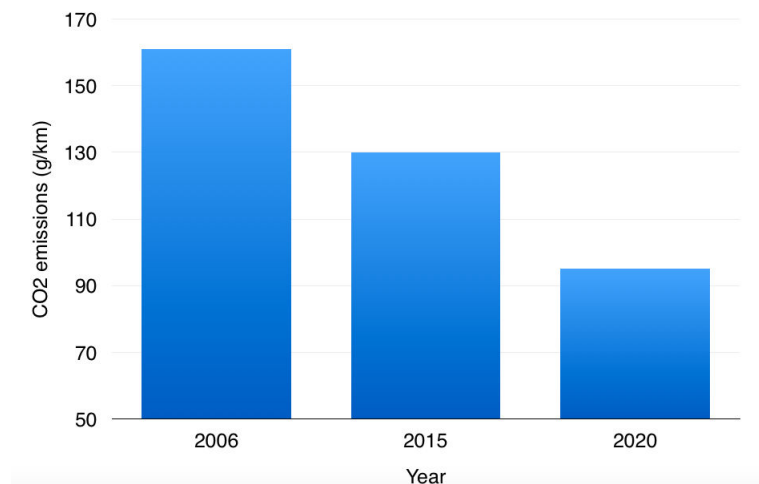


Figure 1.2: Evolution of the legislation in terms of CO₂ emissions (per vehicle).

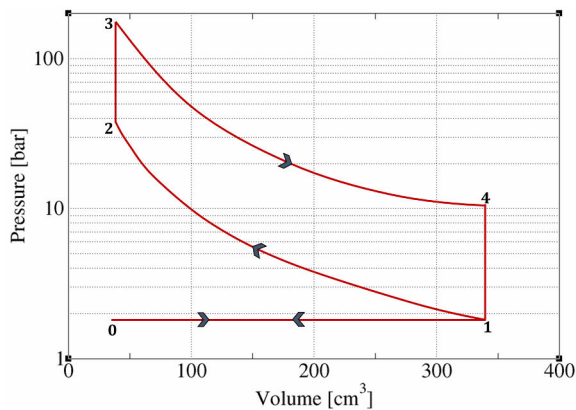
1.2 Basic operation of a modern spark-ignition engine

Most ICE produced in the automotive industry are based on the reciprocating piston principle, which relies itself on the combustion of an air-fuel mixture. The burned gases expansion produced by the reaction applies a direct force on the piston, transforming the chemical energy into mechanical work. ICE mainly consist in two technologies: spark-ignition (gasoline) engines and compression-ignition (diesel) engines. On the one hand diesel engines have a high efficiency but they require complex exhaust after-treatment systems, on the other hand spark-ignition engines have a lower efficiency but their exhaust gases are easier to treat. Nowadays, spark-ignition engines are gaining market shares, mainly due to controversies

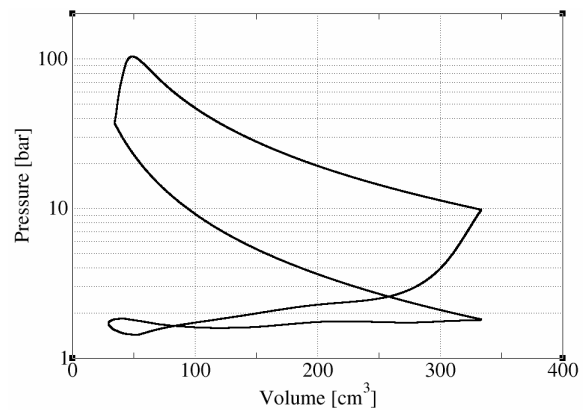
about the pollutant emissions of diesel engines.

The Otto cycle constitutes a simple approximation to describe the basic operation of a four-stroke spark-ignition engine. Figure 1.3a illustrates the idealized thermodynamic Otto cycle in a P-V diagram:

- $0 \rightarrow 1$: Isobaric intake stroke. During the downward movement of the piston, intake valves are opened, the combustible mixture is aspirated through the intake manifold into the cylinder.
- $1 \rightarrow 2$: Adiabatic compression stroke. The valves are closed. The mixture is compressed by the upward piston motion.
- $2 \rightarrow 3$: Isochoric combustion. The piston is at top-dead center (TDC), a spark-discharge ignites the homogeneous air-fuel mixture, and the burned gases expansion increases the pressure in the cylinder.
- $3 \rightarrow 4$: Adiabatic power stroke. Useful mechanical work is produced during this expansion process. The high pressure in the combustion chamber exerts a force on the piston and pushes it towards bottom-dead-center (BDC).
- $4 \rightarrow 1$: Isochoric heat rejection. Exhaust valves open. Since the in-cylinder pressure is higher than the exhaust manifold pressure, burned gases are sucked out of the combustion chamber.
- $1 \rightarrow 0$: Isobaric exhaust stroke. The upward movement of the piston pushes the remaining burned gases out of the cylinder.



(a) Ideal Cycle



(b) Actual Cycle (measured experimentally on the Renault 1.2 TCe 115).

Figure 1.3: P-V diagram of an ideal Otto cycle in comparison to an actual engine cycle.

In a real four-stroke engine, Figure 1.3b shows that there is no such an idealized thermodynamic process:

- The burning speed is not fast enough to be considered as isochoric. First the spark-discharge initiates the combustion at the spark-plug location. Subsequently a turbulent premixed flame develops from the spark-plug, propagates towards the fresh gases at the velocity relative to the flow S_d , and extinguishes at the wall.
- The difference of temperature between the gases inside the cylinder and the walls implies heat transfer at the interfaces, such that there is no adiabatic process in a spark-ignition engine.
- The pressure during the exhaust stroke is higher than during the intake stroke, thereby generating a negative work. It is particularly the case in naturally aspirated engines, in which the air-fuel intake depends solely on the atmospheric pressure.

Over the past century, several strategies have been employed to improve the engine efficiency. Modern spark-ignition engines are now mostly equipped with a turbocharger. It removes some of the energy from the exhaust flow and transfers it to the intake flow, in order to increase the intake pressure. A common practice schematized in Figure 1.4 combines the turbocharger with a smaller engine (reduced engine displacement). This concept called *engine downsizing* [97] brings the engine operation to thermally more efficient high loads. Shown in Figure 1.5, the smallest Specific Fuel Consumption (SFC) values are reached under high loads (high mean effective pressure).

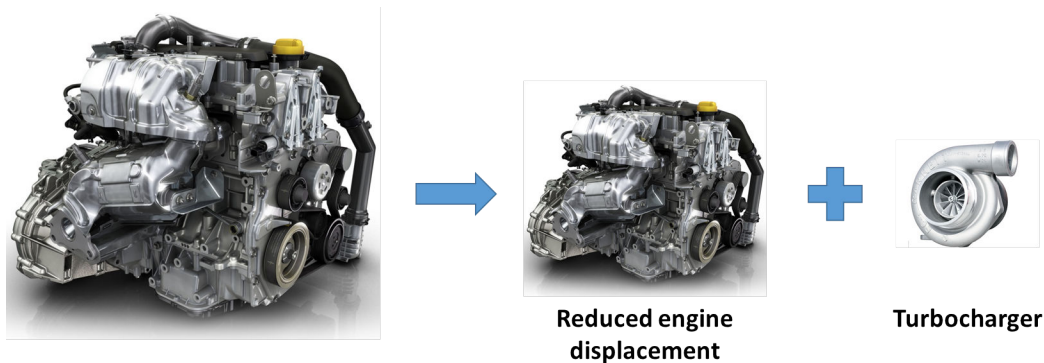


Figure 1.4: Principle of downsized engines.

In addition, the automotive industry has been moving from traditional port fuel injection (PFI) to direct fuel injection (DI). Whereas in PFI engines the fuel is injected in the intake port where it mixes with air, in DI engines only air enters through the intake ports, and the fuel is directly sprayed inside the cylinder. The mass of fuel directly injected in the cylinder can be better controlled to an optimum, thus reducing the consumption of fuel. However, the air-fuel mixing only takes place in the combustion chamber, mainly during the compression stroke. This leaves less time to achieve homogeneous mixture conditions at spark-timing, and the resulting stratified mixture may significantly impact the combustion process.

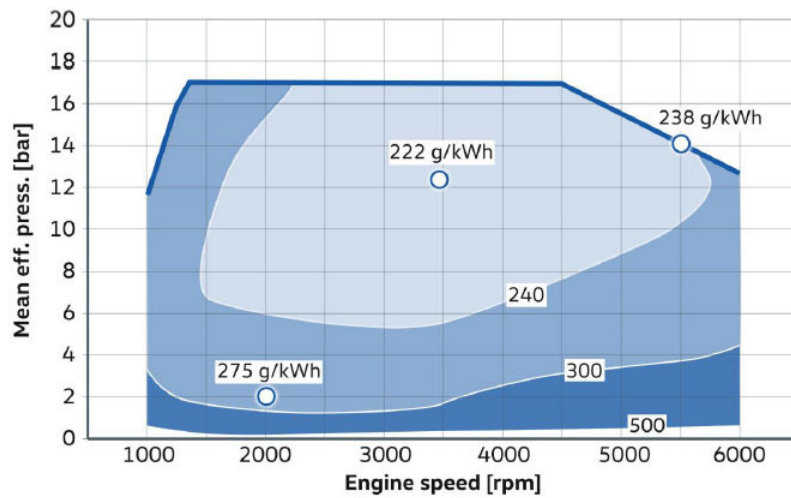


Figure 1.5: Specific Fuel Consumption map of the 1.5L TSI engine by VW. Re-printed from [35].

1.3 Introduction to engine knock

The characteristic of spark-ignition engines is the controlled combustion initiation by the spark-plug. Illustrated in Figure 1.6a and 1.6b, a spark-discharge triggers a turbulent pre-mixed flame that propagates through the combustion chamber in direction to the wall. In a normal combustion scenario, all the fresh gases situated inside the combustion chamber are consumed by the turbulent pre-mixed flame.

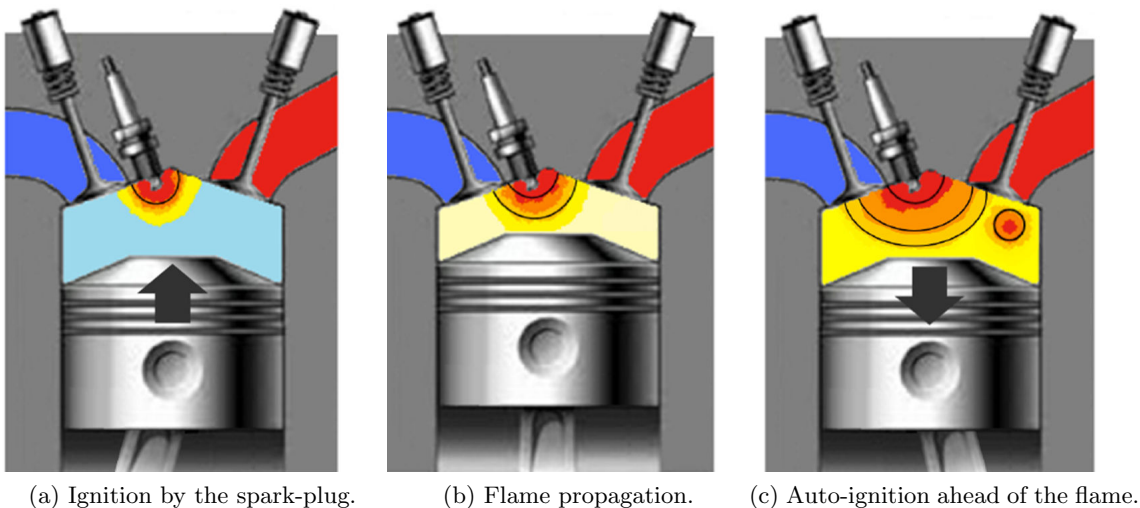


Figure 1.6: Illustration of a knock event in a spark-ignition engine.

Besides this normal combustion scenario, Figure 1.6c schematizes a different one. As the premixed flame propagates, the remaining fresh gases located closest to the walls, the so-called *end-gas*, are compressed between the flame front and walls. They see increasing levels of pressure and temperature, which may lead in extreme cases to the spontaneous ignition in front of the premixed flame front. This sudden auto-ignition is highly exothermic and may generate a pressure wave that reflects on walls and induces high-frequency oscillations in the local cylinder pressure. It is these pressure oscillations, which transmitted to the engine structure produces a characteristic pinging noise that is called *engine knock*. In the literature, auto-ignition and knock have sometimes been allowed to become synonymous, but it should be specified that knock is solely a consequence of auto-ignition. In 1947, Miller [86] simply defines knock as an "objectionable noise outside the engine". Following the terminology of König and Sheppard [71], "*auto-ignition refers to chemical reaction accelerating to spontaneous ignition of the mixture*", while "*the term knock is restricted to the physical manifestation of abnormal oscillations in the cylinder pressure during combustion*".

Knock should not be confused with *rumble*. The former results from a local auto-ignition event after the spark-timing, whereas the latter, illustrated in Figure 1.7, relates to the pre-ignition of the charge, i.e prior to spark-timing. Pre-ignition is also a critical topic in engine developments, but its sources involve different mechanisms as compared to knock [31] [134] [104], which are not the subject of this thesis. Within the framework of this thesis, focus is kept on engine knock.

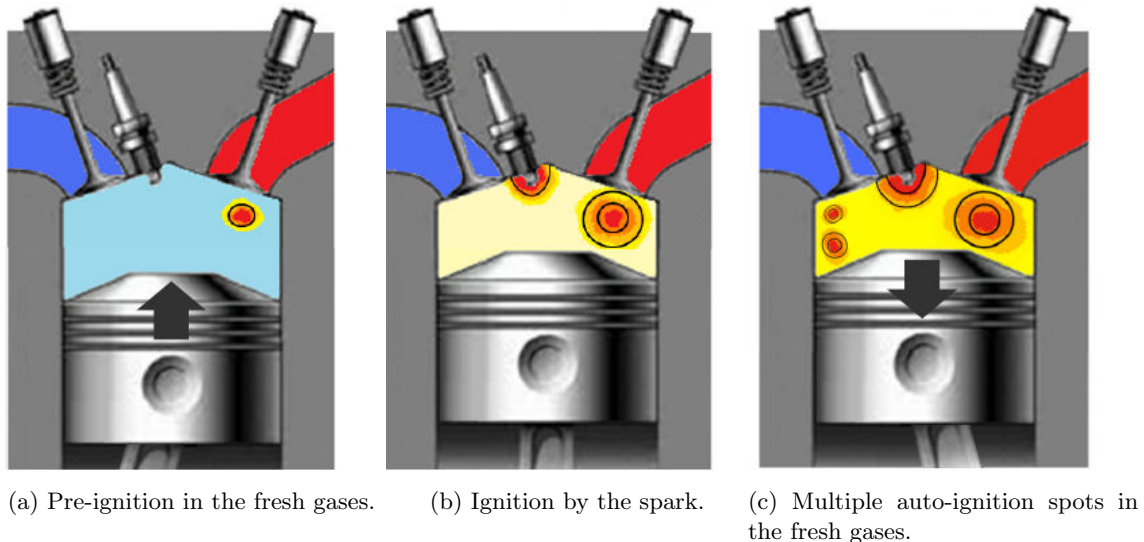


Figure 1.7: Illustration of rumble in a spark-ignition engine.

Knock is known for its negative impact on the engine operation:

- In the case of severe knock, the combustion chamber walls can be subject locally to extreme pressure levels, possibly beyond their design limit, causing the failure of the

engine structure.

- Repeated weak or moderate knock weakens the engine structure by thermomechanical fatigue, progressively leading to an erosion of the combustion chamber walls and so to a reduction of the engine service life. Figure 1.8 shows an example of piston erosion.
- The audible pinging noise characteristic of knock may perturb the driving comfort and is unacceptable in today's vehicles.



Figure 1.8: Erosion of the piston due to knocking combustion

Nowadays, the most effective strategies to limit the appearance of knock often have a negative impact on the engine efficiency. This is why knock is known as a major barrier impeding further improvements of the engine efficiency. This is even more true with the supercharging of the engine that is applied together with downsizing. Indeed the high loads, which result in more severe thermodynamic conditions inside the cylinder, tend to increase the knock tendency.

Knock is a difficult phenomenon to investigate, since auto-ignition depends on the local conditions in the end-gas, which fluctuate from cycle to cycle. This cyclic variability, referred to as *Cyclic Combustion Variability* (CCV) explains that auto-ignition occurs at different locations and timings and not in all engine cycles.

In this context, industrial and research units have developed advanced experimental techniques for visualizing auto-ignition inside the combustion chamber, and accessing characteristic knock variables. Nonetheless, the information extracted is not always sufficient to draw conclusions, since even the most advanced experimental apparatus cannot give a full access to all variables everywhere inside the combustion chamber.

In complement to experiments, computational approaches can be of great support. In particular, the constant increase in computational resources made realistic the use of Large-Eddy Simulation (LES) for studying engine knock. LES naturally solves in time and space the largest turbulent structures of the flow. This was shown in published research to allow reproducing CCV in the engine, and thereby the cyclic varying nature of knock. Thus, LES seems

adapted to bring a new insight into engine knock and support the development of innovative combustion chambers.

1.4 Objective of the thesis

The present thesis finds itself at the center of a partnership between RENAULT and IFPEN, which aims at exploiting LES to investigate knock. It is a continuation of the previous theses by A. Robert [115] and A. Misdariis [87], who demonstrated the ability of LES to predict knock events.

The main objective of this thesis is to contribute to the characterization and understanding of the appearance of knock in an industrial engine, by using the potential of LES shown in previous theses.

In this perspective, the present study includes some important intermediate steps:

- The first step consists in selecting an appropriate LES approach able to predict knock. This LES should include all the physical and chemical phenomena likely to influence knock in the engine: namely internal flow aerodynamics, fuel direct-injection, spark-ignition, turbulent premixed flame propagation, wall heat transfer and auto-ignition.
- In order to perform an as predictive as possible LES, with an accurate prediction of the in-cylinder conditions, a correct modelling of heat transfer at the walls is considered as essential. Hence, a coupled fluid-solid simulation should be performed to accurately estimate the wall temperature distribution, so that it can be imposed as a boundary condition for the LES.
- LES results should be compared to experimental findings in order to assess the accuracy of the simulation in terms of CCV and knock prediction. To do so, a common approach should be applied to the experimental and simulation results.
- LES results should be exploited in order to propose a meaningful characterization of the knock event in an engine cycle. This characterization should allow in particular to analyse and further deepen the understanding of the mechanisms that impact knock.

The long-term objective is that the knowledge resulting from this thesis could help in an industrial context to improve the design of innovative combustion chambers.

The present work relies on the AVBP solver [116], co-developed by IFPEN and CERFACS. It solves for the compressible, reactive Navier-Stokes equations on hybrid, unstructured meshes. It features turbulent combustion models and is able to handle moving grids, necessary for CFD studies of ICE.

1.5 Structure of the manuscript

Part I reviews major research on engine knock, and presents the LES approach used in the course of this thesis to predict its occurrence:

- *Chapter 2* compiles a wide range of published research that contributed over the past century to understand knock. It comprises studies explaining the fundamentals of auto-ignition, as well as experimental and numerical research performed to investigate the knock influencing parameters in engine-like conditions.
- *Chapter 3* describes the LES modelling approach followed in this thesis. It first recalls the LES system of equations to be solved, and then presents the models used to account for the physical and chemical phenomena involved in the combustion chamber.

Part II presents the setting-up and validation of the LES of the industrial RENAULT 1.2 TCe 115 engine:

- *Chapter 4* presents the features of the engine. It also describes the *reference operating point* (ROP), which was selected in an available experimental database and used for the LES.
- *Chapter 5* is dedicated to the calculation of the temperature distribution at the walls. This is a key input for the LES, thus it is calculated in an adequate coupled fluid/solid simulation.
- *Chapter 6* presents the numerical parameters used in the LES. The resulting approach is validated by comparing its predictions with experimental findings at ROP. Finally it proposes a computational spark-timing sweep, simulated to enlarge the database to stronger knocking levels.

Finally, Part III presents the exploitation of the LES database:

- *Chapter 7* introduces a CFD-based indicator used to characterize knock. The results based on this indicator are compared to the one obtained with a commonly used experimental knock indicator.
- *Chapter 8* presents the methodologies and tools developed in order to analyse and identify the mechanisms that control knock. It investigates in particular the link between knock and CCV.

1.6 Congress and publications

Chapter 5 is the subject of a SAE Technical Paper [79], exposed at the SAE WCX17 congress in Detroit, MI (USA).

CHAPTER 1. INTRODUCTION

Chapter 8 was the subject of a presentation at the CRCT 2018 in Toulouse (FRANCE).

Chapter 7 and *Chapter 8* are the subject of a scientific paper (in progress), which will be proposed for publication in the International Journal of Engine Research (IJER).

Chapter 7 and *Chapter 8* will be the subject of a presentation at the LES4ICE 2018 congress in Rueil-Malmaison (FRANCE).

PART I

AUTO-IGNITION AND ENGINE KNOCK MODELLING

Engine knock has been widely investigated in the past, using both experimental or numerical approaches. The objectives of Part I are twofold:

1. To give an overview of the state of the art of the current understanding of engine knock,
2. To present the fundamentals of LES, and to detail the combustion models used in this thesis.

Chapter 2, entitled **A literature review of engine knock**, proposes a review of published research that contributed to a better understanding of engine knock. Knock being the result of auto-ignition in the end-gas, this Chapter first focuses on the auto-ignition mechanisms. Then, focus is put on published research that investigated knock in engine-like conditions.

Chapter 3, entitled **LES modelling approach**, aims at describing the modelling approach used in this study. It starts with a description of the fundamentals of LES, and then presents the combustion models implemented in AVBP code that were used in the course of this thesis.

CHAPTER

2

A literature review on engine knock

Contents

2.1	Auto-ignition of a premixed air-fuel mixture	26
2.1.1	Rating of fuels propensity to knock: the Octane Number	26
2.1.2	Auto-ignition chemistry fundamentals	27
2.1.3	Auto-ignition chemistry modelling	29
2.1.4	Theory of auto-ignition propagation in the surrounding fresh gases .	31
2.2	Knock in spark-ignition engines	33
2.2.1	Optical diagnostics of knock in engines	33
2.2.2	Knock detection based on pressure oscillations analysis	35
2.2.3	Key parameters influencing knock	36
2.2.4	Knock and cyclic combustion variability	38
2.2.5	Knock control in the automotive industry	39
2.3	Summary of the literature review	40

This Chapter aims at providing a state of the art review of published research that contributed to the understanding of the sources and influencing parameters of engine knock. Auto-ignition of the air-fuel mixture being the precursor to engine knock, *Section 2.1* focuses on the auto-ignition phenomenon itself. This section first explains how the fuel resistance to auto-ignition has been defined based on pioneering investigations. It then summarizes the fundamental of auto-ignition chemistry, which, for a given fuel, strongly varies in particular depending on the thermodynamic conditions. It will allow to review different published strategies that can be used to model the onset of auto-ignition in a Computational Fluid Dynamics (CFD). Finally, the propagation of the auto-ignition front according to the surrounding fresh gases conditions will be discussed. *Section 2.2* is based on experimental and computational investigations on knock performed in engine-like conditions. It first proposes an optical observation of the phenomenon to visualize its relation to engine knock. Then, it presents the commonly used strategy used to characterize knock events, and finally discusses the parameters and strategies able to influence such knock events.

2.1 Auto-ignition of a premixed air-fuel mixture

2.1.1 Rating of fuels propensity to knock: the Octane Number

One of the pioneering investigators of engine knock was H. Ricardo, who exposed in the 1920's his theory on the subject and its relation to the fuel [109]. Even if the origins of knock were not understood, he noticed that some fuels were worse than others with regard to the phenomenon. This led in 1921 to a series of tests for the Shell group, in which many fuels were investigated in a variable compression ratio research engine, in order to determine the highest useful compression ratio (H.U.C.R) at which a fuel could be used.

This led the Cooperative Fuel Research Committee to develop a standardized knock testing in the early 1930's, aiming at rating gasoline fuels. Standardization is based on the *Octane Scale*, first proposed in 1927 by G. Edgar [34], and has remained unchanged till present days. The gasoline fuel under investigation is tested in a single cylinder CFR engine with adjustable compression ratio. To evaluate its *Octane Number* (ON), two reference standard hydrocarbons are used to benchmark the fuel under investigation: iso-octane, which is resistant to auto-ignition (ON = 100 by definition), and n-heptane, which easily auto-ignites (ON = 0 by definition). Thus, the ON of the gasoline fuel is the percentage in volume of iso-octane and n-heptane in the mixture of these, that would have the same knock characteristics as the investigated gasoline. For instance, a gasoline fuel with the same knock characteristics as a mixture made of 95% iso-octane and 5% n-heptane in volume fraction has an octane ON = 95. As a result, the higher the ON, the greater the tolerance to knock.

There are two standardized measurement techniques: Research Octane Number (RON) ASTM D2699 and Motor Octane Number (MON) ASTM D2700 [3]. They use the same test engine but within different operating conditions, in recognition of the fact that different fuels exhibit varying auto-ignition propensities under different engine conditions. RON is measured with a low inlet temperature (325K) and speed (600 rpm), MON is measured at higher inlet temperatures (422K) and speed (900 rpm).

Even if the octane scale is still the dominant standard in gasoline fuel rating, there are a number of deficiencies related to this approach [11]:

- It is based on an almost 100 years old engine test, and practical engines operating conditions are markedly different from the ones of the 1930 CFR engine,
- Modern gasoline fuels are made of hundred of species and only contain less than 6% of iso-octane and n-heptane [12],
- Some fuels have an anti-knock quality superior to iso-octane, for instance ethanol,
- Burluka et al. [15] showed that a real gasoline fuels and its representative iso-octane/n-heptane mixture may have different knock onset times.

2.1.2 Auto-ignition chemistry fundamentals

The auto-ignition delay τ_{AI} is a more physical parameter for characterizing auto-ignition than the RON and MON. It represents the time for a homogeneous air-fuel mixture to ignite spontaneously at a certain temperature and pressure. Figure 2.1 shows auto-ignition delays for a stoichiometric mixture of iso-octane. The auto-ignition delay strongly varies as the temperature and pressure change. At relatively high (left side of the graph) and low (right side of the graph) initial temperatures, the auto-ignition delay rapidly increases in proportion to the temperature. These two regions are separated by a Negative Temperature Coefficient (NTC) region, in which the relationship is reversed, i.e the auto-ignition delay increases in proportion to the temperature. The resulting S-shape curve is an indicator of the complex auto-ignition chemistry of the fuel.

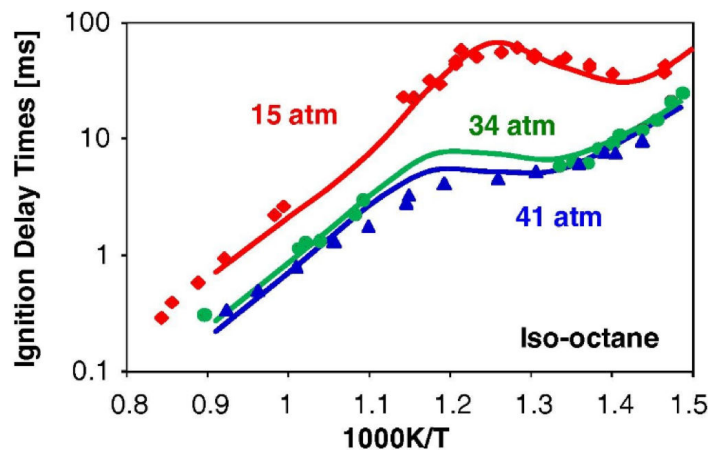


Figure 2.1: Auto-ignition delay τ_{AI} for iso-octane under various operating conditions. Re-printed from Mehl et al. [84].

The auto-ignition of the fuel in contact with air (oxygen) is not a one-step chemical reaction leading to the equilibrium products, mainly CO_2 and H_2O . In reality it is related to the oxidation of the many hydrocarbons that compose the fuel, and consists in multiple successive intermediate reactions involving thousands of intermediate species. Because the predominant intermediate reactions change depending on the pressure, temperature and mixture composition, the oxidation of the fuel does not follow a single pathway [29] [135]. However, reaction pathways can be simply classified into two ranges: high- and low-temperature chemistry [128].

Figure 2.2 uses ignition delays to illustrate the low- and high-temperature ranges for a stoichiometric mixture of iso-octane:

- In the case of a relatively low initial temperature, $T = 700\text{K}$ in Figure 2.2a, auto-ignition of the air-fuel mixture presents a two-stage behaviour. After an induction period $t = \tau_{CF}$, the auto-ignition process reaches a first ignition delay shorter than the auto-ignition delay τ_{AI} . At this instant $t = \tau_{CF}$, the chemical activity in the air-fuel mixture produces a pale blue chemiluminescence denoted as *cool flame* [36] [37]. The cool flame is characterized by a small consumption of the air-fuel mixture and a modest heat release, with a temperature increase that generally does not exceed 200K [108] [107]. Nonetheless, the heat added to the reacting system and the intermediate species generated accelerate reactions for $t > \tau_{CF}$. Thus, the cool flame is followed by a second stage ($t = \tau_{AI}$) that corresponds to the highly exothermic main auto-ignition.
- In the case of a relatively high initial temperature, $T = 900\text{K}$ in Figure 2.2b, auto-ignition occurs in a single-stage after a delay $t = \tau_{AI}$. There is no more cool flame, only the high-temperature chemistry drives the fuel oxidation [129].

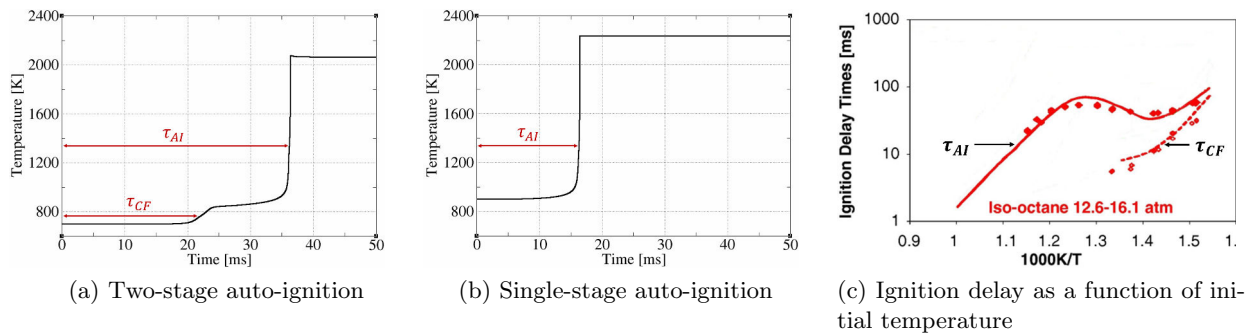


Figure 2.2: Illustration of single-stage and two-stage auto-ignition for iso-octane in air at stoichiometric conditions and $P = 15 \text{ atm}$. (a) and (b) adapted from Yoo et al. [133]. (c) re-printed from Mehl et al. [84].

In Figure 2.2c, one can see that the NTC region ($1.3 < 1000\text{K}/T < 1.5$) results from the two-stage ignition process, and corresponds to a transition between low- and high-temperature ranges. As the initial temperature increases in the NTC region and approaches $1000\text{K}/T = 1.3$ ($T = 770\text{K}$) in the Figure, cool flame reactions slow down, until their impact on the auto-ignition process becomes negligible.

2.1.3 Auto-ignition chemistry modelling

In CFD, selecting a sufficiently realistic model to predict auto-ignition onset is an important step. The most accurate representation of the complex processes is obtained with detailed chemical kinetic schemes able to cover the whole range of conditions met in industrial systems. However, real fuels are complex mixtures of hundreds of hydrocarbon species, and the development of a detailed mechanism comprising all of the compounds, elementary reactions, thermodynamics and molecular transport is intractable.

In order to reduce the degree of complexity, so-called surrogates are employed that represent the main thermodynamic and chemical characteristics of the real fuel, while containing a limited number of compounds requiring a limited number of oxidation steps to be modelled [46]. Commonly used surrogates for gasoline fuels contain iso-octane, n-heptane and toluene ; the so-called toluene reference fuels (TRF). Advances in experimental and kinetic modelling provided a detailed insight into TRF oxidation [28] [29], and allowed to generate detailed chemical kinetic schemes for gasoline surrogates [84]. However, solving detailed mechanisms during the computation remains excessively time consuming and not conceivable in piston engine simulations.

To overcome this difficulty, a first approach is to use reduced chemical kinetic schemes. The objective is to restrict the number of species and intermediate reactions to a minimum that is still able to reproduce key characteristics of the detailed scheme. Several reduced models for gasoline exist to date, such as the Shell model by Halstead et al. [53] or the reduced formulation of the detailed Lawrence Livermore National Laboratory (LLNL) kinetic mechanism by Mehl et al. [83]. As another example, Misdariis et al. [89] developed the Ignition to Propagation Reduced Scheme (IPRS), which was able to correctly predict auto-ignition delays as given by complex chemistry.

As another solution, a way to simplify the description of the complex auto-ignition chemistry is to introduce a progress variable. For instance in conditions where only high-temperature chemistry prevails, it has been shown that the progress towards auto-ignition can be described by the so-called Livengood–Wu integral [80]:

$$I = \int_{t_0}^t \frac{1}{\tau_{AI}} dt \quad (2.1)$$

In Eq. 2.1, I is the variable that describes the progress towards auto-ignition. A value $I = 1$ is a good approximation of when auto-ignition occurs. τ_{AI} can be determined by an empirical correlation [33] [73], but it can be also tabulated a priori with dedicated complex chemistry computations. In tabulation techniques, complex chemistry is solved in a homogeneous reactor for a wide range of operating conditions, and the results are stored in a look-up table. Tabulation techniques are particularly suited for CFD applications, as the simple reading of the auto-ignition progress in the table from known fresh gases conditions significantly reduces CPU costs. However, look-up tables with auto-ignition delays as the only tabulated variable can be used in some particular cases, e.g high performance engines, where only a single stage high-temperature auto-ignition is expected [44]. However in commercial spark-

ignition engines, auto-ignition may include cool flames. Since the heat release due to cool flame chemistry accelerates chemical reactions in the fresh gases, by-passing its contribution may lead to an erroneous estimation of auto-ignition delays.

To overcome this problem, Pires da Cruz [103] proposed an extension that uses tabulated values for τ_{CF} and τ_{AI} . Eq. 2.1 is solved from values for τ_{CF} and τ_{AI} in order to predict the cool flame and auto-ignition delays. However, in a closed vessel as a combustion chamber, such double delays strategy was found to lead to an overestimation of the main auto-ignition delay [22], because it supposes zero heat release during the cool flame period ($t = \tau_{CF} < t < \tau_{AI}$). In reality, low-temperature reactions proceed during the entire cool flame period, slightly but continuously increasing the mass of high temperature burned gases. As a result the in-cylinder pressure gradually increases, and so does the fresh gases temperature.

In response, Colin et al. [22] came to the conclusion that the instantaneous heat release by auto-ignition must be correctly estimated during all the cool flame period. Their approach, known as Tabulated Kinetics of Ignition (TKI), proposes to describe the auto-ignition process through the reaction rate ω_c^{AI} for a progress variable for auto-ignition c^{AI} , the values of which are interpolated in the TKI table, a priori calculated in a homogeneous reactor at constant pressure with complex chemistry. ω_c^{AI} are tabulated as a function of the local pressure, fresh gases temperature, equivalence ratio, dilution rate, and the progress variable c_{AI} . The progress variable for auto-ignition c_{AI} describes the proportion of fuel that is locally consumed by auto-ignition.

In its original formulation [22], the interpolation of ω_c^{AI} in the table was not applied from the beginning of the calculation. An intermediate species was used to calculate the cool flame delay, similarly to [103]. Once it was reached, a certain amount of heat was released, a priori tabulated using complex chemistry calculations. Then, the instantaneous reaction rate ω_c^{AI} was interpolated in the TKI table. This approach has been simplified by Knop et al. [68], and the use of an intermediate species is no more required. Instead, ω_c^{AI} values are interpolated from the beginning of the simulation, i.e from $c_{AI} = 0$. The instantaneous c_{AI} value is given by solving transport equations for respectively the mass fraction of fuel burned by auto-ignition and the mass fraction of a fuel tracer, which are presented later in *Section 3.2.4*. The accuracy of the TKI approach for predicting auto-ignition in spark-ignition engines has been demonstrated in RANS simulations [68], as well as in LES [78] [112] [113].

Within the tabulation category, there are several other models with various degree of complexity, depending on the number of quantities to be reproduced. More advanced tabulation approaches can be found in the literature, such as the Flame Prolongation of Intrinsic low dimensional manifold (FPI) model, which provides a more complete description of the chemistry by accounting for the evolution of all major species [48]. However, this model has never been used to predict auto-ignition in engine-like conditions. Generally, the higher the number of characteristics to be reproduced by the complex chemistry computations, the more complex the algorithm to accurately use the results in the CFD code, and particularly in cases as complex as the simulation of an ICE [61].

2.1.4 Theory of auto-ignition propagation in the surrounding fresh gases

In the early study by Oppenheim [93], the author considered auto-ignition in a perfectly homogeneous mixture. In this case, chemical reactions progress at the same rates in all the fresh gases, and so auto-ignition is reached evenly through the whole mixture. In practice, distributions of temperature and mixture composition are seldom completely homogeneous. This implies a spatial distribution of auto-ignition delays with the result that auto-ignition first appears locally at isolated *hot-spots*, also termed as *exothermic centres*. The sudden highly exothermic auto-ignition reaction at a hot-spot locally generates an overpressure, which propagates into the surrounding at the local sound speed. In the mean time, Zel'dovich [136] showed how gradients of reactivity around the auto-ignition spot create a propagating auto-ignition front, travelling by sequentially proceeding auto-ignition reactions. The propagation velocity of the auto-ignition front u_a was found to be roughly proportional to the reactivity gradient around the hot-spot:

$$u_a \approx \left(\frac{\partial \tau_{AI}}{\partial r} \right)^{-1} \quad (2.2)$$

with r the distance to the auto-ignition source. Based on the work of Zel'dovich, König et al. [70] applied Schlieren images to visualize the auto-ignition front and observe its mean propagation speed. The authors considered the case of a homogeneous mixture composition, such that heterogeneities arise only from temperature gradients. Three major modes of reaction propagation were to be distinguished:

1. **Thermal explosion:** In the case of a perfectly homogeneous temperature field, chemical reactions progress at the same rate at every location, and thus the auto-ignition appears evenly through the whole mixture.
2. **Deflagration:** In the case of strong temperature gradients, the auto-ignition propagation is subsonic, i.e at a velocity lower than the auto-ignition induced pressure wave.
3. **Developing detonation:** In the case of mild temperature gradients, the auto-ignition may in some conditions discussed below result in a detonation. Compared to a deflagration, there is a coupling between the chemical auto-ignition reactions and the resulting pressure wave. The fresh gases are sufficiently reactive so that the pressure wave is able to trigger auto-ignition in its wake, the heat release by auto-ignition feeds the pressure wave to significantly increase its amplitude. Auto-ignition and pressure wave are thus coupled into a so-called developing detonation wave.

The existence of these three modes was confirmed in a coupled experimental and 2-D simulation study by Pan et al. [95]. More recently, Gu et al. [52] used 1-D DNS with detailed chemistry to complete the previous description with two additional modes: the supersonic deflagration or shockless detonation, and the laminar deflagration. However these two modes, corresponding respectively to cases of extremely weak temperature gradients and extremely strong temperature gradients are unlikely under spark-ignition engine conditions.

Among the different modes of propagation, the detonation has received a particular attention in the literature [13] [6]. As it will be discussed in *Section 2.2.3* it is within a detonation mode that the magnitude of the pressure wave reaches extreme and destructive levels [95] [113]. Figure 2.3 summarizes research by Bradley et al. [13] who proposed to delimit conditions that lead to a thermal explosion, developing detonation and deflagration.

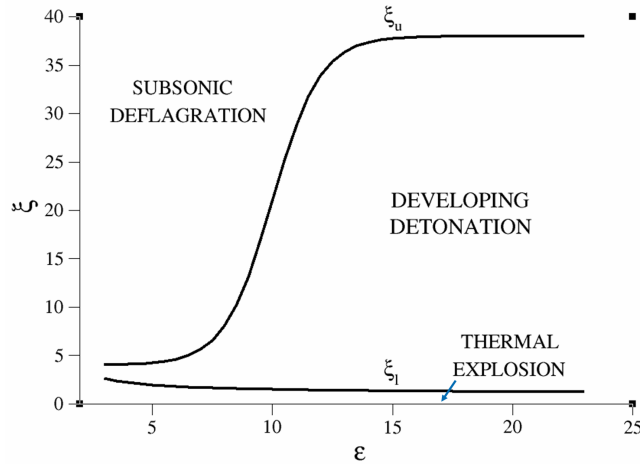


Figure 2.3: Modes of auto-ignitive reaction front propagation identified in the $\xi-\epsilon$ diagram of Bradley. Adapted from Bradley et al. [13].

The Figure exhibits two dimensionless parameters representing the coupling conditions of a developing detonation:

- The first one ξ , directly compares the velocity of the auto-ignition front u_a to the local sound speed a at which the pressure wave travels:

$$\xi = \frac{a}{u_a} \quad (2.3)$$

According to Zel'dovich and Makhviladze [81], chemical resonance clearly occurs at the condition $\xi = 1$. However this value $\xi = 1$ is more an approximate indicator, and in reality the auto-ignition front can develop into a detonation for values under or above unity [52].

- The second parameter ϵ , is given by:

$$\epsilon = \frac{r_0}{a\tau_e} \quad (2.4)$$

where r_0/a is the residence time of the pressure wave travelling at the sound speed a in the hot spot of radius r_0 . It is compared to the excitation time τ_e , which represents the rate to go from 5% to the maximum heat release by auto-ignition. Thus, ϵ compares the

time for the pressure wave to travel for a distance r_0 to the excitation time. It determines if auto-ignition is able to feed the pressure wave sufficiently rapidly to provoke an increase of its magnitude.

These two parameters allow to locate the peninsula for the three regimes. For $0 < \xi < \xi_l$, auto-ignition occurs evenly in the fresh mixture. For $\xi_l < \xi < \xi_u$, a coupling between auto-ignition front and pressure wave is observed. For $\xi_l < \xi$, the auto-ignition front propagation speed is subsonic, i.e behind the pressure wave travelling at the sound speed. One can observe that the developing detonation peninsula thins as τ_e decreases.

2.2 Knock in spark-ignition engines

Given the above understanding of the auto-ignition process, this Section focuses on investigations of the phenomenon under engine-like conditions. The reviewed studies are mostly based on Rapid Compression-Expansion Machines (RCEM) or single cylinder research engines.

2.2.1 Optical diagnostics of knock in engines

Under engine-like conditions, a pure thermal explosion with auto-ignition reactions that progress evenly throughout the whole mixture is improbable [71]. Reactivity gradients in the end-gas are inevitable, resulting from imperfect mixing of the fuel with air and residual burned gases, as well as heat transfer at the walls [96]. This is particularly true in direct-injection engines, in which the short period for the fuel to mix with air may result in significant inhomogeneities in the mixture composition and temperature distribution. Even in the case of a perfectly homogeneous mixture composition, the temperature field inside the combustion chamber is never homogeneous [72]. Kaiser et al. [63] specifically investigated the in-cylinder temperature field by laser-induced fluorescence (LIF). Starting from a homogeneous temperature field at BDC in the combustion chamber, significant thermal inhomogeneities rapidly developed during the compression stroke. The temperature fluctuations varies inside the combustion chamber, reaching 2% of the temperature difference between the gas phase and the wall. Larger fluctuations are more probably located near walls, but these can be easily convected by the turbulent flow toward the middle of the chamber [125].

In single cylinder research engines with optical access, the application of imaging techniques allows a visual observation of the combustion process inside the combustion chamber. In order to visualise auto-ignition, some intermediate species can be used as markers. For instance formaldehyde CH_2O is known as a characteristic radical for cool flame chemistry, while OH can be used as an indicator for the onset of main auto-ignition [66] [107] [117].

Under typical engine conditions, auto-ignition more probably occurs in a two-stage process, i.e cool flame chemistry followed by main auto-ignition [7] [66] [107] [117]. In Figure 2.4, cool flame chemistry was evidenced by the bright light in the end-gas, resulting from the chemiluminescence of CH_2O . As shown by Pöschl et al. [107], the related weakly exothermic reaction only provoke a slight increase of pressure in the cylinder and no oscillations

in the pressure signal. Still in Figure 2.4, cool flame chemistry is rapidly followed by main auto-ignition, materialized by the multiple black spots in the bright end-gas region appearing almost simultaneously at different locations, in response to the non-uniform reactivity in the end-gas. In [117] these auto-igniting hot-spots correspond to local sites of increased temperature as compared to the surrounding end-gas [117] [107]. Bauerle et al. [7] showed that local temperature fluctuations as small as 20 K are sufficient to ignite parts of the end-gas earlier than the surroundings.

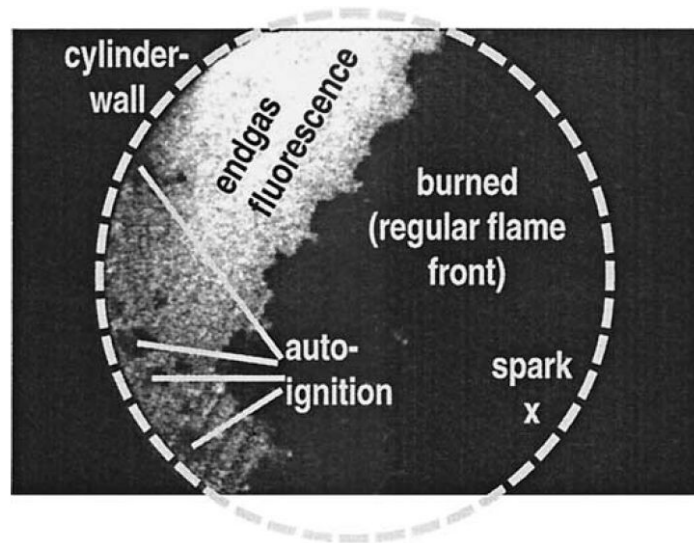


Figure 2.4: Visualization of auto-ignition spots in the end-gas by laser-induced fluorescence (LIF). Re-printed from Schiessl et al. [117]

Based on high-speed images of the auto-ignition and the local pressure measurement in a RCEM, Figure 2.5 taken from [66] illustrates a cycle with auto-ignition in the end-gas, as compared to a cycle without auto-ignition. The premixed flame propagates from the lower-right to the upper-left side.

In the lower set of images, auto-ignition appears on the upper-right side (image B), and then rapidly consumes the surrounding fresh gases. In the mean time, the fast energy release induced by the sudden auto-ignition immediately drives a strong pressure wave, which moves into the surrounding gases at the sound speed [11], and reflects on the wall. As a result, the local pressure shows oscillations characteristic of a knocking cycle.

In comparison, the so-called *regular* or *normal* cycle does not show auto-ignition in the end-gas, and accordingly there are no oscillations in the pressure trace. In [66], the *OH* emission peak characteristic of the onset of auto-ignition perfectly synchronizes with the start of the pressure oscillations. Nonetheless, an auto-ignition event does not necessarily promote engine knock [107], in the sense that no oscillations can be visible in the local pressure signal, although auto-ignition is observed.

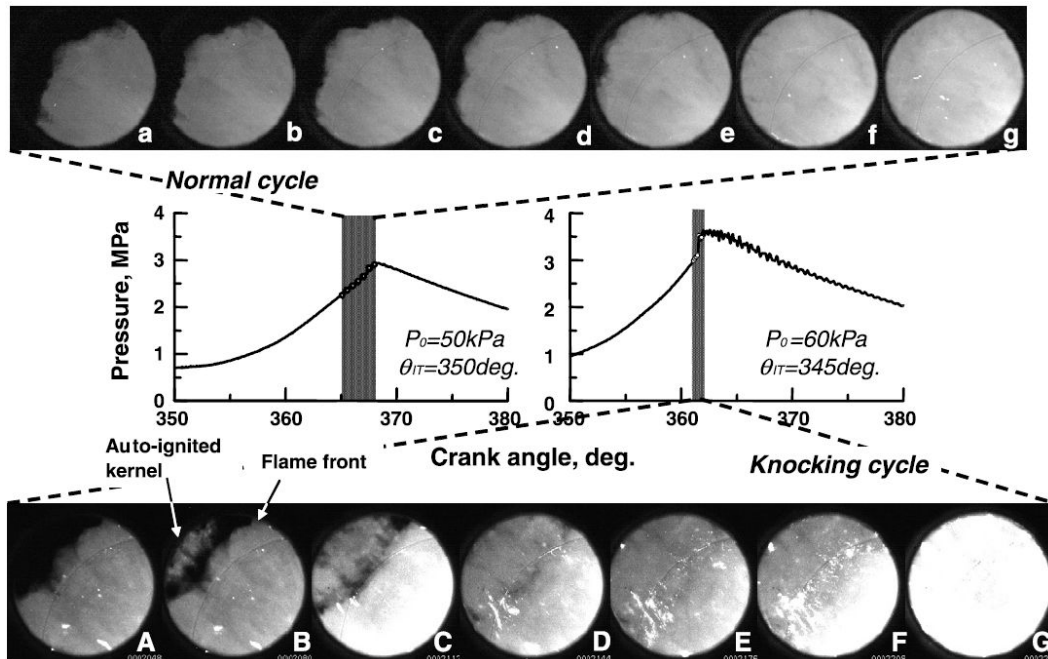


Figure 2.5: High speed images of the combustion in a normal cycle and a knocking cycle, and the impact of the auto-ignition on the in-cylinder pressure signal. Re-printed from Kawahara et al. [65].

2.2.2 Knock detection based on pressure oscillations analysis

As a solution to detect and quantify knock, optical access to an engine during industrial design is not realistic, so that other techniques were developed. Characterization of knock is commonly achieved through the analysis of the in-cylinder pressure oscillations, since they were shown to be connected to auto-ignition. The idea is thus to exploit the pressure signal to determine for each cycle the *Knock Intensity* (KI), which is basically proportional to the amplitude of the oscillations. Multiple methods of analysis exist and they can be easily applied to analyze the local pressure signal (MAPO, IMPO, DKI, SEPO, ROHR) [14] [26] [131].

However, even with the knowledge of KI, establishing a relationship between this quantity and the damage risks is usually based on experience, i.e there is no universal strategy to determine a maximum acceptable knock intensity KI_T [62]. Determination is generally achieved throughout a spark-timing sweep. From late spark-timing, it is progressively advanced to get closer to the optimal spark-timing, i.e the one that lead to an optimal combustion efficiency. Advancing the spark-timing tends to increase the propensity to knock, and so it is advanced until knock becomes audible for the engineer. Hence it is the experience of the test bench engineer, and in particular his audible assessment of the phenomenon that determine the threshold KI_T , and in the mean time the *Knock Limited Spark-Advance* (KLSA), which is the earliest spark-timing that can be set to stay below KI_T . KI_T also determines the percentage of knocking cycles per operating point, that is, the percentage of cycles with $KI > KI_T$. To summarize, KI_T and the resulting KLSA and percentage of knocking cycles fully depend

on the experience of the test bench engineer.

In addition, the local pressure oscillations are only an outward sign of the auto-ignition event, and they are dependent on the sensor type and its location in the combustion chamber [8]. In the experimental studies of Pan et al. [96], König et al. [71] and Pöschl et al. [107], the onset of the pressure oscillations and their amplitude was clearly function of the distance between the pressure transducer and the location of the auto-ignitive hot-spot. These observations were confirmed in a 3D RANS simulation by Corti et al. [25]. In addition, several studies have shown how the use of different methods to analyse the same set of local pressure signal leads to a different hierarchy of knocking cycles in terms of KI [26] [131]. Finally, the question of auto-ignition scenarii remains for the cases of which no pressure oscillations can be recorded.

Despite the limitations in the use of the local in-cylinder pressure oscillations to characterize a knock event, it is still the standard in the automotive industry.

2.2.3 Key parameters influencing knock

Based on the analysis of the local in-cylinder pressure oscillations to characterize the knock event, many studies have attempted to identify the parameters influencing knock.

Experimentally, König et al. [71] found a strong correlation between KI and crank angle of auto-ignition onset. When auto-ignition occurred late in the cycle, no pressure oscillations were recorded. However, when auto-ignition occurred earlier in the cycle (closer to TDC), it developed was followed by strong pressure oscillations. To go deeper in the analysis, KI was correlated on one side to the mass of fresh gases available at auto-ignition onset, and on the other side to the mean fresh gases temperature. If KI was found to be relatively independent of the mass of fresh gases available at auto-ignition onset, it clearly increased as with the mean fresh gases temperature at auto-ignition onset. In a RCEM, Tanoue et al. [122] also investigated the effect of initial temperature on knock. Contrary to the study by König et al. [71], the findings revealed that the mean fresh gases temperature does not directly control KI. Similarly to [71], the results showed that the mass fraction of fresh gases at auto-ignition onset does not directly affect KI.

On the other hand, some research studies have related knock to the residual unburned fraction of fuel at the onset of auto-ignition with success [30] [67]. In the LES of a single cylinder research engine by Robert et al. [112], knock was shown to be roughly proportional to the mass of end-gas consumed by auto-ignition. This led Chevillard et al. [18] to define a Computational Knock Index (CKI), which represents the total proportion of fuel burned by auto-ignition. This computational indicator is particularly interesting since it focuses directly on the auto-ignition event, rather than on the resulting pressure oscillations.

According to Bradley [11], knock is related to the auto-ignition mode, i.e to the reactivity gradient around the auto-ignitive hot-spot. In this context, the most damaging mode appears to be the detonation one, in which the coupling between the pressure wave and the auto-ignition front provoke a wave propagation velocity exceeding a thousand meters per second, as it was experimentally measured in [65] and [107]. In LES, Robert et al. [113] provoked developing detonation auto-ignition wave through an extreme early spark-timing.

Figure 2.6 taken from [113] is an example of the resulting local pressure signal, the peak to peak amplitude of which exceeds a hundred bars. In agreement with the theory of Zeldovich and Bradley, the detonation in Tanoue et al. [122] corresponded to relatively smooth temperature gradients around the auto-igniting hot-spot. Increasing the initial temperature in the fresh gases caused stronger gradients, thereby a slower auto-ignition front propagation, finally resulting in a weaker knock event. This suggest that an appropriate control of the temperature gradients inside the cylinder may help mitigating knock.

According to Poschl et al. [107], the transition to a detonation can be achieved by two mechanisms [107] [113]:

1. First following the description of Zel'dovich [136]. The reactivity gradient favours a fast propagation of the auto-ignition front, at a velocity close to the sound speed, possibly leading to the coupling between the auto-ignition front and the induced pressure wave.
2. The second possibility is the initiation as a consequence of a pressure wave, initiated by a previous auto-ignition spot. When propagating across the combustion chamber, this pressure wave travels through the end-gas, and significantly increases their reactivity. If the pressure wave is strong enough, it can initiate secondary auto-ignition spots in its wake, and if the surrounding unburned gases are reactive enough, a bidirectional coupling of heat release and pressure wave establishes.

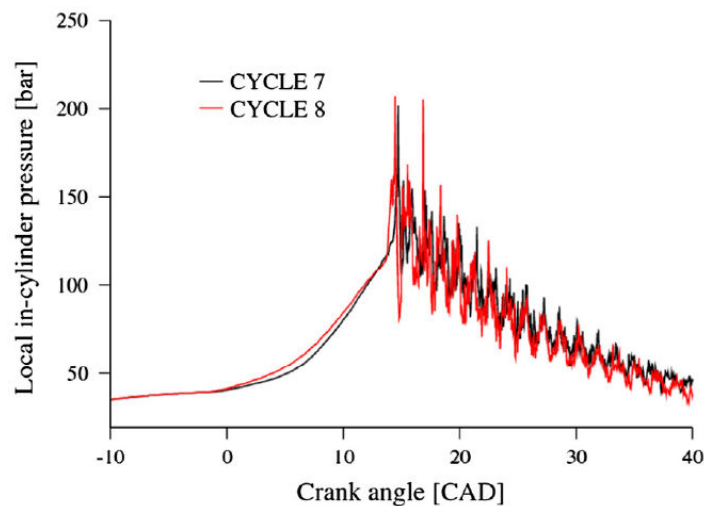


Figure 2.6: Oscillations in the local in-cylinder pressure caused by a transition of auto-ignition mode from deflagration to detonation. Re-printed from Robert et al. [113].

Auto-ignitive developing detonation has focused many attentions, due to its related extreme pressure oscillations that cause a rapid, if not direct, failure of the engine structure. In comparison, the parameters that control weak knock, corresponding to an auto-ignitive deflagration, have received much less attention. In the LES of Robert et al. [113], weak knock

corresponds to one or several auto-ignition spots inside the cylinder, which only consume the surrounding end-gas within a few centimetres around the auto-igniting hot-spot. As suggested in [107], a key role to avoid that weak knock turns into strong knock is the prevention of auto-ignition propagation across a long distance, to prevent any transition from a deflagration to a detonation mode.

2.2.4 Knock and cyclic combustion variability

At fixed operating conditions, spark-ignition engines are characterized by a cyclic variability in the combustion process, which is illustrated in Figure 2.7 by cycle to cycle variations in the in-cylinder pressure signal. This phenomenon is known as Cyclic Combustion Variability (CCV). It is the result of variations in the in-cylinder flow aerodynamics [38], ignition fluctuations [99] and mixture composition [1] [98].

The related cyclic variation of the propagation speed of the flame has two contradicting effects on the knock tendency [82]:

- On the one hand a faster propagation of the premixed flame rapidly consumes the air-fuel mixture, leaving less time for the end-gas to auto-ignite, thereby reducing the knock tendency [57].
- On the other hand, a faster propagation of the premixed flame globally results in an increase of the maximum in-cylinder pressure. This leads to a significant rise in the end-gas temperature, thus accelerating chemical reactions [17], and consequently increasing the knock tendency.

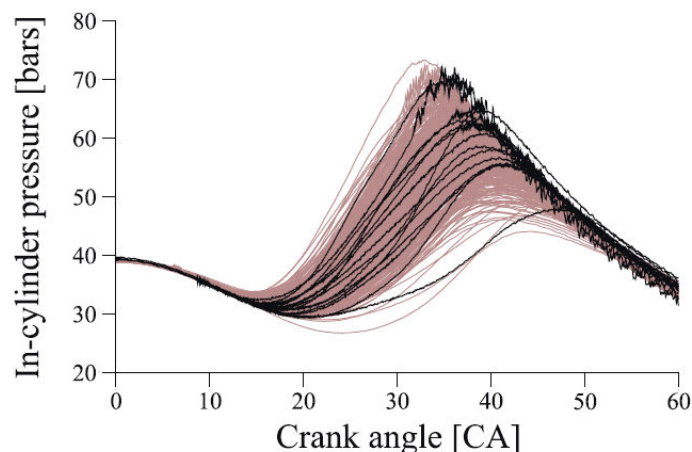


Figure 2.7: Cycle to cycle variations in the local pressure signal recorded experimentally (brown) and by LES (black) at fixed operating conditions. Re-printed from Robert et al. [112].

The cyclic variability in the local interaction between the flame and flow field also affect the flame curvature [69], resulting in significant variations in the flame shape, and thereby to fluctuations in the distribution of end-gas. As each cycle is different, conditions in the end-gas are never reproduced from one cycle to another, and auto-ignition appears neither at the same time nor at the same location [56] [65] [66] [71].

In Kawahara et al. [66], a different relation between the flame shape and auto-ignition is mentioned. The authors observed a negative curvature in the premixed flame shape around some auto-ignition spots, which did not appear in the regular cycles free of auto-ignition. They attributed this curvature to the cool flame chemistry, which could possibly influence the premixed flame propagation. This shows that the premixed flame shape may affect the knock tendency by influencing the distribution of end-gas in the cylinder, and at the same time that the auto-ignition chemistry modifies the flame shape.

2.2.5 Knock control in the automotive industry

Several strategies are relatively well known to mitigate knock in the engine:

- One of the most effective parameters is the spark-timing. Whereas part load conditions (with a moderate cylinder pressure) allow to calibrate the spark-timing to optimal thermal efficiency, a retard of the spark-timing is imposed for the highest loaded (knock sensitive) operating points in order to delay the combustion. This allows reducing the cylinder pressure rise, since the bulk of the combustion process occurs in a larger, faster expanding volume. As a result the temperature increase in the end-gas is reduced, thereby slowing down their chemical activity. However, this retarded spark-timing delays the combustion to sub-optimal phasing as compared to TDC, leading to a sub-optimal thermal efficiency [24]. Moreover, if all the cycles were similar, the definition of KLSA would be clear. Instead, the cyclic variability impose to take extra safety margins in the spark-timing.
- Optimizing heat transfer between the charge and the walls is another way to impact knock. In a spark-ignition engine equipped with a centrally situated spark-plug, Robert et al [112] showed with LES that auto-ignition predominantly appears on the exhaust side, a behaviour which was found to be related to the higher temperatures on the exhaust valves surfaces, as compared to the rest of the combustion chamber. This is why adaptive cooling systems can be designed to optimize convection in the coolant jacket, in particular to remove heat at the hottest wall surfaces [118]. Unfortunately, excessive cooling also increases heat losses, which in turns induces a deterioration of the thermal efficiency.
- Cooled EGR offers many advantages for the engine efficiency and is very effective to improve the knock tolerance [45] and [59]. Indeed EGR reduces the temperature and pressure rise during the engine cycle by increasing the overall constant specific heat of the mixture. Nonetheless, the benefits of EGR with regard to knock strongly varies with the fuel [2], and it is a known fact that high EGR ratios significantly impact the premixed flame propagation [75] and high EGR values can generate CCV [51].

- Finally, the use of high octane number fuels is a direct solution to reduce knock tendency in the engine. For instance, ethanol has excellent anti-knock qualities as indicated by its relatively high 109 RON [5]. Ethanol has long been regarded as the optimal gasoline-alternative for spark-ignition engines, and is nowadays widely used across the world. The benefit in using ethanol-blended gasoline further increases with the use of direct-injection. With DI, the latent heat of vaporization of the fuel can be directly extracted from the charge inside the cylinder, thus cooling it. This cooling effect is increased with ethanol, due to its larger heat of vaporization, as compared to typical gasoline [64] [121]. However, ethanol has a larger energy density, meaning that a higher mass of ethanol-blended fuel must be consumed to have the same efficiency as a standard gasoline.

2.3 Summary of the literature review

From the above literature review, some key information can be summarized:

- Auto-ignition results from the complex chemistry of the fuel when in contact with oxygen, which varies depending on thermodynamic conditions and mixture composition. Depending on the operating condition, auto-ignition in a spark-ignition engine may proceed in two stages: first the cool flame (low-temperature chemistry), rapidly followed by the main auto-ignition (high-temperature chemistry) of high heat release.
- The heat release by the cool flame is too weak to trigger knock, but it accelerates reactions in the fresh gases and ultimately facilitates main auto-ignition. As a result, cool flame chemistry must be taken into account in models to accurately predict the onset of auto-ignition in the engine.
- Reactivity gradients in the combustion chamber are inevitable, due to gradients of temperature and mixture composition. Thus auto-ignition first appears locally at isolated spots. Depending on the reactivity gradients around this spot, an auto-ignition front may propagate in different modes, consuming more or less rapidly the surrounding end-gas.
- Inside the combustion chamber, the sudden local heat release due to auto-ignition may produce a pressure wave. The latter travels across the combustion chamber and reflects at the walls, engendering oscillations of the pressure signal recorded in one point inside the cylinder.
- Under certain conditions, the auto-ignition front may couple with the pressure wave to induce a developing detonation wave. This leads to extreme magnitudes of pressure oscillation.
- Knock is generally characterized based on the pressure oscillations analysis. Nonetheless, these oscillations are solely an outward sign of auto-ignition. Moreover, there is no established relationship between the pressure oscillations and the damage risks on the engine, maybe except in extreme cases such as a developing detonation.

- The auto-ignition scenario depends on the local in-cylinder conditions. Hence, the representation of the mixture and temperature distribution, cylinder flow aerodynamics and CCV is required to accurately predict auto-ignition by simulation. In this context, LES appears as an appropriate approach to deal with engine knock.

CHAPTER

3

LES modelling approach

Contents

3.1	Principle of the LES	44
3.1.1	Concept of the LES	44
3.1.2	LES system of equations	45
3.2	Description of the used LES modelling approach	47
3.2.1	Modelling of the unresolved convective fluxes	48
3.2.2	Turbulent premixed combustion modelling	49
3.2.2.1	Combustion regime in a spark-ignition engine.	49
3.2.2.2	The Extended Coherent Flame Model for LES	50
3.2.3	Spark-ignition modelling	58
3.2.3.1	Modelling of the initial burned gases kernel	60
3.2.3.2	Laminar flame kernel growth and transition towards a prop- agating turbulent premixed flame	61
3.2.4	Auto-ignition modelling	62

This Chapter provides a detailed description of the turbulent reactive flow modelling used in the course of this thesis. The first *Section 3.1* briefly presents the concept of LES and recalls the system of equations to be solved. The second *Section 3.2* focuses on the chosen combustion models, i.e models for the flame initiation resulting from the spark-discharge, for the turbulent premixed flame propagation and for auto-ignition in the fresh gases.

3.1 Principle of the LES

This first Section introduces the concept of filtering, which is the basis of LES and leads to the governing LES system of equations.

3.1.1 Concept of the LES

The simulation of turbulent flows requires resolving for a wide range of length and time scales, which all affect the flow field and the combustion process. A complete resolution of all scales can be achieved with Direct Numerical Simulation (DNS), but its cost prevents the simulation of practical systems such as ICE. In order to reduce the CPU costs, the basic principle of LES is to perform a spatial low-pass filtering of the instantaneous Navier-Stokes equations. Illustrated in Figure 3.3, the objective is to explicitly resolve the largest turbulent scales of the flow, while the effects of the smaller ones (smaller than the filter size) are modelled.

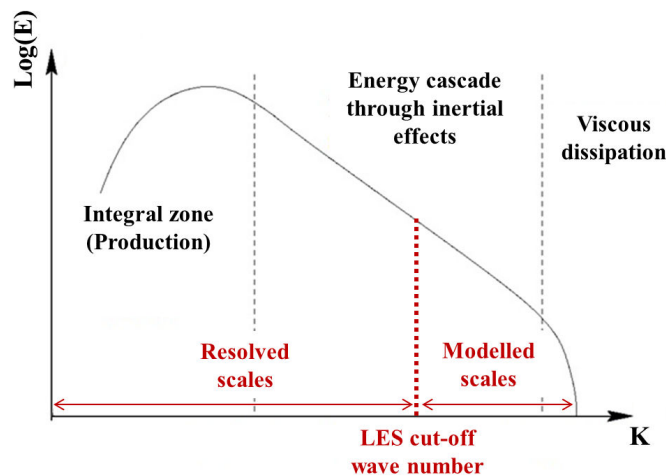


Figure 3.1: Conceptual representation of the LES on the turbulent energy spectrum plotted as a function of the wave number.

Conceptually, the LES approach is well adapted to the study of turbulent reactive flows [105]:

- Large turbulent eddies containing most of the energy are resolved, and their knowledge can be used to build models for the smaller ones. The use of models is probably well suited to describe the small eddies, since they are assumed to have more universal features.
- Solving for the large eddies provides a better description of the turbulence/combustion interaction (as compared to the RANS approach that only provides a statistical description), thereby giving access to the exact location of the flame, at least at the resolved scale.
- The turbulent flow is explicitly solved in time, making it possible to capture the combustion instabilities, and in our particular case CCV in the engine.

3.1.2 LES system of equations

From a mathematical point of view, the quantity \bar{Q} corresponding to the large scales is obtained by the convolution product between this quantity Q and the filter G_Δ :

$$\bar{Q}(x) = \int_{\Omega} Q(x') G_\Delta(x - x') dx' \quad (3.1)$$

where Ω is the computational domain, Δ the filter size and x the position vector.

This filtering operation allows to separate the quantity Q in a resolved part $\bar{Q}(x)$ and an unresolved part, the sub-grid scale (SGS) part, which corresponds to the small unresolved scales of the flow. This decomposition is similar to a Reynolds decomposition for the RANS equations, and results in the same issues in the case of a compressible flow. Thus, by analogy with the Favre decomposition, the density weighted filtering operation, known as Favre filtering, is introduced:

$$\tilde{Q} = \frac{\overline{\rho Q}}{\bar{\rho}} \quad (3.2)$$

The associated unresolved fluctuations are noted Q'' and obey Eq. 3.3.

$$Q = \tilde{Q} + Q'' \quad (3.3)$$

In practice, the filtering operation relies on the computational mesh: the filter size diminishes as the mesh is refined, and the turbulent flow is better resolved. Hence the filtering operation does not explicitly intervene in the simulation, except in the SGS models used to close the unresolved terms, see *Section 3.2*.

The Favre filtering operator is applied to the instantaneous Navier-Stokes equations for reactive flows. The resulting complete system of equations can be found in the book of Poinot & Veynante [105]. As it will be pointed out, the present study uses simplified form of these

equations: Soret and Duffour effects are neglected and the diffusion coefficients for species are equal. The present LES system of equations using the Einstein's summation convention is here described:

Filtered conservation equation of momentum:

$$\underbrace{\frac{\partial \bar{\rho} \tilde{u}_i}{\partial t}}_I + \underbrace{\frac{\partial \bar{\rho} \tilde{u}_i \tilde{u}_j}{\partial x_j}}_{II} = - \underbrace{\frac{\partial \bar{P}}{\partial x_j}}_{III} + \underbrace{\frac{\partial \bar{\tau}_{ji}}{\partial x_j}}_{IV} - \underbrace{\frac{\partial}{\partial x_j} (\bar{\rho} (\tilde{u}_i \tilde{u}_j - \tilde{u}_i \tilde{u}_j))}_V + \underbrace{\tilde{S}_i}_{VI} \quad (3.4)$$

From the left to right there are: the filtered time-dependent term (I), the resolved convection term of momentum (II), the filtered pressure gradient (III), the viscous dissipation (IV) for which the filtered deviatoric stress tensor is given by Eq. 3.5, the unresolved convection term of momentum (V), and a volumetric source term (VI) accounting for external forces such as the moving parts in a piston engine.

$$\bar{\tau}_{ji} = \bar{\rho} \nu \left(\frac{\partial \tilde{u}_i}{\partial x_j} + \frac{\partial \tilde{u}_j}{\partial x_i} \right) - \frac{2}{3} \bar{\rho} \nu \frac{\partial \tilde{u}_p}{\partial x_p} \delta_{ji} \quad (3.5)$$

with ν being the kinematic viscosity and δ_{ji} the Kronecker delta.

Filtered conservation equation for species:

$$\underbrace{\frac{\partial \bar{\rho} \tilde{Y}_k}{\partial t}}_I + \underbrace{\frac{\partial \bar{\rho} \tilde{u}_j \tilde{Y}_k}{\partial x_j}}_{II} = - \underbrace{\frac{\partial \overline{V_{k,i} Y_k}}{\partial x_j}}_{III} - \underbrace{\frac{\partial}{\partial x_j} (\bar{\rho} (\tilde{Y}_k \tilde{u}_j - \tilde{Y}_k \tilde{u}_j))}_V + \underbrace{\tilde{\omega}_k}_{VI} \quad (3.6)$$

This equation is valid for any species k . From the left to right there are: the filtered time-dependent term (I), the resolved convection term for species k (II), the filtered viscous molecular diffusion of species k (III) that is closed in Eq. 3.7 using Fick's law (valid under the assumption of equal diffusivity for all species), the unresolved convection term for species k (IV) and the filtered reaction rate accounting for combustion (V).

$$\overline{V_{k,i} Y_k} = -\bar{\rho} \frac{\nu}{Sc} \frac{\partial \tilde{Y}_k}{\partial x_j} \quad (3.7)$$

Filtered conservation equation for total energy e_t :

$$\underbrace{\frac{\partial \bar{\rho} \tilde{e}_t}{\partial t}}_I + \underbrace{\frac{\partial (\bar{\rho} \tilde{e}_t + \bar{P}) \tilde{u}_j}{\partial x_j}}_{II} = \underbrace{\frac{\partial \bar{\tau}_{ji} \tilde{u}_j}{\partial x_j}}_{III} - \underbrace{\frac{\partial \bar{q}_i}{\partial x_j}}_{IV} - \underbrace{\frac{\partial}{\partial x_j} ((\bar{\rho} e_t + \bar{P}) \tilde{u}_j - (\bar{\rho} \tilde{e}_t + \bar{P}) \tilde{u}_j)}_V + \underbrace{\tilde{Q}}_{VI} \quad (3.8)$$

From the left to right there are: the filtered time-dependent term (I), the resolved convection of total energy (II), the viscous dissipation (IV), the heat flux (V) given by Eq. 3.9 using Fourier's law (assuming that Soret and Duffour effects are negligible), the unresolved convection of total energy (V), and a source term (VI) representing for instance the energy brought by the spark-plug or the heat losses at the walls, not to be confused with the combustion heat release that is already included in the total energy.

$$\bar{q}_i = \lambda \frac{\overline{\partial T}}{\partial x_j} \quad (3.9)$$

The LES system of equations includes unresolved terms accounting for phenomena at the SGS level. For closing the system, these terms require adequate models which are presented in the following Section.

3.2 Description of the used LES modelling approach

Direct-injection spark-ignition engines involve many physical phenomena inside the combustion chamber. Illustrated in Figure 3.2, these phenomena (turbulence, combustion, spray injection) are related to a wide range of characteristic length scales, which cannot all be resolved on LES meshes of practical interest. In order to account for the phenomena that occur at the SGS level, SGS models are employed. Only the models used in the present study are detailed in this Section.

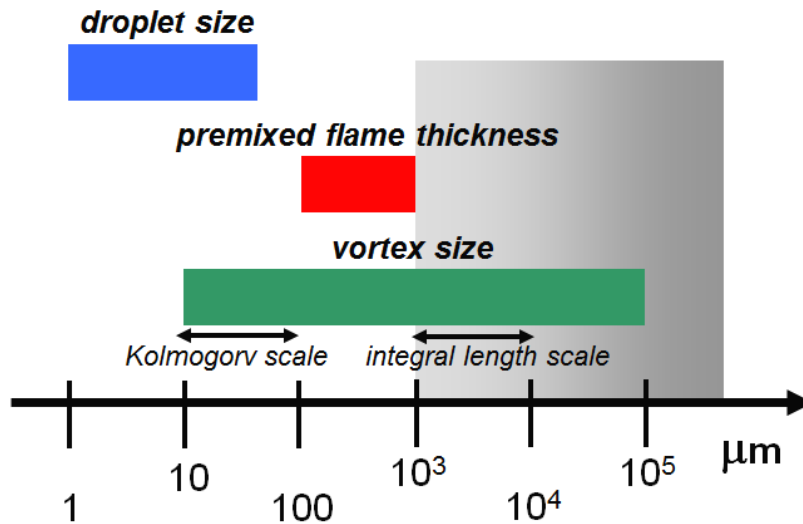


Figure 3.2: Illustration of typical length scales in a piston engine, relatively to the scales resolved on typical LES meshes (grey square).

3.2.1 Modelling of the unresolved convective fluxes

One difficulty in LES modelling results from the appearance of unresolved convection terms at the SGS level. Table 3.1 lists those terms which account for the unresolved convection of momentum (the so-called Reynolds tensor), species and total energy:

- In the momentum equation, the unresolved convection term, referred to as *Reynolds tensor*, is generally closed using the Boussinesq eddy-viscosity assumption. The Reynolds tensor is hereby described using the viscous tensor used for Newtonian fluids, but with a turbulent viscosity ν_t .
- Using a gradient approach, convection terms for species and total energy are also modelled by additional diffusion terms.

Convection term	Unresolved part	Modelled by
Momentum	$\bar{\rho}(\widetilde{u_i u_j} - \widetilde{u_i} \widetilde{u_j})$	$-2\nu_t \widetilde{S_{ij}^*} + \frac{2}{3} k_{sgs} \delta_{ij}$
Species	$\bar{\rho}(\widetilde{Y_k u_j} - \widetilde{Y_k} \widetilde{u_j})$	$-\bar{\rho} \frac{\nu_t}{Sc_t} \frac{\partial \widetilde{Y_k}}{\partial x_j}$
Energy	$(\overline{\rho e_t + P})_{u_j} - (\bar{\rho} \widetilde{e_t} + \bar{P}) \widetilde{u_j}$	$-\bar{\rho} c_p \frac{\nu_t}{Pr_t} \frac{\partial \widetilde{T}}{\partial x_j}$

Table 3.1: Modelling of unresolved convection terms in the spatially filtered Navier-Stokes equations. $\bar{\rho}$ is the filtered density, $\widetilde{u_i}$ is the component of the filtered velocity vector $\widetilde{\mathbf{u}}$ in the direction i , $\widetilde{Y_k}$ is the filtered mass fraction of species k , $\widetilde{e_t}$ is the total energy, \bar{P} is the filtered pressure, ν_t is the turbulent kinematic viscosity to be modelled, $\widetilde{S_{ij}^*}$ is the trace-less symmetric part of the strain rate tensor, k_{sgs} is the SGS kinetic energy, C_p is the specific heat capacity, Pr_t and Sc_t are respectively the turbulent Prandtl and Schmidt numbers.

In particular, the closure of the unresolved convection term for species allows rewriting the filtered conservation equation for species k in a more compact form:

$$\frac{\partial \bar{\rho} \widetilde{Y_k}}{\partial t} + \frac{\partial \bar{\rho} \widetilde{u_j} \widetilde{Y_k}}{\partial x_j} = \frac{\partial}{\partial x_j} \left(\bar{\rho} \left(\frac{\nu}{Sc} + \frac{\nu_t}{Sc_t} \right) \frac{\partial \widetilde{Y_k}}{\partial x_j} \right) + \bar{\omega}_k \quad (3.10)$$

Finally and in order to fully close the three unresolved convection terms for momentum, species and total energy, three parameters are to be determined:

- The turbulent Prandtl number Pr_t and the turbulent Schmidt Sc_t number. In this study, Pr_t and Sc_t are fixed constant such as to obtain a turbulent Lewis number $Le_t = Sc_t/Pr_t = 1$, i.e equivalent heat and species diffusivity.

- The turbulent kinematic viscosity ν_t . This can be determined using for instance the models of Smagorinsky [119], dynamic Smagorinsky [47] or Sigma [92] [123]. Misdariis et al. [88] compared the three enumerated models in the LES of a single-cylinder engine. Their study revealed no significant impact of the SGS models on global quantities such as the flow kinetic energy or the global heat release during the premixed flame propagation, but still the Sigma model allowed a more realistic description of the turbulence/combustion interaction.

3.2.2 Turbulent premixed combustion modelling

The prerequisite for the simulation of engine knock is the correct representation of the combustion by the turbulent premixed flame, which is represented in the filtered transport equation for species by the source term $\bar{\omega}_k$. This Section deals with its modelling.

3.2.2.1 Combustion regime in a spark-ignition engine.

The choice of an adequate combustion model for $\bar{\omega}_k$ can be done using a physical approach, based on the analysis and comparison of the various time scales involved in turbulent premixed combustion. This analysis leads to the turbulent premixed combustion diagram known as the Borghi-Peters diagram [100], and presented in Figure 3.3.

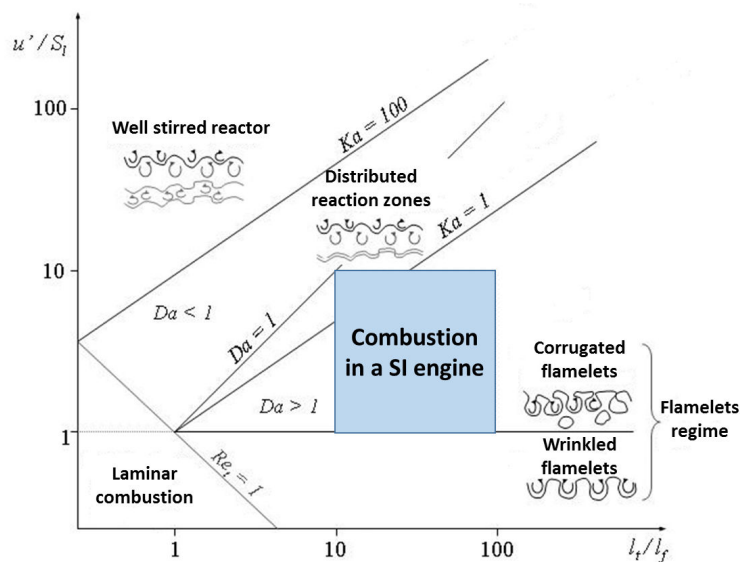


Figure 3.3: Premixed turbulent combustion diagram by Peters [100]. l_t is the integral length scale, l_f the laminar flame thickness (noted δ_L in the rest of the manuscript), u' is the turbulent velocity and S_L is the laminar flame speed. The flame structure in a spark-ignition engine can be estimated to be mostly located in the flamelet regime (Blue area). Re-printed from Richard [110].

Depending on the turbulence and flame characteristic length and velocity scales, this diagram allows to indicate the combustion regime for premixed turbulent combustion and suggests scenarii for the interaction between the flame and the turbulent eddies. Each regime is delineated by non-dimensional numbers:

- The Karlovitz number Ka compares the chemical time scale τ_c to the Kolmogorov time scale τ_k :

$$Ka = \frac{\tau_c}{\tau_k} \quad (3.11)$$

- The Damköhler number Da is the ratio between the turbulent integral time scale τ_t and the chemical time scale τ_c :

$$Da = \frac{\tau_t}{\tau_c} \quad (3.12)$$

In the case of a direct-injection spark-ignition engine, the flame structure can be estimated to be mainly located in the corrugated flamelet regime (blue square in Figure 3.3). In this regime where $Da \gg 1$, the chemical time scale is short compared to the turbulent one ($\tau_c < \tau_k < \tau_t$). This flamelet regime corresponds to a thin reaction zone, distorted and convected by the flow field. The turbulent eddies are able to wrinkle the flame, but unable to affect the reaction zone structure so that the turbulent flame can be considered as locally laminar. Using the flamelet assumption, a geometrical analysis can describe the flame as an infinitely thin interface separating fresh and burnt gases. The flame propagation speed is then controlled by the wrinkling of this interface, which increases the flame surface area.

3.2.2.2 The Extended Coherent Flame Model for LES

Based on the previous analysis of the turbulence/combustion interaction, three main models for premixed turbulent combustion can be found in the literature: the G-equation model [101], the TF-LES (Thickened Flame-LES) model [21] and the ECFM-LES (Extended Coherent Flame Model for LES) [126] [110], which has been used in the course of this thesis. ECFM was initially a RANS model [20], meant to be an extension of the original CFM model [10], able to deal with partially premixed mixtures and variable fresh gases temperature. ECFM was then adapted to LES.

3.2.2.2.1 Use of a LES combustion filter

The typical flame thickness δ_L in a spark-ignition engine is about 0.01 to 0.1 mm, and is much smaller than the mesh resolutions in current use ($\Delta_x \approx 0.5\text{mm}$). Illustrated in Figure 3.4, the LES filter, which relies on the computational mesh, allows to resize the chemical reaction zone to the size of a mesh cell. However, solving for the flame front on one cell would involve steep gradients of the filtered quantities, and hereby it cannot be directly resolved per se. To

overcome this problem, the flame front is filtered at a larger scale $\hat{\Delta} = n_{res}\Delta_x$, with n_{res} an integer typically of the order of 5 to 10.

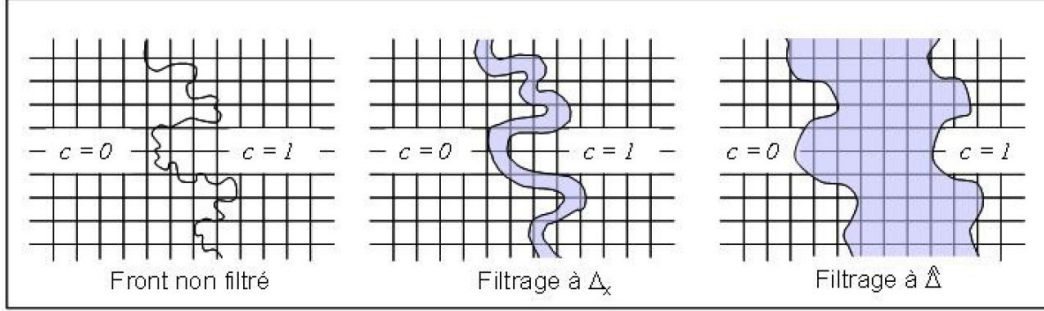


Figure 3.4: Principle of the flame front filtering as in ECFM-LES. Re-printed from [110].

The progress of combustion through the filtered flame front is described by a filtered progress variable for combustion \tilde{c} (its calculation is addressed later in *Section 3.2.2.2.3*). Its value ranges from $\tilde{c} = 0$ in the fresh gases to $\tilde{c} = 1$ in the burned gases.

3.2.2.2.2 Species and energy transport equations at scale $\hat{\Delta}$

ECFM-LES relies on a simplified description of the mixture, which is reduced to only seven primary chemical species: $O_2, N_2, CO_2, H_2O, CO, H_2$ and the fuel. The fuel is modelled by a single component surrogate C_xH_y , for which thermodynamic data were tabulated a priori. For each of the seven species k , the filtered transport equation for species k is solved at the scale $\hat{\Delta}$:

$$\frac{\partial \bar{\rho} \tilde{Y}_k}{\partial t} + \frac{\partial \bar{\rho} \tilde{u}_j \tilde{Y}_k}{\partial x_j} = - \frac{\partial}{\partial x_j} \left(\bar{\rho} \left(\frac{\nu}{Sc} + \frac{\hat{\nu}_t}{Sc_t} \right) \frac{\partial \tilde{Y}_k}{\partial x_j} \right) + \bar{\omega}_k \quad (3.13)$$

In Eq. 3.13, the turbulent viscosity filtered at the LES combustion filter size $\hat{\Delta}$ is given by:

$$\hat{\nu}_t = C_v \hat{u}' \hat{\Delta} \quad (3.14)$$

C_v was estimated in the work of Richard [110] to be approximately 0.12. The velocity fluctuations \hat{u}' associated to $\hat{\Delta}$ are estimated supposing that the spectral structure of turbulence follows the Kolmogorov cascade:

$$\hat{u}' = u' \left(\frac{\hat{\Delta}}{\Delta_x} \right)^{1/3} \quad (3.15)$$

with u' being the norm of the velocity fluctuations:

$$u' = |\bar{\mathbf{u}}'| = |c_2 \Delta_x^3 \nabla^2 (\nabla \times \bar{\mathbf{u}}')| \quad (3.16)$$

where c_2 is a modelling constant given in [21], and $\nabla \times$ the rotational operator.

In all CFM models, the flame front is described as an infinitely thin interface separating the fresh and burned gases. Hence the fuel is divided into two parts: the fuel present in the unburned "u" (fresh) gases \tilde{Y}_F^u and the fuel present in the burned "b" gases \tilde{Y}_F^b . Transport equations are defined for the unburned and burned fuel mass fractions:

$$\frac{\partial \bar{\rho} \tilde{Y}_F^x}{\partial t} + \frac{\partial \bar{\rho} \tilde{u}_j \tilde{Y}_F^x}{\partial x_j} = \frac{\partial}{\partial x_j} \left(\bar{\rho} \left(\frac{\nu}{Sc} + \frac{\hat{\nu}_t}{Sc_t} \right) \frac{\partial \tilde{Y}_F^x}{\partial x_j} \right) + \bar{\omega}_F^x \quad (3.17)$$

where the subscript x denotes either the unburned part "u" or the burned "b" part. Finally, a transport equation for the sensible enthalpy is solved:

$$\frac{\partial \bar{\rho} \tilde{h}_s}{\partial t} + \frac{\partial \bar{\rho} \tilde{u}_j \tilde{h}_s}{\partial x_j} = -\frac{\partial P}{\partial t} + \frac{\partial}{\partial x_j} \left(\bar{\rho} \left(\frac{\nu}{Sc} + \frac{\hat{\nu}_t}{Sc_t} \right) \frac{\partial \tilde{h}_s}{\partial x_j} \right) + \tilde{Q} + \bar{\omega}_{h_s} \quad (3.18)$$

The only remaining terms to be closed are the source terms for the combustion in the transport equations for the species and enthalpy. To do so, ECFM-LES uses the flame surface density concept. It relates the reaction rate for the progress variable for combustion, noted $\tilde{\omega}_c$, to the flame surface density (FSD) under the following expression:

$$\bar{\omega}_c = \bar{\rho}^u S_L \bar{\Sigma}_{\tilde{c}} \quad (3.19)$$

where ρ_u is the fresh gases density, and $\bar{\Sigma}_{\tilde{c}}$ the FSD accounting for the flame/turbulence interaction (its calculation is addressed later in *Section 3.2.2.2.4*). The laminar flame speed S_L , which accounts for the chemistry features, is computed from the correlation by Metghalki & Keck [85]:

$$S_L = S_L^0 \left(\frac{T^u}{T_0} \right)^\alpha \left(\frac{P^u}{P_0} \right)^\beta (1 - 2.1 \chi_{EGR}) \quad (3.20)$$

with S_L^0 being the laminar, unstretched flame speed under reference conditions of pressure ($P_0 = 1 \text{ atm}$) and temperature ($T_0 = 298 \text{ K}$), and χ_{EGR} the volume rate of EGR. The two coefficients α and β are function of the fuel composition and equivalence ratio ϕ . For instance, these are for iso-octane:

$$\alpha_{iso-octane} = 2.18 - 0.8(\phi - 1) \quad (3.21)$$

$$\beta_{iso-octane} = -0.16 + 0.22(\phi - 1) \quad (3.22)$$

From the above reaction rate for combustion $\tilde{\omega}_c$, source terms in the transport equations for species k are deduced from Eq. 3.23.

$$\bar{\omega}_k = Y_{k|u}^u \bar{\omega}_c \quad (3.23)$$

$Y_{k|u}^u$ is the conditional unburned mass fraction of species k and defined in the next *Section 3.5*.

Then the source term in the transport equation for the sensible enthalpy is simply:

$$\bar{\omega}_{h_s} = - \sum_k h_k^0 \bar{\omega}_k \quad (3.24)$$

where h_k^0 is the enthalpy of formation for species k .

The reaction rate term in the transport equation for the burned gases mass fraction $\bar{\omega}_F^b$ represents the post-oxidation reactions in the burned gases, and is computed using a two step model (consumption of the fuel in the burned gases and equilibrium reactions of the CO_2 - CO system) [114].

3.2.2.2.3 Unburned and burned gases states

Currently developed spark-ignition engines often use a direct-injection system. With such a technology, the fuel has less time to mix with air in the combustion chamber and the resulting mixture is not perfectly homogeneous at spark-timing. Inhomogeneities in the mixture directly intervene in the reaction rate through the density in the fresh gases ρ^u , the equivalence ratio ϕ and the fresh gases temperature T^u (used to compute S_L). Therefore, a correct computation of the reaction rate requires an accurate description of the fresh and burned gases states.

As for the local gas composition, this is achieved by introducing tracers for species k noted \tilde{Y}_{Tk} . Tracers are convected and diffused exactly like any real species, except that they are not consumed by the premixed flame. Their transport equations are identical to Eq. 3.13 but with no source term for combustion. As only four atomic elements are present (O,C,H,N), only three tracer species equations are required. In fact, the tracer for species k , \tilde{Y}_{Tk} , represents the mass fraction of species k in the fresh gases conditioned to the fresh gases, noted $\tilde{Y}_{k|u}^u$:

$$\tilde{Y}_{Tk} = \tilde{Y}_{k|u}^u = \frac{m_k^u}{m^u} \quad (3.25)$$

$\tilde{Y}_{k|u}^u$ is not to be confused with \tilde{Y}_k^u , which compares the mass of species k contained in the fresh gases, m_k^u , to the total mass in the cell, m (unburned + burned). The conditioning technique allows to determine the burned gases composition in the cell through the mass balance equation:

$$\tilde{Y}_k = (1 - \tilde{c}) \tilde{Y}_{k|u}^u + \tilde{c} \tilde{Y}_{k|b}^b \quad (3.26)$$

In practice, this progress variable for combustion \tilde{c} is not computed based on a transport equation, instead it is deduced from the fuel mass fraction and its tracer:

$$\tilde{c} = 1 - \frac{\tilde{Y}_F^u}{\tilde{Y}_{TF}} \quad (3.27)$$

Because the flame front is considered as infinitely thin and thereby there can be no accumulation of mass within this interface, Eq. 3.27 simply states that the progress variable is proportional to the fraction of fuel mass that has been burned since the beginning of combustion.

As for the fresh gases temperature, it is determined using a transport equation for the unburned gases enthalpy \tilde{h}_s^u . The knowledge of \tilde{h}_s^u and $\tilde{Y}_{k|u}^u$ allows to compute the fresh gases temperature T^u . The mass balance equation (Eq. 3.26) can be rewritten for the sensible enthalpy to estimate the burned gases sensible enthalpy:

$$\tilde{h}_s = (1 - \tilde{c}) \tilde{h}_s^u + \tilde{c} \tilde{h}_s^b \quad (3.28)$$

Knowing \tilde{h}_s^b and $\tilde{Y}_{k|b}^b$ allows to compute the burned gases temperature T^b .

Finally, the densities in the fresh gases, $\bar{\rho}^u$, and burned gases, $\bar{\rho}^b$, are computed:

$$\bar{\rho}^u = \frac{\bar{P}}{r^u T^u} \quad (3.29)$$

$$\bar{\rho}^b = \frac{\bar{P}}{r^b T^b} \quad (3.30)$$

with r^u and r^b being respectively the specific gas constants in the fresh and burned gases.

Figure 3.5 summarizes all the transported variables in the fresh and burned gases.

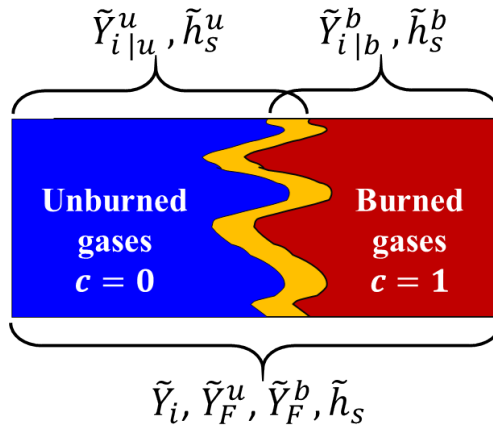


Figure 3.5: Summary of the variables transported in the fresh and burned gases.

3.2.2.2.4 Flame surface density transport equation

Knowing the unburned and burned gases states, we need to estimate the FSD $\bar{\Sigma}$. To start with, $\bar{\Sigma}$ represents the flame surface ∂A per unit volume ∂V . It can be expressed from the progress variable for the reaction c [9]:

$$\bar{\Sigma} = |\overline{\nabla c}| \quad (3.31)$$

In practice, $\bar{\Sigma}$ can be estimated alternatively using an algebraic expression or a transport equation, as it is retained here. For sake of clarity, the following equations will be written in vector form, with \mathbf{u} the velocity vector. Introducing the filtering operator conditioned to the flame front s for any quantity Q given by:

$$\langle Q \rangle_s = \frac{\int_0^1 Q |\nabla c| \delta(c - c^*) dc^*}{\bar{\Sigma}} \quad (3.32)$$

Veynante et al. [127] proposed a transport equation for the filtered FSD $\bar{\Sigma}$:

$$\underbrace{\frac{\partial \bar{\Sigma}}{\partial t}}_I + \underbrace{\nabla \cdot (\langle \mathbf{u} \rangle_s \bar{\Sigma})}_{II} = - \underbrace{\langle \mathbf{nn} : \nabla \mathbf{u} - \nabla \cdot \mathbf{u} \rangle_s \bar{\Sigma}}_{III} - \underbrace{\nabla \cdot (\langle S_D \mathbf{n} \rangle_s \bar{\Sigma})}_{IV} + \underbrace{\langle S_D \nabla \cdot \mathbf{n} \rangle_s \bar{\Sigma}}_V \quad (3.33)$$

with S_D being the propagation speed normal to the front and $\langle \mathbf{n} \rangle_s$ the local normal to the flame front pointing towards the fresh gases, analogue to the one used in RANS:

$$\langle \mathbf{n} \rangle_s = - \frac{\nabla \bar{c}}{\bar{\Sigma}} \quad (3.34)$$

Several contributions appear in Eq. 3.38:

- (I) is the time-dependent term,
- (II) corresponds to the convective transport of $\bar{\Sigma}$,
- (III) accounts for the straining of the flame by all the turbulent structures of the flow,
- (IV) represents the planar propagation of the flame front,
- (V) represents the curvature source term.

In practice, the above FSD equation is not directly solved for $\bar{\Sigma}$. Indeed $\bar{\Sigma}$ includes a laminar anti-diffusive contribution, which may lead to numerical instabilities [111]. Consequently a new FSD $\bar{\Sigma}_{\bar{c}}$ is introduced:

$$\bar{\Sigma}_{\tilde{c}} = \overline{|\nabla c|} - \underbrace{|\nabla \tilde{c}| + |\nabla \tilde{c}| + (\bar{c} - \tilde{c}) \nabla \cdot \mathbf{N}}_{\text{laminar contribution}} \quad (3.35)$$

where \bar{c} is the progress variable filtered in the sense of Reynolds and is estimated using the relation:

$$\bar{c} = \tilde{c} \frac{\bar{\rho}}{\rho^b} \quad (3.36)$$

and \mathbf{N} the local normal to the iso-surface \tilde{c} :

$$\mathbf{N} = -\frac{\nabla \tilde{c}}{|\nabla \tilde{c}|} \quad (3.37)$$

Despite $\bar{\Sigma}_{\tilde{c}}$ differs from $\bar{\Sigma}$, the total flame surfaces over the combustion chamber volume $\int \bar{\Sigma}_{\tilde{c}} dV$ and $\int \bar{\Sigma} dV$ are equal, and so a similar expression of the transport equation can be used for $\bar{\Sigma}_{\tilde{c}}$, although this time it is a model equation and not an exact equation:

$$\frac{\partial \bar{\Sigma}_{\tilde{c}}}{\partial t} + \nabla \cdot (\langle \mathbf{u} \rangle_s \bar{\Sigma}_{\tilde{c}}) = -\langle \mathbf{nn} : \nabla \mathbf{u} - \nabla \cdot \mathbf{u} \rangle_s \bar{\Sigma}_{\tilde{c}} - \nabla \cdot (\langle S_D \mathbf{n} \rangle_s \bar{\Sigma}_{\tilde{c}}) + \langle S_D \nabla \cdot \mathbf{n} \rangle_s \bar{\Sigma}_{\tilde{c}} \quad (3.38)$$

3.2.2.2.5 Closure of the flame surface density equation

Schematized in Figure 3.6, each term identified in Eq. 3.38 (convective transport, stretching, planar propagation and curvature) can be divided into a resolved and unresolved part. The resulting transport equation for $\bar{\Sigma}_{\tilde{c}}$ is written as:

$$\frac{\partial \bar{\Sigma}_{\tilde{c}}}{\partial t} + T_{res} = T_{sgs} + S_{res} + S_{sgs} - P_{res} + C_{res} + C_{sgs} \quad (3.39)$$

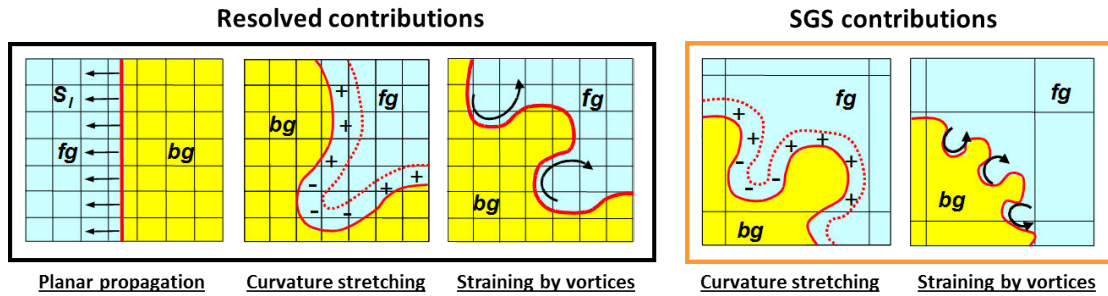


Figure 3.6: Schematic of the resolved and sub-grid scale contributions in the FSD equation.

Each right term in Eq. 3.39 can be expressed of two ways, whether the normal $\langle \mathbf{n} \rangle_s$ or \mathbf{N} is used. Richard [110] showed that the use of \mathbf{N} is more convenient numerically and more appropriate for the use of $\bar{\Sigma}_{\tilde{c}}$. The resolved terms in Eq. 3.39 are thus:

- The resolved convective transport T_{res} :

$$T_{res} = +\nabla \cdot (\tilde{\mathbf{u}} \bar{\Sigma}_{\tilde{c}}) \quad (3.40)$$

- The stretching of the flame by the resolved turbulent structures of the flow S_{res} , known as the resolved strain rate, is given by:

$$S_{res} = (\nabla \cdot \tilde{\mathbf{u}} - \mathbf{N} \mathbf{N} : \nabla \tilde{\mathbf{u}}) \bar{\Sigma}_{\tilde{c}} \quad (3.41)$$

- The resolved planar propagation P_{res} and the resolved curvature C_{res} are respectively defined in Eq. 3.42 and Eq. 3.43. They still guarantee a flame propagation when turbulence tends to zero, and describes the resolved flame front propagation relative to the flow at the velocity S_D . As illustrated in Figure 3.6, it is interesting to note that the resolved curvature can act either as a source term (FSD creation) or a sink term (FSD destruction) depending on the sign of $(\nabla \cdot \mathbf{N})$. It is positive in convex regions, while negative in concave regions.

$$P_{res} = \nabla \cdot (S_D \mathbf{N} \bar{\Sigma}_{\tilde{c}}) \quad (3.42)$$

$$C_{res} = S_D (\nabla \cdot \mathbf{N}) \bar{\Sigma}_{\tilde{c}} \quad (3.43)$$

The propagation velocity S_D is given by:

$$S_D = (1 + \tau \tilde{c}) S_L \quad (3.44)$$

where τ is the thermal expansion through the flame front expressed as the ratio of the unburned gases density to the burned gases density, according to the relation $1 + \tau \tilde{c} = (\rho^u / \rho)$.

Then, the unresolved contributions in Eq. 3.38 should be closed:

- The convective transport by the unresolved structures of the flow T_{sgs} is modelled by a gradient-type assumption:

$$T_{sgs} = -\frac{\mu_t}{S_{c_t}} \nabla \bar{\Sigma}_{\tilde{c}} \quad (3.45)$$

- The flame stretch by the unresolved structures of the flow S_{sgs} , known as the unresolved strain rate. As shown by Colin et al. [21] and illustrated in Figure 3.7, the resolved turbulent structures (at scale Δ_x), the dimension of which is smaller than the flame

thickness (of size $\hat{\Delta}$), cannot wrinkle the flame front and so they should be included in S_{sgs} .

$$S_{sgs} = \alpha_{cfm} \Gamma \left(\frac{\hat{u}'}{S_L}, \frac{\hat{\Delta}}{\delta_L} \right) \frac{\hat{u}'}{\hat{\Delta}} \bar{\Sigma}_{\tilde{c}} \quad (3.46)$$

One can find in Eq. 3.46 the efficiency function Γ , the expression of which was proposed by Charlette et al. [16] and then modified by Richard [110]. α_{cfm} is a constant of the model, set at 0.6 in the present study.

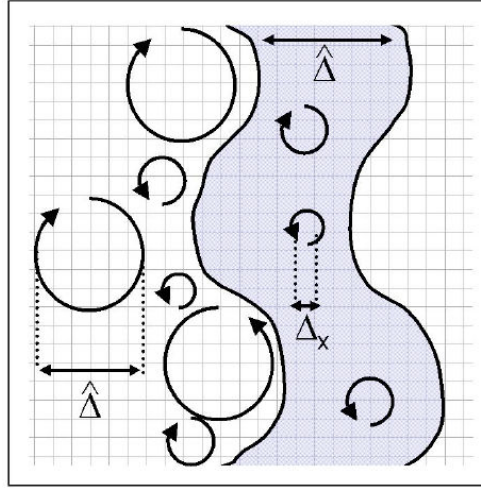


Figure 3.7: Illustration of the turbulence/flame interaction: only vortices whose dimension is larger than $\hat{\Delta}$ manage to wrinkle the flame front. Reprinted from [110].

- Finally, the influence of the curvature on the flame front wrinkling at the unresolved level is given by:

$$C_{sgs} = -\beta_0 S_L \frac{(\bar{\Sigma}_{\tilde{c}} - \bar{\Sigma}_{lam}) \bar{\Sigma}_{\tilde{c}}}{1 - \tilde{c}} + \beta_c S_L \frac{1 + \bar{\tau}}{\tilde{c}} (\bar{\Sigma}_{\tilde{c}} - \bar{\Sigma}_{lam}) \bar{\Sigma}_{\tilde{c}} \quad (3.47)$$

β_0 and β_c are constant values respectively equal to 1 and $\frac{4}{3}$. $\bar{\Sigma}_{lam}$ is the laminar part of FSD and is defined as:

$$\bar{\Sigma}_{lam} = |\nabla \tilde{c}| + (\bar{c} - \tilde{c}) \nabla \cdot \mathbf{N} \quad (3.48)$$

3.2.3 Spark-ignition modelling

Contrary to diesel engines, spark-ignition engines are based on the control of combustion onset. In theory, compression ratios are meant to avoid the auto-ignition of the charge, instead combustion is activated by the spark-plug, which generates a spark in the combustion

chamber. Figure 3.8 illustrates the spark-ignition process as in a typical spark-ignition engine. It consists in:

- **Initiation and breakdown:** The energy is stored in a primary coil, see Figure 3.9. As soon as the circuit is closed, the energy is released in the secondary coil, thereby generating a strong difference of potential between the electrodes. If the electric field reaches a sufficiently high voltage ($\approx 50\,000V$), it results in the ionization of the gas molecules by collisions, forming a plasma channel.
- **Arc discharge:** The spark-plug continues to provide energy to the discharge channel. The latter is stretched by the gas flow, leading in extreme cases to a discharge blow-off or discharge short-circuiting [55].
- **Flame kernel formation:** The stretched discharged channel continuously supplies energy to a wide air-fuel mixture area and achieves the formation of a self-sustained flame kernel. The flame kernel grows and evolves into a propagating turbulent premixed flame.



Figure 3.8: Ignition process from spark-discharge to turbulent premixed flame propagation. Reprinted from [55].

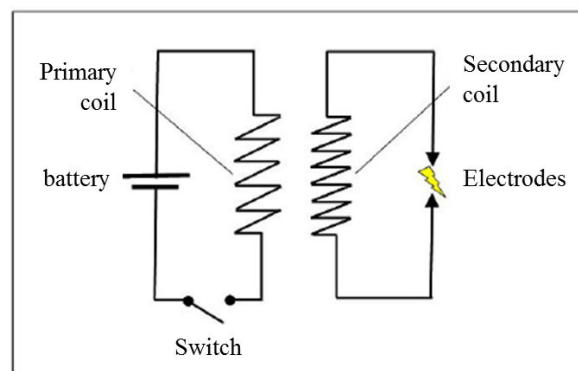


Figure 3.9: Simplified scheme of the spark ignition system. Reprinted from [110].

The meticulous description of these phenomena is still a topic of research. Within the framework of this thesis, the ignition process is modelled by the Imposed Stretch Spark Ignition Model for LES (ISSIM-LES) [23]. It provides a simplified description of the spark-ignition:

- The energy is deposited in the form of an initial kernel of burned gases: the electrical circuit leading to the spark-discharge is modelled, and allows to determine the mass and volume of the burned gases to be deposited.
- The early growth of the initial flame kernel is modelled. It also ensures the transition towards ECFM-LES.

3.2.3.1 Modelling of the initial burned gases kernel

At the spark-ignition timing t_{spark} , an electric arc of length l_{spark} is generated between the electrodes. ISSIM-LES allows estimating thanks to a 0D model the electric power and the resulting energy supplied to the gas mixture. A critical energy of ignition $E_c(t)$ is determined by the model, the value of which corresponds to the minimum energy required for combustion to start.

As soon as $E(t_{ign}) > E_c(t_{ign})$, the spark-ignition timing t_{ign} is known. Then the mass of burned gases m_{ign}^b contained in the volume V_{ign} to be deposited in the combustion chamber is calculated from the laminar flame thickness δ_L :

$$m_{ign}^b = \rho^u l_{spark} 4\pi \delta_L^2 \quad (3.49)$$

In order to ensure a correct resolution of the initial flame kernel on the LES mesh, it is filtered at the combustion filter size $\hat{\Delta}$, and deposited as a sphere within a radius r_{ign}^b :

$$r_{ign}^b = \left(\frac{3}{4\pi} \int \bar{c}_{ign} dV \right)^{1/3} \quad (3.50)$$

according to a gaussian profile of \bar{c} :

$$\bar{c}_{ign} = C_0 \exp \left(- \left(\frac{|x - x_{spark}|}{0.6 \hat{\Delta}} \right)^2 \right) \quad (3.51)$$

where x_{spark} is the vector of spark-plug coordinates, and C_0 a constant that guarantee the relation:

$$\int \bar{c}_{ign} dV = V_{ign}^b = \frac{4}{3} \pi (r_{ign}^b)^3 \quad (3.52)$$

The source term for combustion is modified to take into account the spark-ignition, i.e to impose the value $\bar{c}_{ign}(x, t_{ign})$ in the combustion chamber:

$$\bar{\omega}_c = \max \left(\rho^u S_L \bar{\Sigma} \bar{c}, \rho^b \frac{(\bar{c}_{ign} - \bar{c})}{dt} \right) \quad (3.53)$$

with dt the computational time step.

Finally, a source term is also introduced in the FSD equation:

$$\bar{\omega}_{\Sigma}^{ign} = \max \left(0, \frac{\Sigma_{ign} - \bar{\Sigma}_{\tilde{c}}}{dt} \right) \quad (3.54)$$

where $\Sigma_{ign} = \frac{3\bar{c}}{r_{ign}^b}$ guarantees that the integral over the combustion chamber volume leads to the initial deposited flame surface $4\pi(r_{ign}^b)^2$.

This initial phase, although of importance, is extremely fast in an engine, and accordingly it only lasts for a few iterations during the computation. The laminar flame kernel growth is described in the next Section.

3.2.3.2 Laminar flame kernel growth and transition towards a propagating turbulent premixed flame

Immediately after the flame kernel deposit, the real radius of the flame is smaller than the combustion filter size $\hat{\Delta}$. Hence the generation of FSD during the ignition process starts at the SGS level and finishes at the resolved level as the flame kernel grows. A source term for the SGS curvature S_{ign} (varying like $2/r^b$) is thus added in the balance for the FSD to model the flame kernel growth as long as it is smaller than the filter size. A transition coefficient $\alpha_{ign}(x, t)$ is also introduced to ensure the transition from the ignition at SGS level to the resolved propagating turbulent premixed flame. The filtered FSD equation becomes:

$$\begin{aligned} \frac{\partial \bar{\Sigma}_{\tilde{c}}}{\partial t} + T_{res} = & T_{sgs} + \alpha_{ign} (S_{res} + C_{res}) - (\nabla \cdot S_D \mathbf{N} \bar{\Sigma}_{\tilde{c}}) + S_{sgs} + \alpha_{ign} C_{sgs} \\ & + (1 - \alpha_{ign}) \underbrace{\frac{2(1 + \tau)}{3} \frac{S_L \bar{\Sigma}_{\tilde{c}} (\bar{\Sigma}_{\tilde{c}} - \bar{\Sigma}_{lam})}{\tilde{c}}}_{S_{ign}} + \bar{\omega}_{\Sigma}^{ign} \quad (3.55) \end{aligned}$$

The transition coefficient is given by:

$$\alpha_{ign}(x, t) = \frac{1}{2} \left(1 + \tanh \left(\frac{r^{b+}(t) - 1}{0.015} \right) \right), \quad r^{b+}(t) = \frac{r^b(t)}{0.65\hat{\Delta}} \quad (3.56)$$

It remains close to 0 during spark-ignition in order to cancel the resolved terms in Eq. 3.55, which are replaced by S_{ign} . When the ignition process is over, $\alpha_{ign} = 1$, the flame kernel radius is close to the combustion filter size $\hat{\Delta}$ and so $r^{b+}(t)$ is close to unity. S_{ign} cancels and ECFM-LES operates as described in the previous *Section 3.2.2.2*.

Based on Eq. 3.56, the calculation of the transition coefficient requires to determine the laminar flame kernel radius r^b . Its temporal evolution can be described by the following

relation, assuming a spherical kernel shape:

$$\frac{\partial r^b}{\partial t} = (1 + \tau)S_L \quad (3.57)$$

However, such a relation alone allocates all the burned gases volume to only one flame kernel, making it impossible to model multiple spark-ignitions. To overcome this problem Colin et al. [23] proposed to introduce a quantity Ψ :

$$\bar{\rho}\Psi = \frac{2\bar{\rho}\tilde{c}}{r^b} = \frac{2}{3}\tilde{c}\Sigma_{ign} \quad (3.58)$$

Its evolution is described by a transport equation, Eq. 3.59. It allows to define r^b and α_{ign} locally, and so to model multiple and simultaneous spark-ignitions.

$$\bar{\rho}\frac{\partial\Psi}{\partial t} + \nabla \cdot (\tilde{\rho}\tilde{\mathbf{u}}\Psi) = \nabla \cdot \left(\frac{\hat{\mu}_t}{Sc_t} \nabla\Psi \right) - (1 + \tau) \frac{S_L}{r^b} \bar{\rho}\Psi + \frac{2}{r^b} \bar{\omega}_c + \bar{\omega}_\Psi^{ign} \quad (3.59)$$

where $\tilde{\omega}_{Psi}^{ign}$ is an additional source term for Ψ given by:

$$\bar{\omega}_\Psi^{ign} = \max \left(0, \frac{2/3 \rho^b \Sigma_{ign} - \bar{\rho}\Psi}{dt} \right) \quad (3.60)$$

3.2.4 Auto-ignition modelling

In order to handle auto-ignition in the end-gas, ECFM-LES is combined with the Tabulated Kinetics of Ignition (TKI) model as proposed by Robert et al. [112]. As explained in *Section 3.2.2.2*, ECFM-LES is derived using a bimodal description of the gases state, and the distribution between fresh and burned gases in a mesh cell is given by the progress variable for the reaction \tilde{c} . Any filtered quantity $\tilde{\phi}$ can be decomposed as such (see Eq. 3.26 and Eq. 3.28):

$$\tilde{\phi} = (1 - \tilde{c}) \tilde{\phi}|^u + \tilde{c} \tilde{\phi}|^b \quad (3.61)$$

where $\tilde{\phi}|^u$ and $\tilde{\phi}|^b$ respectively correspond to the fresh and burned gases state.

When introducing auto-ignition, fresh gases can be burned either by the premixed flame or by auto-ignition. Hence the progress variable for combustion \tilde{c} needs to be decomposed into a progress for the premixed flame, noted \tilde{c}_Σ , and a progress for auto-ignition, noted \tilde{c}_{AI} . The decomposition of the gases state in each mesh cell as a function of \tilde{c}_Σ corresponds to the line 'AI/b states' in Figure 3.10. The decomposition of $\tilde{\phi}$ becomes:

$$\tilde{\phi} = (1 - \tilde{c}_\Sigma) \tilde{\phi}|^{AI} + \tilde{c}_\Sigma \tilde{\phi}|^b \quad (3.62)$$

The new conditional state $\tilde{\phi}^{AI}$ corresponds to the fresh gases not consumed by the premixed flame, i.e they are available for auto-ignition. These fresh gases are further decomposed into an unburned part (not consumed, neither by the premixed flame nor by auto-ignition) and a burned part by auto-ignition. This second decomposition, which corresponds to the 'u/b' states line in Figure 3.10, is purely formal as it allows to keep only two states in the gases description, unburned and burned, while the auto-ignition zone is in fact homogeneous:

$$\tilde{\phi}^{AI} = (1 - \tilde{c}_{AI}) \tilde{\phi}^u + \tilde{c}_{AI} \tilde{\phi}^b \quad (3.63)$$

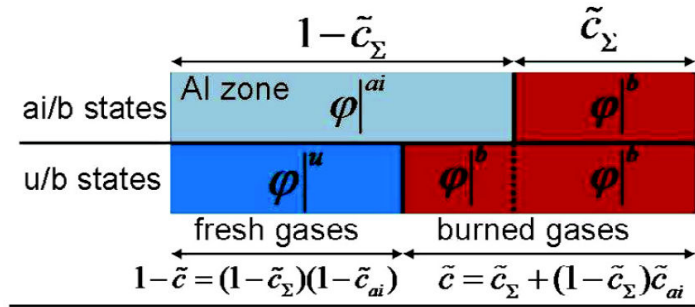


Figure 3.10: Schematic representation of the model. Re-printed from [112].

Adding Eq. 3.62 into Eq. 3.63, and replacing $\tilde{\phi} = \tilde{c}$ provides a relation between the three progress variables \tilde{c} , \tilde{c}_{AI} and \tilde{c}_Σ :

$$(1 - \tilde{c}) = (1 - \tilde{c}_{AI})(1 - \tilde{c}_\Sigma) \quad (3.64)$$

Estimation of the progress variables \tilde{c} and \tilde{c}_{AI}

The estimation of \tilde{c} , given by Eq. 3.27, requires to determine the fuel mass fraction present in the fresh gases \tilde{Y}_F^u and the fuel tracer \tilde{Y}_{TF} . As mentioned in *Section 3.2.2.2.3*, \tilde{Y}_{TF} is a passive scalar given by a transport equation with no source term, and \tilde{Y}_F^u is estimated using the transport equation:

$$\frac{\partial \bar{\rho} \tilde{Y}_F^u}{\partial t} + \nabla \cdot (\bar{\rho} \tilde{u}_j \tilde{Y}_F^u) = -\nabla \cdot \left(\bar{\rho} \left(\frac{\nu}{Sc} + \frac{\hat{\nu}_t}{Sc_t} \right) \nabla \tilde{Y}_F^u \right) + \bar{\omega}_F^u \quad (3.65)$$

The reaction rate $\bar{\omega}_F^u$ is given by:

$$\bar{\omega}_F^u = -\tilde{Y}_{TF} \left((1 - \tilde{c}_{AI})(\bar{\omega}_c^\Sigma + \bar{\omega}_c^{ign}) + (1 - \tilde{c}_\Sigma)\bar{\omega}_c^{AI} \right) \quad (3.66)$$

In Eq. 3.66, $\bar{\omega}_c^\Sigma$ is the standard source term of ECFM-LES, see Eq. 3.19, and $\bar{\omega}_c^{ign}$ is the ISSIM-LES spark-ignition source term:

$$\bar{\omega}_c^{ign} = \bar{\rho}^b \max(0, \tilde{c}_{ign} - \tilde{c}_\Sigma) dt^{-1} \quad (3.67)$$

with \tilde{c}_{ign} being the initial target gaussian profile of \tilde{c}_Σ , which was given by Eq. 3.51.

The reaction rate for the auto-ignition $\bar{\omega}_c^{AI}$ is given by the TKI model [22]:

$$\bar{\omega}_c^{AI} = \bar{\omega}_c^{TKI} \left(\bar{P}, \tilde{T}_u, \tilde{\Phi}, \tilde{Y}_D, \tilde{c}_{AI} \right) \quad (3.68)$$

The instantaneous $\bar{\omega}_c^{TKI}$ is directly read in the TKI table and is function of the temperature in the fresh gases \tilde{T}_u , the pressure \bar{P} , the equivalence ration $\tilde{\Phi}$, the dilution rate \tilde{Y}_D and the advanced variable for auto-ignition \tilde{c}_{AI} , which is defined as:

$$\tilde{c}_{AI} = \frac{\tilde{Y}_F^{AI}}{\tilde{Y}_{TF}} \quad (3.69)$$

The fuel mass fraction consumed by auto-ignition \tilde{Y}_F^{AI} is estimated through its transport equation similar to Eq. 3.65, with a reaction rate $\bar{\omega}_F^{AI}$ defined as:

$$\bar{\omega}_F^{AI} = \tilde{Y}_{TF} \bar{\omega}_c^{AI} \quad (3.70)$$

Estimation of the progress variable \tilde{c}_Σ linked to the premixed flame

Once \tilde{c} and \tilde{c}_{AI} are known, \tilde{c}_Σ is deduced from Eq. 3.64:

$$\tilde{c}_\Sigma = \frac{\tilde{c} - \tilde{c}_{AI}}{1 - \tilde{c}_{AI}} \quad (3.71)$$

To avoid any division by 0, the value $\tilde{c}_\Sigma = 1$ is imposed as soon as \tilde{c}_{AI} tends to 1.

PART II

LES OF AN INDUSTRIAL DIRECT-INJECTION SPARK-IGNITION ENGINE

This Part is dedicated to the generation of the LES of an industrial spark-ignition direct-injection engine. The objective is here to build a computational database, to be used later to investigate the mechanisms that impact knock. The engine under investigation is the RENAULT 1.2 TCe 115, embedded in the Clio IV and Megane IV. The engine performances were experimentally examined a priori by RENAULT on an industrial test bench.

The structure of Part II is as follows:

Chapter 4, entitled **The RENAULT 1.2 TCe 115 engine**, presents the engine under investigation. It describes its geometrical characteristics upon which a computational geometry was selected. It also details the operating point serving as a basis for the LES.

Chapter 5, entitled **Wall Temperature Distribution by CHT Simulation**, is dedicated to the CHT calculation of the wall temperature distribution. Such a distribution is a required input data for the LES, particularly when aiming at predicting engine knock.

Finally, *Chapter 6*, **LES of the RENAULT 1.2 TCe 115 Engine**, presents the results of the LES. They are compared to experimental measurements in order to assess the accuracy of the simulation.

CHAPTER

4

The RENAULT 1.2 TCe 115 engine

Contents

4.1	Engine characteristics and geometry	68
4.2	Choice of the reference operating point	70

This Chapter presents the industrial RENAULT engine under analysis. The first *Section 4.1* starts with a brief description of its main features. Based on the real engine geometry, it also describes how the computational domain was built for the LES. In the second *Section 4.2*, a reference operating point is selected in the experimental database to serve as a basis for setting-up the LES. The conditions for the reference operating point are detailed.

4.1 Engine characteristics and geometry

The studied engine is the four-stroke turbocharged direct-injection spark-ignition RENAULT 1.2 TCe 115 engine. Its main characteristics are listed in Table 4.1.

Number of cylinders	4
Number of valves	16
Bore / Stroke	72.2 mm / 73.2 mm
Compression ratio	9.8
Engine displacement	1200 cm ³
Max Power	85 kW
Direct-injection system	6 holes

Table 4.1: Main characteristics of the RENAULT 1.2 TCe 115 engine.

The corresponding real engine geometry is schematized in Figure 4.1. A passed research [74] published based on the AVBP code has demonstrated the possibility to perform LES of a four cylinder engine. However, such a simulation remains very expensive, and it was not used in the present study. Instead, the computational domain was limited to one specific cylinder, thereby allowing to allocate the CPU resources to the computation of a substantial number of cycles. The cylinder which was computed, referred to as Cylinder 1 in Figure 4.1, is located on the valve train side. It was selected because it does not share its intake and exhaust ports with another cylinder (unlike Cylinder 2 or 3) and it is located far away from the inlet of the intake manifold. The latter condition simplifies the specification of the inlet conditions, since we expect it to be less affected by back-flows from the cylinder, and thus to have a more uniform flow at the inlet.

The resulting computational domain is shown in Figure 4.2 and consists of the following parts:

- The combustion chamber (delimited by the cylinder-roof, liner, piston head, spark-plug, fuel direct-injector and valves bottom),
- The intake and exhaust valves,

- The intake and exhaust ports,
- The intake manifold. The junctions with the intake ports for Cylinder 2,3 and 4 were closed.

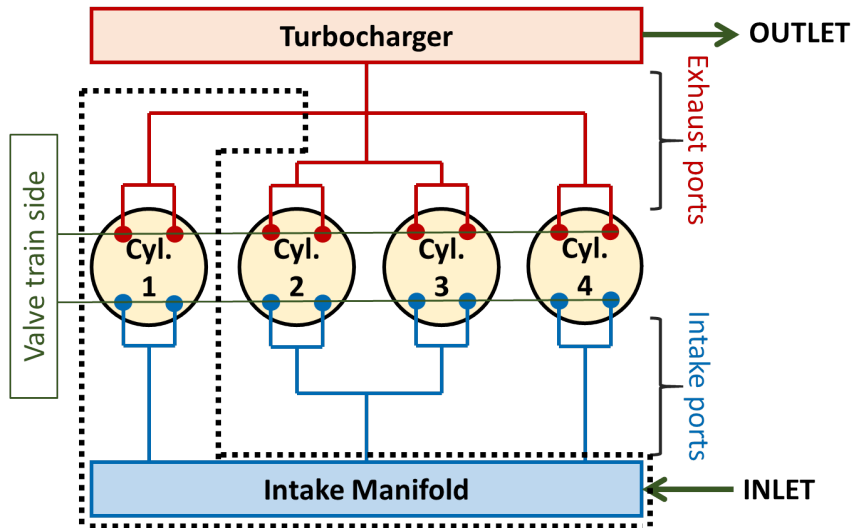


Figure 4.1: Schematic of the RENAULT 1.2 TCE 115 engine. Only Cylinder 1 is simulated. The dotted lines delineates the computational domain.

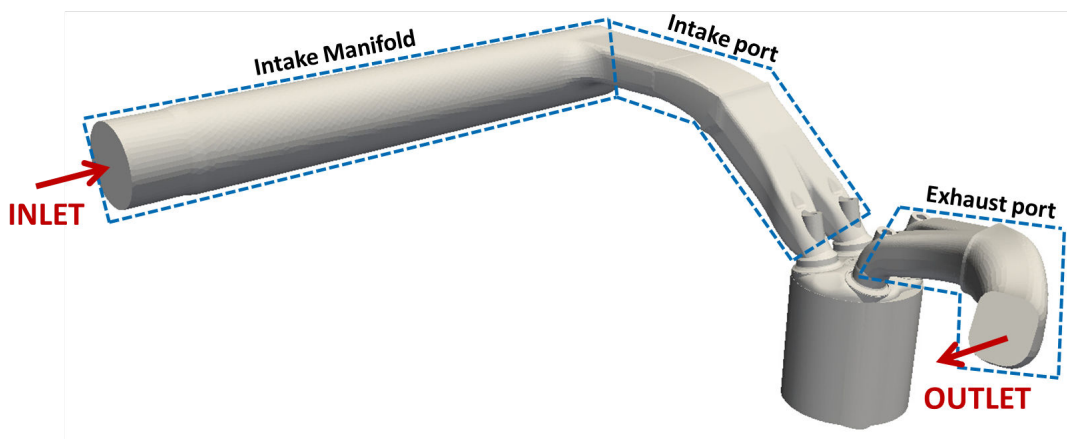


Figure 4.2: Computational domain for Cylinder 1 with the combustion chamber, intake and exhaust ports, and the intake manifold.

Figure 4.3 shows a top view of Cylinder 1, in which the locations of the spark-plug and the direct-injector are indicated. The spark-plug is situated centrally, and its geometry is included

in the computational domain, as we suppose it is likely to influence the flame kernel growth during the first instants of combustion. As for the direct-injector, it is situated laterally on the intake side between the intake valves.

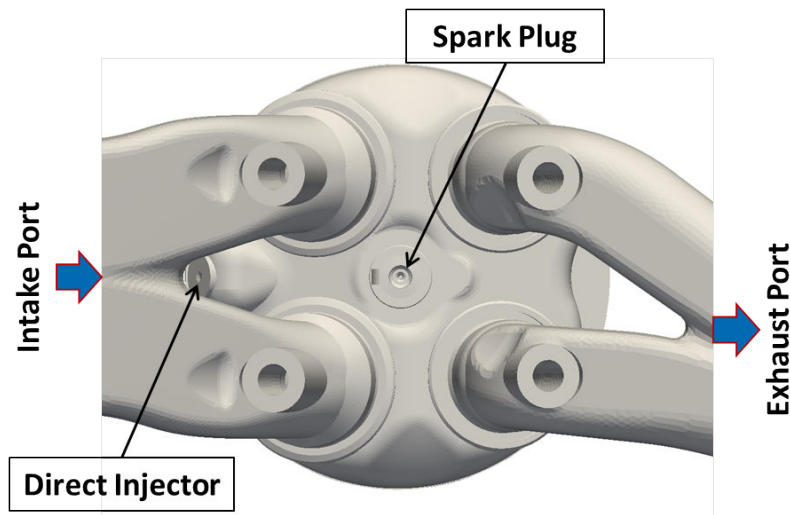


Figure 4.3: Top view of Cylinder1. The spark-plug is located centrally, the fuel injector is situated laterally on the intake side between the intake valves.

4.2 Choice of the reference operating point

The engine performances were experimentally examined on an industrial test bench for a wide range of engine speeds. The objective of the testing was to determine for each engine speed the *Knock Limiting Spark Advance* (KLSA). KLSA represents the limiting spark-advance resulting in an acceptable maximum knock intensity. It is set by the operator to optimize the trade-off between protecting the engine from damaging knock and maximizing the torque.

The simulation of the entire range of operating points available in the test bench database would be extremely expensive and is not required to meet our objectives. Instead, a single point has been selected in the database, which is referred to as *Reference Operating Point* (ROP) in the rest of the manuscript. Table 4.2 summarizes the conditions at ROP. They correspond to a full-load/maximum torque operating point at 2500 rpm engine speed. This engine speed is particularly interesting, since it is frequently encountered by the engine in its everyday life. The spark-timing $ST = -5.3^\circ CA$ ($-5.3^\circ CA$ before TDC) was designated by the car manufacturer as the KLSA at this engine speed.

Figure 4.4 shows the valve lift laws at ROP. The valve overlap is large (intake and exhaust valves are simultaneously opened for $88^\circ CA$), in order to sweep residual burned gases out of the combustion chamber.

Engine speed	2500 rpm
IMEP	23.45 bars
Equivalence ratio	1.05
Spark timing	5.3 °CA before TDC
Start of injection	320 °CA before TDC
Number of holes	6
Hole diameter	142 μm
Injection Pressure	135 bars
Liquid Fuel Temperature	320 K

Table 4.2: Operating conditions at the reference operating point.

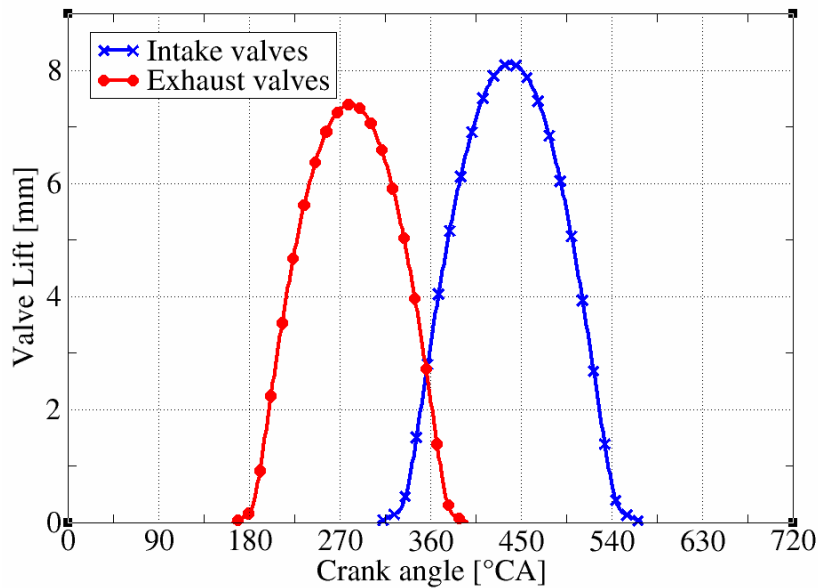


Figure 4.4: Intake and Exhaust valve lift. The overlap reaches 88 crank angle.

The fuel used in the engine tests is a surrogate gasoline composed of toluene ($C_6H_5CH_3$), iso-octane (C_8H_{18}) and n-heptane (C_7H_{16}). Its RON 95/MON 87 matches typical fuels distributed at the petrol station. The surrogate is directly injected into the cylinder through a 6 holes injector. The direct-injection starts during the intake stroke, i.e long before combustion TDC so that the fuel-air mixture is as homogeneous as possible at spark-timing. At such an early start of injection, the piston is still close to TDC, and the piston bowl shape was specifically designed to redirect the spray towards the spark-plug, see Figure 4.5. Finally, the injection duration was calibrated to achieve an average equivalence ratio $\phi = 1.05$ inside the

combustion chamber.

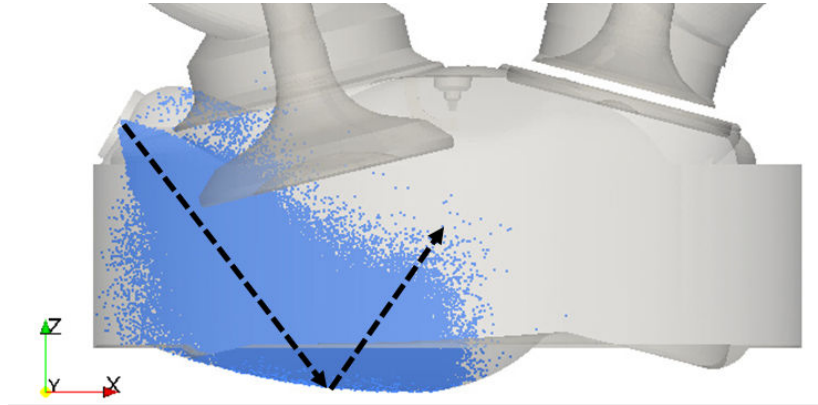


Figure 4.5: Visualization of the direct-injection 12 CA after the start of injection. The fuel is propelled against the bowl-shaped piston and redirected towards the spark-plug.

Pressure and temperature at the inlet and outlet boundaries of the computational domain were deduced from a system simulation. The 0D-1D model of the full engine previously calibrated by RENAULT was used. Figure 4.6a and 4.6b show the resulting temporal evolution of the pressure signal respectively at the inlet and outlet boundaries.

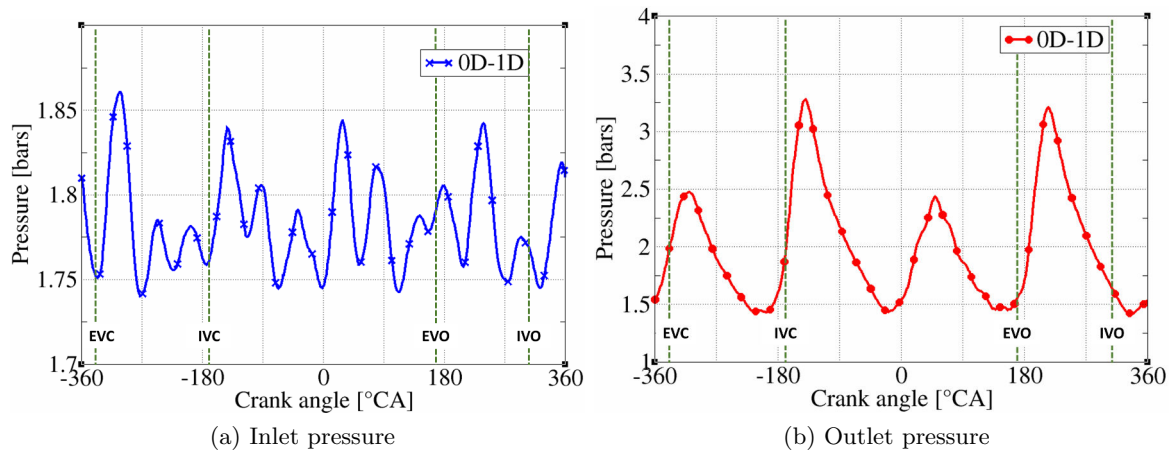


Figure 4.6: Inlet and Outlet pressure signals from 0D-1D simulation. Exhaust Valves Opening (EVO) and Closure (EVC) are highlighted as well as Intake Valves Opening (IVO) and Closure (IVC).

The outlet pressure signal exhibits four peaks with significant magnitudes (up to 3.25 bars). The last peak corresponds to the exhaust phase of *Cylinder 1*, while the other ones result from the exhaust phases of *Cylinder 2*, *3* and *4*. The difference of magnitude between the peaks 1-3 (*Cylinder 3* & *Cylinder 2* respectively) and 2-4 (*Cylinder 4* & *Cylinder 1* respectively)

is due to the specific shape of the exhaust manifold which feeds a twin scroll turbine. In Figure 4.6a, the inlet pressure shows a more irregular pattern, but with fluctuations of smaller amplitude. As compared to the outlet boundary, the inlet boundary is far from the cylinders and consequently less impacted by their dynamics.

In the following, all these data are used for the LES of the engine at ROP. Prior to this, one could have noticed that the experimental data lack of a description of the temperature at the walls, the distribution of which is a key input for the LES. Therefore, the estimation of the temperature distribution at the walls is handled in the next *Chapter 5*.

CHAPTER

5

Wall Temperature Distribution by CHT
Simulation

Contents

5.1	CHT methodology	76
5.2	Computational domain for the CHT simulation	77
5.3	Computational set-up	79
5.3.1	Computational mesh	79
5.3.2	RANS approach for the combustion simulation	80
5.3.3	Boundary conditions	81
5.3.4	Material properties	82
5.4	Results and Validation	83
5.4.1	Validation of the RANS simulation	83
5.4.2	Validation of the CHT predictions	84
5.5	Conclusion	86

In most 3D CFD simulations, the wall temperatures are usually imposed based on experimental findings or from 0D-1D calculations that cannot furnish a detailed temperature distribution at the walls. Therefore the wall temperatures are kept uniform for each solid component and unchanged throughout the simulation. This approach can provide the global amount of heat flux at the wall but some localized effects could be missing due to such oversimplifying boundary conditions, especially when investigating engine knock [39] [40]. As a possible solution, the use of Conjugate Heat Transfer (CHT) allows a more realistic prediction of heat transfer, by solving for the wall temperatures through the thermal coupling between gas flow and the surrounding solid components. The definition of the boundary conditions is thus pushed back to locations where they are well defined a priori.

This Chapter presents the setting-up and validation of a CHT simulation of the RENAULT engine, performed to yield an as accurate as possible distribution of wall temperatures, so that it could be later imposed as boundary condition for the LES. The CHT was performed based on a simulation of the in-cylinder flow and combustion with the CONVERGE CFD Software. The study was the subject of a published SAE Technical Paper [79], exposed at the SAE WCX17 congress in Detroit, MI (USA).

5.1 CHT methodology

CHT simulations involve both the gas flow and the surrounding solid components, and heat transfer at the interfaces is directly solved by the thermal coupling. Such calculations present challenges because the time scales in the gas flow and solid components have an important disparity:

- On the one hand, a characteristic time scale for the reactive gas flow can be estimated based on a combustion time scale as:

$$\tau_{flame} = \frac{\delta_L}{S_L} = 10^{-4} s \rightarrow 0.75^\circ CA \text{ at } 2500 \text{ rpm} \quad (5.1)$$

with δ_L the laminar flame thickness (of the order of 0.05 mm) and S_L the laminar flame speed (of the order of 1 m.s⁻¹).

- On the other hand, a characteristic time scale for heat conduction in the solid walls can be estimated for a 1 cm deep wall made of carbon steel:

$$\tau_{solid} = \frac{A\rho c_p}{\lambda} = 26.3 s \rightarrow 548 \text{ cycles at } 2500 \text{ rpm} \quad (5.2)$$

where λ , ρ and c_p are respectively the conductivity, density and heat capacity of the material.

The solid time scale is several orders of magnitude larger than the gas time scale. Such a difference makes it excessively time consuming to solve for the gas and solid domain together,

as in a strong coupling approach [90]. Nonetheless, this difference also means that the solid can to a first order be assumed to be insensitive to fast heat flux variations, such that it only sees a mean heat flux coming from the gas flow. Hence, the gas and solid parts can be solved separately using a weak coupling approach. Illustrated in Figure 5.1, different time steps are used for the gas and solid to accelerate convergence towards a steady-state in the solid domain, and the calculation operates as follows:

1. The solid domain is initialized with spatially averaged uniform temperatures. Heat transfer at the interfaces between the gas flow and solid components, as well as heat conduction in the solid walls are solved together using a so-called transient solver. The point-wise Heat Transfer Coefficients (HTC) and near-wall temperatures in the gas are computed and saved internally in the memory, in order to be used in the second step. This first step is carried out over a full engine cycle with combustion calculation.
2. The gas domain is "paused" at the end of the engine cycle. The instantaneous local HTC and near-wall temperatures are time-averaged, and used as boundary conditions for a steady-state resolution of heat conduction in the solid walls. The steady-state calculation is carried out until convergence of the temperature in the solid domain.
3. Then, the gas domain is "un-paused". A new transient step begins, with an up-dated temperature distribution at the interfaces between the gas flow and solid components.

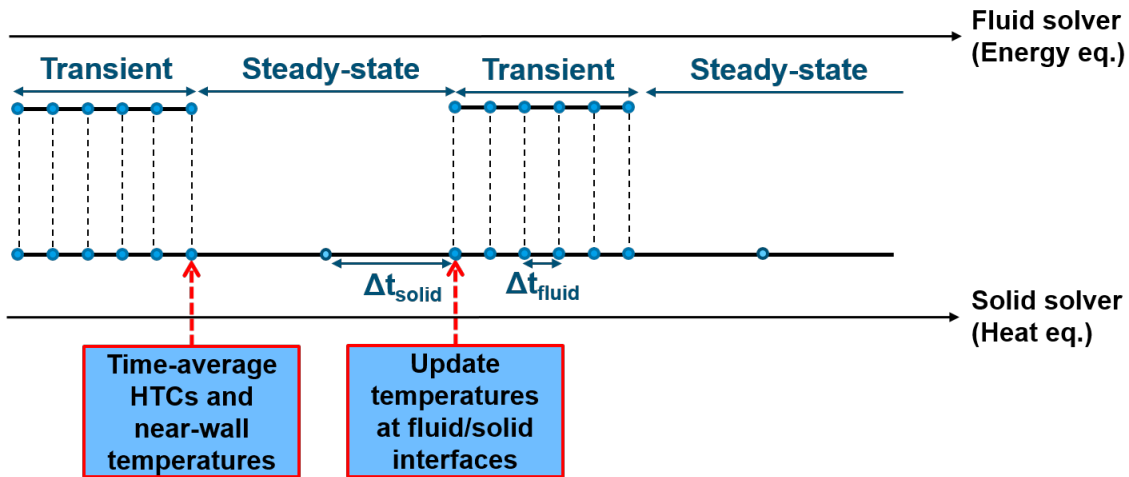


Figure 5.1: Schematic of the weak thermal coupling as implemented in CONVERGE CFD.

5.2 Computational domain for the CHT simulation

In order to perform a CHT simulation, the solid components surrounding the combustion chamber were added to the computational domain presented in *Section 4.1*. This addition further increases the complexity and spatial extent of the domain, therefore some simplifications have been adopted to control the CPU cost.

As shown in Figure 5.2, the symmetrical geometry of the engine allowed to reduce the domain to only two cylinders, referred to as Cylinder 1 (the one computed by LES), and Cylinder 2. The gas flow in Cylinder 2 is not computed, and a specific strategy will be applied to consider its impact on the temperature distribution in the solid domain.

Moreover, the temperature gradients along the liner and piston surfaces are assumed to be relatively small [43], such that their accurate estimation was considered as not relevant in this study. Therefore in Figure 5.2, the piston and engine block geometries were removed from the solid domain, meaning that no CHT applies at the liner and piston surfaces. On the contrary, the temperature distribution on the cylinder roof and valves surfaces are expected to be strongly inhomogeneous, and so all the solid components ahead of the cylinder roof were included.

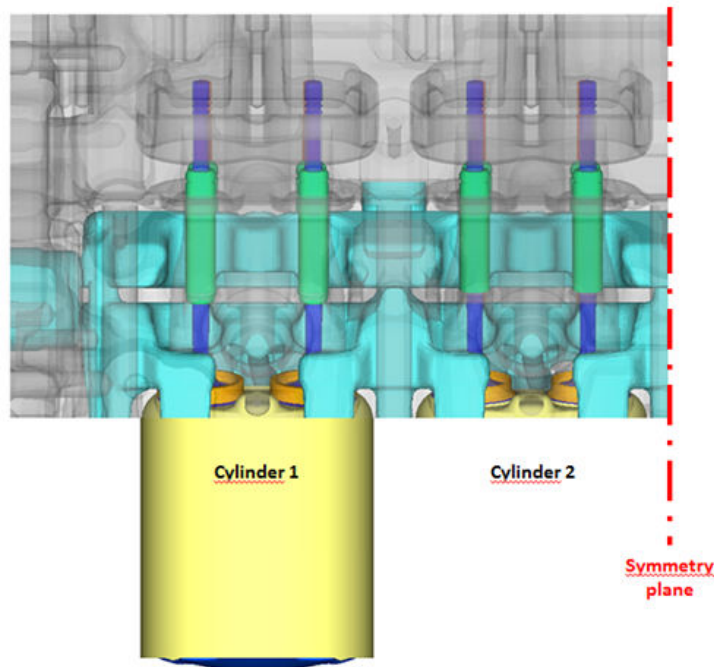


Figure 5.2: View of the solid parts of the computational domain used in the CHT calculation.

Eventually, Figure 5.3 shows a cut plane of the computational domain through Cylinder 1. The gas domain which is simulated is highlighted in yellow. Coloured in blue is coolant jacket boundary. The water flow in the coolant jacket should be considered with care, since it drives the heat removal inside the solid components, and thereby partly dictates the temperature distribution at the gas/solid interfaces. Here the water flow was not simulated, and a solution to model its impact is proposed in *Section 5.3.3*. All the solid components are here summarized:

- The engine head coloured in grey,

- The intake and exhaust valves,
- The sodium rods inside the exhaust valves, which increase heat transfer from the bottom towards the top,
- The valve guides, which drive the translational movement of the valves,
- The valve seats, on which the valves bump when in closed position.

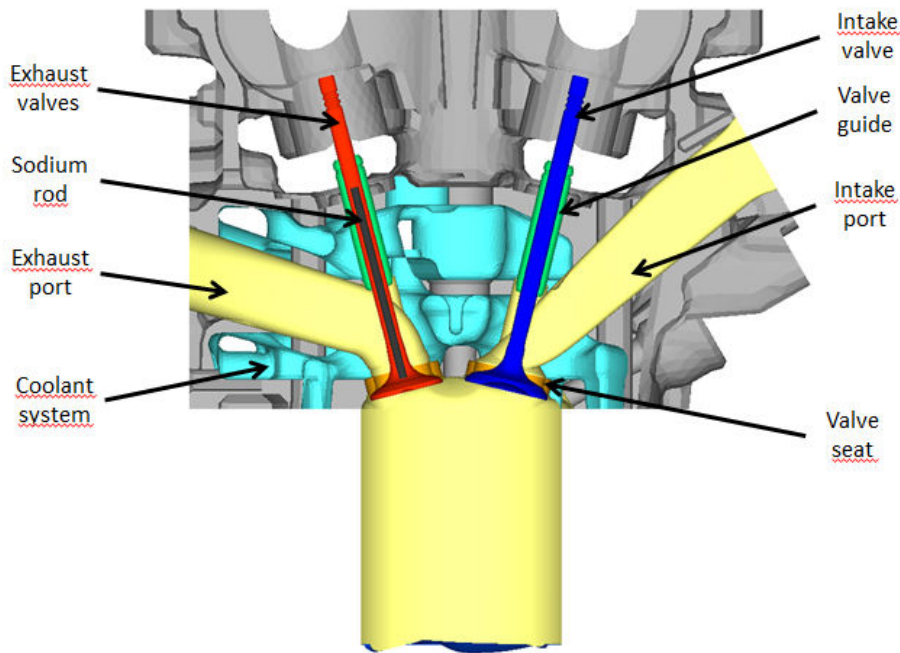


Figure 5.3: Cut view of the computational domain.

5.3 Computational set-up

The CHT simulation was performed with CONVERGE CFD Software. The code semi-implicitly solves the RANS equations for the gas flow and the heat equation for the solid domain on structured meshes.

5.3.1 Computational mesh

The gas and solid domains were discretized using the automatic hexahedric meshing tool implemented in CONVERGE CFD Software. This one employs a cut-cell method to discretize the boundaries. The mesh sizes used in the simulation are given below:

- As for the gas domain, the base grid size inside the combustion chamber was set to $\Delta_x = 1 \text{ mm}$, with a specific refinement at $\Delta_x = 0.5 \text{ mm}$ around the spark-plug during the first instants of the flame kernel growth. Close to the combustion chamber, Δ_x was respectively 1 mm in the intake stroke and 2 mm in the exhaust strokes. The mesh was further coarsened to $\Delta_x = 4 \text{ mm}$ at the farthest ends of the gas domain (near the inlet and outlet boundaries). Then, an Automatic Mesh Refinement (AMR) technique was used to refine the mesh up to $\Delta_x = 0.5 \text{ mm}$ in the combustion chamber, in order to better capture velocity and temperature gradients.
- As for the solid domain, the cell size ranges from $\Delta_x = 1 \text{ mm}$ close to the combustion chamber to $\Delta_x = 4 \text{ mm}$ at the top extremity of the domain. Finally, a specific refinement was imposed around solid/solid interfaces ($\Delta_x = 1 \text{ mm}$) and gas/solid interfaces ($\Delta_x = 0.5 \text{ mm}$) where wall heat transfer are solved.

As a result, the mesh ranges from 1 to 3 million cells during the engine cycle, depending on the position of the piston and the AMR.

5.3.2 RANS approach for the combustion simulation

The combustion in the gas flow is solved with a RANS approach. This appears justified as compared to a LES approach for the following reasons:

- Given the fact that the solid domain only requires at first order an evaluation of mean wall heat fluxes from the gas, and the fact that RANS can effectively predict such a phase average, it is computationally more effective than LES, which would require cycle averaging and yield temporal details, anyway of very small impact on the wall thermal behaviour,
- Misdariis et al. [90] demonstrated in a CHT-LES calculation that the cycle with the highest mean heat flux gives the same results as the one with the lowest mean heat flux, and so the impact of cycle to cycle variations on the wall temperature could be neglected.

Spark-ignition	ISSIM [23]
Flame Propagation	ECFM [20]
Turbulence	RNG k- ϵ [132]
Momentum Law-of-the-wall	Lauder and Spalding [76]
Heat flux Law-of-the-wall	Han and Reitz [54]

Table 5.1: Summary of the RANS models used in the simulation.

RANS models used in the simulation are summarized in Table 5.1. In order to remain consistent with the LES combustion models presented in *Chapter 3*, RANS versions of ISSIM and ECFM were used for combustion modelling. It was assumed that knock at ROP is too weak to significantly impact the wall temperature distribution, and so no auto-ignition model was activated. The turbulent viscosity ν_t was calculated with the RNG k- ϵ model. Transfer of momentum and heat fluxes at the wall boundaries were estimated with standard law-of-the-wall approaches.

5.3.3 Boundary conditions

The definition of the boundary conditions at the external limits of the domain are detailed in this Section. As listed in Table 5.2, a convection boundary condition was imposed on the engine head envelop, through a uniform HTC and far field temperature T_{air} along the boundary. Similarly, a convection boundary condition was imposed on the oil passages boundaries, through an adequate uniform far field temperature T_{oil} and HTC along the boundaries. Then, a particular attention was devoted to the coolant jacket boundary, since it drives the heat removal inside the solid walls. For this reason, a convection boundary condition was also used, but to the difference that it was imposed through a spatial distribution of HTC and a uniform far field temperature $T_{coolant}$. The HTC distribution was derived a priori from a thermal analysis performed by RENAULT at the same operating conditions. The choice of a uniform far field temperature $T_{coolant}$ was justified by the negligible temperature fluctuations in the coolant flowing throughout the jacket, as it was indicated by RENAULT.

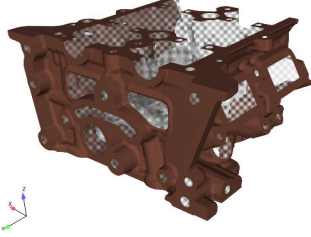
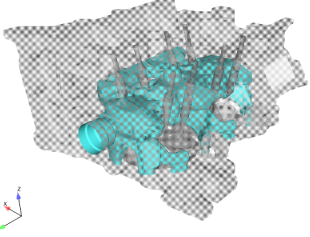
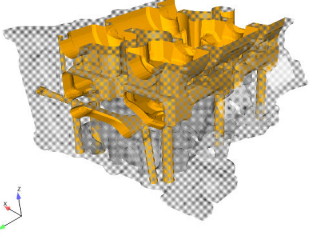
Engine head envelop	Coolant jacket	Oil passages
		
Convection:	Convection:	Convection:
<ul style="list-style-type: none"> • T_{air} • Uniform HTC 	<ul style="list-style-type: none"> • $T_{coolant}$ • Spatial distribution of HTC 	<ul style="list-style-type: none"> • T_{oil} • Uniform HTC

Table 5.2: Convection boundary conditions imposed on the external limits of the solid domain.

At the cylinder head gasket shown in Table 5.3, i.e at the surface boundary of the engine head that is in practice in contact with the removed engine block, a boundary condition with conduction was imposed. It was imposed through a uniform HTC and a spatial distribution of temperature. The uniform HTC was chosen in agreement with the supposedly uniform contact between the block and the engine-head. However, the temperature distribution along the block surface in contact with the engine head is strongly non-uniform, and this is why a spatial distribution of temperature, again derived from an a priori thermal analysis, was imposed.

Then, in order to consider the impact of combustion in Cylinder 2 that was not simulated, uniform temperatures were imposed respectively at the bottom surface boundaries of the intake and exhaust valves, as well as on the cylinder-roof.

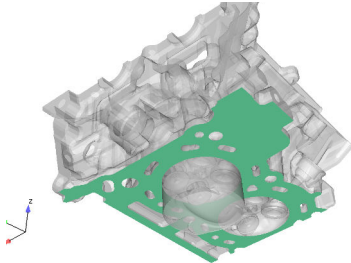
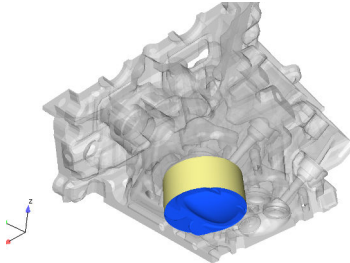
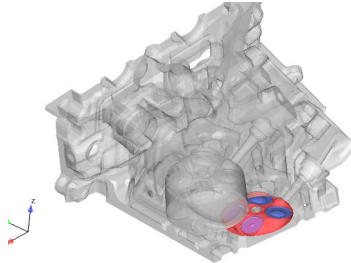
Cylinder head gasket	Liner & Piston	Cylinder 2 boundaries
		
Conduction:	Fixed temperatures:	Fixed temperatures:
<ul style="list-style-type: none"> • Spatial distribution of T • Uniform HTC 	<ul style="list-style-type: none"> • T_{liner} (yellow) • T_{piston} (blue) 	<ul style="list-style-type: none"> • $T_{valves}^{int.}$ (violet) • $T_{valves}^{exh.}$ (pink) • T_{roof} (red)

Table 5.3: Boundary conditions imposed on the external limits of the solid domain.

Finally, for all the remaining boundaries bordering the gas domain and not solved through the thermal coupling, i.e the intake and exhaust ports far from the cylinder, as well as the liner and the piston boundaries, uniform temperatures were directly imposed on each element.

5.3.4 Material properties

Inside the solid domain, solid components react differently to temperature gradients according to their composition. In order to correctly reproduce the thermal behaviour of each solid component, accurate material properties (conductivity, density and specific heat) were separately specified for the engine head, intake valves, exhaust valves, valve guides and valve seats, and this for a wide range of temperature conditions. In practice, the sodium rods,

which increase heat transfer inside the exhaust valves from the bottom to the top, are liquid. In the simulation they were mimed by a solid material with equivalent thermal properties.

On each solid/solid interface, a contact resistance was imposed to model heat transfer between the two solid components. Values are not given due to confidentiality reasons. A particular condition prevails between the valves and seats due to the periodic contact. Indeed a contact resistance exerts when the valves are closed. This no longer applies when the valves are opened, and heat transfer between the gas flow and the valves and seats is solved through the thermal coupling.

5.4 Results and Validation

Three cycles were enough for the RANS-CHT simulation to converge towards a steady state, both in the gas and solid domains. This is illustrated in Figure 5.4 by the trapped mass inside the cylinder for the three cycles. The results for Cycle 3 are compared to the experimental findings.

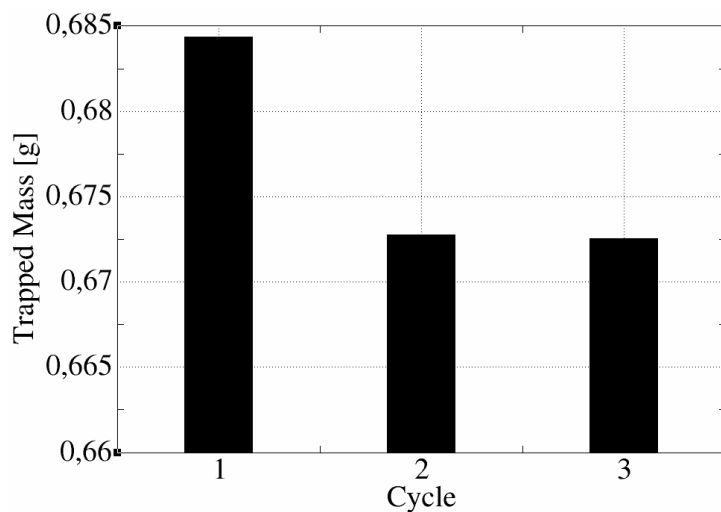


Figure 5.4: Trapped mass inside the combustion chamber right before spark-timing for Cycles 1, 2 and 3.

5.4.1 Validation of the RANS simulation

Shown in Figure 5.5, the simulated mean in-cylinder pressure signal is used to assess the accuracy of the RANS simulation. It is compared to the experimental mean in-cylinder pressure signal, obtained by averaging the 500 experimental pressure signals on a crank angle basis.

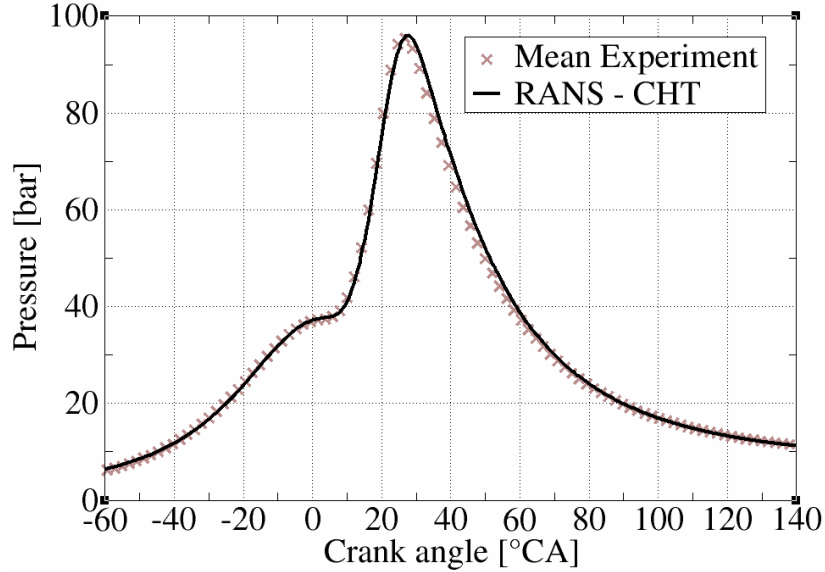


Figure 5.5: Temporal evolution of the mean in-cylinder pressure signals at ROP for the RANS simulation of combustion used in the CHT approach.

The mean experimental pressure signal is well reproduced by the RANS simulation during the compression stroke. Pressure levels coincide at spark-timing ($ST = -5.3$ CA), and the increase of pressure due to combustion are also in agreement. The maximum mean experimental peak pressure \bar{P}_{max} is relatively well captured both in magnitude and timing by the RANS simulation. If one assumes small cycle to cycle fluctuations, it means that the mean combustion heat release is correctly reproduced, which is a necessary condition to predict heat transfer at the gas/solid interfaces with accuracy. Finally, the overall satisfactory agreement during the power stroke suggests that heat losses through the walls are properly represented.

5.4.2 Validation of the CHT predictions

The CHT predictions are compared to the temperature data experimentally measured by RENAULT with the engine running at ROP. Shown in Figure 5.6, these temperatures are given by a set of four thermocouples. They were inserted inside the engine head at a distance of 1.5 to 2 mm perpendicular to the cylinder-roof. Thermocouples are designated according to their respective location: between the exhaust valves (TEE), between the intake valves (TII), between the intake and exhaust valves on the flywheel side (TIEFW), and between the intake and exhaust valves on the valve train side (TIEVT).

Experimental findings and CHT results are summarized in Figure 5.7. First, the order of magnitude is well reproduced, with temperature levels around 430 K. The difference of temperature between the experimental measurements and CHT predictions ranges from 3 to 8 K. Then, it seems that the CHT method is also able to capture with a satisfactory accuracy the relative difference of temperature between the four locations. The smallest temperature value is rightly found at TII, while the largest temperature value is well predicted at TEE. Then, the temperature value at TIEFW is slightly larger than the one at TIEVT due to the

proximity with the second Cylinder on the fly-wheel side, as it was the case in the experiment.

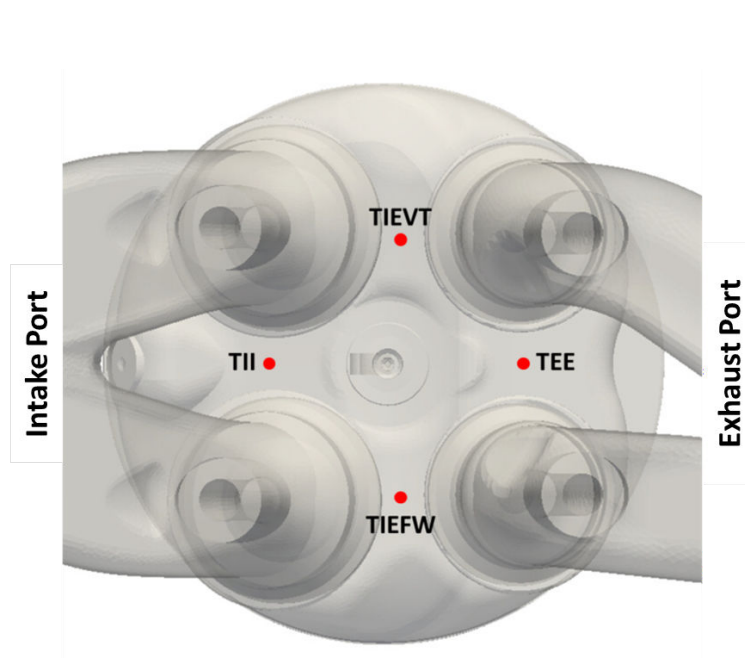


Figure 5.6: Top view of the combustion chamber. Indicated are the positions of the four thermocouples, set at 1.5 to 2 mm ahead of the cylinder-roof.

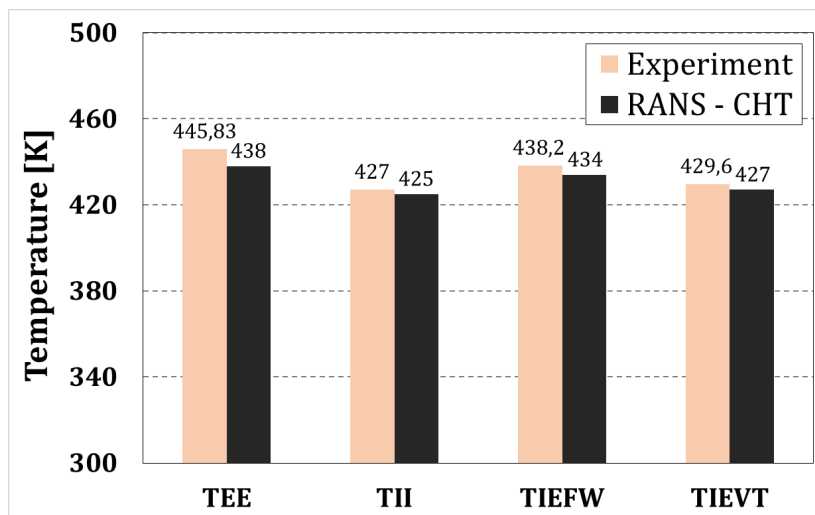


Figure 5.7: CHT vs. Experiment: Local temperature predicted/measured at each of the four thermocouples location.

Resulting from the RANS-CHT simulation, Figure 5.8 shows the predicted temperature dis-

tribution at the gas/solid interfaces, which will be used in the next *Chapter 6* as boundary conditions for the LES. The temperature is globally higher on the exhaust side (right side on Figures) than on the intake side (left side on Figures), a difference which can be explained by the presence of the hot burned gases inside the exhaust ports. As in the studies of Fontanesi et al. [41] [42] [39], the large disparities of temperature along the cylinder-roof and valves surfaces confirm that imposing a uniform temperature along each wall boundary constitutes a strong oversimplifying approximation. The difference of temperature easily reaches 100 K on the cylinder-roof and 200 K on the valves bottom, a difference which may lead to strong temperature inhomogeneities in the flow field inside the cylinder [63]. The highest temperatures around 650 K were found on the exhaust valves, thereby identified as the critical components in terms of temperature levels. Finally, Figure 5.8c underlines the importance of modelling the sodium rod inside the exhaust valves. As compared to the intake valves, the higher conductivity of the sodium increases heat transfer from the bottom to the top of the valves, with the effect of reducing the temperature at the bottom.

5.5 Conclusion

This Chapter presented a RANS-CHT simulation applied to the RENAULT engine under investigation. The thermal coupling allowed to solve heat transfer at the gas/solid interfaces, thereby providing an estimation of the wall temperature distribution where strong gradients were expected. The RANS approach for the simulation of combustion was first validated by comparison with the mean experimental in-cylinder pressure signal. Then, the CHT predictions were compared to experimental findings in order to assess the validity of the present methodology. Following this validation, the wall temperature distribution predicted by CHT will be imposed as boundary conditions for the LES.

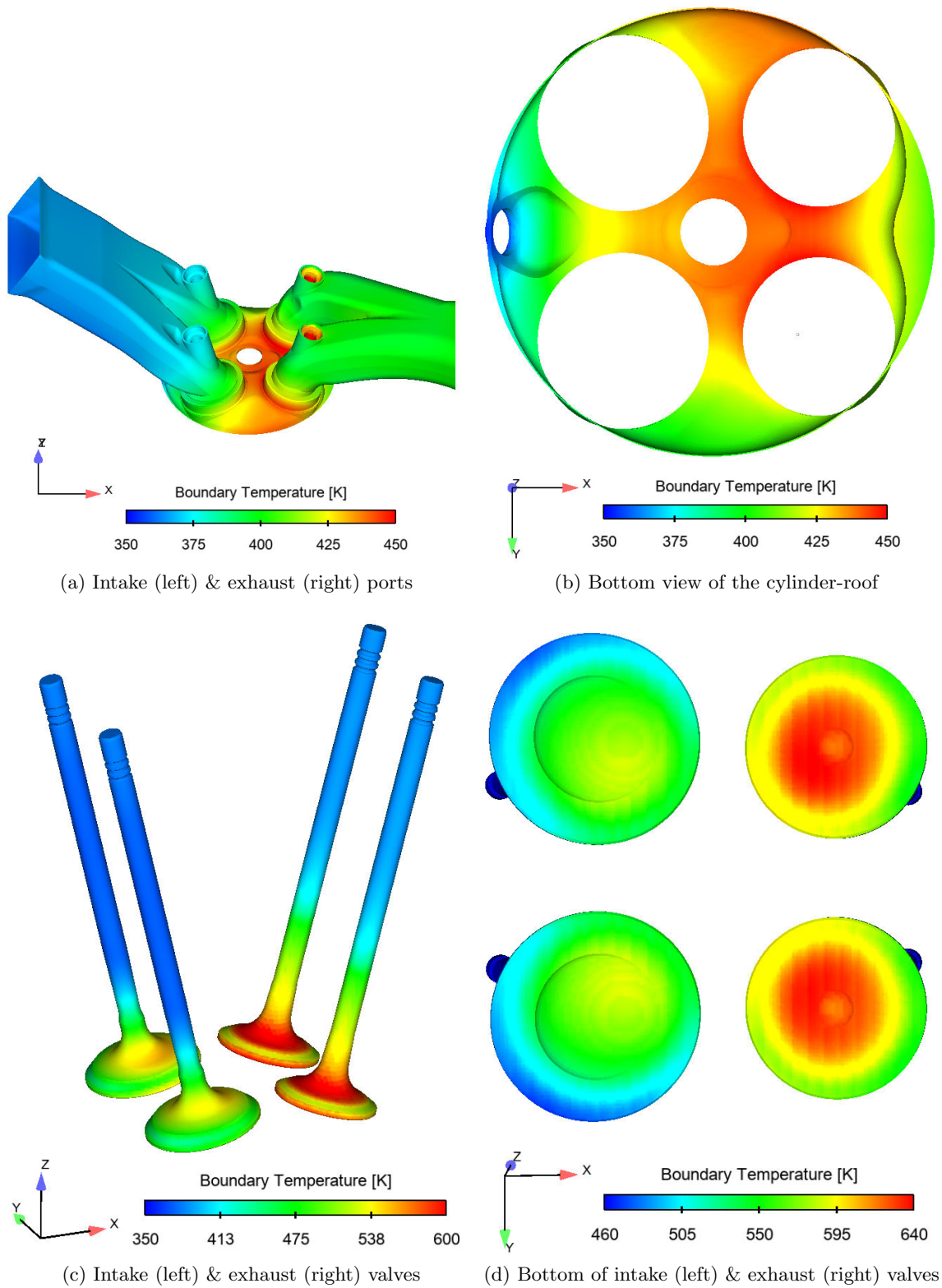


Figure 5.8: Temperature distribution along surfaces predicted by the RANS-CHT calculation.

CHAPTER

6

LES of the RENAULT 1.2 TCe 115 Engine

Contents

6.1	Numerical set-up	90
6.1.1	Computational meshes	90
6.1.2	Inlet and outlet boundary conditions	92
6.1.3	Direct fuel injection	93
6.1.4	Numerical parameters and combustion modelling	94
6.1.5	Wall boundary condition	95
6.2	Validation of the LES at ROP	96
6.2.1	Check on actual and target boundary conditions	96
6.2.2	Quality of the LES	97
6.2.3	Comparison between LES and experimental results	98
	6.2.3.1 Cyclic combustion variability at ROP	99
	6.2.3.2 Knock at ROP	102
6.3	Spark-timing sweep	104
6.4	Summary of Part II	108

This Chapter is dedicated to the LES of the RENAULT engine. The objective is to build a LES database, representative of the engine behaviour, and substantial enough to allow a meaningful statistical analysis.

The first *Section 6.1* details the numerical set-up. It includes the mesh, inlet/outlet and wall boundary conditions, as well as the injection strategy and combustion modelling. The second *Section 6.2* presents the LES results at ROP. The accuracy of the simulation in terms of cyclic combustion variability (CCV) and knock is assessed by comparison with experimental findings. In the last *Section 6.3*, the simulated cycles at ROP are used as the basis for a spark-timing sweep, the aim of which is to enlarge the database to weaker and stronger knock levels.

6.1 Numerical set-up

The LES was performed with the AVBP code [49] [50] [91], co-developped by CERFACS and IFPEN. The code explicitly solves the filtered compressible multi-species Navier-Stokes equations on unstructured meshes with a cell-vertex finite-volume formulation [27].

6.1.1 Computational meshes

The computational domain presented in *Chapter 4* was discretized with tetrahedra using CENTAUR 10.6. Unstructured meshes make it easier to smoothly refine in specific locations (e.g around valve seats and spark-plug), while coarsening the mesh far away from the combustion chamber. An engine cycle is here subdivided into several phases, for each of which a single mesh was generated. Within a phase i , the grid nodes on the wall boundary are moved due to the piston and valves motion. The displacement is handled by the Arbitrary Lagrangian Eulerian (ALE) method [58] [91]. This one propagates the imposed movement of the grid nodes (the ones at the wall) to the rest of the mesh, while keeping the same connectivity. The deformation of the mesh continues until at least one cell gets an unacceptable, highly irregular shape. At this instant a new mesh (corresponding to phase $i + 1$) is generated, it is in turn deformed, and so on. This way, a set of 60 meshes was generated to cover an entire engine cycle and guarantee an acceptable mesh quality.

For each phase, the minimum cell volume was tightly controlled. Indeed in the explicit solver AVBP, the time step Δt is driven by the CFL number (that should be smaller than one in this simulation to ensure stability), and by the smallest cell volume in the mesh. The estimation of the time step in a one dimensional case is given by:

$$\Delta t = \frac{CFL \Delta x}{(|u| + c)} \quad (6.1)$$

where $|u|$ is the norm of the velocity in the cell, c is the sound speed and Δx is the length of the cell. The CFL being imposed by the numerical scheme, this implies that the smallest cell volume had to be optimized as large as possible, while keeping cell sizes small enough to

resolve steep gradients in narrow regions. Besides, an effort was made to keep cells shape as close as that to an ideal tetrahedron.

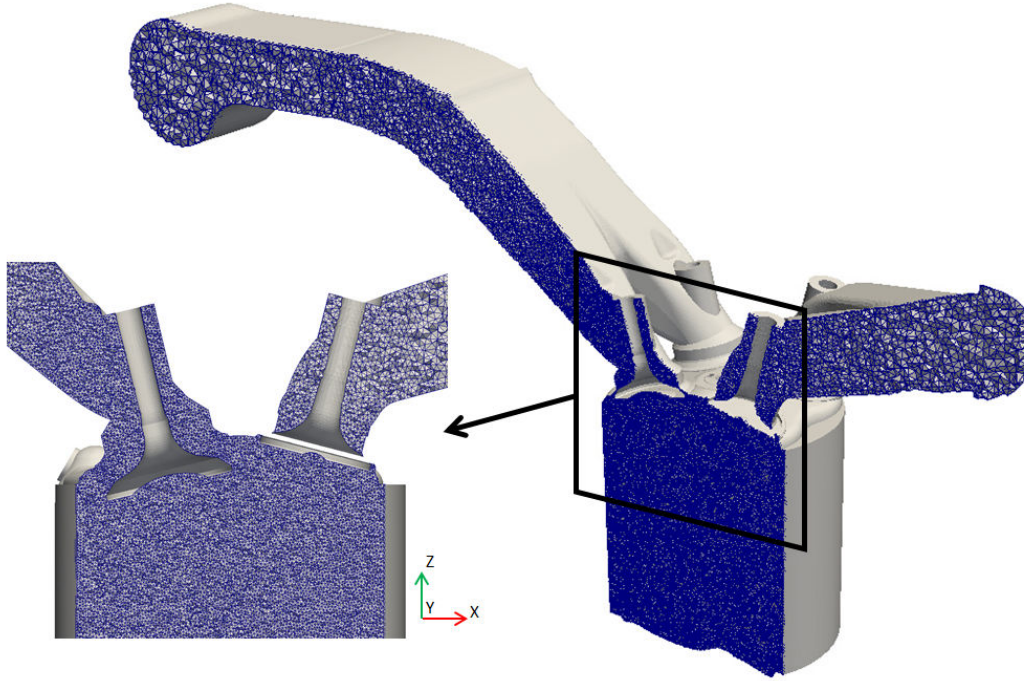


Figure 6.1: View of the LES tetrahedric mesh during the intake stroke.

Figure 6.1 shows a cut plane of the mesh during the intake stroke. The number of cells strongly evolves during one cycle, ranging from 2.8 millions at TDC (Top-Dead-Center) to 12.1 millions at BDC (Bottom-Dead-Center):

- The mesh size in the combustion chamber was fixed at $\Delta x = 0.6$ mm. It is progressively refined until $\Delta x = 0.15$ mm around the spark plug, only during the first instants of the flame kernel growth.
- Through the intake port, the mesh is gradually coarsened from $\Delta x = 0.6$ mm close to the intake valves, to $\Delta x = 2.5$ mm at the inlet boundary.
- As for the exhaust port, the mesh size is rapidly coarsened from $\Delta x = 0.6$ mm around the exhaust valves, to $\Delta x = 4$ mm at the outlet boundary, in order to keep the cell number as low as possible.
- Finally, a specific meshing condition was applied to the valves curtain, that is to the varying volume between the valves and seats. First, the residual valve lift was set at 0.3 mm, meaning that the valves are considered to be in closed position for lower valve lifts. Then, for relatively low-lift phases, the cell size was indirectly imposed to guarantee a minimum of four cells (five nodes) along the height of the curtain.

6.1.2 Inlet and outlet boundary conditions

In the case of a piston engine simulation, the flow at the inlet can be alternately incoming and outgoing due to back-flow, even if this feature is damped by the long distance between the inlet and the simulated Cylinder 1. It is also the case at the outlet, where exhaust gases of cylinders 2, 3 and 4 can enter the exhaust port of Cylinder 1. Thus, an `INOUT_RELAX_P_T_Y` boundary condition is particularly suited, since it distinguishes and handles accordingly with incoming and outgoing flows. When the flow is incoming, pressure, temperature and species mass fractions are imposed, while only the pressure is imposed for outgoing flows.

The `INOUT_RELAX_P_T_Y` is a type of Navier-Stokes Characteristic Boundary Conditions (NSCBC), the principle of which is detailed in [106]. It operates as follows: derivatives of the Navier-Stokes equations normal to the boundary can be recast as the amplitude of characteristic waves crossing the boundary. The outgoing waves can be computed from the flow variables in the computational domain, while incoming waves need to be determined. The incoming waves are computed as proportional to the difference between the actual thermodynamic state at the boundary nodes and the reference signals resulting from experiments or 0D-1D simulations. The pressure, temperature and species mass fraction are thus followed in a soft way by controlling the acoustic wave reflection at the boundary.

The proportionality constant that controls the reflective behaviour at the inlet and outlet boundaries is known as the relaxation coefficient and is imposed by the user. A strong relaxation coefficient (tending to infinity) induces a perfectly reflecting boundary that follows exactly the target signal, while a small relaxation coefficient (close to zero) does not follow exactly the target signal, but minimizes reflections. An ideal value represents a compromise between these two extrema. The relaxation coefficients imposed in the simulation are reported in Table 6.1.

Relaxation coefficient	Inlet boundary	Outlet boundary
Pressure	3000	5000
Temperature	3000	1000
Species	3000	5000

Table 6.1: Relaxation coefficients imposed at the inlet and outlet boundaries.

Since the fuel in the studied engine is directly injected into the cylinder, only air was introduced at the inlet boundary. A complete oxidation of the fuel was assumed in the combustion chamber, so that the outlet composition is that given in Table 6.2.

	Inlet boundary	Outlet boundary
Y_F	0	0
Y_{O_2}	0.233	0
Y_{N_2}	0.767	0.71735
Y_{CO_2}	0	0.20615
Y_{H_2O}	0	0.0765

Table 6.2: Incoming species mass fractions imposed for the LES at the inlet and outlet boundaries of the domain.

6.1.3 Direct fuel injection

The multi-components gasoline surrogate used in the experiment was modelled by a representative single-component fuel. This single-component fuel was defined with respect to the thermodynamic properties of the multi-components surrogate.

The spray model is based on a Lagrangian formalism, i.e it relies on the transport of statistical fluid particles accounting for the main characteristics of the spray. The particles dynamics is described by the Lagrangian system of equations, detailed in [60]. Under the assumption of isolated particles, this system of equations describes the motion of inertial particles subject to drag forces due to the difference of velocity between the flow and particles. The contribution to the gas flow is introduced in the filtered Navier-Stokes equations by additional source terms for the mass, species, momentum, and total energy. This approach requires new models, since particles (the diameter of which ranges from 1 to 20 μm in this study) are not resolved on LES meshes. The liquid fuel evaporation is modelled using the evaporation model of Spalding [120] considering only heat diffusion from the particle surface to the surrounding gas flow.

The spray generated by the direct-injector was experimentally studied in a constant volume vessel at 135 bars, corresponding to the injection pressure at ROP. The resulting flow rate profile imposed for the LES is shown in Figure 6.2. The positive (respectively negative) slope corresponds to the opening (respectively closure) of the injector. The period of injection (length of the plateau) was determined with respect to the experimental mean equivalence ratio inside the combustion chamber, $\phi = 1.05$. A Malvern measurement system was used to determine the characteristic particle diameters of the spray. They served as input parameters to determine a Rosin-Rammler distribution, here adopted to describe the particle size distribution.

As explained in *Section 4.2*, the piston is close to TDC at the start of injection, and the bowl shape piston redirect the spray towards the spark plug. In order to model this effect, Figure 6.3 illustrates the simple elastic rebound condition accounting for moving parts, which had to be implemented in AVBP code. In reality, particles can rebound, slip, splash or stick on the walls depending on local conditions, thus requiring a complex interaction model. Such a model is currently under development at IFPEN.

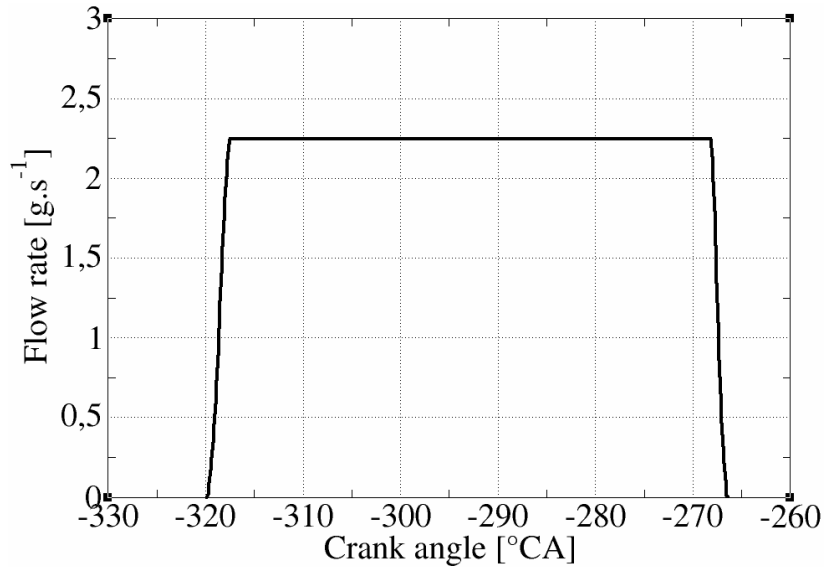


Figure 6.2: Flow rate profile of the injected fuel.

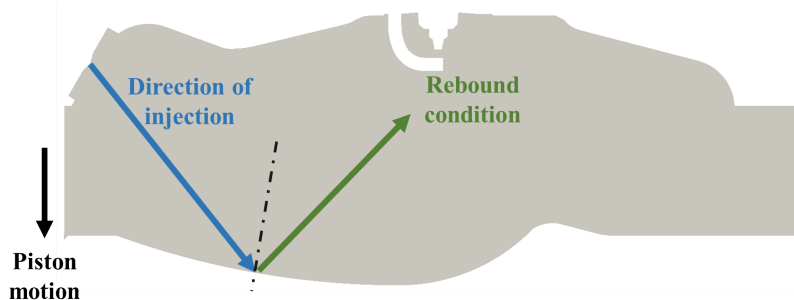


Figure 6.3: Schematic of the rebound condition implemented in AVBP.

6.1.4 Numerical parameters and combustion modelling

The set of numerical parameters used for the LES is summarized in Table 6.3. The second order accurate in time and space Lax-Wendroff (LW) [77] convective scheme was used for discretization. It was previously used in several LES of piston engines [38] [51], and was recently compared to high order convective schemes (TTGC and TTG4A) [88]. The Lax-Wendroff scheme is a priori more dissipative than the high order numerical schemes, but it is a good compromise to perform a LES with acceptable overall accuracy and CPU time.

Combustion modelling includes spark-ignition, turbulent premixed flame propagation and auto-ignition. The different aspects and the corresponding models employed in the simulation are summarized in Table 6.4. These models were detailed in *Chapter 3*. Tabulated values used for the TKI-LES model were generated for the surrogate fuel for the wide range of pressure, temperature and equivalence ratio found in the combustion chamber.

Parameter	Default Value
Convective scheme	Lax-Wendroff
CFL number	0.9
Fourier number	0.1
Sub-grid scale model	Sigma
Artificial viscosity model	Colin's sensor [19]
Artificial viscosity coeff.	$\epsilon_2=0.1 / \epsilon_4=0.005$

Table 6.3: Set of parameters used for the LES.

Aspect	Model
Spark-ignition	ISSIM-LES [23]
Premixed flame propagation	ECFM-LES [126] [112]
Auto-ignition	TKI-LES [112]

Table 6.4: Set of combustion models for the LES.

6.1.5 Wall boundary condition

In order to avoid the resolution of thermal and aerodynamics boundary layers, the logarithmic law-of-the-wall approach by Diwakar was used [32]. It assumes that the flow between the wall and the first off-wall node has the same structure as that of the near-wall region over a flat plate. Based on the knowledge of the filtered velocity parallel to the wall \tilde{u}_1 and temperature \tilde{T}_1 at the first off-wall node situated at a normal distance y_1 from the wall, the law-of-the-wall approach directly provides a friction velocity \tilde{u}_τ , as well as a wall friction τ_w . It also provides a wall heat flux modelled as:

$$\tilde{\Phi} = \rho_w C_p u_\tau \frac{(T_w - \tilde{T}_1)}{\tilde{T}_1^+} \quad (6.2)$$

In Eq. 6.2, \tilde{T}_1^+ is the non-dimensional temperature given by the temperature law-of-the-wall, ρ_w is the density at the wall, and T_w the wall temperature. One can see that T_w is a first order parameter to estimate wall heat transfer, and this is why it has been accurately estimated by CHT, see *Chapter 5*.

It should be recalled that the law-of-the-wall approach relies on many assumptions which are strictly speaking not satisfied for an in-cylinder flow: plane walls, steady flow, no adverse pressure gradient, negligible transverse velocity, no chemical reaction. Nonetheless, it allows estimating instantaneous wall friction and heat flux that have the right order of magnitude,

at least in the mean.

6.2 Validation of the LES at ROP

Based on the modelling approach and numerical set-up previously described, a first set of 36 consecutive LES cycles was computed at the ROP. The average computational time for a single engine cycle was roughly 12000 CPU hours (≈ 2 days on 256 cores). The first two cycles were strongly impacted by the initial conditions and were thus removed from the database.

6.2.1 Check on actual and target boundary conditions

As shown in Figure 6.4a and 6.4b, the imposed relaxation coefficients allow to follow the target inlet and outlet pressure signals coming from the 0D-1D simulation, while limiting artificial reflection.

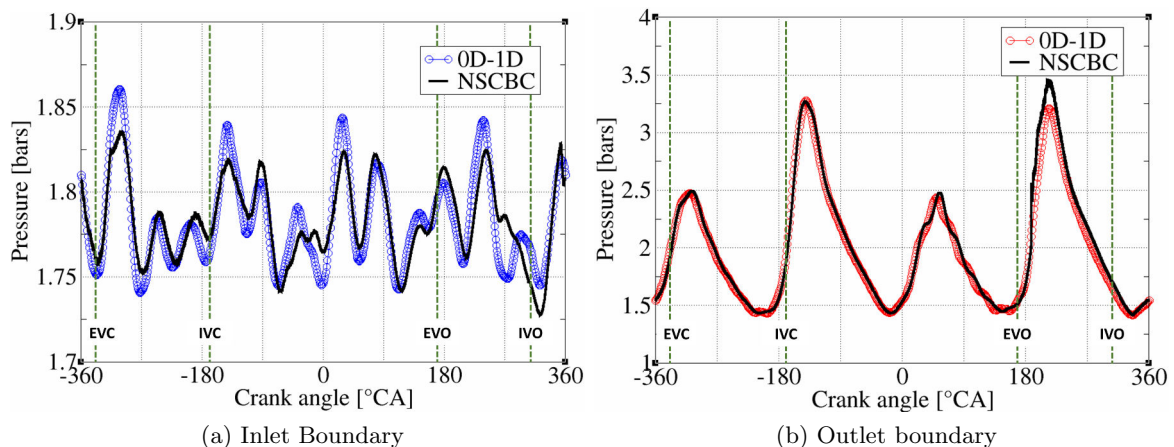


Figure 6.4: Target (0D-1D simulation) and actual (NSCBC) pressure signals recorded at the inlet boundary. Exhaust Valves Opening (EVO) and Closure (EVC) are highlighted as well as Intake Valves Opening (IVO) and Closure (IVC).

At the inlet boundary, the actual pressure signal satisfactorily follows the rapid changes of the target signal. The small differences of magnitude between actual and target signals are due to outgoing waves. At the outlet boundary, strong variations of pressure are closely followed thanks to the high relaxation coefficient (5000). However, as a result of such a large relaxation coefficient, there were significant wave reflections at the outlet boundary, leading to numerical instabilities. To avoid numerical issues, an artificial viscosity patch was added at the outlet boundary. This allows (together with the coarse mesh at this location) to damp the reflective waves and limit their impact on the flow dynamics inside the exhaust port.

6.2.2 Quality of the LES

The quality of the LES was first assessed by means of the ratio between the SGS kinematic viscosity ν_t over the molecular kinematic viscosity ν . Figure 6.5 shows instantaneous fields of ν_t/ν over ν for Cycle 3 at four different instants.

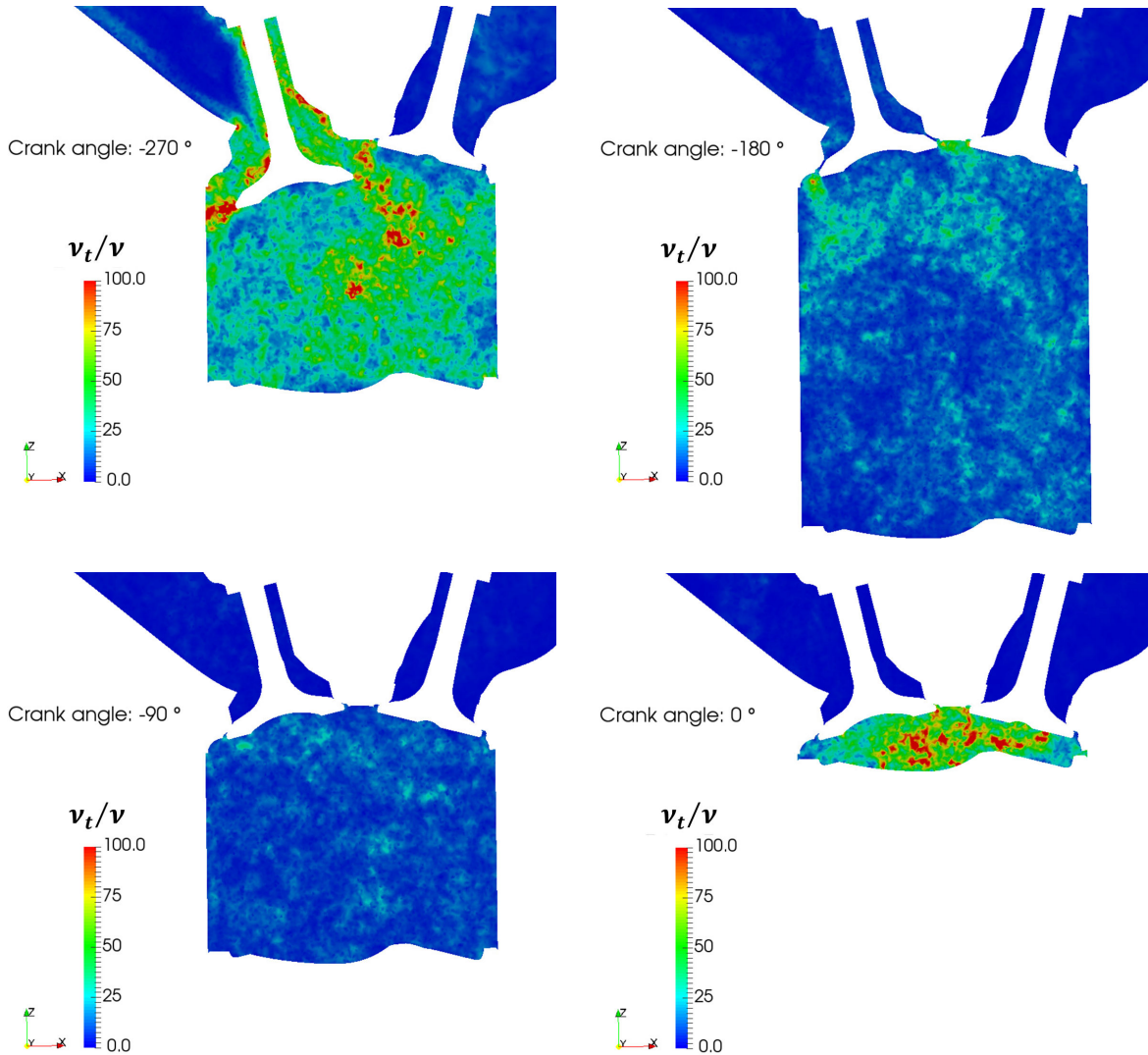


Figure 6.5: Instantaneous ν_t/ν field for Cycle 3 at four different instants. During the intake stroke, at BDC, during the compression stroke and at combustion TDC. Intake (exhaust) valves are on the left (right) respectively.

At BDC (-180°CA) and during the compression stroke (-90°CA), the used LES approach allows resolving a large part of the turbulence spectrum, with ν_t/ν values mostly around 10

in the center of the domain, and a few peaks of 30 in certain regions. During the intake stroke (at -270°CA), the mesh does not allow to solve the strong gradients generated by the high speed jets between the valves and seats, with ν_t/ν values of 100 at some locations. At combustion TDC (0°CA), the large scales of the turbulent intake flow has cascaded down to smaller eddies that cannot be resolved on the employed mesh. This explains the large ν_t/ν ratio obtained at this instant.

Certifying that such ratios are indeed acceptable requires to validate the mesh and estimate the numerical dissipation ν_{num} , since they both impact ν_t levels. On the one hand validating the mesh would require running new simulations with refined meshes, and would be extremely costly and was thus not preformed in this study. On the other hand the numerical dissipation is hardly quantifiable. Hence the ratios obtained should be used carefully as a basis to which future piston engine LES could be compared.

Looking at the ratio ν_t/ν gave information on the resolution of the turbulent eddies, but for combustion another aspect must be checked: a non negligible fraction of the flame surface should be resolved, that is the SGS wrinkling, defined as the ratio between the total flame surface $S_{res} + S_{sgs}$ and the resolved flame surface S_{res} , should remain as small as possible. In Figure 6.6, with a 15 to 25% resolution of the flame front, corresponding to an SGS wrinkling of 3 to 5.5, one can consider that a non negligible fraction of the flame is resolved although higher resolution should be considered to reduce the wrinkling to smaller values.

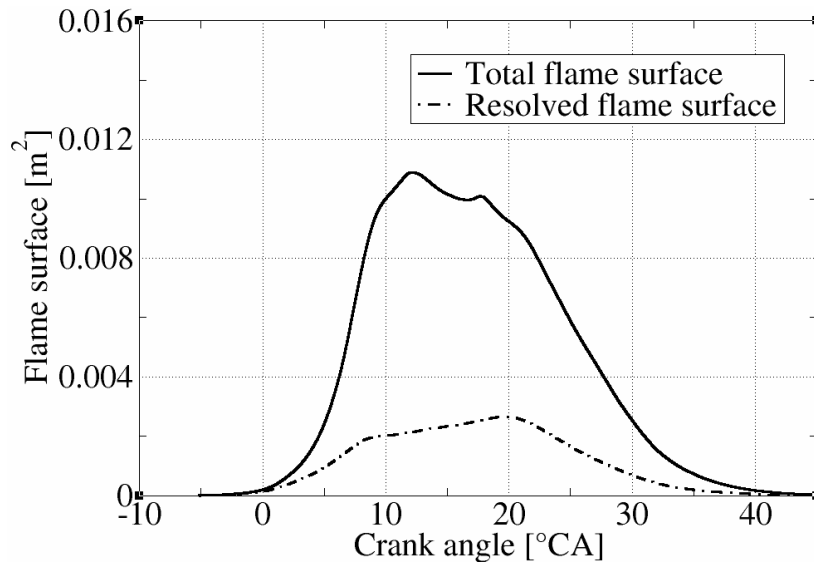


Figure 6.6: Total and resolved flame surface for Cycle 3.

6.2.3 Comparison between LES and experimental results

The accuracy of the LES was assessed by comparison with experimental measurements. In particular we evaluated the ability of the LES to fairly capture CCV and to predict knock

events. To do so, the only available experimental datum is the temporal evolution of the in-cylinder pressure. It was measured by a pressure transducer situated on the cylinder dome. In the LES, a numerical probe was set at the same location.

6.2.3.1 Cyclic combustion variability at ROP

Figure 6.7a compares the pressure signals recorded for the 34 consecutive LES cycles (Cycle 3 to Cycle 36) with the 500 experimental cycles. During the compression stroke, the LES pressure signals superimpose with the experimental ones, and the pressure levels at spark-timing ($ST = -5,3$ CA) coincide. During the combustion, 4 cycles over the 34 simulated were found relatively under the experimental envelop. They suggest that some aspect might not have been accurately represented by the LES approach. The particular reason was not identified, but it is likely that the simplified spray/wall interaction (rebound condition) significantly impacts the mixing of the fuel with air, possibly leading to some deviation in the mixture distribution. With the perspective to investigate knock based on a numerical database representative of the engine behaviour, these 4 cycles were simply left aside. Thus, the database consists in the 30 simulated cycles visually inside the experimental pressure envelop, as displayed in Figure 6.7b.

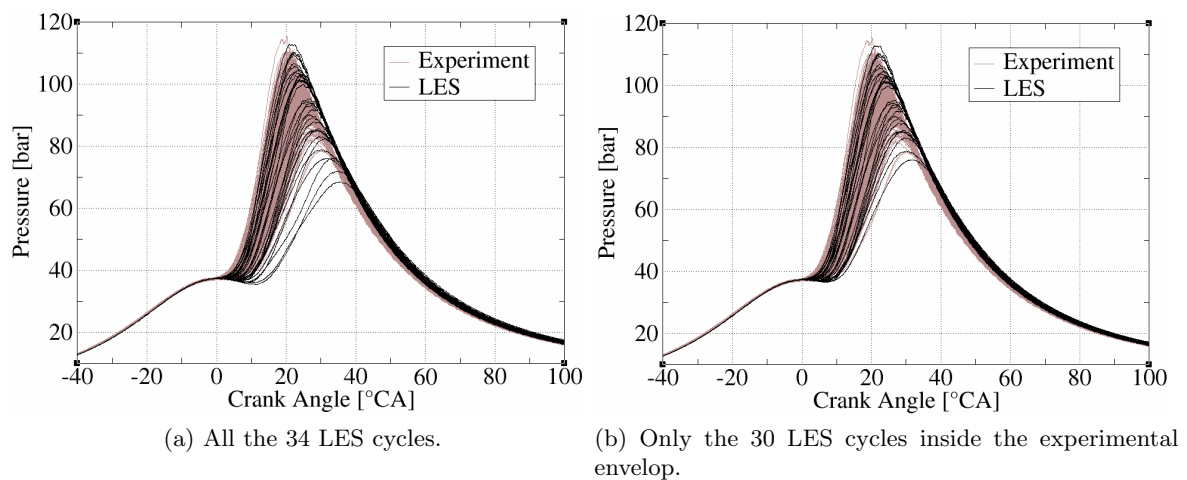


Figure 6.7: Temporal evolution of the in-cylinder pressure signals at ROP, for the LES cycles compared with the 500 experimental cycles.

Figure 6.8 shows the Matekunas diagram, which is another way to represent CCV. It plots the maximum in-cylinder pressure P_{max} over the crank angle at which it occurs CAP_{max} . CAP_{max} values predicted by LES are slightly shifted to larger crank angles, but still they globally remain inside the experimental envelop. One can further observe the satisfactory agreement in the linear decrease of P_{max} as a function of CAP_{max} . It is known that such evolution characterizes a stable operating point [51].

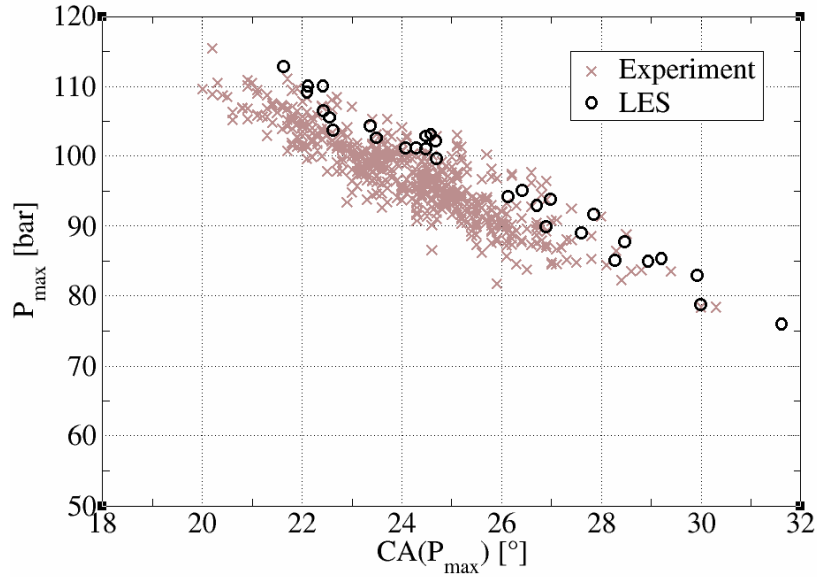


Figure 6.8: P_{\max} over $CA_{P_{\max}}$ (Matekunas diagram), for the 30 LES cycles compared with the 500 experimental cycles.

In a more quantified way, the *Indicated Mean Effective Pressure* ($IMEP$) is introduced for each engine cycle i :

$$IMEP_i = - \frac{\int P dV}{V_d} \quad (6.3)$$

with P the pressure signal recorded over the engine cycle i integrated over the varying combustion chamber volume dV , and V_d the displacement volume. $IMEP_i$ quantifies the work produced over an engine cycle, with regard to the displacement volume.

Then, the mean performance of the engine is introduced through the mean value $\langle IMEP \rangle$. It simply corresponds to the ensemble average of $IMEP$ based on a sample of N engine cycles:

$$\langle IMEP \rangle = \sum_{i=1}^N \frac{IMEP_i}{N} \quad (6.4)$$

Finally, the degree of variability of the engine is quantified through the coefficient of variation $COV(IMEP)$:

$$COV(IMEP) = \frac{\sqrt{\sum_{i=1}^N \frac{(IMEP_i - \langle IMEP \rangle)^2}{N}}}{\langle IMEP \rangle} \quad (6.5)$$

It is the ratio between the standard deviation of $IMEP_i$ and its ensemble average $\langle IMEP \rangle$.

In the same way, $\langle CAP_{max} \rangle$ is introduced as the ensemble average of CAP_{max} based on a sample of N engine cycles, as well as the coefficient of variation $COV(CAP_{max})$.

Because the number of LES cycles (30) is considerably smaller than the number of experimental cycles (500), any statistical comparison must be concluded with care. Indeed, it is likely that the use of 30 cycles is not enough to perfectly capture the mean engine behaviour as given by 500 cycles, but it would not mean that these 30 simulated cycles are not representative of the combustion in the engine. To allow a meaningful quantitative comparison, Figure 6.9 illustrates how the experimental cycles are divided into sub-sets of 30 cycles.

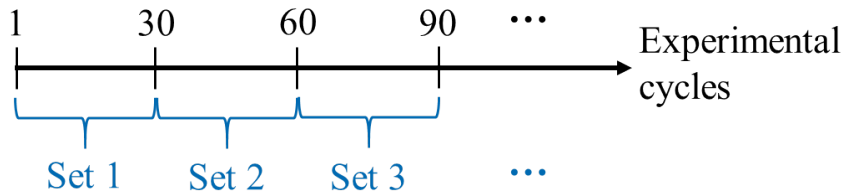


Figure 6.9: Range of the experimental cycles into sub-sets of 30 cycles.

$\langle IMEP \rangle$, $\langle CAP_{max} \rangle$ and their respective coefficient of variations are calculated for each sub-set. The two sub-sets with respectively the minimum and maximum values for each quantity, noted Set_{min} and Set_{max} , determine an envelop in which LES results should remain. In Table 6.5, the 30 LES cycles are compared with the 30 cycles sub-sets. $\langle IMEP \rangle$ based on LES lie within the experimental envelop defined by Set_{min} and Set_{max} . However, $COV(IMEP)$ predicted by LES is slightly larger than the Set_{max} value, and tends to indicate that the engine variability is slightly overestimated by LES. Nonetheless, the value is relatively close to the experimental measurements.

	$\langle IMEP \rangle$ [bars]	$COV(IMEP)$ [%]
Expe. (mean over 500 cycles)	23.45	1.5
Expe. ($Set_{min} \rightarrow Set_{max}$)	23.28 \rightarrow 23.64	1.1 \rightarrow 1.8
LES	23.60	2.0

Table 6.5: $\langle IMEP \rangle$ and $COV(IMEP)$ at ROP based on the LES and experimental samples.

Similarly, Table 6.6 gathers $\langle CAP_{max} \rangle$ and $COV(CAP_{max})$ for the LES and experiment. It confirms the previous observation, that is $\langle CAP_{max} \rangle$ is globally delayed in the simulation. In addition, $COV(CAP_{max})$ is overestimated by LES. Still, the value is close enough to the experimental measurements to consider the LES cycles as representative of the engine behaviour.

	$\langle \text{CAP}_{\max} \rangle$ [$^{\circ}\text{CA}$]	$\text{COV}(\text{CAP}_{\max})$ [%]
Expe. (mean over 500 cycles)	24.16	7.1
Expe. ($Set_{\min} \rightarrow Set_{\max}$)	23.44 \rightarrow 24.88	5.0 \rightarrow 8.5
LES	25.63	10.7

Table 6.6: $\langle \text{CAP}_{\max} \rangle$ and $\text{COV}(\text{CAP}_{\max})$ at ROP based on the LES and experimental samples.

6.2.3.2 Knock at ROP

The capability of the simulation to predict knock is now assessed. The validation requires using a common post-processing methodology to similarly quantify knock in the simulation and experiment, and therefore be based on the analysis of the instantaneous in-cylinder pressure signals. The Maximum Amplitude of Pressure Oscillations (MAPO) [14] was chosen in this study. It is one among the many existing methods commonly used to estimate the knock intensity (KI) for each engine cycle. The MAPO analysis was similarly applied to the experimental and LES pressure signals. It allows to define two quantities:

- The maximum knock intensity KI_{\max} , simply taken as the individual cycle with the largest KI.
- The percentage of knocking cycles. It corresponds to the percentage of engine cycles for which KI outreaches a threshold level KI_T defined by the operator on the test bench. At ROP, a KI_T value of 0.159 bar was deduced.

The same experimental sub-sets, each consisting of 30 consecutive cycles, were used to validate the LES results. Table 6.7 compares the maximum knock intensities KI_{\max} . The KI_{\max} level predicted by LES is smaller than the experimental one, and close to the minimum found in the 30 cycles sub-sets.

	KI_{\max} [bar]
Expe. ($Set_{\min} \rightarrow Set_{\max}$)	0.38 \rightarrow 0.9
LES	0.39

Table 6.7: Maximum knock intensity KI_{\max} at ROP based on the LES and experimental samples.

Then, Table 6.8 shows the results for the percentage of knocking cycles. The difference between Set_{\min} and Set_{\max} is extremely large, ranging from 26.7 to 63.3% of knocking cycles, corresponding to a ratio $Set_{\max}/Set_{\min} = 2.37$. Shown in Figure 6.10, this ratio slowly converges when increasing the number of cycles per sub-set. It indicates that 30 cycles

are certainly not enough to represent the mean engine behaviour in terms of knock. However, as it was stated before, it does not prevent the 30 LES cycles to be representative of potential knock events in the engine. In the same Table 6.8, the percentage of knocking cycles in LES is smaller than the experimental mean value (i.e based on 500 cycles) and very close to the minimum found with the 30 cycles sub-sets, but still within the experimental envelop.

	Knocking cycles [%]
Expe. (mean over 500 cycles)	44.4
Expe. ($Set_{min} \rightarrow Set_{max}$)	26.7 \rightarrow 63.3
LES	30

Table 6.8: Percentage of knocking cycles at ROP based on the LES and experimental samples.

To summarize, the maximum knock intensity and percentage of knocking cycles remain in the experimental envelop, but they tend to indicate a slight underestimation of knock by LES. Nonetheless, the simulation results remain sufficiently consistent with experimental findings to consider the set of 30 LES cycles as representative of the engine behaviour.

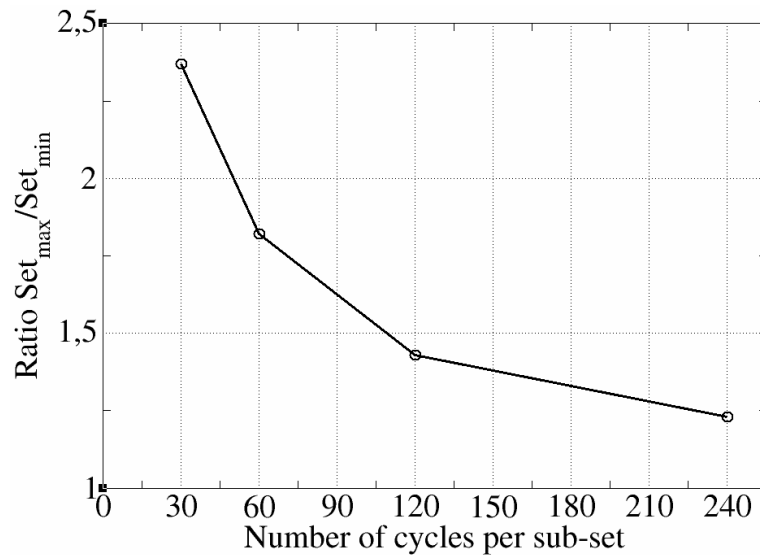


Figure 6.10: Ratio Set_{max}/Set_{min} of the percentage of knocking cycle, as a function of the number of cycles per sub-set.

6.3 Spark-timing sweep

Based on the LES cycles at ROP ($ST = -5.3^\circ CA$), new simulations were computed in order to enlarge the database to weaker and stronger knock events. To do so, the exact same boundary conditions were used, that is the same valve lift laws and fuel direct-injection parameters, and only the spark-timing was changed. The set of new simulations consists of one retarded spark-timing [$-3.3^\circ CA$] and four advanced spark-timings [$-7.3^\circ CA$, $-9.3^\circ CA$, $-11.3^\circ CA$]. In order to limit CPU costs, the methodology proposed in [112] and illustrated in Figure 6.11 was adopted:

1. The instantaneous field at $11.8^\circ CA$ before combustion TDC for the 30 LES cycles at ROP are used to create different initial conditions.
2. Starting from the initial conditions, each cycle is independently re-computed in parallel with different spark-timings, until the end of the combustion process.

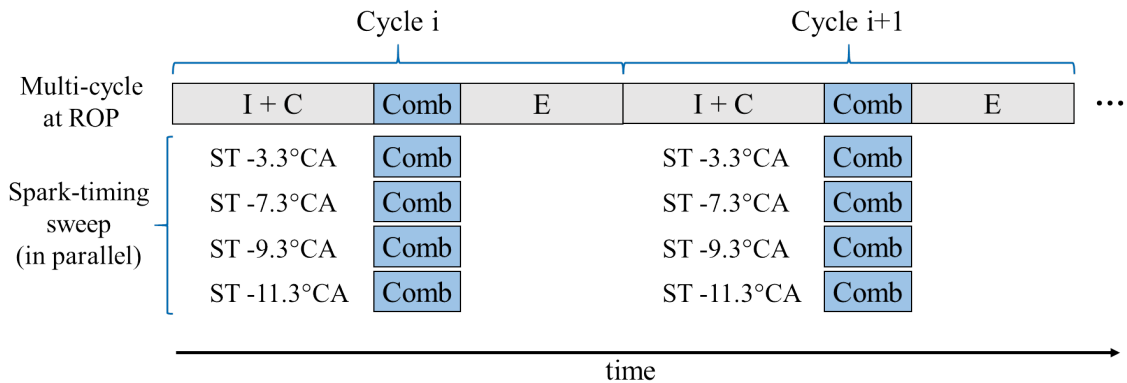


Figure 6.11: Spark-timing sweep methodology. I = Intake stroke, C = Compression stroke, $Comb$ = Combustion, E = Exhaust stroke. Only the combustion phases are re-computed in parallel. (Adapted from [87]).

This strategy is valid to the condition that the individual cycles are independent. The accuracy of this hypothesis is verified in Figure 6.12. $IMEP$ of cycle i is plotted as a function of $IMEP$ of the previous cycle $i - 1$. There is no regular pattern, meaning that no obvious relation exists between a cycle and the following one.

The new database consists of 150 LES combustion cycles. The temporal evolution of the in-cylinder pressure is drawn in Figure 6.13 for the 30 simulated cycles at each of the five spark-timings. The pressure signals at the new spark-timings cannot be compared to experimental data, since the variation in spark-timings on the industrial test bench was performed at iso- $IMEP$. This means that the experimental spark-timing sweep went along with changes in the inlet conditions.

In Figure 6.13, one can observe a faster increase of the in-cylinder pressure (i.e steeper slopes) as spark-timing is advanced, resulting from a faster combustion process. The CAP_{max} globally decreases, leading to higher P_{max} values in agreement with the linear correlation between the two quantities. Such an increase in the maximum pressure suggests higher $IMEP$ levels, synonym of an increased engine efficiency. However, the largest pressure levels also seem to correspond to more pronounced pressure oscillations, which are characteristic of knock.

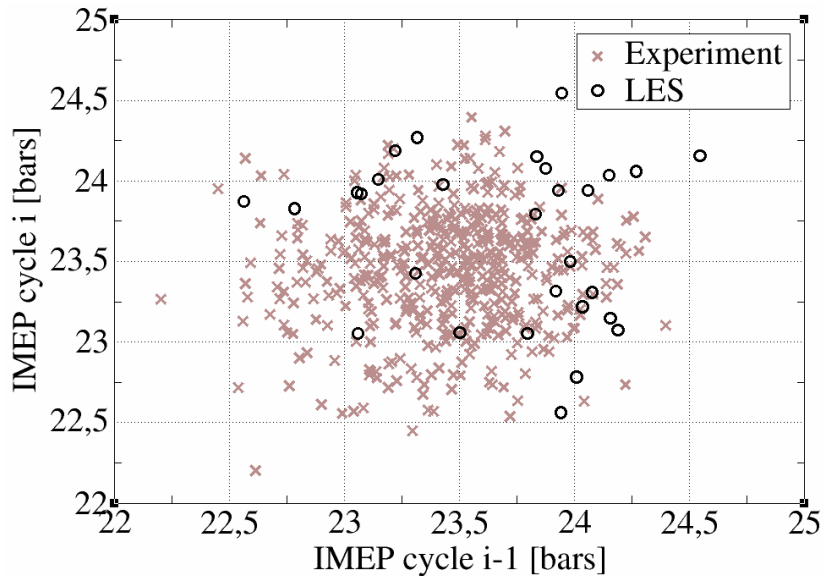


Figure 6.12: $IMEP$ of cycle i versus $IMEP$ of cycle $i-1$.

Figure 6.14 shows an overall increase of KI in proportion to the spark-advance, with a maximum knock intensity rising from $KI_{max} = 0.23$ bar at $ST = -3.3$ °CA to $KI_{max} = 1.65$ bar at $ST = -11.3$ °CA. These levels can be considered as indicating a weak knock. In comparison, KI levels in the single-cylinder LES by Robert et al. [112] easily reached tens to hundred bars for the most advanced spark-timings.

Finally, Figure 6.15 shows the evolution the percentage of knocking cycles as a function of spark-timing. This percentage increases in proportion to the spark-advance. All these results are in agreement with the commonly used knock control strategy, which consists in retarding the spark-timing to avoid strong knock events. One can further observe in Figure 6.15 that the 44.4 % of knocking cycles at ROP in the experiment is reached between $ST = -5.3$ °CA and $ST = -5.3$ °CA in LES, and probably around -6.5 °CA. This can be interpreted as an error of about 1° in KLSA.

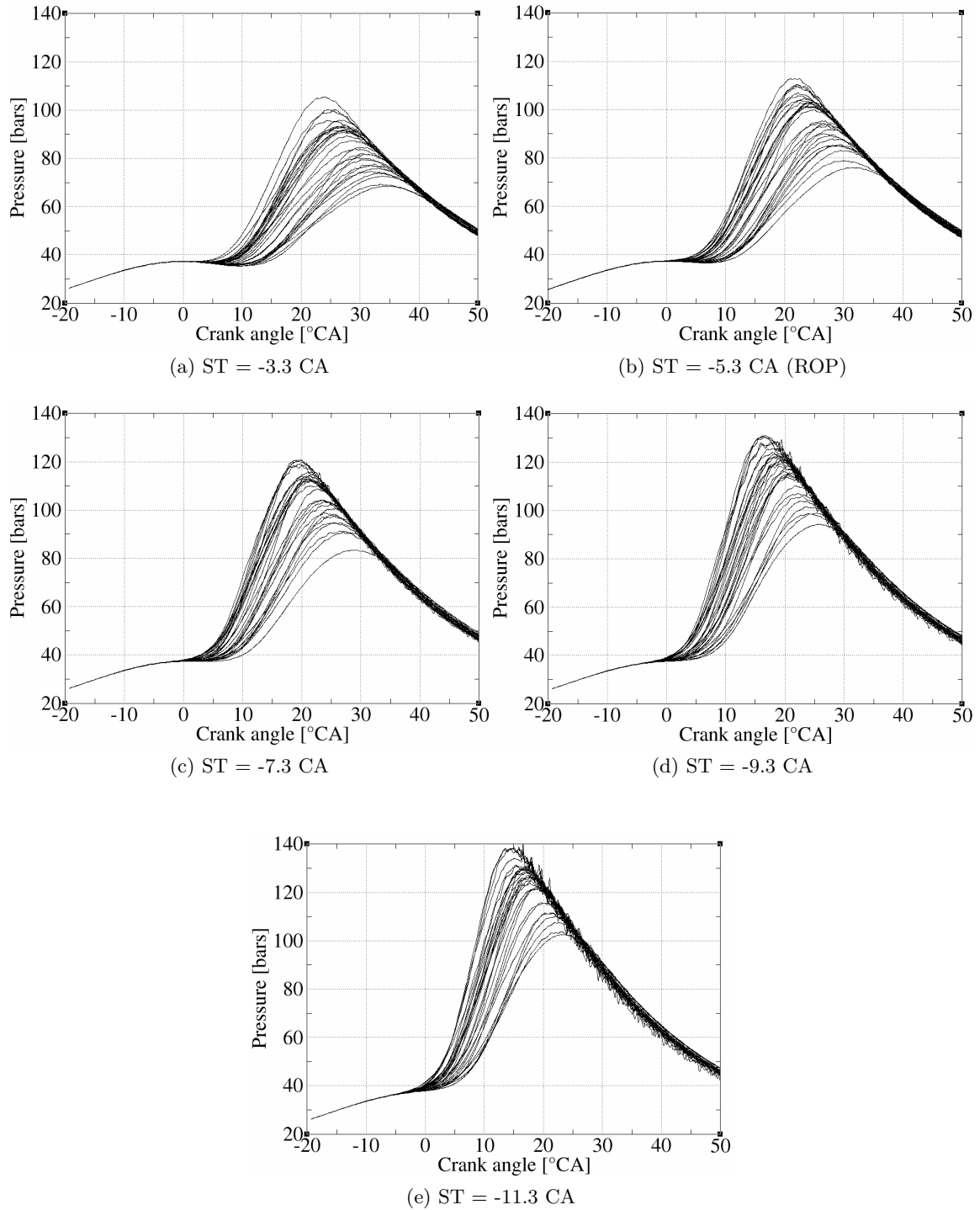


Figure 6.13: LES in-cylinder pressure signals for the 30 cycles at each of the five spark-timings.

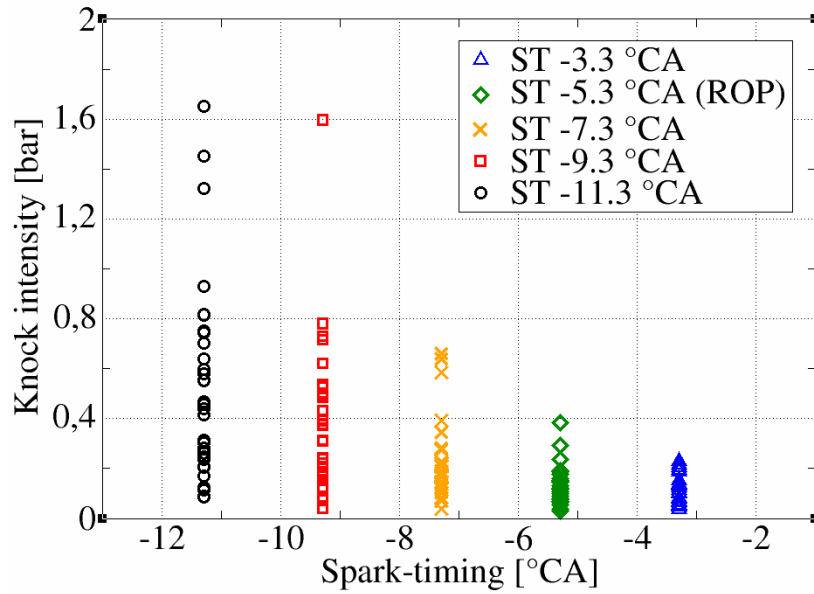


Figure 6.14: Knock intensity predicted by LES as a function of spark-timing. 0 CA corresponds to combustion TDC.

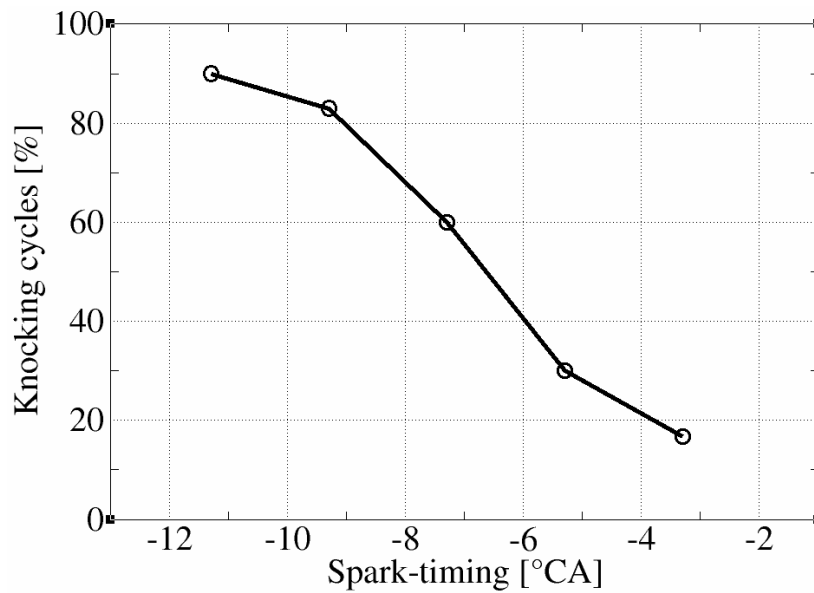


Figure 6.15: Percentage of knocking cycles predicted by LES as a function of spark-timing. 0 CA corresponds to combustion TDC

6.4 Summary of Part II

This Part presented the development of a LES approach to simulate knock in an industrial RENAULT engine.

Chapter 4 presented the computational domain based on the real engine geometry. The operating point directly selected in the experimental database to serve as ROP for the LES was then described.

Then, *Chapter 5* presented a RANS-CHT simulation performed to predict the temperature distribution at the walls. The CHT methodology was validated over thermocouple data, thus allowing the use of the wall temperature distribution as boundary condition for the LES.

Finally, *Chapter 6* first presented the LES numerical set-up that was used to simulate combustion in the engine. At ROP, 36 cycles were simulated. The two first were removed due their strong dependency towards initial conditions. Then, the remaining 34 cycles were compared to experimental findings. Four of these LES cycles were considered as non-representative of the engine behaviour, and were simply removed from the database. A validation of the remaining 30 LES cycles was performed to assess the accuracy of the simulation in terms of CCV and knock prediction. The satisfactory agreement between LES and experiment at ROP allowed to use those cycles as a basis to enlarge the computational database to both weaker and stronger knock events. This was achieved through a spark-timing sweep of five different spark-timings. As expected, it was found that advancing the spark-timing led to stronger knock events (in terms of local pressure oscillations inside the combustion chamber). In the final *Part III*, the resulting LES database of 150 combustion cycles is used to investigate knock.

PART III

LES ANALYSIS OF ENGINE KNOCK

This final Part of the manuscript is dedicated to the analysis of knock in the RENAULT industrial engine, based on the developed LES database. It has two main objectives:

- The first objective is to define an indicator that allows to accurately quantify knock. Usual knock indicators are based on the recorded in-cylinder pressure signal, which is often the only experimental data available to characterize knock. In LES, the direct access to any local quantity inside the combustion chamber allows different approaches to characterize such a phenomenon.
- In order to reduce knock in the engine, the second objective is to exploit the LES results to improve our understanding of the phenomenon, and propose some guidelines and methodologies of analysis in order to reduce its occurrence.

This Part is structured as follows:

Chapter 7, entitled **Characterization of Engine Knock**, points out the limitations resulting from the use of pressure oscillations-based knock indicators to characterize knock. In response, it proposes to use a CFD-based indicator, termed as *Computational Knock Index* (CKI), which focuses on the source of knock: auto-ignition.

Chapter 8, entitled **Investigations of Engine Knock**, first includes an analysis of the impact of CCV on knock. It is followed by an analysis for identifying the origins of CCV. Then, an approach is proposed to yield a more local description of auto-ignition in the cylinder. This approach is used to explore characteristic scenarii that may favour large or small CKI.

CHAPTER

7

Characterization of Engine Knock

Contents

7.1	Limits of pressure oscillations-based indicators	112
7.1.1	Impact of the probe location	112
7.1.2	Impact of the method of analysis	113
7.2	A CFD-based indicator to quantify auto-ignition	114
7.2.1	Definition of the Computational Knock Index	115
7.2.2	Removing cool flame impact in the CKI calculation	115
7.3	Computational Knock Index vs. Knock Intensity	120
7.3.1	Definition of a knocking cycle	120
7.3.2	Correlation between CKI and KI	121
7.4	Conclusion	123

Accurately characterizing knock events is a crucial topic in the development of spark-ignition engines. In the past, several studies have used the auto-ignition induced pressure oscillations in many different ways to define KI. Even if such a pressure oscillations based indicator is the reference in knock studies, its use presents some limitations, as it does not trace the origins of knock but rather its effect. As another proposal to characterize knock events, this Chapter proposes to use a computational based indicator: *Computational Knock Index* (CKI). As compared to KI, CKI directly focuses on the origins of knock: the auto-ignition in the end-gas. This computational indicator is then used to characterize knock in the simulated cycles. CKI results are analysed and compared to KI findings.

7.1 Limits of pressure oscillations-based indicators

The definition of KI consists of a two step process: first the measurement of the in-cylinder pressure, second the analysis of the pressure signal. This type of techniques was first defined in the context of experimental studies, where the pressure signal (measured by a pressure transducer located on the cylinder dome) is often the only available data to evidence knock. Its main advantage is an ease of implementation in both experiments and simulations, which clearly simplifies the validation of computations against experimental findings. However, KI is likely to depend on the position of the probe and the selected method of analysis, i.e on parameters external to the origins of knock.

7.1.1 Impact of the probe location

As mentioned above, the in-cylinder pressure is measured by a pressure transducer (or a numerical probe in a 3D simulation) located on the cylinder dome. Experimental studies by Pan et al. [96] and Pöschl et al. [107] have shown how the pressure signal, and in particular the amplitude of the oscillations, varies depending on the location of the pressure transducer. In a RANS simulation, Corti et al. [25] found that the relative position of the probe with respect to the location of auto-ignition drives the amplitudes of the pressure oscillations. Present LES results allow to further investigate this dependency. To do so, a ring of 18 numerical probes, numbered from 1 to 18, was a priori placed inside the combustion chamber. The locations of the numerical probes are drawn in Figure 7.1. The same a posteriori MAPO analysis was applied to each of the recorded pressure signals, so that differences in the signals are the only potential source of KI variations. For the sake of clarity, this Section only discusses the results for LES Cycle 5 at ROP.

Figure 7.2 shows KI as a function of the location of the numerical probe. According to the probe location, KI varies by a factor 1.6, from 0.124 to 0.196 bar. For the present operating conditions, it is recalled that the maximum acceptable knock intensity threshold KI_T used to differentiate regular (non-knocking) from knocking cycles was set by the experimental operator at 0.159 bar. Thus, the variations in KI introduced by the choice of the probe location are sufficient to consider this cycle as both regular and knocking. 60% of the numerical probes indicate a knocking cycle, i.e 39% of the probes indicate a regular (non-knocking) cycle, showing the lack of reliability in the method.

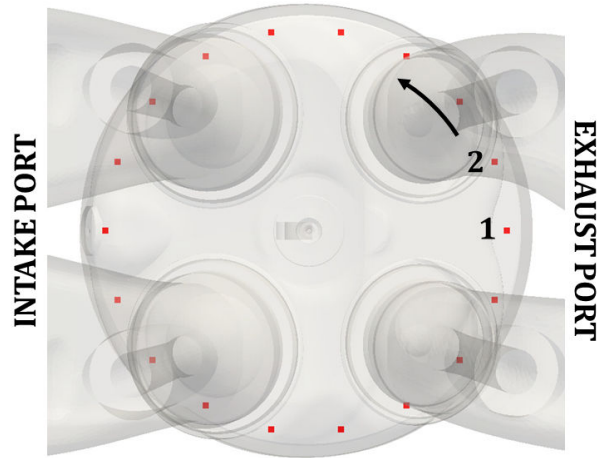


Figure 7.1: Top view of the combustion chamber. Position of 18 numerical probes inside the combustion chamber.

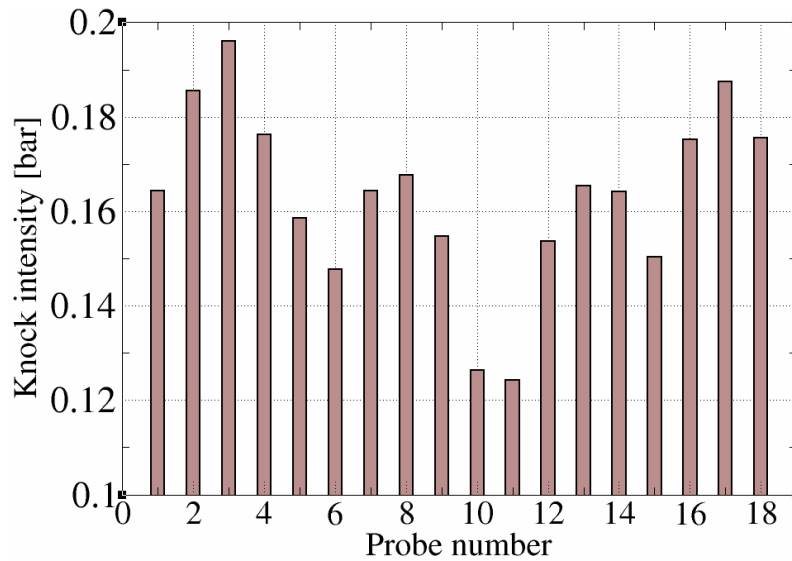


Figure 7.2: KI (by MAPO analysis) predicted from the 18 numerical probes for Cycle 5 at ROP.

7.1.2 Impact of the method of analysis

In order to obtain a KI value from the oscillating pressure signal, multiple methods have been presented in the literature, so that there are as many definitions of KI as methods of analysis. We can cite the presently used MAPO analysis, but also the SEPO, IMPO, DKI, KPPK... [14] [131]. In order to evidence the bias introduced by the selected method of analysis, two typical methods, namely the MAPO and KPPK, were applied to the same set of pressure signals. This set gathers the pressure signal recorded at the same location for each of the 30

LES cycles at ROP. The KPPK analysis is based on a first running average stage, the aim of which is to remove the high frequency oscillations from the pressure signal, in order to provide a smoothed pressure signal. Then, KI is simply the local maximum gap between the actual and smoothed pressure signals.

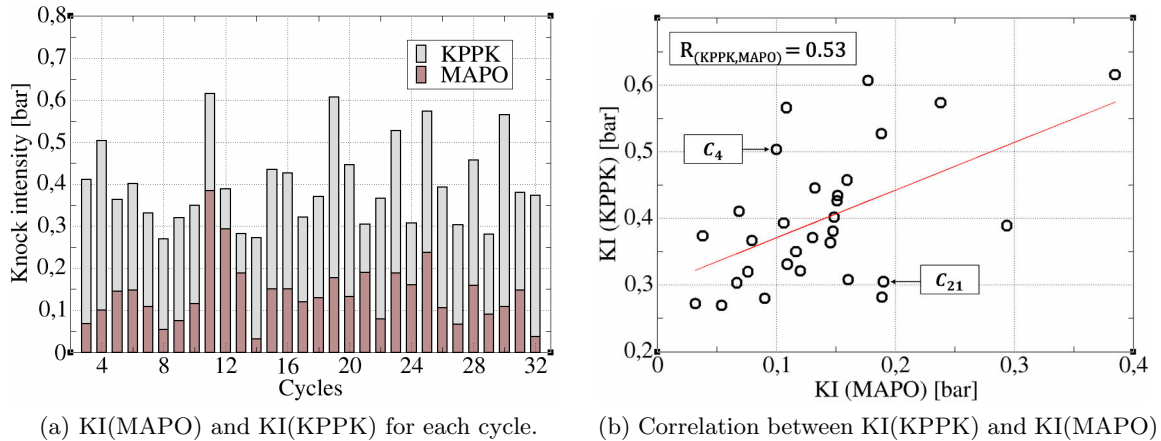


Figure 7.3: KI resulting from two different methods of pressure signal analysis: MAPO and KPPK.

Figure 7.3 compares KI resulting from the KPPK and MAPO analyses. Since the same set of pressure signals was used to apply the two methods of analysis, the change in the method is the only source of variations in KI. In Figure 7.3a, the KPPK analysis constantly provides larger levels of KI, as compared to the MAPO analysis. Then, Figure 7.3b shows a quite weak correlation between the two methods. As a consequence, changing the method of analysis results in a different hierarchy between knocking cycles. For instance, the MAPO analysis predicts that Cycle 4 has a smaller KI than Cycle 21, while the KPPK analysis says the opposite. Such results find an echo in the work of Worret et al. [131]. The authors investigated the correlation between KI respectively defined by MAPO and IMPO analyses. Even if a stronger correlation was exhibited, MAPO and IMPO were found to yield a different hierarchy between knocking cycles.

To conclude, it was evidenced that the knock intensities as obtained through usual pressure signal analyses, are strongly influenced by parameters that have nothing to do with the origins of knock. In this context, KI is just as much a property of the probe location and the selected method of analysis as a characterization of the knock phenomenon. Therefore, the next Section proposes to use a more robust CFD-based indicator.

7.2 A CFD-based indicator to quantify auto-ignition

The development of 3D piston engine simulations has opened up new possibilities to characterize knock events. Indeed 3D computations offer a direct access to any quantity everywhere inside the combustion chamber, and thus the knock detection is no more limited to the anal-

ysis of the pressure signal. This led to the use of CKI, initially introduced by Robert et al. [115] and used by Chevillard et al. [18] in a RANS study. This indicator characterises the origin of knock, i.e auto-ignition, and does thus not suffer from the limitations exposed above of methods based on pressure oscillations analysis.

7.2.1 Definition of the Computational Knock Index

The definition of CKI is based on the description of the combustion as proposed in the ECFM-ISSIM-TKI formalism, see *Chapter 3*. Eq. 7.1 recalls the reaction rate for the overall combustion process $\tilde{\omega}_c$:

$$\tilde{\omega}_c = (1 - \tilde{c}_{AI})(\tilde{\omega}_c^\Sigma + \tilde{\omega}_c^{ign}) + (1 - \tilde{c}_\Sigma)\tilde{\omega}_c^{AI} \quad (7.1)$$

It is split into reaction rates for:

1. Spark-ignition and propagation of the turbulent premixed flame $\overline{\omega}_c^{ign} + \overline{\omega}_c^\Sigma$
2. Auto-ignition $\overline{\omega}_c^{AI}$

Those reaction rates are locally defined at each cell of the computational domain and at each time step. Such a description of combustion allows to define CKI:

$$CKI(n) = \frac{\int \int \tilde{\omega}_c^{AI} dV dt^n}{\int \int \tilde{\omega}_c^{AI} dV dt^n + \int \int (\tilde{\omega}_c^\Sigma + \tilde{\omega}_c^{ign}) dV dt^n} * 100 \quad (7.2)$$

In Eq. 7.2, $\int dV$ and $\int dt^n$ respectively denote the space integral over the combustion chamber volume V followed by the time integral over the entire engine cycle n . The numerator simply corresponds to the mass of fresh gases being consumed by auto-ignition. The denominator states the total mass of fresh gases being consumed by auto-ignition and premixed flame propagation. As a result, CKI(n) quantifies the proportion of fresh gases being consumed by auto-ignition during the engine cycle n . It is bound between 0 and 100 %: CKI(n) = 0 % means no auto-ignition in cycle n , whereas CKI(n) = 100 % indicates that all available fresh gases are consumed by auto-ignition.

7.2.2 Removing cool flame impact in the CKI calculation

In the formulation of CKI, the reaction rate for auto-ignition $\tilde{\omega}_c^{AI}$ is locally given by the TKI model. In order to accurately predict the onset of auto-ignition, the model includes both cool flame (low-temperature chemistry) and main auto-ignition (high-temperature chemistry) features. Based on LES Cycle 5 at ROP, Figure 7.4 shows how the cool flame and main auto-ignition manifest in the temporal evolution of $\int \tilde{\omega}_c^{AI} dV$. The cool flame is materialized by a first smooth peak, quickly followed by a sharp peak that characterizes the subsequent main

auto-ignition. Despite the major role of the cool flame in the overall auto-ignition process, its presence alone is not sufficient to induce a knock event, because the heat release is too gradual to induce a local overpressure [107].

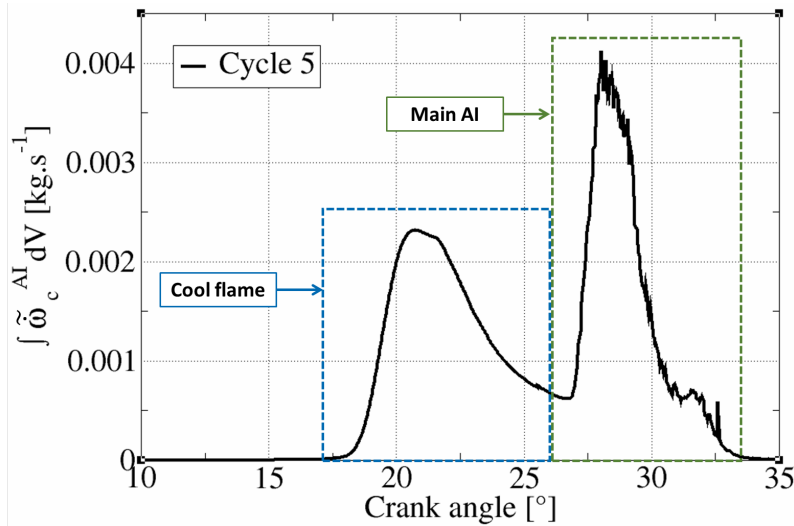


Figure 7.4: Visualization of cool flame and main auto-ignition (main AI) on the space integral of the reaction rate $\int \tilde{\omega}_c^{AI} dV$, for LES Cycle 5 at ROP.

For the same cycle, Figure 7.5 zooms around the auto-ignition period, i.e from the cool flame onset till the end of main auto-ignition. During the cool flame period, the maximum pressure P_{max} observed in the cylinder stays very close to the instantaneous spatially averaged mean pressure P_{mean} . Then, the ratio P_{max}/P_{mean} suddenly increases at the onset of main auto-ignition, which tends to confirm that main auto-ignition is responsible for the pressure wave generation.

As an improvement to the CKI formulation proposed in [18], it seems appropriate to neglect the impact of the cool flame, so that CKI only stands for the proportion of fresh gases consumed by main auto-ignition. Based on Figure 7.4, removing the impact of the cool flame is equivalent to filter the first smooth peak of heat release. This may be achieved by conditioning the space integral for the reaction rate $\int \tilde{\omega}_c^{AI} dV$ to sufficiently large values of the progress variable for auto-ignition \tilde{c}_{AI} . Indeed, it is known that the cool flame only consumes a small fraction of the local fresh gases, which should correspond to a small increase of \tilde{c}_{AI} . Figure 7.6 shows the temporal evolution of the maximum local \tilde{c}_{AI} found in the combustion chamber. The cool flame period does correspond to a smooth increase of the progress variable \tilde{c}_{AI}^{max} . At the peak of reaction rate linked to the cool flame, $\tilde{c}_{AI}^{max} = 0.07$. Then, as soon as the main auto-ignition appears, \tilde{c}_{AI}^{max} sharply increases to $\tilde{c}_{AI}^{max} \approx 1$. As a first tentative to remove the contribution of the cool flame, the space integral for the reaction rate $\int \tilde{\omega}_c^{AI} dV$ was conditioned to \tilde{c}_{AI} larger than the threshold $\tilde{c}_{AI}^T = 0.1$.

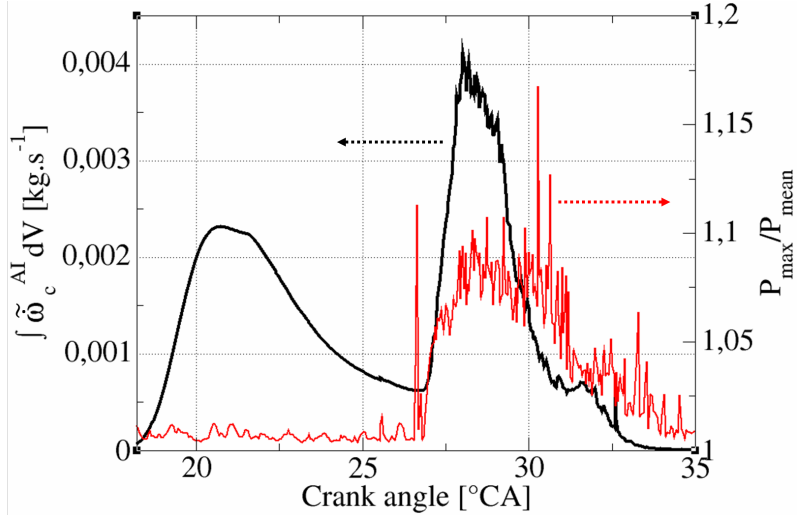


Figure 7.5: Space integral of the reaction rate $\int \tilde{\omega}_c^{AI} dV$ and temporal evolution of the maximum to instantaneous spatially averaged mean cylinder pressure P_{max}/P_{mean} , for LES Cycle 5 at ROP.

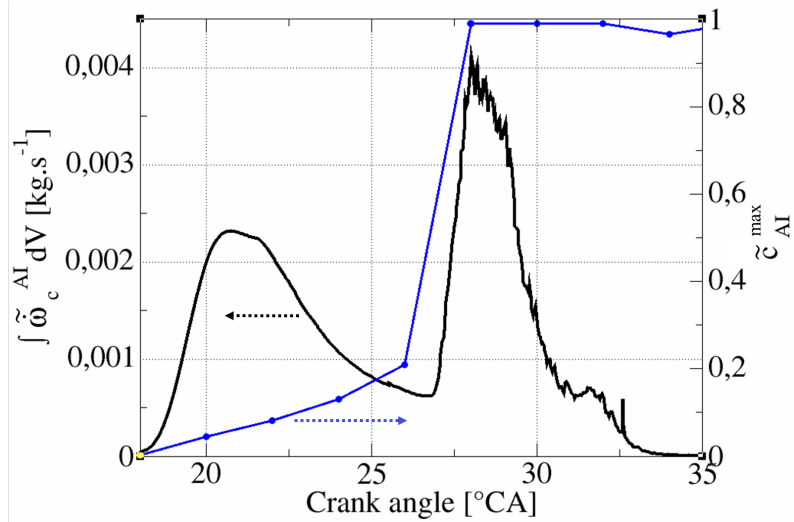


Figure 7.6: Space integral of the reaction rate $\int \tilde{\omega}_c^{AI} dV$ and temporal evolution of \tilde{c}_{AI}^{max} , for LES Cycle 5 at ROP.

The CKI formulation is thereby re-written as follows:

$$CKI(n) = \frac{\int \int_{(\tilde{c}_{AI} > 0.1)} \tilde{\omega}_c^{AI} dV dt^n}{\int \int_{(\tilde{c}_{AI} > 0.1)} \tilde{\omega}_c^{AI} dV dt^n + \int \int (\tilde{\omega}_c^{\Sigma} + \tilde{\omega}_c^{ign}) dV dt^n} * 100 \quad (7.3)$$

This was first tested on Cycle 5 at ROP. As shown in Figure 7.7a, the threshold $\tilde{c}_{AI}^T = 0.1$

efficiently removes the cool flame smooth peak from the space integral, such that only the sharp peak characteristic of main auto-ignition remains. In order to further illustrate the choice for the threshold value, the same procedure is applied to LES Cycle 17 at ROP. Before thresholding, Figure 7.7b shows the smooth peak characteristic of the cool flame, but there is no apparent subsequent main auto-ignition. After thresholding, the space integral remains at 0, and $\text{CKI}(17) = 0\%$ accordingly, indicating no main auto-ignition in the cycle.

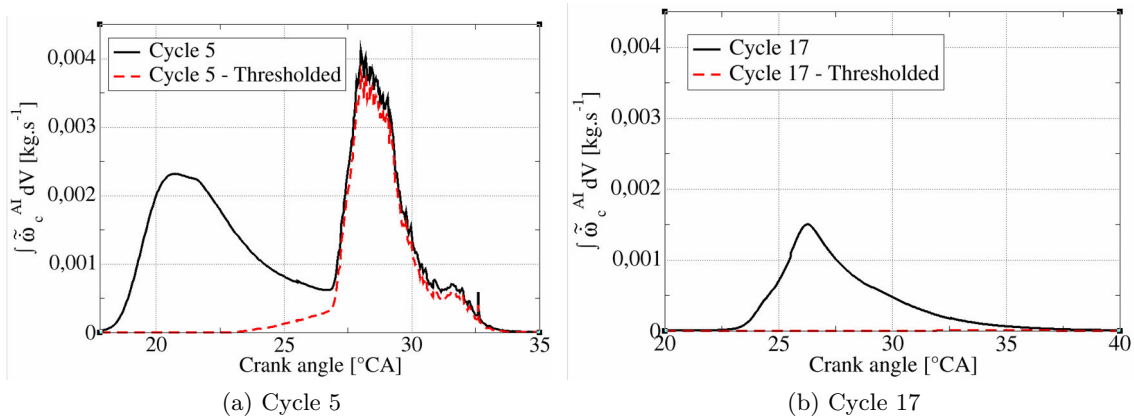


Figure 7.7: Space integral of the reaction rate $\int \tilde{\omega}_c^{AI} dV$ before and after thresholding.

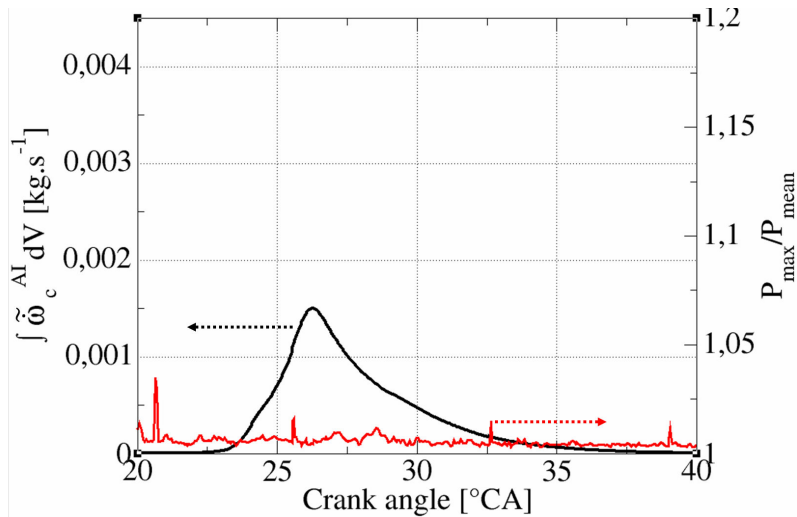


Figure 7.8: Space integral of the reaction rate $\int \tilde{\omega}_c^{AI} dV$ and temporal evolution of the maximum to instantaneous spatially averaged mean cylinder pressure P_{\max}/P_{mean} , for LES Cycle 17 at ROP.

Despite the absence of main auto-ignition in Cycle 17, one could see in Figure 7.3 a non negligible KI level, which is a priori not in agreement with our previous assumption, that is, only main auto-ignition is responsible for the pressure wave generation. However Figure 7.8

confirms that the maximum pressure P_{max} observed in the cylinder is very close to the instantaneous spatially averaged mean pressure P_{mean} during the cool flame period, meaning that the cool flame is not responsible for the detected KI. Explaining why the MAPO and KPPK analysis predicted knock without any pressure oscillations generated by auto-ignition was not the purpose of this thesis. Nonetheless, we could mention two reasons that might explain such a result:

- There could be some pressure oscillations, the origins of which are other than auto-ignition,
- There could be some limitations in the techniques used to process the pressure signal, leading to a misinterpretation of the signal and finally indicating knock where it should not.

The initial and the new (thresholded) CKI formulations were applied to the set of 30 LES cycles at ROP. Figure 7.9 superimposes the two quantities to understand the effect of the thresholding on CKI. Before the thresholding, all cycles have significant CKI. After the thresholding, CKI levels are inevitably smaller than prior to it, since the part of the reaction rate during the auto-ignition process which was due to cool flame chemistry has been removed. For some cycles (e.g Cycle 6, 8 and 17), CKI even falls to 0. This would indicate that the initial CKI (before thresholding) for these cycles was only the result of cool flame chemistry. Among the cycles with significant CKI after thresholding, it seems that the removal of the cool flame contribution in the heat release by auto-ignition has slightly changed the classification between these cycles. For instance, the CKI value was slightly larger for Cycle 9 than Cycle 7 before thresholding, while it is the opposite after thresholding. Nonetheless, the cycles with the largest CKI before thresholding are still the one with the largest values after thresholding.

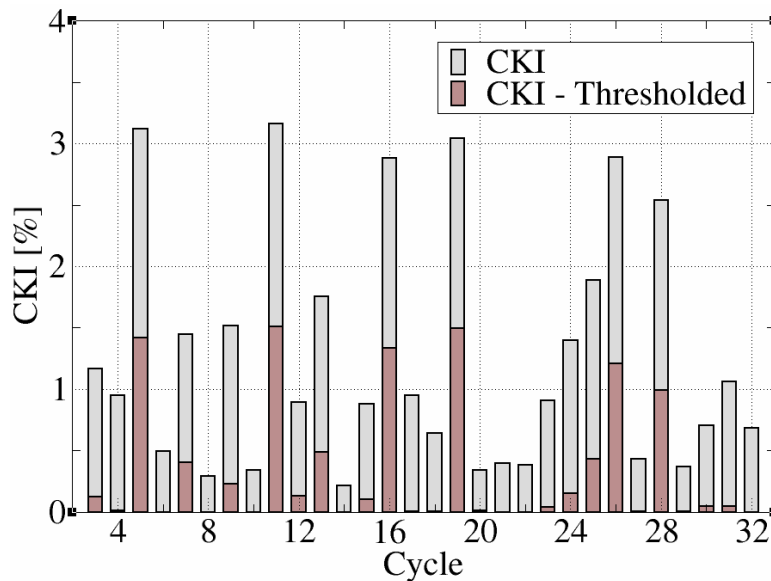


Figure 7.9: Comparison of CKI levels before and after thresholding, applied to each of the 30 LES cycles at ROP.

In the rest of the manuscript CKI refers to its thresholded formulation.

7.3 Computational Knock Index vs. Knock Intensity

CKI was then calculated for each of the 30 LES cycles at each of the five spark-timings. This Section compares the results based on CKI to the ones found on KI (by MAPO analysis), and which have been previously exposed in *Section 6.3*.

7.3.1 Definition of a knocking cycle

The introduction of CKI requires to re-define a proper classification between a regular (non-knocking) and a knocking cycle. Such a classification is schematized in Figure 7.10, and presented in comparison to the KI-based classification. With KI, the classification relates to the establishment of a limit of maximum acceptable knock intensity KI_T . This threshold value is commonly set by the operator on the test bench, and is subject to his audible assessment of the knocking sound, see *Section 2.2.2*.

With CKI, the definition of a knocking cycle would also require the specification of a maximum acceptable CKI, noted CKI_T . Such a limit should not be related to KI_T , since the latter depends on the assessment of the operator on the test bench. Moreover, as it will be shown later, CKI and KI are not perfectly equivalent in terms of knock prediction. In the present study, CKI_T was fixed by analysis of the in-cylinder field. In some cycles, negligible traces of main auto-ignition were found at some dispersed and isolated cells, leading to extremely small CKI. A value of $CKI_T = 0.01\%$ allowed to avoid considering these cycles as knocking. In practice, it would be useful to perform a more refined analysis to determine a meaningful acceptable CKI limit.

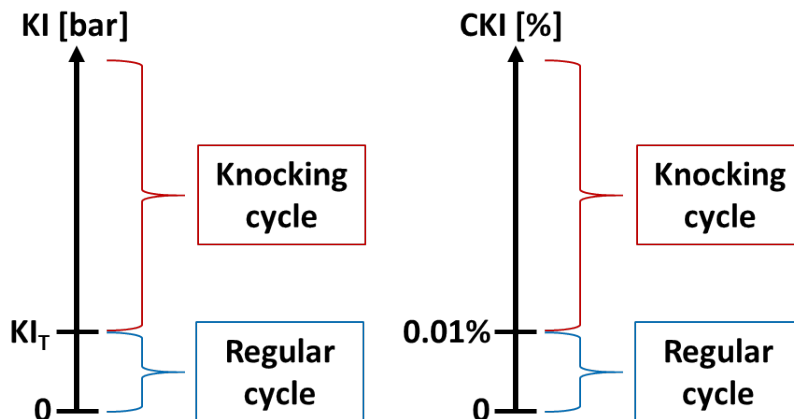


Figure 7.10: Schematic of the classification between normal (non-knocking) and knocking cycles. KI_T is the maximum acceptable KI value set by the operator.

7.3.2 Correlation between CKI and KI

Given the CKI-based classification of the regular and knocking cycles, Figure 7.11 displays the resulting percentage of knocking cycles predicted by LES as a function of the spark-timing. It is compared to the percentage of knocking cycles found on KI (by MAPO analysis), using a maximum acceptable knock intensity $KI_T = 0.159$ bar. One can observe that the use of CKI results in the same tendency as KI, that is the percentage of knocking cycles increases when advancing the spark-timing.

However, the percentage of knocking cycles predicted by CKI is constantly larger than the one predicted by KI. As a phenomenological reason, it is possible that some auto-ignition spots lead to significant CKI levels, but they merely induce weak pressure waves which are rapidly dumped while travelling across the combustion chamber, such that they were not detected by the numerical probe. Nonetheless, it must also be recalled that the KI-based percentage of knocking cycles directly depends on the threshold value KI_T set by the operator. Even slightly reducing KI_T would artificially result in a larger percentage of knocking cycles.

This is also true for CKI, i.e moving CKI_T also impacts the resulting percentage of knocking cycles. As it is shown in Figure 7.12, the percentage of knocking cycles per spark-timing naturally decreases as CKI_T increases. Nonetheless, the trend, that is the increase of the percentage of knocking cycles in proportion to the spark-advance, is still valid. Consequently, the difference between the CKI- and KI-based percentages of knocking cycles at each spark-timing is meaningless, and the important information is that the two indicators behave in a similar way in response to the spark-advance.

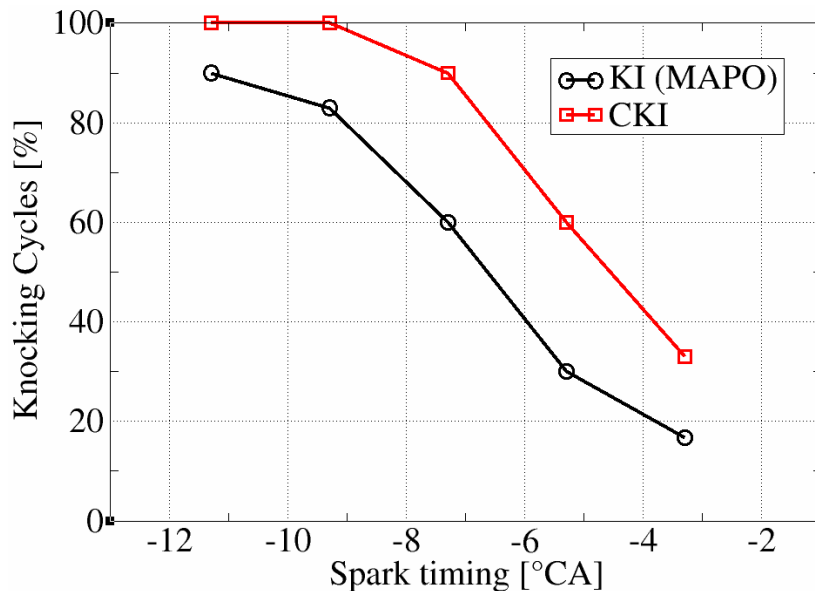


Figure 7.11: Percentage of LES knocking cycles as a function of the spark-timing respectively based on KI (by MAPO analysis) and CKI, using maximum acceptable limits $KI_T = 0.159$ bars and $CKI_T = 0.01\%$. $0^\circ CA$ corresponds to combustion TDC.

Then, Figure 7.13 shows CKI levels (left graph) and KI levels (right graph) respectively for the 150 LES cycles sorted by spark-timing. Same as KI, CKI globally increases as the spark-timing is advanced. In particular, the maximum CKI per spark-timing increases, as it was also the case for the maximum KI.

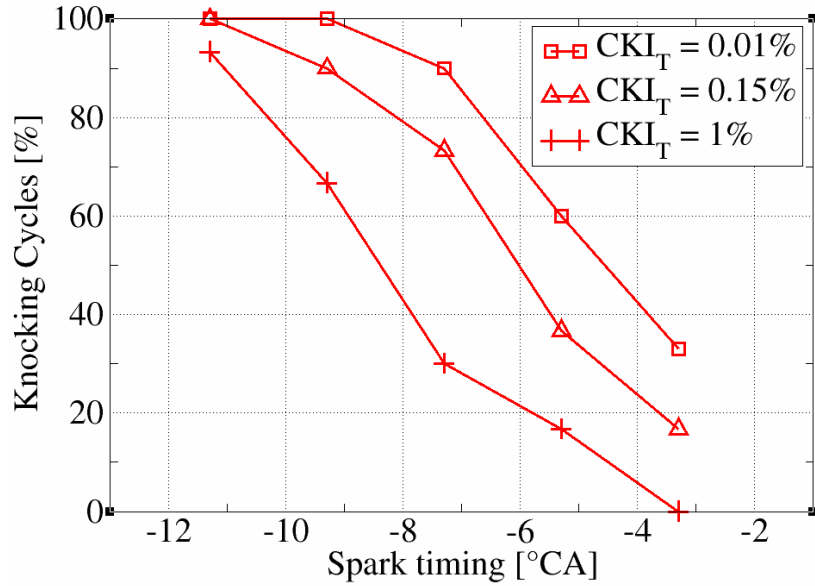


Figure 7.12: Percentage of knocking cycles per ST based on CKI, using various CKI_T .

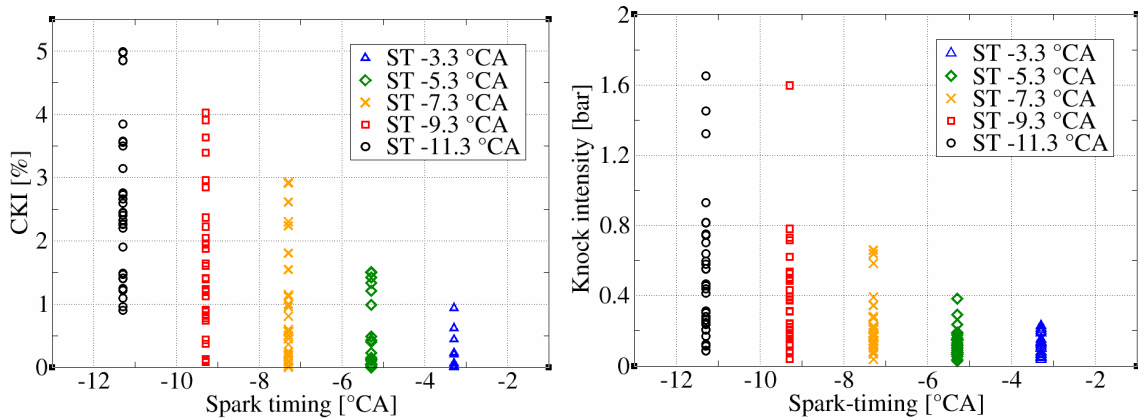


Figure 7.13: CKI (left graph) and KI by MAPO analysis (right graph) respectively for each of the 30 LES cycles for each of the five spark-timings, distributed as a function of the spark-timing. $0^\circ CA$ corresponds to combustion TDC.

To summarize, CKI and KI have similar behaviours in response to a spark-advance:

- First an increase in the percentage of knocking cycles,
- Second an increase of their respective maximum values.

Such similarities suggest that the two indicators may globally relate the same story, and so a correlation might exist between CKI and KI. Indeed, Figure 7.14 shows a significant correlation between the two, quantified by a linear correlation coefficient of Bravais-Pearson $R = 0.83$. In the present case, larger CKI values directly corresponds to larger mass of fresh gases consumed by auto-ignition, since cycle to cycle variations in the trapped mass (and therefore variations in the denominator of Eq. 7.2) are negligible (not shown here). Thereby the above correlation suggests, at least in a first order, that the mass of fresh gases consumed by main auto-ignition is the main factor controlling the knock intensity. It would confirm the previous findings by Robert et al. [112]. Nonetheless, the relation between CKI and KI is not perfectly linear, and so the ranking between knocking cycles differs according to the selected indicator. For instance, Cycle 9 at the spark-timing $ST = -11.3$ °CA, noted $C_9^{-11.3}$ in Figure 7.14, has a larger CKI than Cycle 18 of same spark-timing, noted $C_{18}^{-11.3}$, but a smaller KI.

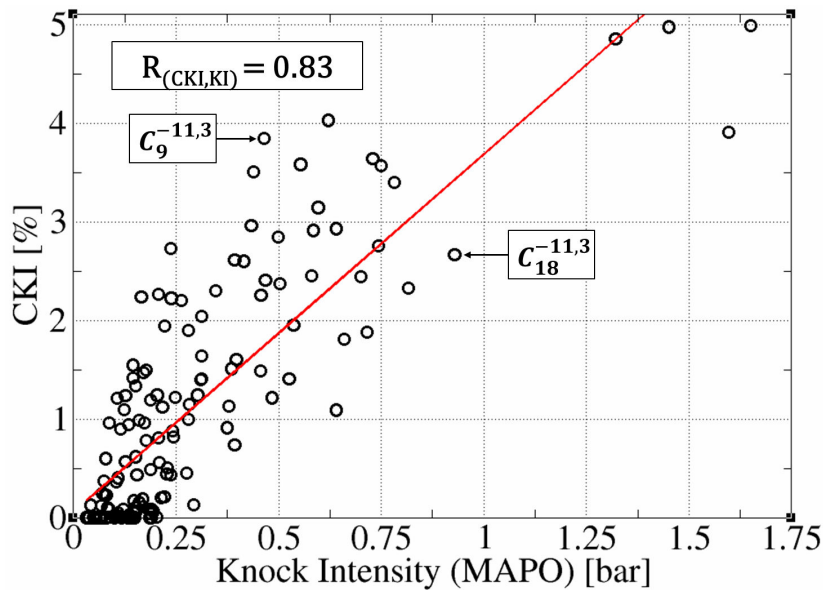


Figure 7.14: CKI correlated to KI (by MAPO analysis). Each circle corresponds to an individual cycle (each of the 30 LES cycles for each of the five spark-timings are represented).

7.4 Conclusion

This chapter introduced a CFD-based indicator, CKI, to characterize the knock event in an engine cycle. Contrary to KI indicators which are based on the analysis of the cylinder pressure signal, CKI focuses on the origins of knock, and allows to by-pass the bias introduced

when determining KI. Starting from the definition proposed in [18], the CKI formulation has been modified to only accounts for the high heat release main auto-ignition, since this was identified as the cause of knock in the literature. Despite strong differences in their definition, CKI and KI exhibit similar behaviours in response to a spark-timing sweep. A strong correlation was found between the two, suggesting that the auto-ignition induced pressure wave partly depends on the proportion of fresh gases consumed by main auto-ignition. Still CKI and KI result in a different ranking between knocking cycles.

In the rest of the study, CKI is used as the indicator to characterize knock in the engine cycles. It must be recalled that this indicator only traces the proportion of fresh gases consumed by main auto-ignition. There is no study relating this proportion with the damaging nature of knock, and so this aspect will not be addressed.

CHAPTER

8

Investigations of Engine Knock

Contents

8.1	Knock and combustion speed	126
8.1.1	Correlation between CKI and combustion speed	126
8.1.2	Exploring the origins of the combustion speed variability at ROP	128
8.1.2.1	Timing of appearance of the combustion speed variability	129
8.1.2.2	Specific characteristics of the fast and slow combustion cycles	129
8.1.3	CKI as a function of CA₅₀ for the 150 simulated cycles	140
8.2	Knock and premixed flame shape	141
8.2.1	Correlation between CKI and the remaining proportion of fuel mass	141
8.2.2	Characterizing the flame shape	145
8.2.3	Analysis of individual cycles	147
8.2.3.1	Exploring the distribution of end-gas	148
8.2.3.2	Exploring the first auto-ignition spots	152
8.2.3.3	Characterizing the secondary auto-ignition spots	154
8.2.3.4	Summary of the analysis on individual cycles	159
8.2.4	Statistical analysis	161
8.3	Summary of Part III	164

This Chapter exploits the acquired LES database and the Computational knock index to improve our comprehension of knock in an industrial spark-ignition engine. It is organized into two sections:

- In the first *Section 8.1*, CKI is correlated with the CCV observed in the engine at ROP, in order to investigate the impact of the combustion speed variability on knock. Then, the origins of the combustion speed variability are investigated.
- In the second *Section 8.2*, a methodology to locally describe the flame shape and auto-ignition is proposed. It serves to identify some characteristic scenarii in the combustion chamber that may act in favour of large or small CKI.

8.1 Knock and combustion speed

8.1.1 Correlation between CKI and combustion speed

Figure 8.1a re-prints the CCV observed in the 30 simulated cycles at ROP, based on the temporal evolution of the in-cylinder pressure. Figure 8.1b shows the corresponding variability of fuel consumption speed. A fast cycle, that is with a sharp and strong increase of the in-cylinder pressure, corresponds to a fast consumption of fuel, resulting from a rapid propagation of the premixed flame across the combustion chamber.

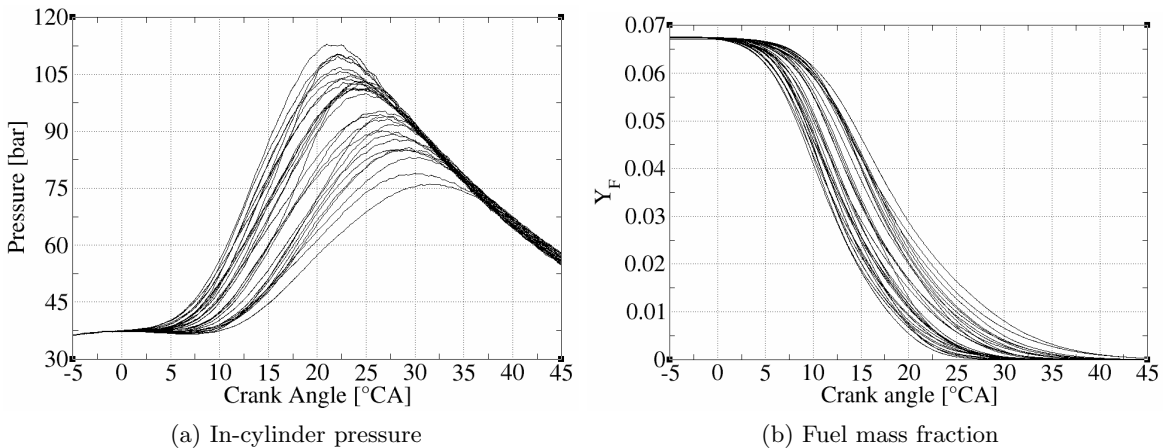


Figure 8.1: Illustration of the CCV observed in the LES results at ROP based on the temporal evolution of (a) the in-cylinder pressure signal and (b) the fuel mass fraction

Figure 8.2 shows how CCV are quantified through the variability in the fuel consumption speed. It is based on the estimation of the crank angle at which half of the fuel is consumed, noted CA_{50} . The fast combustion cycles are characterized by early CA_{50} , and inversely the slow combustion cycles are characterized by late CA_{50} .

In this way, the relation between knock and CCV at ROP is displayed in Figure 8.3 in the form of CKI as a function of CA_{50} . The Figure exhibits late CA_{50} cycles with negligible CKI on the right side of the graph, i.e with no auto-ignition in the fresh gases. In opposition, there are early CA_{50} cycles on the left side of the graph with more significant CKI levels. This representation makes apparent a threshold value around $15^\circ CA$, noted CA_{50}^T , which separates the "knock free" region on the right, from the "possible knock region" on the left (it will be further confirmed in *Section 8.1.3*). Inside the possible knock region, the largest CKI levels are found for the earliest CA_{50} cycles, while the smallest CKI values correspond to the latest CA_{50} cycles. It suggests that CKI increases as CA_{50} diminishes.

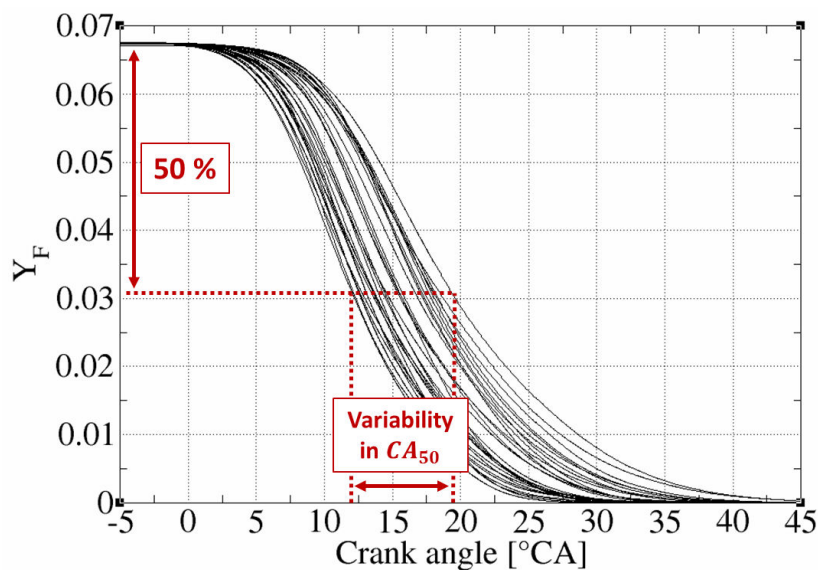


Figure 8.2: Estimation of CA_{50} based on the temporal evolution of the fuel mass fraction Y_F .

It is interesting to note that this relation is in contradiction with the general thinking, which states that increasing the combustion speed tends to reduce the knock tendency, since the fresh gases have less time to auto-ignite. In the present case it appears to be the opposite. To explain this result, Figure 8.4 shows the temporal evolution of the mean in-cylinder fresh gases temperature for the 30 simulated cycles at ROP. Each cycle is coloured by its corresponding CA_{50} . The trend indicates that a fast combustion goes along with high temperatures in the fresh gases, which is known to globally decrease auto-ignition delays. In the present study, the occurrence of auto-ignition solely for the earliest CA_{50} cycles suggests that the reduction of the time left for the fresh gases to auto-ignite (as a result of a faster propagation of the flame) is more than compensated by a stronger reduction of auto-ignition delays, due to the higher temperature levels in the cylinder.

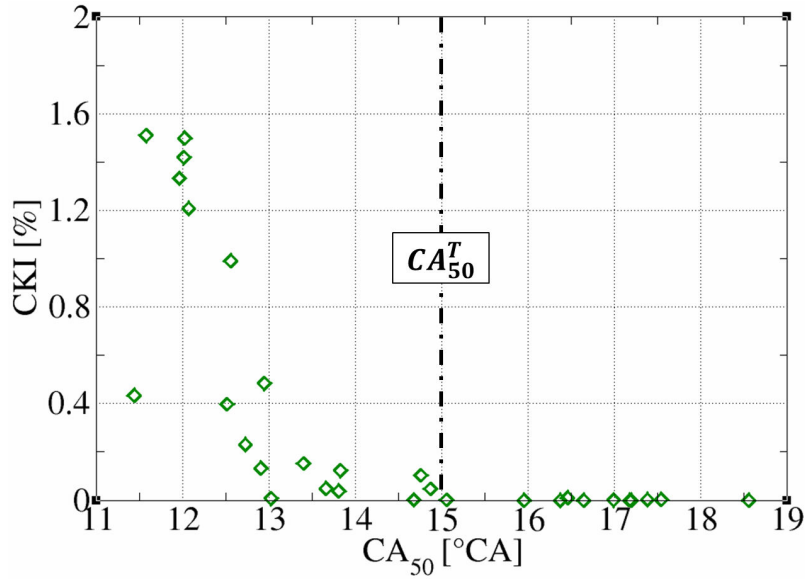


Figure 8.3: Scatter plot of CKI as a function of CA_{50} for the 30 LES cycles at ROP. Each diamond represents one LES cycle.

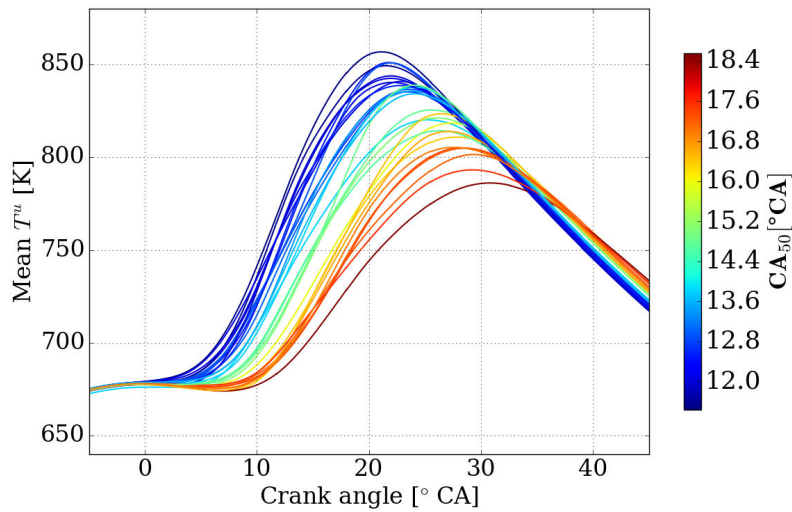


Figure 8.4: Temporal evolution of the mean in-cylinder fresh gases temperature for the 30 simulated cycles at ROP, coloured by their respective CA_{50} .

8.1.2 Exploring the origins of the combustion speed variability at ROP

In response to the impact of the combustion speed variability on CKI, this Section aims at identifying its origins. It consists in pointing out the timing and the location of its main sources.

8.1.2.1 Timing of appearance of the combustion speed variability

In the same way as the CA_{50} indicator, CA_{02} (crank angle at which 2% of the fuel mass fraction is consumed) is introduced. CA_{02} gives a measure of the speed at which the early flame kernel generated by the spark discharge is growing, i.e it characterizes the first instants of the combustion process. Figure 8.5 shows CA_{50} as a function of CA_{02} for the 30 simulated cycles at ROP. The linear correlation coefficient of Bravais-Pearson $R_{(CA_{50},CA_{02})} = 0.905$ indicates a strong correlation, close to linear. It means that variations introduced during the first instants of the premixed flame kernel growth determine to a large extent its ensuing propagation: a fast (respectively slow) initial flame kernel growth more probably leads to a globally fast (respectively slow) overall premixed flame propagation. It should be noticed that such ascendancy of the initial flame kernel growth in a spark-ignition engine was also pointed out in the LES studies of Enaux et al. [38], Truffin et al.[124] and Vermorel et al.[126], in the experimental studies of Aleiferis et al. [1] and Peterson et al. [102], as well as in the survey of Ozdor et al. [94].

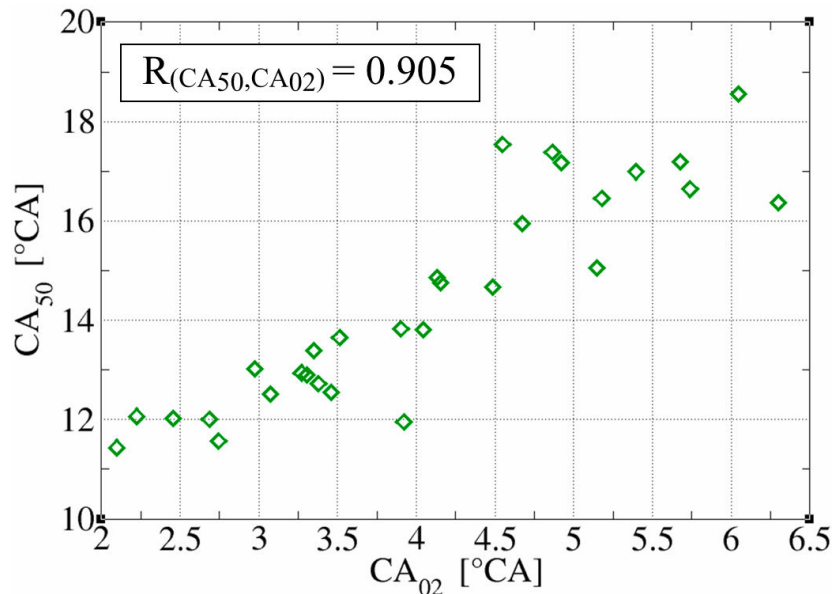


Figure 8.5: Scatter plot of the CA_{50} as a function of the CA_{02} for the 30 LES cycles at ROP. Each diamond represents one LES cycle. Indicated is the correlation coefficient of Bravais-Pearson $R_{(CA_{50},CA_{02})}$.

8.1.2.2 Specific characteristics of the fast and slow combustion cycles

In order to explore the sources of the variability in the premixed flame propagation, emphasis is put around spark-timing, since it was found to be a key stage. During its early growth, the initially laminar and spherical flame kernel becomes progressively wrinkled and turbulent. Many factors can have an impact during this early stage: thermodynamic conditions, in-

cylinder flow dynamics (flow motion, velocity levels, intensity of the turbulence) [99] [126] [38], mixture composition (local equivalence ratio, rate of dilution) [1] [98] [102] are among the most important ones. These factors are investigated with the attempt to identify common characteristics of the early CA_{02} cycles, in opposition to the late CA_{02} cycles.

8.1.2.2.1 Mean in-cylinder conditions

As a first step, some possible correlation between the early premixed flame growth and the mean in-cylinder state were examined. In Figure 8.6 CA_{02} is thus correlated to different global parameters [124]: namely the dilution rate, the trapped mass, the mean in-cylinder fresh gases temperature at spark-timing, and the mean in-cylinder equivalence ratio.

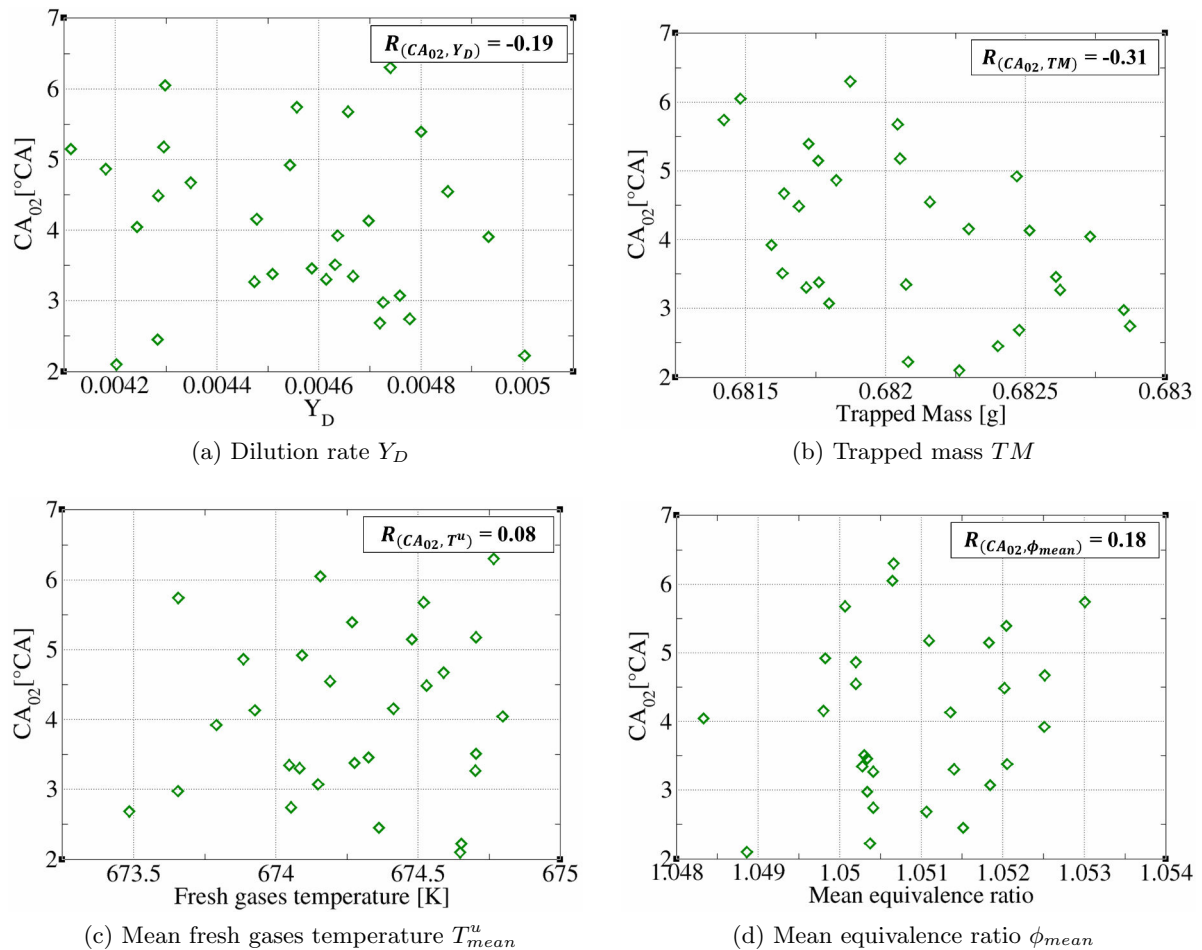


Figure 8.6: Correlation between CA_{02} and different global parameters. Indicated are the correlation coefficients of Bravais-Pearson $R_{X,Y}$.

No significant correlation was found with the investigated global parameters. In Figure 8.6a,

the dilution rate is probably too low to have a significant impact on the combustion speed. Such a low dilution rate results from the absence of an exhaust gas recirculation system in this engine, and by the large valves overlap (intake and exhaust valves are simultaneously opened for 46 °CA). This way the entering fresh gases largely expel the residual burned gases out of the combustion chamber.

In Figure 8.6b, one can observe negligible variations in the trapped mass (TM), quantitatively materialized by a small coefficient of variation $COV(TM) = 0.10\%$. This level of variation is probably too small to have a significant impact on combustion.

Similarly, Figure 8.6d reveals no clear tendency between CA_{02} and the mean in-cylinder fuel-air equivalence ratio ϕ_{mean} . This is not surprising, since there are low variations in the trapped mass, and the same mass of fuel is injected for each of the 30 cycles.

Finally in Figure 8.6c, the mean in-cylinder temperature right before spark-timing is approximately the same for the 30 cycles.

The different correlations between CA_{02} and the above global quantities revealed no tendency. The variability in the combustion speed is more likely to be explained by the local cycle to cycle variations in the in-cylinder field. Such an assumption is investigated in the next Section.

8.1.2.2.2 Analysis of conditionally averaged cycles

To emphasize the common local characteristics of the early (respectively the late) CA_{02} cycles, Figure 8.7 describes the adopted strategy. It consists in defining two sets of cycles:

- *Set 1* with the six (20%) earliest CA_{02} cycles
- *Set 2* with the six (20%) latest CA_{02} cycles

Then, the sets are used separately to build conditionally ensemble averaged cycles:

- C_{early} represents the phase average of the cycles in *Set 1*
- C_{late} represents the phase average of the cycles in *Set 2*

Since the variability in the combustion speed appears during the first instants of the premixed flame propagation, the characteristics specific to C_{early} and C_{late} are expected to be found near the spark-plug around spark-timing. The two conditionally averaged cycles are thereby analysed at 6 °CA before combustion TDC, i.e right before spark-timing ($ST = -5.3$ °CA). Shown in Figure 8.8, the combustion chamber is cut by three cut planes through the spark-plug: namely MID_{XZ} , MID_{YZ} and MID_{XY} . They allow a detailed insight into the local conditions around the spark-plug. In these cut planes, differences between C_{early} and C_{late} are explored in the 3D flow dynamics, as well as in the distribution of the laminar flame speed S_L . As indicated by Eq. 3.20, S_L is the combustion variable accounting for the local equivalence ratio and the local fresh gases temperature. Only the relevant cut planes are displayed in the manuscript. Figures will systematically be oriented so that the left side corresponds to the intake side, and the right side to the exhaust side.

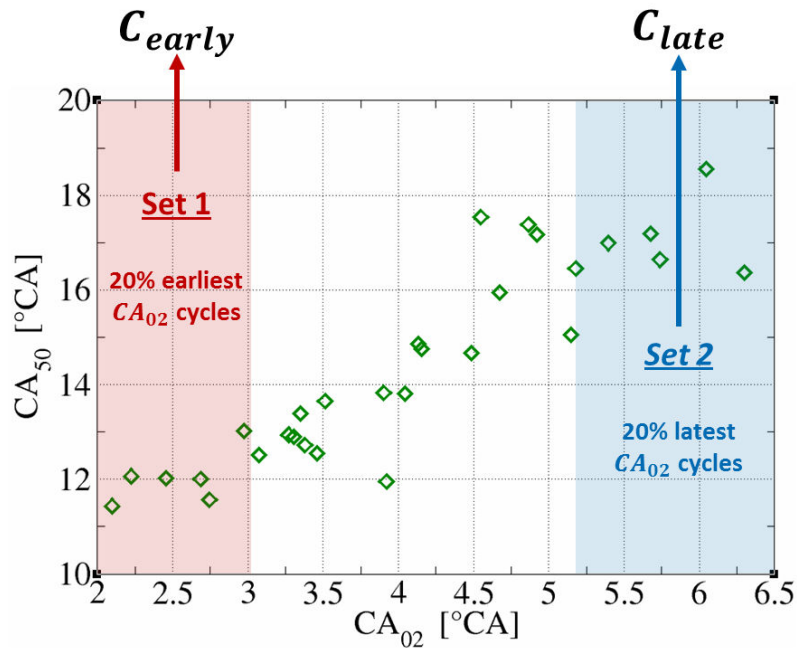


Figure 8.7: Definition of the conditionally averaged cycle C_{early} (respectively C_{late}) from the 20% earliest (respectively latest) CA_{02} cycles.

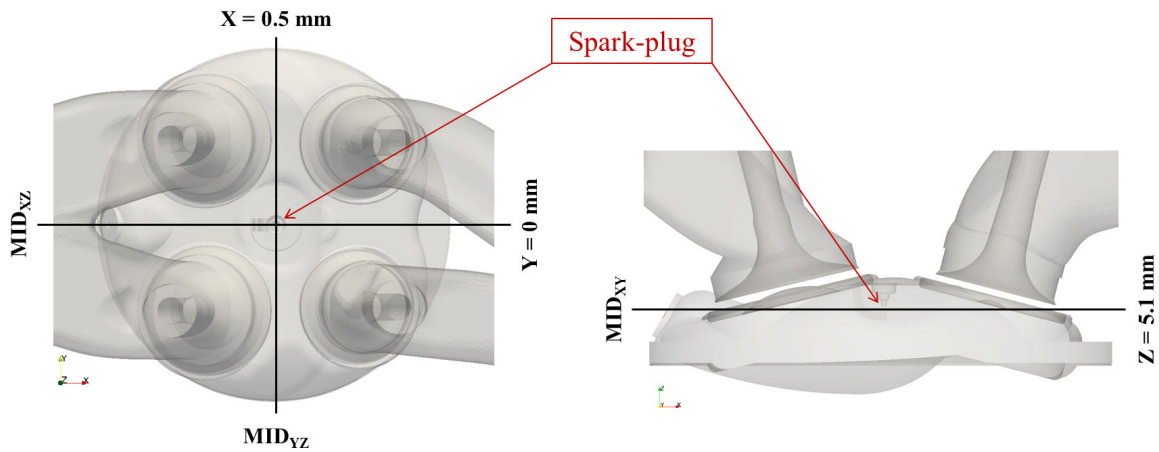


Figure 8.8: Illustration of the cut planes through the spark-plug MID_{XZ} and MID_{YZ} . Intake ports are on the left of the figure, exhaust ports on the right.

Figure 8.9 shows the resolved velocity magnitude right before spark-timing in the cut plane MID_{XZ} . There are similarities in the flow dynamics: for instance the coherent tumble motions on the intake side of the combustion chamber (left of the spark plug) with comparative velocity levels close to the cylinder-roof and piston bowl. On the exhaust side (right of the

spark-plug), the flow is identically oriented toward the spark-plug. However, C_{early} stands out with substantially larger velocity levels close to the spark-plug ($|\tilde{u}_{XZ}| > 14 \text{ m.s}^{-1}$), as compared to C_{late} ($|\tilde{u}_{XZ}| < 10 \text{ m.s}^{-1}$). The proximity of such a high velocity region to the spark-plug makes it likely that it interacts with the premixed flame kernel (as it will be confirmed later).

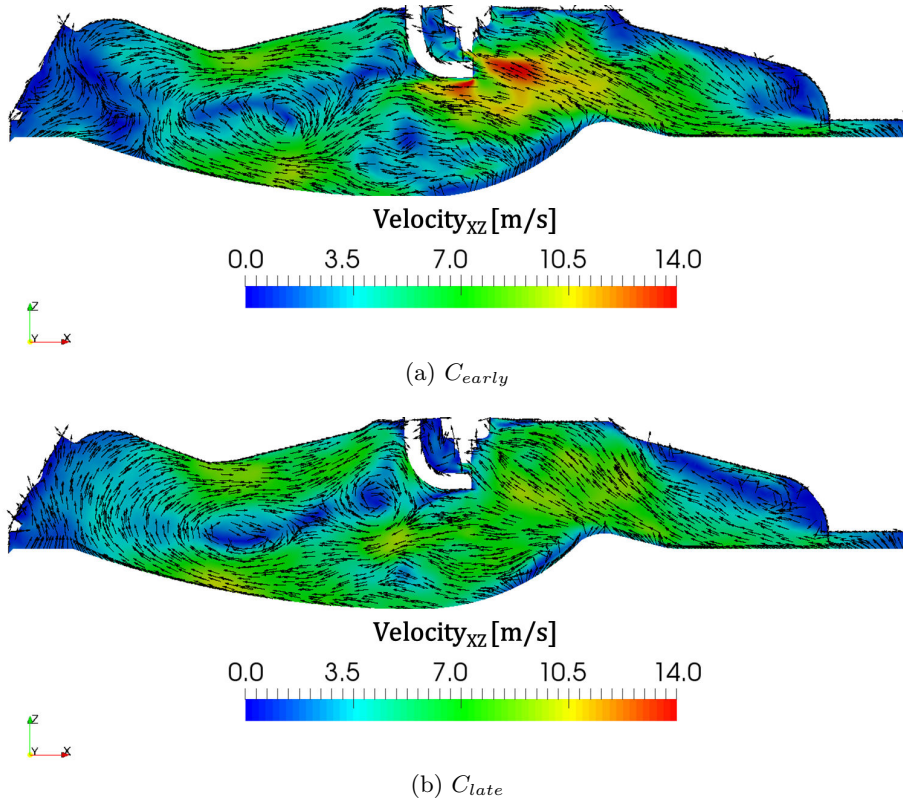


Figure 8.9: Magnitude field of the 3D resolved velocity projected in plane MID_{XZ} for the two conditionally averaged cycles taken at 6°CA before combustion TDC (0.7°CA before spark-timing).

In the same cut plane MID_{XZ} , Figure 8.10 displays the distribution of laminar flame speed S_L . Around the spark plug, C_{early} shows a relatively homogeneous distribution of laminar flame speed around 1.15 m.s^{-1} . On the opposite, C_{late} is characterized by stronger inhomogeneities in the vicinity of the spark-plug. There are in particular two distinct regions: a first one, slightly on the right, showing large laminar flame speeds ($S_L > 1.20 \text{ m.s}^{-1}$), and a second one, slightly on the left, which distinguishes itself by small laminar flame speeds ($S_L < 1 \text{ m.s}^{-1}$). Figure 8.11 shows the same distribution in the cut plane MID_{XY} . Zooming close to the spark-plug confirms the presence of the large and small S_L regions respectively distributed on either side of the spark-plug center in C_{late} . It also confirms that the distribution of S_L is more homogeneous in C_{early} .

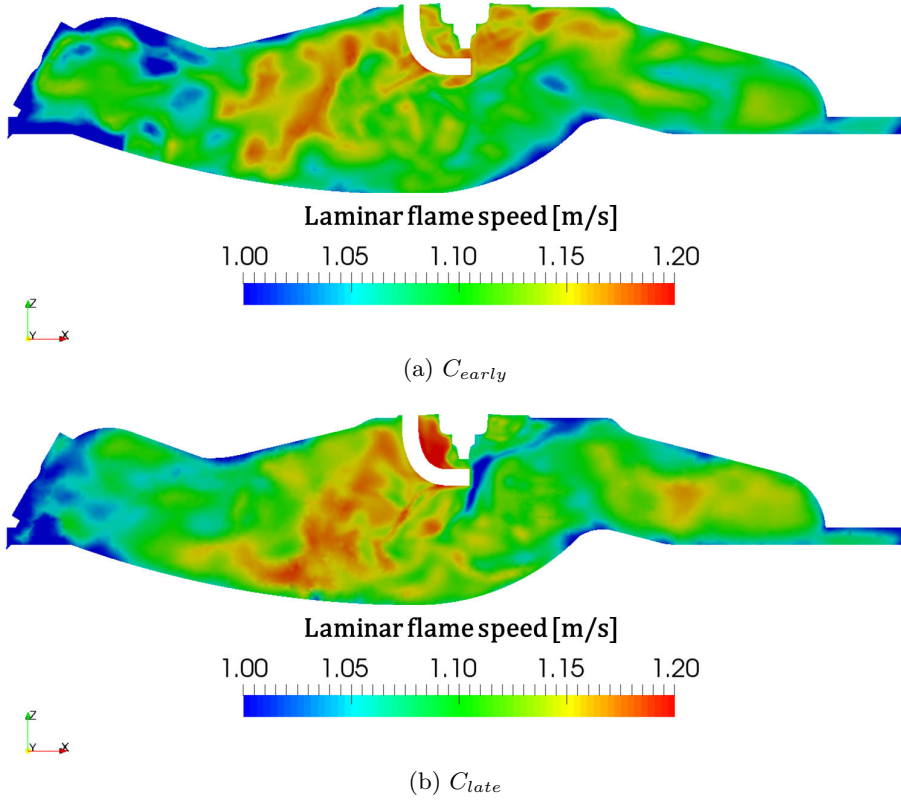


Figure 8.10: Field of the laminar flame speed in the cut plane MID_{XZ} for the two conditionally averaged cycles taken at $6^\circ CA$ before combustion TDC ($0.7^\circ CA$ before spark-timing).

In order to determine if the distinct characteristics in the 3D fields well interact with the premixed flame kernels in C_{early} and C_{late} respectively, Figure 8.12 shows probability density functions (PDF) for the resolved velocity magnitude and the laminar flame speed. They were built for each conditionally averaged cycle at $3.3^\circ CA$ after spark-timing and conditioned to the fresh gases right ahead of the premixed flame fronts. This was achieved by solely considering in the PDF the mesh nodes inside the cylinder with a progress variable $0.001 < \tilde{c}_\Sigma < 0.01$. Thereby the PDFs represent the distribution of laminar flame speed and resolved velocity magnitudes seen respectively by the premixed flame kernel in C_{early} and C_{late} .

In Figure 8.12a, the PDFs of the laminar flame speed show that the premixed flame in C_{early} sees a fairly homogeneous distribution of S_L , centred around a mean value $S_L = 1.16 m.s^{-1}$. In comparison, a similar mean laminar flame speed, $S_L = 1.14 m.s^{-1}$, was found in C_{late} . However the distribution around this mean is much more spread, as it was previously suggested by the 3D field of the laminar flame speed.

Then, the PDFs for the resolved velocity magnitudes are shown in Figure 8.12b. Significant differences were found in the mean values seen by the premixed flame fronts: $6.1 m.s^{-1}$ in C_{early} and only $4.2 m.s^{-1}$ in C_{late} . The flame front in C_{early} sees a wider range of velocity magnitudes, as opposed to C_{late} . In particular, the flame front in C_{early} is subject to large

velocity levels reaching 14 m.s^{-1} , and which are not found in C_{late} . The analysis of the respective PDFs confirms that the differences between C_{early} and C_{late} , previously observed around the spark-plug right before spark-timing, are seen by the premixed flame fronts during the first instants of the combustion process. Nonetheless, an in-depth study is still required to determine the relative contribution of each factor on the combustion speed.

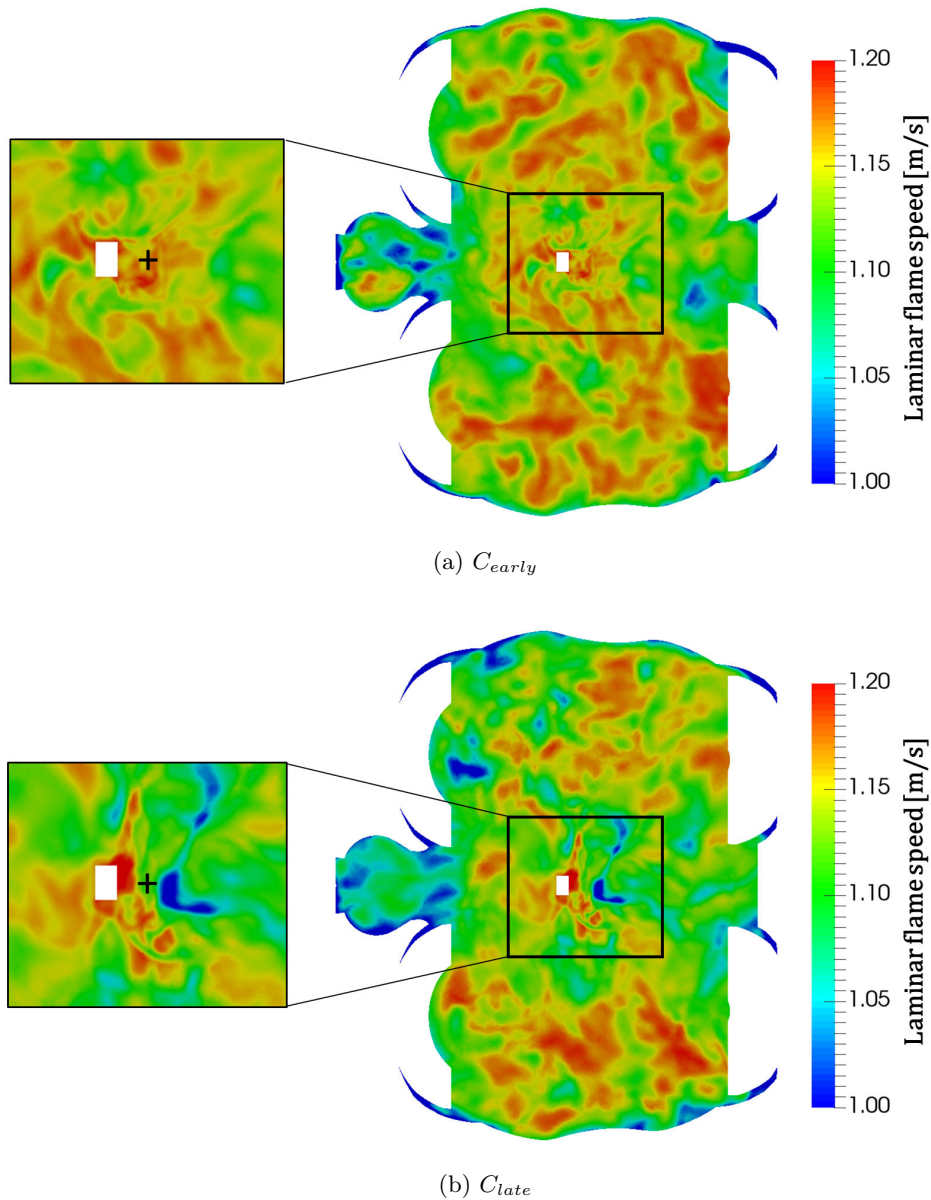


Figure 8.11: Field of the laminar flame speed in the cut plane MID_{XY} for the two conditionally averaged cycles taken at $6^\circ CA$ before combustion TDC ($0.7^\circ CA$ before spark-timing). The cross indicates the center of the spark-plug.

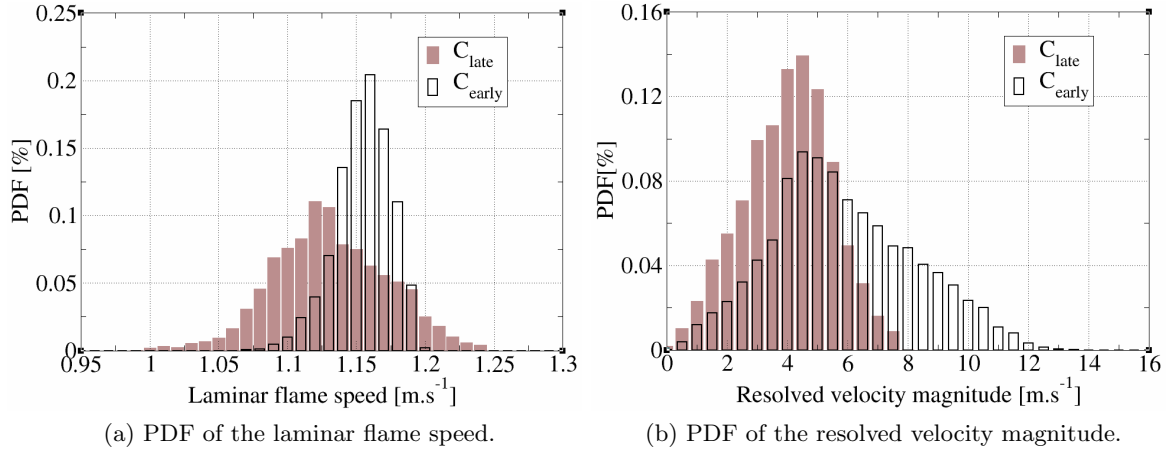


Figure 8.12: PDF of the laminar flame speed and the resolved velocity magnitude conditioned to the fresh gases ahead of the premixed flame front. PDF were built from in-cylinder conditions at 3.3 °CA after the spark-timing

8.1.2.2.3 Analysis of the source terms in the FSD transport equation

During the first instants of the combustion process, a rapid growth of the flame kernel results from a fast increase of the flame surface. Within the ECFM-LES approach, the total flame surface S_{flame}^{tot} can be easily obtained by integrating the flame surface density $\bar{\Sigma}_{\tilde{c}}$ over the combustion chamber volume V :

$$S_{flame}^{tot} = \int \bar{\Sigma}_{\tilde{c}} dV \quad (8.1)$$

Figure 8.13 shows its temporal evolution for the 6 earliest (respectively latest) CA_{02} cycles that were used to build C_{early} (respectively C_{late}). The 6 earliest CA_{02} cycles correspond to a rapid increase of the total flame surface, as compared to the 6 latest CA_{02} cycles which globally show a slow rise of S_{flame}^{tot} . Consequently, it is possible to identify the main contributing factors to a fast premixed flame propagation by analysing the respective order of magnitude of the source terms (and the effect they model) in the transport equation for $\bar{\Sigma}_{\tilde{c}}$. This transport equation has been detailed in *Section 3.2.2.2.5* and is recalled below:

$$\frac{\partial \bar{\Sigma}_{\tilde{c}}}{\partial t} = P + T_{res} + \alpha(S_{res} + C_{res}) + T_{sgs} + S_{sgs} + \alpha C_{sgs} + (1 - \alpha)S_{ign} + \bar{\omega}_{\Sigma}^{ign} \quad (8.2)$$

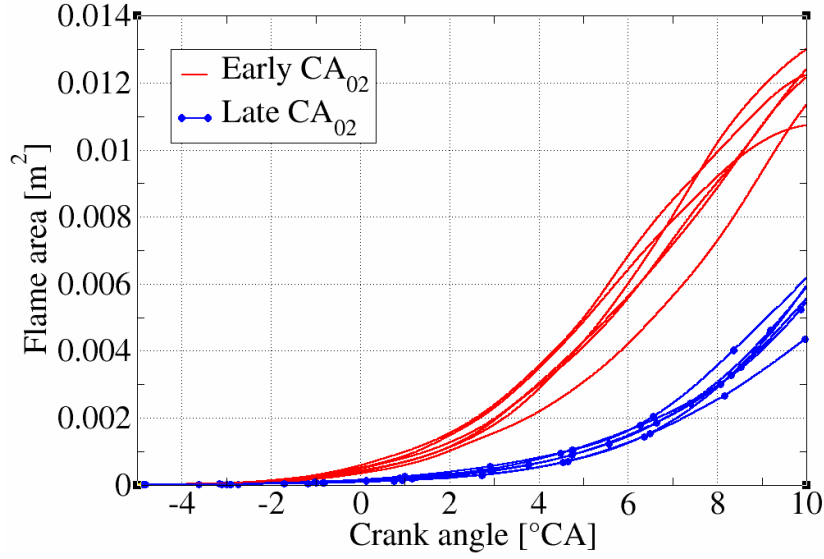


Figure 8.13: Temporal evolution of the total flame surface during the first instants of the premixed flame propagation for the 6 earliest (respectively latest) CA_{02} cycles.

In Eq. 8.2, the resolved and SGS transport, T_{res} and T_{sgs} , and the planar propagation, P , are not source terms of FSD. In fact, there are only five source terms that may locally generate or destroy FSD. Their expression normalised by $\bar{\Sigma}_{\tilde{c}}$ are listed below and the effect they model are recalled:

- The ignition stretch accounts for the propagation of the early laminar flame kernel resulting from the spark-discharge, which is too small to be resolved on the LES mesh:

$$(1 - \alpha_{ign})S_{ign}/\bar{\Sigma}_{\tilde{c}} = (1 - \alpha_{ign})\frac{2}{3}\frac{(1 + \tau)}{\tilde{c}}S_L(\bar{\Sigma}_{\tilde{c}} - \bar{\Sigma}_{lam}) \quad (8.3)$$

- The resolved strain rate describes the stretching of the flame by the resolved structures of the flow:

$$\alpha S_{res}/\bar{\Sigma}_{\tilde{c}} = \alpha_{ign}(\nabla \cdot \tilde{u} - \mathbf{NN} : \nabla \tilde{u}) \quad (8.4)$$

- The SGS strain rate models the stretching of the flame by all the unresolved structures of the flow:

$$S_{sgs}/\bar{\Sigma}_{\tilde{c}} = \alpha_{cfm}\Gamma \left(\frac{\hat{u}'}{S_L}, \frac{\hat{\Delta}}{\delta_L} \right) \frac{\hat{u}'}{\hat{\Delta}} \quad (8.5)$$

- The resolved curvature effect accounts for the flame surface creation by the resolved flame curvature:

$$\alpha C_{res}/\bar{\Sigma}_{\tilde{c}} = \alpha_{ign}S_d \nabla \cdot (\mathbf{N}) \quad (8.6)$$

Its sign depends on the local curvature $\nabla \cdot (\mathbf{N})$, i.e positive in convex regions and negative in concave regions.

- The SGS curvature models the effect of the unresolved curvature on the flame front wrinkling:

$$\alpha_{ign} C_{sgs} / \bar{\Sigma}_{\tilde{c}} = \alpha_{ign} \left(-\beta_0 S_L \frac{(\bar{\Sigma}_{\tilde{c}} - \bar{\Sigma}_{lam})}{1 - \tilde{c}} + \beta_c S_L \frac{1 + \bar{\tau}}{\tilde{c}} (\bar{\Sigma}_{\tilde{c}} - \bar{\Sigma}_{lam}) \right) \quad (8.7)$$

When located on the fresh gases side inside the filtered flame front, \tilde{c} tends to 0. The second term in Eq. 8.7 dominates so that the unresolved curvature contributes to FSD creation. When going through the flame front towards the burned gases, \tilde{c} gets closer to 1. The first term in Eq. 8.7 becomes dominant, thus the unresolved curvature mainly destroys FSD.

Figure 8.14 shows the temporal evolution for these five source terms, for the 6 earliest and the 6 latest CA_{02} cycles during the first instants of the combustion process. Figure 8.14a focuses on the ignition stretch. At spark-timing, it is the dominant source term of FSD, but its impact rapidly decreases over time due to the fast transition from an unresolved flame kernel to a fully resolved flame kernel. Still there are noticeable differences during this short ignition phase, with in particular some late CA_{02} cycles exhibiting smaller ignition stretch levels directly after spark-timing. These same cycles stand out with larger values a few crank angles later (from -4°CA to -2.5°CA) as compared to the other cycles, probably due to the slower transition of the laminar flame kernel to a fully turbulent premixed flame propagation. However, the short period of influence of the ignition stretch factor ($\approx 2^\circ\text{CA}$), as well as the similar profiles of some early and late CA_{02} cycles makes it difficult to explain the variability in the combustion speed based solely on the laminar flame kernel growth.

On the opposite, the four other terms apply during the fully turbulent premixed flame propagation phase and evidence a clearer distinction between the early and late CA_{02} combustion cycles. In particular, the resolved strain rate in Figure 8.14c) and the SGS strain rate in Figure 8.14d) both generate much more FSD in the early CA_{02} cycles than in the late ones, especially during the first instants of the turbulent premixed flame propagation. Moreover, they appear to be the dominant source terms to the generation of FSD during this stage, as compared to the resolved and unresolved curvature. In Figure 8.14b), the resolved curvature even generates slightly more FSD for the late than the early CA_{02} cycles. This could be explained by the fact that a slow flame tends to further experience turbulence, and is thereby more wrinkled. Finally, Figure 8.14e) shows that the unresolved curvature is negative during the displayed period. This means that it mainly acts on the burned gases side of the flame front to destroy FSD. We noticed that the temporal evolution for the unresolved curvature is more unstable as compared to the other source terms of the FSD transport equation, but the reasons were not investigated in the course of this study.

This analysis of the source terms in the transport equation for $\bar{\Sigma}_{\tilde{c}}$ points out the resolved and SGS strain rate as the main contributors to the generation of FSD. They respectively describe the stretching of the flame by the resolved and unresolved structures of the flow. This suggests that the specific flow structure identified in the vicinity of the spark-plug and

shown to interact with the flame front is largely responsible for the rapid growth of the premixed flame. As a consequence, there is an interest in better control the flow dynamics at this very location around spark-timing, in order to reduce the variability in the premixed flame propagation and the subsequent variability in CKI.

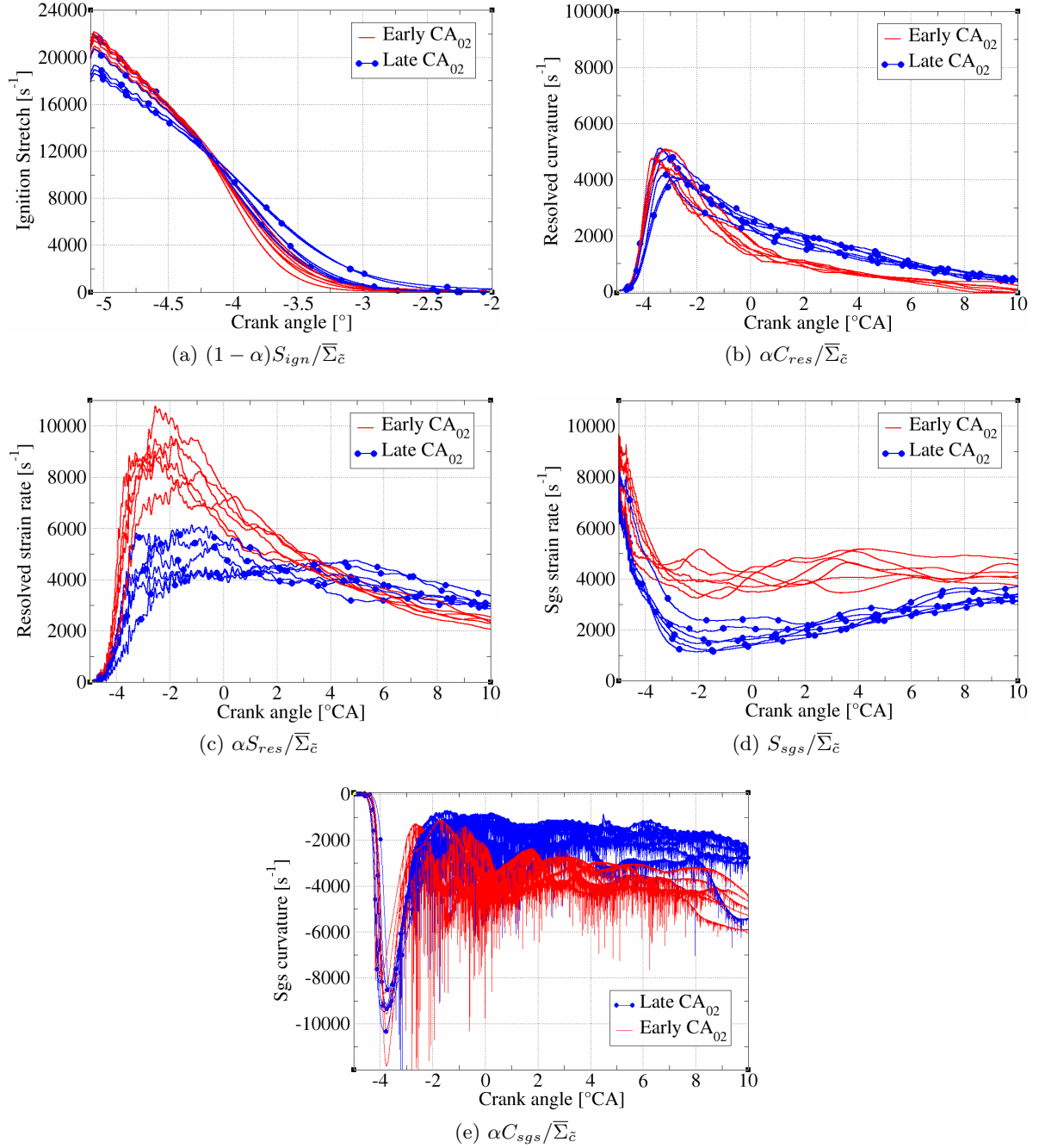


Figure 8.14: Temporal evolution of the productive/destructive source terms in the FSD equation for the 6 fastest (respectively slowest) combustion cycles used to build C_{early} (respectively C_{late}).

8.1.3 CKI as a function of CA_{50} for the 150 simulated cycles

CA_{50} has been used until now to estimate the variability in the premixed flame propagation, i.e the combustion speed. This indicator is also commonly used in the automotive industry to assess the optimal combustion phasing (in terms of engine efficiency) regardless of the engine operating conditions [4]. Shown in Figure 8.15, it allows to plot on a same graph CKI as a function of CA_{50} for each of the 30 LES cycles at each of the five spark-timings. As it was suggested in *Section 8.1.1*, the Figure confirms the presence of a knock free region on the right side, and a knocking region on the left side with significant CKI. It also emphasizes the existence of a threshold value CA_{50}^T independent of the spark-timing, which separates the two regions. CA_{50}^T is here located at 15°CA and is termed as the *knock limiting combustion phasing*. Moreover, the trend on the knocking region confirms the global increase of CKI as CA_{50} diminishes.

Even if CA_{50} appears as a useful indicator to optimize the combustion phasing with regard to knocking combustion, it is not easily monitored for a running engine. The common strategy to adapt the combustion phasing and control the knock occurrence consists in retarding the spark-timing. In the present study, Figure 8.16 shows how the spark-timing allows to push back the combustion phasing and thereby to reduce the CKI level, at least in the mean. However, the same Figure evidences that retarding the spark-timing also tends to increase the variability in CA_{50} , here defined per spark-timing as the difference between the maximum to the minimum CA_{50} . It means that even for the latest spark-timing $ST = -3.3^\circ\text{CA}$, the strong variability results in some cycles being below the knock limited combustion phasing.

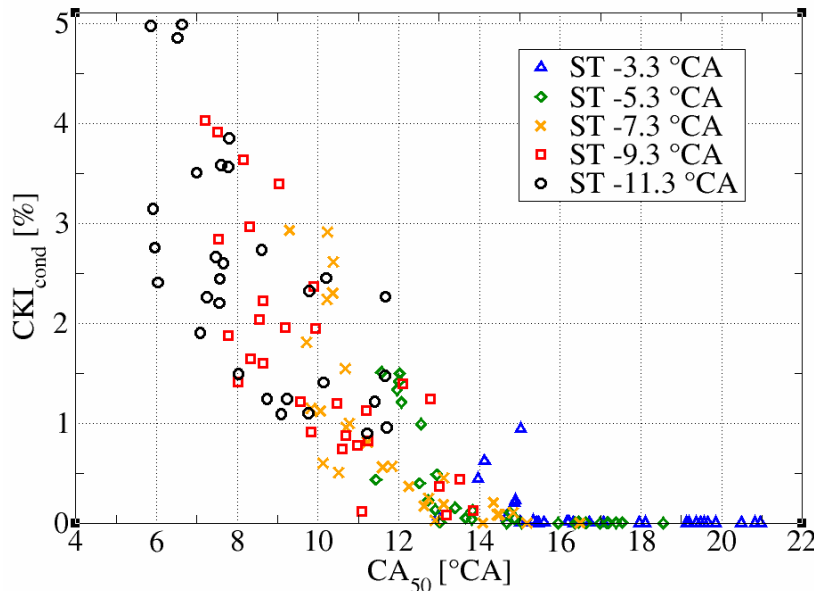


Figure 8.15: Scatter plot of CKI as a function of CA_{50} for each of the 30 LES cycles at each of the five spark-timings. Each symbol represents one LES cycle.

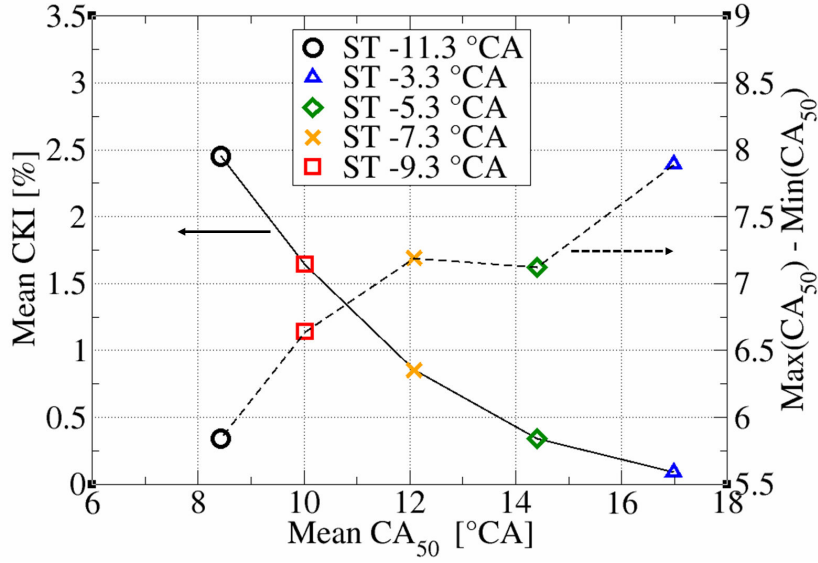


Figure 8.16: Mean CKI (left ordinate axis) as a function of the mean CA_{50} for each of the five spark-timings. Indicated on the right ordinate axis is the gap between the maximum to minimum CA_{50} per spark-timing.

8.2 Knock and premixed flame shape

In the previous *Section 8.1*, CKI was used to show the impact of the variability in the combustion speed on auto-ignition. As a further step, we then attempted to identify some characteristic scenarii in the combustion chamber that may distinguish cycles exhibiting large and small CKI levels. The analysis is based on a more detailed observation and description of the premixed flame shape and the auto-ignition spots within the combustion chamber.

8.2.1 Correlation between CKI and the remaining proportion of fuel mass

First, the proportion of the initial fuel mass in the combustion chamber still unburned at the onset of main auto-ignition is introduced. It is noted $\mathcal{Y}_F^u(t = t_{AI})$ and given by:

$$\mathcal{Y}_F^u(t = t_{AI}) = \left(1 - \frac{Y_F^u(t = ST) - Y_F^u(t = t_{AI})}{Y_F^u(t = ST)} \right) * 100 \quad (8.8)$$

with $Y_F^u(t = t_{AI})$ the mass fraction of fuel in the combustion chamber at the onset of main auto-ignition, and $Y_F(t = ST)$ the mass fraction of fuel in the combustion chamber at spark-timing.

Figure 8.17 shows the correlation between CKI and $\mathcal{Y}_F^u(t = t_{AI})$. The correlation coefficient of Bravais-Pearson $R_{(CKI, \mathcal{Y}_F^u(t = t_{AI}))} = 0.89$ between the two quantities indicates a strong

correlation, close to linear. The CKI level is thus quasi-proportional to the amount of fresh gases still unburned at the onset of main auto-ignition. These fresh gases are termed as *end-gas* in the rest of the study.

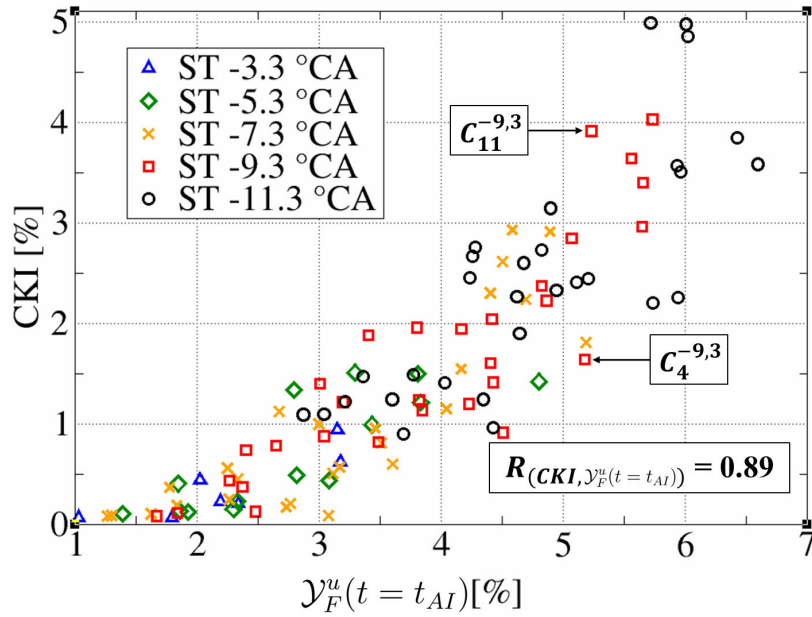


Figure 8.17: Scatter plot of CKI as a function of $\mathcal{Y}_F^u(t = t_{AI})$. Each symbol represents one simulated knocking cycle. Indicated is the correlation coefficient of Bravais-Pearson $R_{(CKI, \mathcal{Y}_F^u(t = t_{AI}))}$.

A reason for such a strong correlation is illustrated in Figure 8.18. It shows top views of the combustion chamber at six different crank angles for the arbitrarily chosen Cycle 11 at $ST = -9.3$ °CA, noted $C_{11}^{-9,3}$. The spark-triggered premixed flame and the auto-ignition front are materialized through iso-contours of their respective advance variable, $\tilde{c}_\Sigma = 0.7$ for the premixed flame and $\tilde{c}_{AI} = 0.3$ for the auto-ignition. This yields a qualitative visualization of the propagation of the auto-ignition front, compared to the one of the premixed flame front. In the displayed cycle, the first auto-ignition spot is identified at 18.6°CA on the exhaust side of the combustion chamber (right side on the view). Only 0.2°CA later, multiple auto-ignition spots are visible on this same side. Then, between the two instants 18.8°CA and 19°CA , the auto-ignition fronts rapidly propagate into the surrounding end-gas, whereas the premixed flame did not travel a long distance. The same tendency is observed with a secondary auto-ignition spot, appearing at 19°CA on the intake side of the combustion chamber (left side on the view).

In order to quantify this visual analysis, the absolute propagation speed of the auto-ignition front is estimated using the displacement of the iso-contour $\tilde{c}_{AI} = 0.3$ between two images. The speed, approximately 200 m.s^{-1} , remains much below a detonation (the Chapman-Jouguet velocity for a detonation varies depending on the local thermodynamic conditions, but is typically around 2000 m.s^{-1} [113]). It is nonetheless more than one order of magnitude

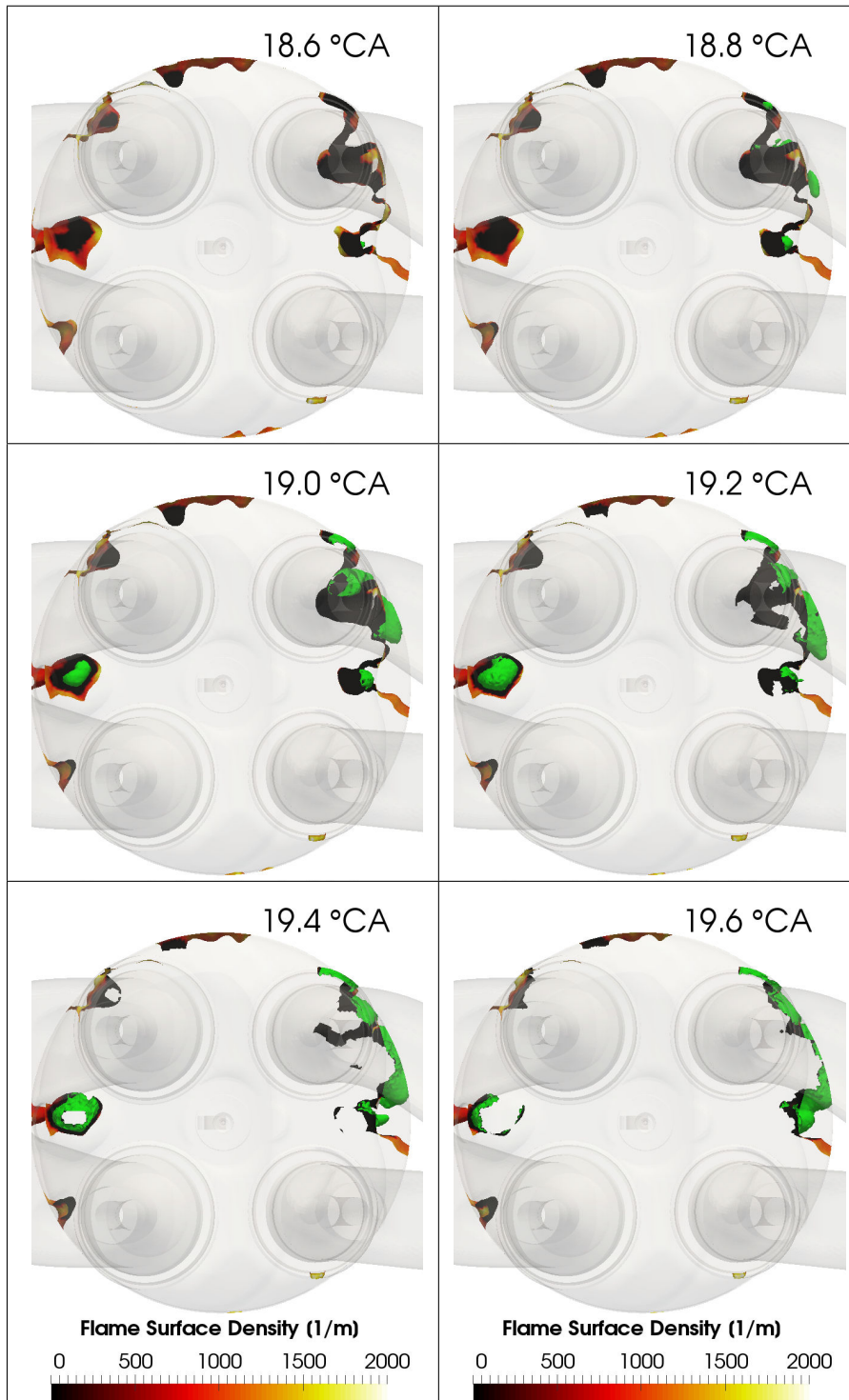


Figure 8.18: Top views of the premixed flame and auto-ignition fronts for Cycle 11 at $ST = -11^\circ CA$, $C_{11}^{-9.3}$. The premixed flame front is materialized by an iso-contour $\tilde{c}_\Sigma = 0.7$ and coloured by the flame surface density, while the auto-ignition front is materialized by an iso-contour $\tilde{c}_{AI} = 0.3$, and coloured in green. $0^\circ CA$ corresponds to combustion TDC. Intake valves are on the left, exhaust valves on the right.

larger than the absolute propagation speed of the premixed flame front ($< 10 \text{ m.s}^{-1}$). Such fast auto-ignition front continues to propagate through the end-gas until it reaches either a wall boundary or the premixed flame front. Therefore, it can be assumed in this cycle that once auto-ignition appears at a hot-spot, it consumes the entire mass of end-gas in its surrounding. A similar behaviour was observed in different knocking cycles, even at small CKI (they are not shown here for seek of clarity). That is, even if auto-ignition fronts velocity vary depending on the local conditions [136] [13], it stays in the present case sufficiently larger than the premixed flame front speed to consider that the auto-ignition wave consumes all the end-gas in its surrounding.

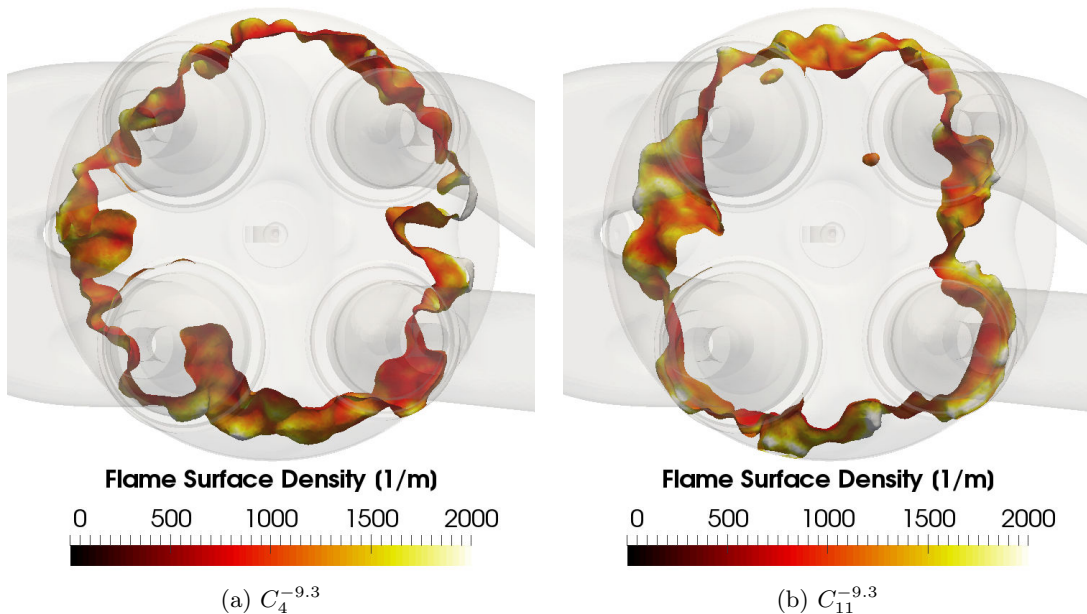


Figure 8.19: Illustration of the cyclic variability in the premixed flame shape based on two individual $\text{iso-}\mathcal{Y}_F^u(t = t_{AI})$ cycles, taken at a few crank angles before the onset of auto-ignition. Shown are iso-surfaces of $\tilde{c}_\Sigma = 0.5$. On each picture the intake is on the left and the exhaust on the right.

However, despite the strong correlation between CKI and $\mathcal{Y}_F^u(t = t_{AI})$, there is still a substantial dispersion of CKI at $\text{iso-}\mathcal{Y}_F^u(t = t_{AI})$. For instance, Cycle 4 at the spark-timing $\text{ST} = -9.3 \text{ }^\circ\text{CA}$, noted $C_4^{-9.3}$ in Figure 8.17, has a similar $\mathcal{Y}_F^u(t = t_{AI})$ as $C_{11}^{-9.3}$, but a more than two times smaller CKI. Figure 8.19 brings a possible explanation to such a difference. It displays top views of the combustion chamber for the two individual cycles, taken a few crank angles before the onset of main auto-ignition. One can observe differences in the flame shape between the two. On one hand $C_4^{-9.3}$ exhibits a fairly cylindrical premixed flame shape. On the other hand, $C_{11}^{-9.3}$ shows a more elliptic shape, with a flame front close to the cylinder wall at the top and bottom of the figure (i.e on the valve train and flywheel sides) but a larger distance between the flame and the cylinder wall on the right and left of the figure (i.e on the exhaust and intake sides). Such variability in the flame shape induces cyclic variations in the radial distribution of end-gas. This creates variations in both the location and the size

of pockets of end-gas, i.e in the local mass of fresh-gases around an auto-ignition spot. It is thereby assumed that the variability in the end-gas distribution may affect the proportion of fresh gases consumed by the auto-ignition. Such assumption is investigated in the following.

8.2.2 Characterizing the flame shape

A methodology inspired by the AVL "visio-knock" instrumentation [130] is proposed to characterize the flame shape, the aim of which is to estimate the end-gas distribution in the combustion chamber. Schematized in Figure 8.20, the methodology relies on the partitioning of the combustion chamber into angular sections of equal angle θ . At the considered crank-angle, LES data give access to the mass of end-gas in the angular section i of volume V_i :

$$m_i^u = \int \rho^u (1 - \tilde{c}_\Sigma) dV_i \quad (8.9)$$

with ρ^u the fresh gases density and \tilde{c}_Σ the progress variable for the premixed flame. The mass of end-gas in section m_i^u is then divided by the angle θ of the section:

$$\check{m}_i^u = \frac{m_i^u}{\theta} \quad (8.10)$$

The resulting quantity \check{m}_i^u accounts for the mass of end-gas per angle degree in section i .

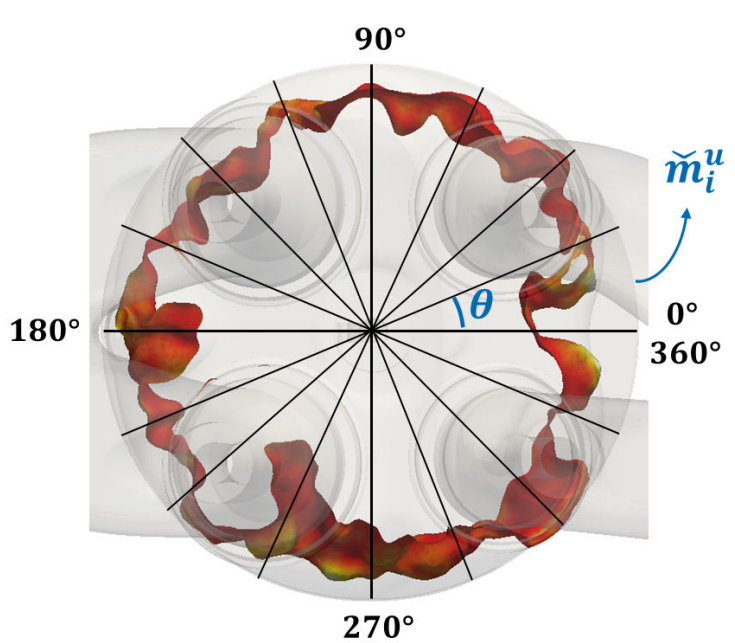


Figure 8.20: Schematic of the combustion chamber partitioning in sections of equivalent angle θ .

The choice of the angle θ is conditioned on one side by the flame wrinkling (θ must be small enough to capture the resolved wrinkling of the flame) and on the other side by the mesh size Δ_x (θ must be large enough to have a minimum number of mesh cells in the section). Figure 8.21 displays polar representations of the distribution of \check{m}_i^u in cycle $C_{11}^{-9.3}$ at the onset of main auto-ignition, for respectively three different angles θ :

- $\theta = 7.5^\circ$: the combustion chamber is partitioned into 48 Sections,
- $\theta = 4^\circ$: the combustion chamber is partitioned into 90 Sections,
- $\theta = 3^\circ$: the combustion chamber is partitioned into 120 Sections.

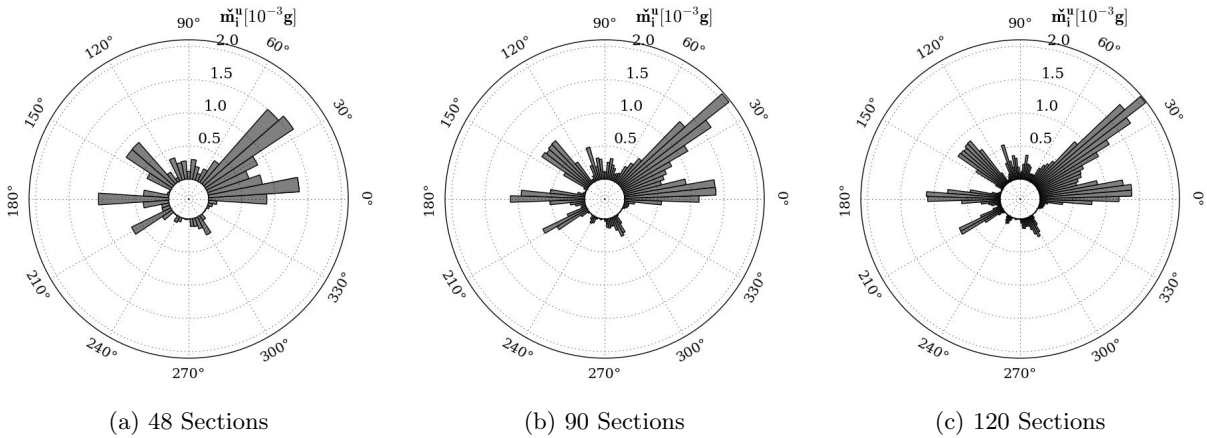


Figure 8.21: Polar representation of the distribution of \check{m}_i^u along the cylinder using three different partitioning. The length of the bar directly indicates the level of \check{m}_i^u in the section i . On the Figures the intake is on the left side and the exhaust on the right side.

On each polar plot, the length of the bar directly represents the level of \check{m}_i^u in section i . The absence of a bar in a section means that the flame has already reached the wall boundary at this location, i.e there is no end-gas there. The most refined partitioning, 90 and 120 sections, seem to provide very similar patterns. The partitioning in 48 sections already allows to distinguish the overall profile, even if some local variations seem to be missed. This is more easily visible in Figure 8.22, which gathers the three partitioning in the same plot. The profiles with 90 and 120 sections are perfectly superimposed, indicating that the partitioning with $\theta = 4^\circ$ is sufficient not to impact the result, probably because the flame wrinkling is adequately captured. When coarsening the partitioning to 48 sections, differences in the contour are visible, especially on the exhaust side (right side in the Figure). This is probably because the partitioning is too coarse to capture the flame wrinkling. As a result, the partitioning of the combustion chamber in the rest of the study consists in 90 sections of equal angle $\theta = 4^\circ$.

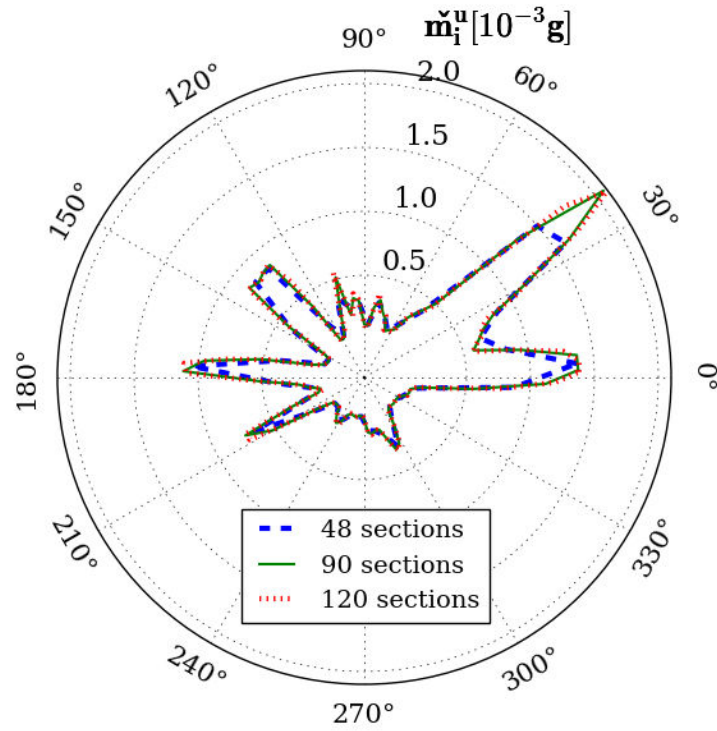


Figure 8.22: Distribution of \bar{m}_i^u along the cylinder using three different partitioning.

8.2.3 Analysis of individual cycles

As a potential tool to understand the dispersion in CKI at iso- $\mathcal{Y}_F^u(t = t_{AI})$, the partitioning was applied to a set of six individual cycles corresponding to $5\% < \mathcal{Y}_F^u(t = t_{AI}) < 5.5\%$. They are highlighted in Figure 8.23 and listed in Table 8.1 by decreasing CKI.

Cycle number	Spark-timing	CKI [%]	Notation
11	-9.3 °CA	3.91	$C_{11}^{3.91\%}$
5	-9.3 °CA	2.84	$C_5^{2.84\%}$
14	-11.3 °CA	2.44	$C_{13}^{2.44\%}$
13	-11.3 °CA	2.41	$C_{13}^{2.41\%}$
5	-7.3 °CA	1.81	$C_5^{1.81\%}$
4	-9.3 °CA	1.64	$C_4^{1.64\%}$

Table 8.1: Notation for the six individual cycles with $5\% < \mathcal{Y}_F^u(t = t_{AI}) < 5.5\%$. Cycles are listed by decreasing CKI.

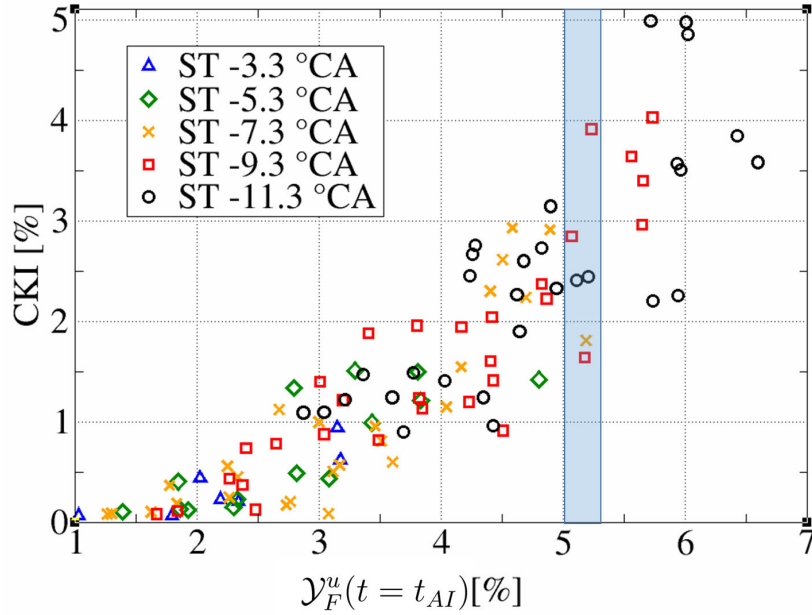


Figure 8.23: Scatter plot of CKI as a function of $\mathcal{Y}_F^u(t = t_{AI})$. Each symbol represents one LES knocking cycle. Highlighted in blue is the set of cycles under analysis.

On one side there is one extreme large CKI cycle: $C_{11}^{3.91\%}$. On the other side there are two extreme small CKI cycles: $C_5^{1.81\%}$ and $C_4^{1.64\%}$. In-between there are three intermediate CKI cycles: $C_5^{2.84\%}$, $C_{14}^{2.44\%}$ and $C_{13}^{2.41\%}$.

8.2.3.1 Exploring the distribution of end-gas

The six individual cycles are respectively analysed at the onset of main auto-ignition, i.e the crank-angle at which the first auto-ignition spot appears. Shown in Figure 8.24, the total masses of end-gas in the combustion chamber at this instant, noted m^u , are similar for the six cycles. Thus, at the onset of main auto-ignition, the six cycles have the same proportion of unburned fuel in the same mass of end-gas.

Figure 8.25 shows for the six cycles the radial distribution of the total mass of end-gas. Globally, the distribution is never perfectly homogeneous along the cylinder, instead the fresh gases are more or less accumulated in some locations, the so-called *end-gas pockets*. The notion of end-gas pocket is more easily illustrated in Figure 8.26 with cycle $C_{11}^{3.91\%}$. This cycle exhibits five pockets, which are coloured in green. They are defined by successive adjacent sections, the \tilde{m}_i^u of which is larger than the section averaged mass of end-gas per angle degree, noted \bar{m}_i^u and given by:

$$\bar{m}_i^u = \frac{1}{N} \sum_{i=1}^N \tilde{m}_i^u \quad (8.11)$$

with $N = 90$ the number of sections used.

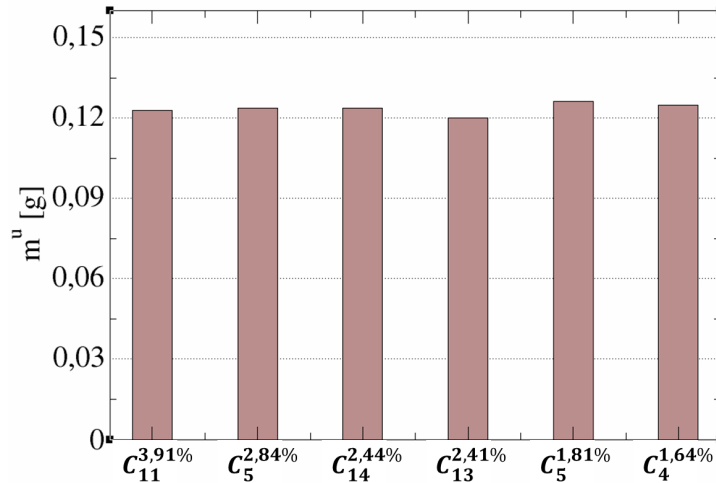


Figure 8.24: Total mass of end-gas m^u at the onset of main auto-ignition for the six individual cycles under analysis. Cycles are listed by decreasing CKI.

In cycle $C_{11}^{3.91\%}$, one can see that most of the end-gas is accumulated in one large pocket, which is situated on the exhaust side of the combustion chamber (from 352° to 48°). Summarized in Table 8.2, this largest pocket contains 45.7% of the total mass of end-gas in the combustion chamber. The other cycles do not exhibit such a large pocket, thereby suggesting that the particular distribution of end-gas in cycle $C_{11}^{3.91\%}$ might play a role in its large CKI. However, the sizes of the largest pocket in the five other cycles respectively do not verify the hierarchy in terms of CKI.

The two cycles exhibiting the smallest CKI, $C_4^{1.64\%}$ and $C_5^{1.81\%}$, have in common a quite homogeneous radial end-gas distribution along the cylinder, as compared to cycle $C_{11}^{3.91\%}$. The two distributions are nonetheless strongly different. For instance the largest pocket of end-gas in cycle $C_5^{1.81\%}$ is located on the exhaust side (from 352° to 48°), while it is more situated on the intake side in cycle $C_4^{1.64\%}$ (from 92° to 124°). In cycle $C_4^{1.64\%}$, some significant end-gas pockets are found on the flywheel side (bottom of the Figure), while cycle $C_5^{1.81\%}$ shows a negligible amount of end-gas on this same side.

In a similar way, no clear similarities could be pointed out in the three intermediate cycles. Indeed the visual comparison of $C_5^{2.84\%}$, $C_{14}^{2.44\%}$ and $C_{13}^{2.41\%}$ do not allow to draw common characteristics, neither in the radial distribution of the end-gas pockets, nor in their sizes. In Table 8.2, the largest pocket in the three cycles does not contain the same mass of end-gas.

Thus, the strict analysis of the distributions of end-gas showed strong differences for six individual cycles, and even between cycles of similar CKI. Such differences did not allow to draw a clear tendency on the relation between the end-gas distribution and CKI.

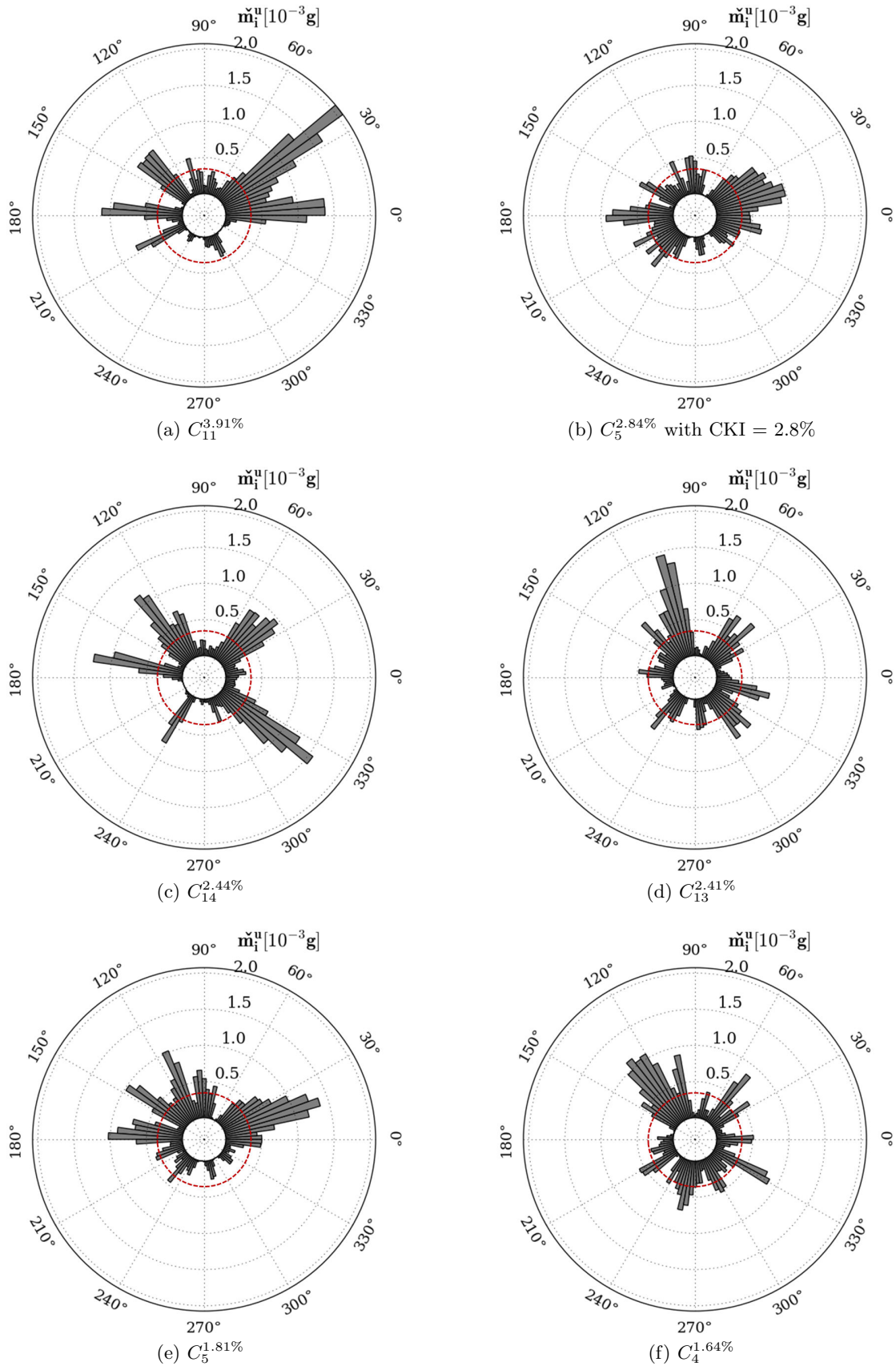


Figure 8.25: Distribution of \bar{m}_i^u for each of the 6 individual cycles under analysis. The bold dotted circle corresponds to \bar{m}_i^u in the cycle.

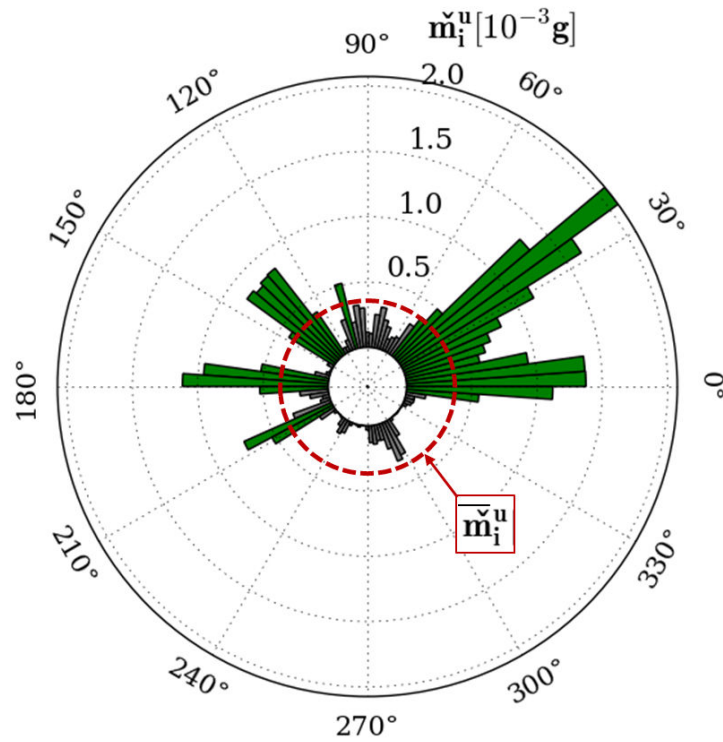


Figure 8.26: Illustration of the notion of end-gas pockets based on cycle $C_{11}^{3.91\%}$. There are five pockets in this cycle, highlighted in green.

Cycle	Proportion of m^u
$C_{11}^{3.91\%}$	45.7%
$C_5^{2.84\%}$	34.9%
$C_{14}^{2.44\%}$	20.6%
$C_{13}^{2.41\%}$	21.4%
$C_5^{1.81\%}$	30.8%
$C_4^{1.64\%}$	30.7%

Table 8.2: Proportion of the total mass of end-gas m^u contained in the largest pocket of end-gas for each of the six cycles under analysis. Cycles are listed by decreasing CKI.

8.2.3.2 Exploring the first auto-ignition spots

As a first step, this Section focuses on the first auto-ignition spots appearing in the six cycles. An in-depth analysis of the auto-ignition conditions in the distribution of end-gas will be discussed later.

Given the end-gas distribution, the radial position of the first auto-ignition spot is marked in Figure 8.27 by white circles. Multiple markers in the cycles $C_{11}^{3.91\%}$, $C_{14}^{2.44\%}$ and $C_4^{1.64\%}$ indicate that many different auto-ignition spots appeared simultaneously at different locations in the end-gas. $C_{14}^{2.44\%}$ has the particularity to have two first auto-ignition spots in two distinct pockets of end-gas.

Globally, the first auto-ignition spots are predominantly found on the exhaust side of the combustion chamber (right side on each figure). This tendency was also reported in the study of Robert et al. [112] in a single cylinder engine. It is not surprising since the higher temperatures at the walls on this side of the combustion chamber (see *Section 5.4.2*) are expected to result in higher temperatures in the near end-gas [63], as compared to the one situated on the intake side of the combustion chamber. Among the six cycles, only cycle $C_4^{1.64\%}$ has its first auto-ignition spot on the intake side. The pockets in which these first auto-ignition spots appear contain a significant mass of end-gas. With the assumption that the auto-ignition spot consumes the entire mass of end-gas in its surrounding, large pockets on the exhaust side are likely to be critical in terms of CKI, since they offer a large amount of fresh gases in the region where the first auto-ignition spots are predominantly found.

To quantify the correlation between the first auto-ignition spots and CKI level, the mass of end-gas consumed by these first auto-ignition spots, m_{AI_1} , is estimated. Assuming a much faster propagation of the auto-ignition spot as opposed to the premixed flame front, m_{AI_1} can simply be estimated as:

$$m_{AI_1} = m_p^u \quad (8.12)$$

with m_p^u the amount of fresh gases contained in the pockets in which the first auto-ignition spots occur. Results are presented in Figure 8.28 for the six cycles, and compared with CKI. The Figure does not evidence any clear correlation between CKI and m_{AI_1} , since the two quantities give different hierarchies between cycles. The largest CKI cycle $C_{11}^{3.91\%}$ does correspond to the largest mass of end-gas consumed by the first auto-ignition spots and the two smallest CKI cycles have similar m_{AI_1} values, but considerably different levels are found for the three intermediate CKI cycles. In particular, cycle $C_{13}^{2.41\%}$ corresponds to the smallest m_{AI_1} level.

The first analysis showed that CKI is not solely the result of the earliest auto-ignition spot. An in-depth analysis of the local conditions in the end-gas distribution is required to include the secondary (subsequent) auto-ignition spots.

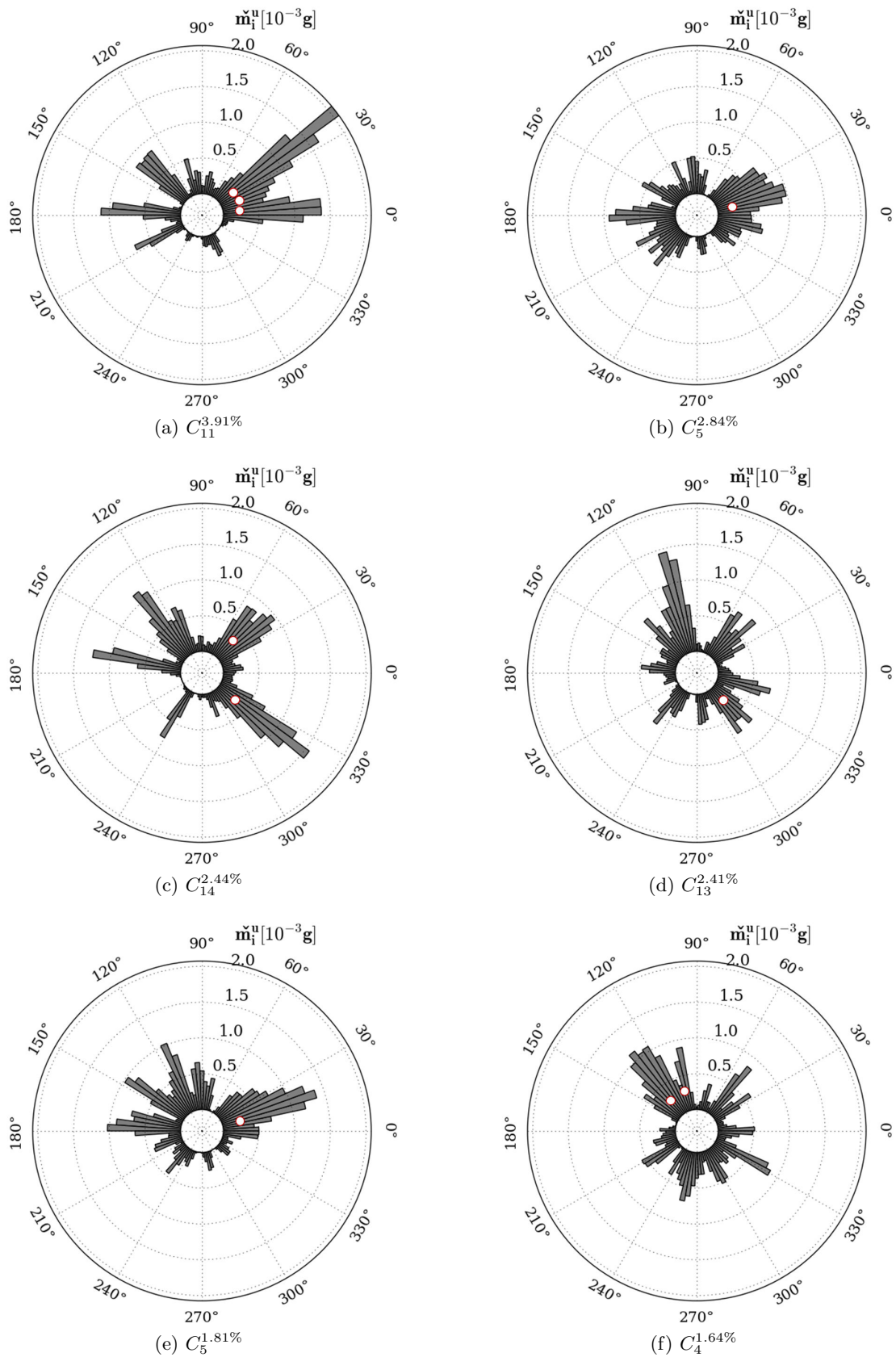


Figure 8.27: Distribution of \check{m}_i^u for the 6 individual cycles under analysis. Highlighted are the location of the first auto-ignition spots. Multiple circles on a cycle means that auto-ignition first appears simultaneously in different locations.

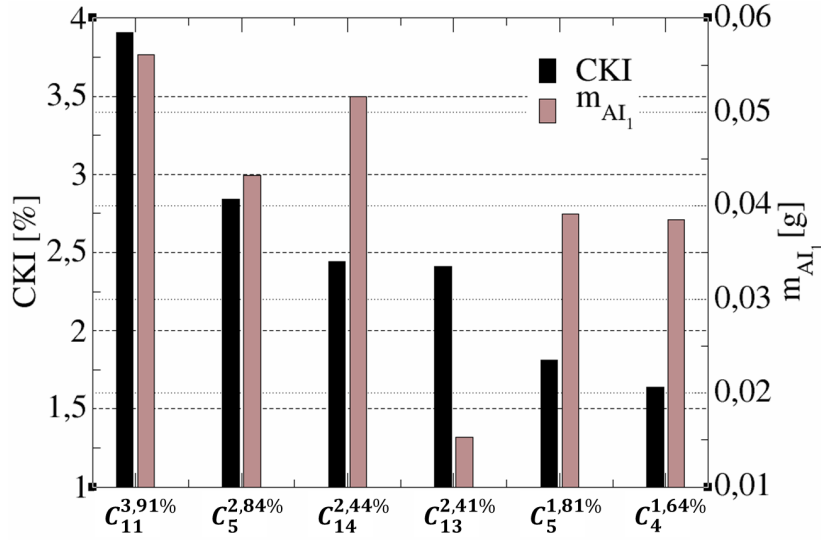


Figure 8.28: CKI and mass of fresh gases consumed m_{AI_1} by the first auto-ignition spots for the six individual cycles under analysis. Cycles are plotted by decreasing CKI.

8.2.3.3 Characterizing the secondary auto-ignition spots

Considering the thermodynamic state in the combustion chamber at the instant of the first auto-ignition, it is possible with the TKI model to estimate for each node of the mesh inside the combustion chamber the remaining time till main auto-ignition, i.e the time until $\tilde{c}_{AI} = 0.1$. Indeed the elapsed time $t(\tilde{c}_{AI})$, i.e the time between $\tilde{c}_{AI} = 0$ and the \tilde{c}_{AI} value at the present instant, is tabulated. It is thus possible to define locally the remaining time till main auto-ignition as:

$$\tau_{AI} = t(\tilde{c}_{AI} = 0.1) - t(\tilde{c}_{AI}) \quad (8.13)$$

Then, the auto-ignition delay in section i , $\tau_{AI,i}$, is taken as the local minimum delay in the section till main auto-ignition:

$$\tau_{AI,i} = \min [\tau_{AI,i}(1), \tau_{AI,i}(2), \dots, \tau_{AI,i}(j), \dots, \tau_{AI,i}(n)] \quad (8.14)$$

with n the number of nodes in section i . The resulting distribution of auto-ignition delays expressed in crank angle degree is shown in Figure 8.29 for the six cycles. Since each cycle is analysed at the onset of the first auto-ignition spots, delays in the sections in which they appear equal 0 accordingly. Globally, one can observe smallest auto-ignition delays on the exhaust side of the combustion chamber (right side on Figures) as compared to the intake side (left side on Figure), confirming that the conditions on the exhaust side are the most favourable for fast auto-ignition in the cylinder.

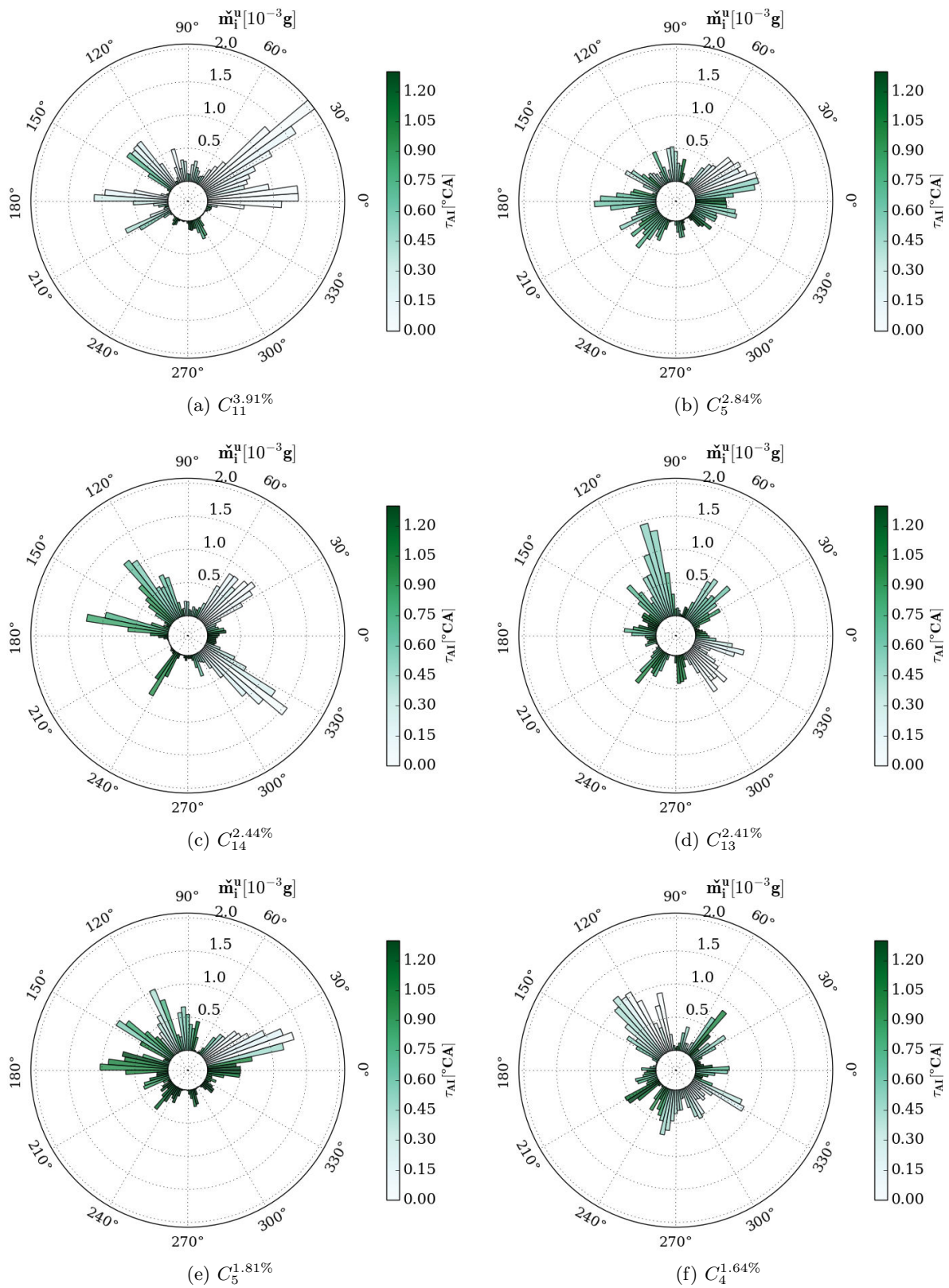


Figure 8.29: Distribution of \check{m}_i^u for the 6 individual cycles under analysis, coloured by the auto-ignition delay $\tau_{AI,i}$ in the sections.

The six cycles are then analysed in group: first the largest CKI cycle $C_{11}^{3.91\%}$, then the two smallest CKI cycles $C_5^{1.81\%}$ and $C_4^{1.64\%}$, and finally the three intermediate CKI cycles $C_5^{2.84\%}$, $C_{14}^{2.44\%}$ and $C_{13}^{2.41\%}$.

Analysis of the largest CKI cycle: $C_{11}^{3.91\%}$

In Figure 8.29a, the pocket of end-gas consumed by the first auto-ignition spots (ranging from 352° to 48°) shows near 0 auto-ignition delays in almost all sections that compose this pocket. The entire pocket is in a state close to auto-ignition, which is consistent with the multiple first auto-ignition spots in it. A small part of the end-gas is left in three secondary pockets situated on the intake side, respectively from 124° to 148° , from 124° to 148° and from 200° to 208° . These secondary pockets contain at least one or more sections characterized by extremely small auto-ignition delays ($\tau_{AI} < 0.3^\circ CA$), which therefore are expected to rapidly auto-ignite.

However, such short auto-ignition delays alone do not guarantee that all the end-gas in these pockets will be consumed by auto-ignition. It depends on the propagation speed of the premixed flame, which may consume a significant amount of end-gas before the auto-ignition wave reaches them. To quantify this, the mass fraction of end-gas $f_{AI,i}$ actually consumed by auto-ignition in section i is introduced:

$$f_{AI,i} = \frac{m_i^{AI}}{m_i^u} \quad (8.15)$$

m_i^{AI} is the mass of end-gas actually consumed by main auto-ignition in section i . With the assumption of a rapid propagation of the auto-ignition front, it is taken as the mass of end-gas still in section i at the instant at which the auto-ignition spot appears in this section. This way, if no auto-ignition is recorded in section i , $f_{AI,i} = 0$ accordingly. On the opposite, $f_{AI,i} = 1$ in the sections consumed by the first auto-ignition spots.

Figure 8.30 shows respectively the end-gas distribution for cycle $C_{11}^{3.91\%}$ coloured by the auto-ignition delay, and the mass fraction of end-gas consumed by auto-ignition. The secondary pockets on the intake side characterized by small auto-ignition delays in fact correspond to large mass fractions of end-gas consumed by auto-ignition. The auto-ignition delays were short as compared to the premixed flame propagation, such that the premixed flame had no time to consume a large mass of the rest of the end-gas prior to the secondary auto-ignitions. Thus, the largest CKI cycle $C_{11}^{3.91\%}$ is characterized by:

- A large proportion of the end-gas concentrated in one pocket located on the exhaust side (the favoured side for fast auto-ignition),
- The rest of the end-gas gathered in a few pockets, all in a state close to auto-ignition.

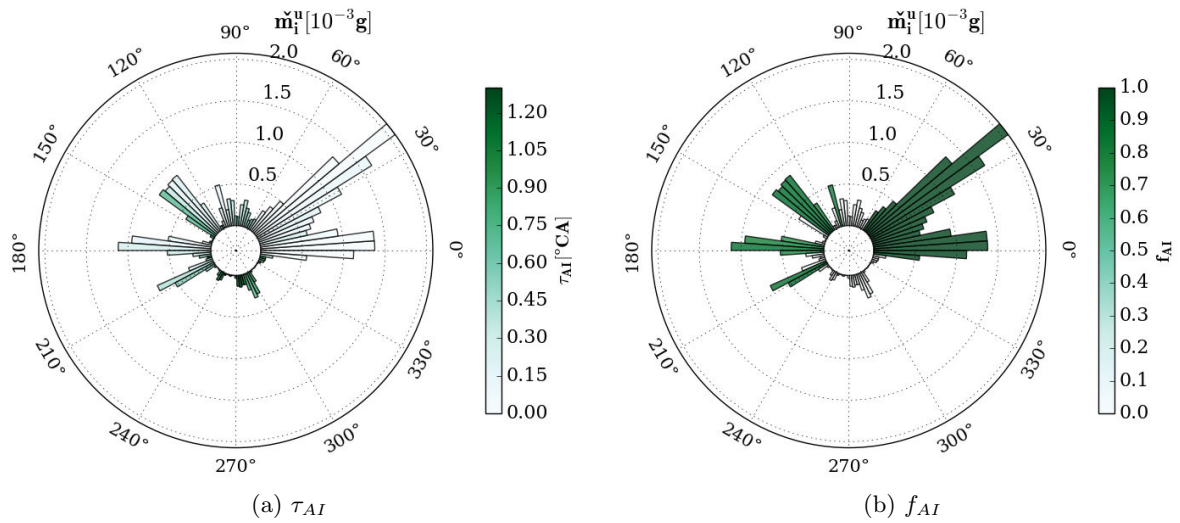


Figure 8.30: Distribution of \dot{m}_i^u for cycle $C_{11}^{3.91\%}$, coloured by (a) the auto-ignition delay $\tau_{AI,i}$ and (b) the fraction of end-gas consumed by auto-ignition $f_{AI,i}$ in the sections.

Analysis of the smallest CKI cycles: $C_4^{1.64\%}$ and $C_5^{1.81\%}$

Figure 8.31 shows respectively for $C_4^{1.64\%}$ and $C_5^{1.81\%}$ the auto-ignition delays and the mass fraction of end-gas consumed by auto-ignition in the sections.

Displayed in Figure 8.31a, $C_4^{1.64\%}$ shows near 0 auto-ignition delays in almost the entire pocket consumed by the first auto-ignition spots (from 92° to 124°), which is in agreement with the multiple auto-ignition spots identified in it. Surprisingly, the same Figure also evidences small auto-ignition delays in a large band on the flywheel side (bottom on Figures), from 252° to 336° . This is at first sight not consistent with the small CKI for the cycle. Nonetheless, the right Figure shows a negligible consumption of end-gas by auto-ignition in this region. It means that the premixed flame has already burned a large proportion of the end-gas prior to auto-ignition. Still some secondary auto-ignition spots are found around 48° , 192° , 312° and also at 332° , but the resulting consumption of end-gas by these spots is limited to one or two sections. It is likely that the quite homogeneous radial distribution of the end-gas pockets in the cycle avoids the presence of large pockets, thus limiting the amount of end-gas around the auto-ignition spots.

In Figure 8.31b, $C_5^{1.81\%}$ is characterized by large auto-ignition delays in extremely small secondary pockets on the flywheel side (bottom of the figure), that leave no time for auto-ignition to occur before the arrival of the premixed flame. On the valve train side (top on Figures), the rest of the end-gas exhibit relatively small auto-ignition delays. In a similar way as in $C_4^{1.64\%}$, the quite homogeneous radial distribution on this side of the combustion chamber makes that the few auto-ignition spots are restrained to one or two sections. There is nonetheless a non-negligible amount of end-gas consumed by auto-ignition on the intake side (around 180°), despite large auto-ignition delays. A possible reason to such result will be given in Section 8.2.4.

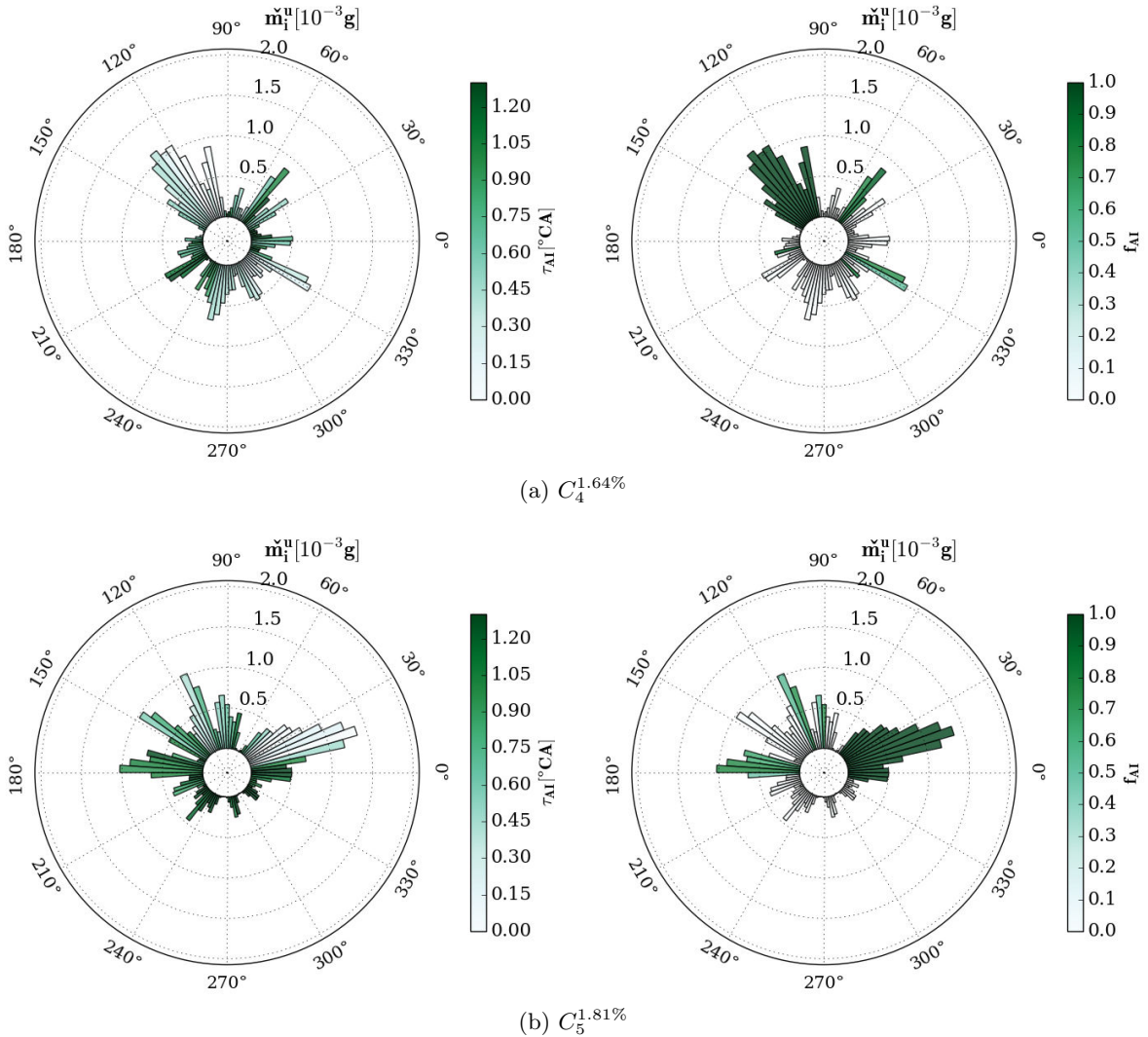


Figure 8.31: Distribution of \dot{m}_i^u for the two smallest CKI cycles, coloured by the auto-ignition delay $\tau_{AI,i}$ (left Figures) and the fraction of end-gas consumed by auto-ignition $f_{AI,i}$ (right Figures) in the sections.

To summarize, the two small CKI cycles have in common:

- A similar mass of end-gas consumed by the first auto-ignition spots, significantly smaller than in the largest CKI cycle $C_{11}^{3.91\%}$.
- A quite homogeneous radial distribution of the rest of the end-gas, leaving only a small amounts of end-gas around the secondary auto-ignition spots.

Analysis of the intermediate CKI cycles: $C_{14}^{2.44\%}$, $C_{13}^{2.41\%}$ and $C_5^{2.84\%}$

In $C_{14}^{2.44\%}$, it is recalled that the first auto-ignition spots consumed the two pockets situated on the exhaust side, which represents a significant mass of end-gas, similar to $C_{11}^{3.91\%}$. In Figure 8.32a, the rest of the end-gas in $C_{14}^{2.44\%}$, are gathered in a few secondary pockets on the intake side, similarly to cycle $C_{11}^{3.91\%}$. However, as opposed to $C_{11}^{3.91\%}$, these secondary pockets are characterized by larger auto-ignition delays. In the right Figure, there is accordingly a smaller mass fraction of end-gas consumed by auto-ignition. In particular, the substantial pocket between 104° and 144° does not present any trace of auto-ignition, meaning that the local conditions left no time for auto-ignition to occur prior to the arrival of the premixed flame. Thus, in comparison to cycle $C_{11}^{3.91\%}$, the smaller CKI in cycle $C_{14}^{2.44\%}$ is explained by less favourable conditions to rapid auto-ignitions in the secondary pockets.

As previously stated, the three intermediate CKI cycles have very different distributions of end-gas. In the cycle $C_5^{2.84\%}$ represented in Figure 8.32b, the pocket consumed by the first auto-ignition spot, on the exhaust side, is characterized by $f_{AI,i} = 1$. As opposed to $C_{14}^{2.44\%}$, the rest of the end-gas is quite homogeneously distributed into small pockets dispatched from 80° to 248° . These pockets are characterized by quite small auto-ignition delays. On the right Figure, one can observe that multiple auto-ignition spots appeared in as many small end-gas pockets. All together, it represents a quite significant mass of end-gas consumed by auto-ignition. Therefore cycle $C_{14}^{2.44\%}$ and cycle $C_5^{2.84\%}$ exhibit different auto-ignition scenarii, despite similar CKI. In cycle $C_{14}^{2.44\%}$ there are two major pockets consumed by two separated first auto-ignition spots, and then only a small fractions of the rest of the end-gas, gathered in a few secondary pockets, are actually consumed by secondary auto-ignitions. In cycle $C_5^{2.84\%}$, there is only one large pocket totally consumed by a first auto-ignition spot, followed by multiple secondary auto-ignition spots that consume as many small end-gas pockets.

As for $C_{13}^{2.41\%}$, Figure 8.32c shows another scenario. The end-gas distribution is quite homogeneous along the cylinder, and the pocket of end-gas consumed by the first auto-ignition spot represents a relatively small mass of end-gas. Among the rest of the end-gas, four pockets with quite small auto-ignition delays. They are respectively located from 36° to 60° , from 96° to 120° , from 128° to 140° , and from 340° to 352° . The delays are short enough to induce auto-ignition in the four pockets prior to the arrival of the premixed flame front, and large fractions of the end-gas in these pockets are actually consumed by auto-ignition. In cycle $C_{13}^{2.41\%}$, CKI results from the rapid appearance of multiple auto-ignition spots in different end-gas pockets.

Thus, despite similar CKI, the analysis of the three intermediate cycles evidenced strong differences in the path leading to such intermediate CKI.

8.2.3.4 Summary of the analysis on individual cycles

The direct individual analysis of six individual cycles with iso- Y_F^{CAI} evidenced that auto-ignition spots predominantly appear on the exhaust side of the combustion chamber. With the assumption of a fast propagation of the auto-ignition wave, large pockets of end-gas on this side of the combustion chamber represent a significant amount of fresh gases to be

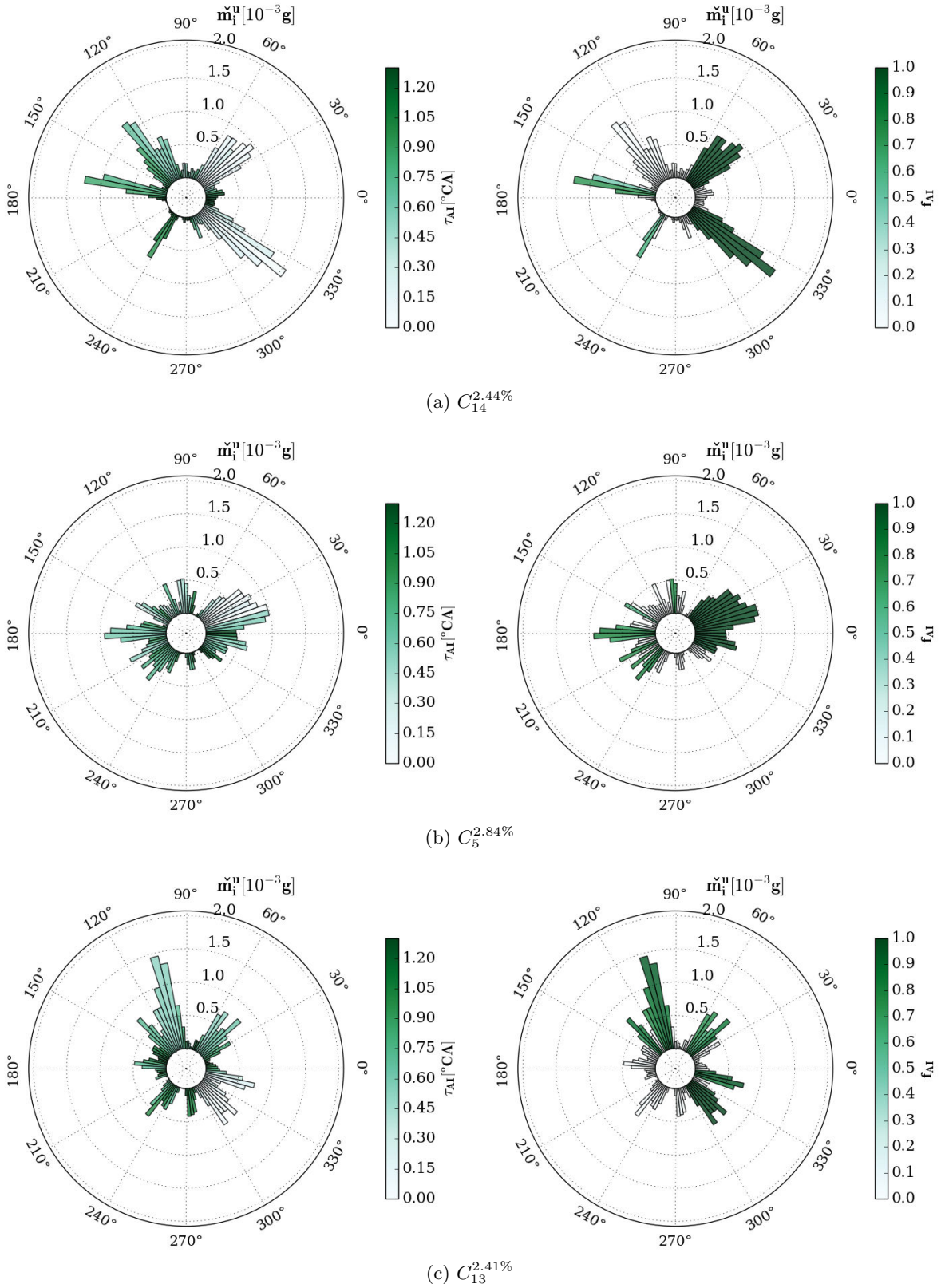


Figure 8.32: Distribution of \tilde{m}_i^u for the three intermediate CKI cycles, coloured by the main auto-ignition delay $\tau_{AI,i}$ (left Figures) and the fraction of end-gas consumed by auto-ignition $f_{AI,i}$ (right) in the sections.

consumed by auto-ignition. The largest CKI cycle was characterized in particular by a large proportion of the end-gas in a single pocket located on the exhaust side. In comparison, the two smallest CKI cycles were characterized by a more homogeneous radial distribution of end-gas, which may restrain the auto-ignition spots to only small end-gas pockets. However, the three intermediate CKI cycles displayed strong differences in their distribution of end-gas, probably the reason to the strong different scenarii of auto-ignition.

The CKI is probably the result of a combination between the radial distribution of end-gas pockets, their sizes, the local auto-ignition delays in the pockets and the local propagation speed of the premixed flame. It means that CKI only provides a global estimation of the auto-ignition in a cycle, but it does not distinguish the multiple scenarii that can take place in the cylinder.

In the following, a different approach is proposed to describe auto-ignition in the engine. Still based on the partitioning method, it gives a 2D statistical description of the radial end-gas distribution together with the statistical local conditions regarding auto-ignition. This allows to statistically distinguish the critical locations in terms of auto-ignition.

8.2.4 Statistical analysis

The statistical analysis is based on the same six individual cycles, used to build ensemble averaged quantities. First, the averaged mass of fresh gases per angle degree $\langle \check{m}_i^u \rangle$ in section i is determined as:

$$\langle \check{m}_i^u \rangle = \frac{1}{N_C} \sum_{j=1}^{N_C} \check{m}_i^u(j) \quad (8.16)$$

with N_C the number of cycles, and j the cycle index. From the averaged value, cycle-to-cycle variations in the end-gas distribution can be quantified as its standard deviation $\sigma_{\check{m}_i^u}$:

$$\sigma_{\check{m}_i^u} = \sqrt{\frac{\sum_{j=1}^{N_C} (\check{m}_i^u(j) - \langle \check{m}_i^u \rangle)^2}{N_C}} \quad (8.17)$$

Figure 8.33 displays the statistical end-gas distribution along the cylinder, coloured by the level of variability. The region with statistically the largest accumulation of end-gas is on the exhaust side, between 352° and 56° . A significant mass of end-gas is also identified on the intake side, respectively from 90° to 152° , and from 164° to 188° . These locations also exhibit the largest variabilities. On the opposite, a large part of the combustion chamber (from 188° to 315°) statistically contains a small mass of end-gas, and exhibit small standard deviations. Thus on average, the premixed flame propagates more rapidly on this side of the combustion chamber, with small cyclic variations in its shape.

In order to correlate the averaged end-gas distribution with auto-ignition, the weighted averaged auto-ignition delay $\langle \tau_{AI,i} \rangle_w$ and the weighted averaged mass fraction of end-gas con-

sumed by auto-ignition $\langle f_{AI,i} \rangle_w$ in section i are defined respectively as:

$$\langle \tau_{AI,i} \rangle_w = \sum_{j=1}^{N_C} \tau_{AI,i}(j) * \frac{\check{m}_i^u(j)}{\check{m}_{i,tot}^u} \quad (8.18)$$

$$\langle f_{AI,i} \rangle_w = \sum_{j=1}^{N_C} f_{AI,i}(j) * \frac{\check{m}_i^u(j)}{\check{m}_{i,tot}^u} \quad (8.19)$$

with $\check{m}_{i,tot}^u = \sum_{j=1}^{N_C} \check{m}_i^u(j)$.

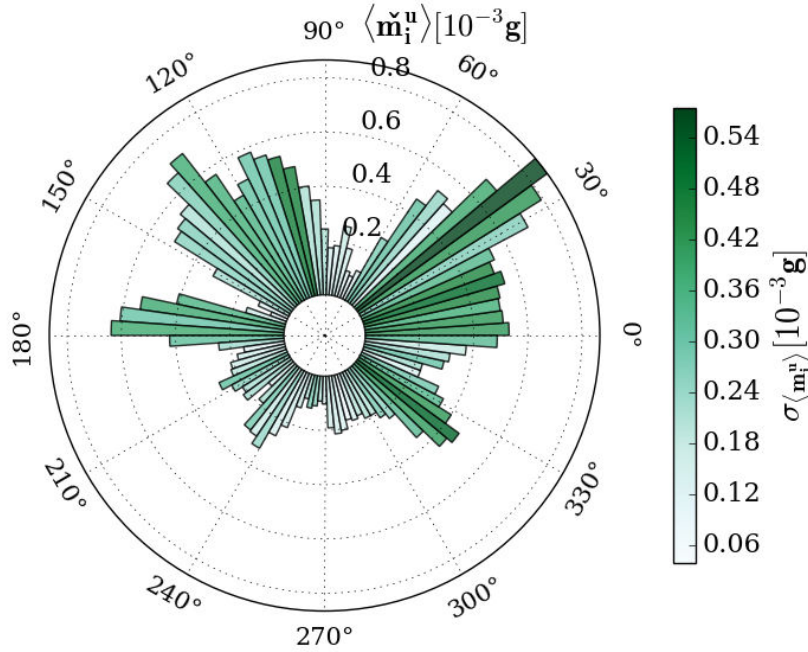


Figure 8.33: Distribution of the ensemble average $\langle \check{m}_i^u \rangle$ coloured by its standard deviation $\sigma_{\check{m}_i^u}$.

These quantities are represented in Figure 8.34. First, there is a good matching between the auto-ignition delay and the mass fraction of end-gas consumed by auto-ignition, i.e that the locations of small τ_{AI} corresponds to large f_{AI} , and conversely. It means that the statistical distribution of auto-ignition delays already provides a good estimation of the locations in which a large portion of the end-gas will be consumed by auto-ignition.

As suggested in the analysis of the individual cycles, the smallest auto-ignition delays and the largest averaged mass fractions of end-gas burned by auto-ignition are statistically found on the exhaust side, in the region with the largest accumulation of end-gas. This side of the combustion chamber is clearly pointed out as the most critical in terms of auto-ignition, since it provides a significant mass of end-gas to the auto-ignition front. In comparison, the second

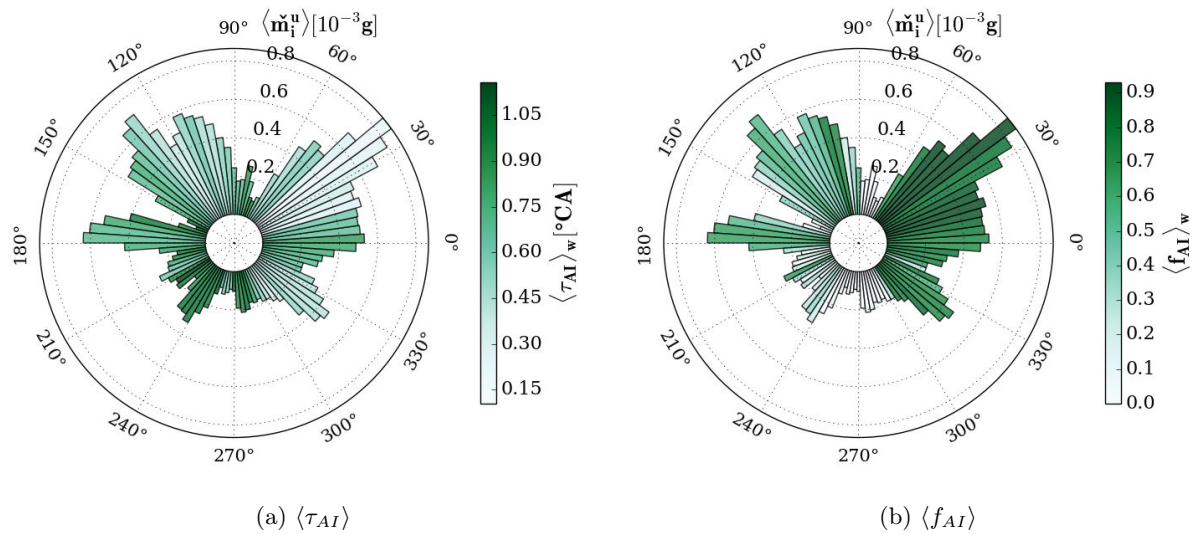


Figure 8.34: Statistical end-gas distribution along the cylinder with each section coloured by (a) the ensemble averaged auto-ignition delay and (b) the ensemble averaged mass fraction of end-gas consumed by auto-ignition.

region with a large concentration of end-gas (between 90° and 152°) exhibits substantially larger auto-ignition delays, resulting in the present case in a smaller averaged mass fraction of end-gas consumed by auto-ignition. Thereby this region is indicated as less critical in terms of auto-ignition, despite the significant mass of end-gas.

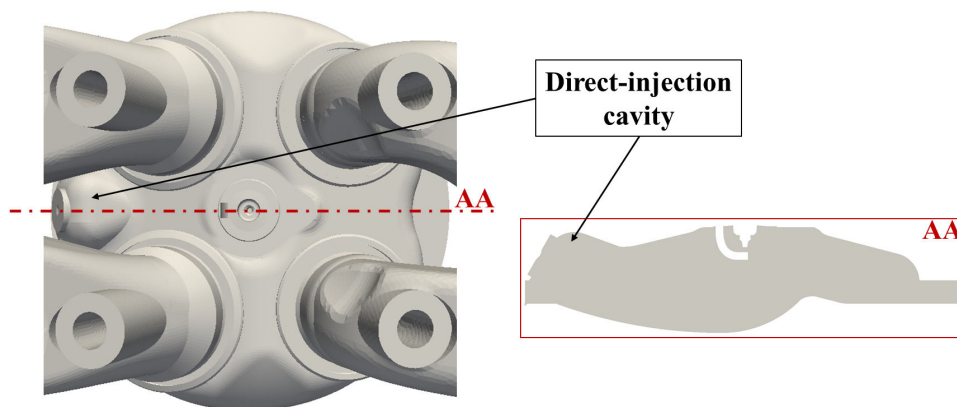


Figure 8.35: Zoom on the direct-injection cavity.

Finally, the last identified major pocket, ranging from 164° to 188° , corresponds to quite large

auto-ignition delays, but still non negligible mass fractions of end-gas are consumed by auto-ignition. Figure 8.35 shows that this region corresponds to the location of the direct-injection cavity. It would be interesting to analyse the conditions in this cavity. Such investigation was not carried out in the course of this study. However it can be assumed that the premixed flame fails to propagate in the cavity (probably due to a small turbulence level), in such a way that even large auto-ignition delays result in a significant mass consumed by auto-ignition. Finally, it is interesting to note that the region corresponding to small masses of end-gas (from 188° to 315°) also corresponds to the region with the largest auto-ignition delays, and accordingly negligible mass fractions of end-gas consumed by auto-ignition.

The above statistical analysis was based on the six individual cycles with $5\% < \mathcal{Y}_F^u(t = t_{AI}) < 5.5\%$. It would be interesting to perform the same analysis based on a different set of cycles with iso- $\mathcal{Y}_F^u(t = t_{AI})$, and verify if the same conclusions can be drawn.

8.3 Summary of Part III

The LES database was used in this Part to develop a comprehensive understanding of knock in an industrial engine.

Chapter 7 focused on the definition of an indicator to characterize knock events. The first solution would have been to base this indicator on the analysis of the local pressure oscillations inside the combustion chamber, as it is usually done in experimental studies to define a knock intensity. However, it was shown that the resulting KI strongly depends on parameters which are external to knock: namely the location of the probe inside the combustion chamber and the method of analysis used to post-process the knock characteristic pressure oscillations. Consequently, it was chosen to use the Computational Knock Index, which focuses on the sources of knock: auto-ignition. Indeed it quantifies the proportion of fresh gases in the cylinder consumed by auto-ignition.

The initial formulation described in [18] was here modified to remove the cool flame effect in its calculation, since cool flame chemistry cannot itself trigger knock. Thus, the new CKI formulation only accounts for the proportion of fresh gases consumed by main auto-ignition. Then, the sensitivity of CKI was investigated through a spark-timing sweep, and the predicted results were compared to a usual KI (here given by MAPO analysis). It was shown that the two indicators have relatively similar behaviours in response to the spark-advance: first a rise in the percentage of knocking cycles, second an increase of their respective maximum value. Nonetheless, there was not a linear correlation between CKI and KI, leading to differences in the ranking between knocking cycles depending on the selected knock indicator.

In *Chapter 8*, CKI was used to investigate the impact of CCV, characterized by cyclic variations in CA_{50} , on knock. In the present case, it was found a threshold value CA_{50}^T . For larger CA_{50} , i.e relatively slow combustion cycles, there was no trace of main auto-ignition, and therefore this region could be termed as knock-free. On the opposite side for smaller CA_{50} , i.e relatively fast burning cycles, most cycles exhibited a significant proportion of fresh gases consumed by main auto-ignition. In this region, the trend showed an increase of CKI as CA_{50} diminished. Due to substantial CCV levels, only a small percentage of engine cycles can be

located below CA_{50}^T , but these cycles impose to take safety margins to guarantee knock-free conditions.

Consequently, the origins of CCV were examined, since a better control of the engine variability could allow a reduction of the safety margins. As a key parameter, an important flow structure in the vicinity of the spark plug, right at the spark-timing, was identified. It was shown that, when present, it interacts with the flame front, and generates a faster increase of the flame surface through turbulence. In comparison, the mixture and temperature distributions, here materialized by the laminar flame speed, have relatively less impact on the premixed flame propagation.

Then, a methodology of analysis was proposed to give a more detailed description of auto-ignition inside the cylinder. It is based on the partitioning of the combustion chamber into angular sections of equal angular lengths. The methodology, applied to different cycles at iso-mass of fuel available at the onset of auto-ignition, showed that CKI results from several auto-ignition spots inside the combustion chamber. Depending on the size of the end-gas pockets, auto-ignition delays in these pockets, and the local premixed flame propagation speed, a more or less larger proportion of end-gas can be locally consumed by auto-ignition. Strongly different scenarii of auto-ignition were observed between the individual cycles under investigations, even for the ones with similar CKI. It showed that CKI only provides a global estimation of auto-ignition in a cycle, but it cannot distinguish the multiple scenarii that takes place inside the combustion chamber. Consequently, a statistical analysis was proposed to identify critical locations in terms of auto-ignition in the combustion chamber, corresponding to regions with a large accumulation of end-gas and short auto-ignition delays.

Conclusions and Perspectives

Engine knock is one of the main limiting phenomenon in the use of turbocharged downsized spark-ignition engines, since it prevents the engine to fully exploit its potential. In order to address knock, the LES approach is particularly interesting, due to its ability to deal with such a cyclic varying phenomenon. Previous thesis have demonstrated the capability of LES to reproduce knock events in engine-like conditions [115] [87]. As a further step, the present thesis aimed at capitalizing the previous research by developing a LES database on an industrial engine, and exploit it to understand and characterize the mechanisms that control the appearance of knock.

Developments and methodologies

For this study, the industrial RENAULT 1.2 TCe 115 engine was chosen, since its analysis on a test bench showed knock. An important effort was made to perform an as predictive as possible LES, with a computational domain fully based on the real engine geometry, and with test bench data given by RENAULT. Predicting knock events is a complex topic, since the auto-ignition is very sensitive to the local conditions inside the cylinder. Hence, all the interacting physical and chemical phenomena likely to influence these conditions have been included in the simulation: internal flow dynamics, direct injection, spark-ignition, premixed flame propagation, wall heat transfer and auto-ignition chemistry.

Regarding wall heat transfer, a methodology allowing to determine realistic wall temperature distributions was proposed, since it is a key input for the LES. It consisted in a RANS-CHT simulation, for which the coupling between the gas phase inside the cylinder and the surrounding solid components allowed to solve heat transfer at the interfaces. In this way, an accurate wall temperature distribution could be imposed as boundary condition for the LES. Then, a set of 30 cycles was simulated at a single operating point, frequently encountered by

the engine in its everyday life and presenting a weak knock. LES results were compared to experimental findings, both in terms of cyclic variability and knock. Subsequently, a spark-timing sweep was simulated to extend the database to weaker and stronger knock levels, providing a substantial LES database of 150 individual combustion cycles to investigate the mechanisms that impact knock.

The second important development resulted from the choice of an indicator to characterize knock. Contrary to the usual experimental ones based on the analysis of the characteristic pressure oscillations resulting from knocking combustion, the choice was made to rather focus on the source of knock, which is main auto-ignition. As a result, the Computational Knock Index (CKI) proposed in [18] was chosen. In its initial form, it represents the proportion of fresh gases consumed by the overall auto-ignition process, i.e cool flame and main auto-ignition. Since past research had indicated that cool flames do not themselves induce knock, the previous formulation was modified, in such a way that it only quantifies the proportion of fresh gases consumed by main auto-ignition. Such a quantification fully exploits the computational access to any local quantity inside the combustion chamber, and takes advantage of the separate description of the premixed flame propagation and auto-ignition as proposed by the ECFM-TKI formalism.

Finally, two analyses were performed to investigate the mechanisms that impact the appearance of knock. First, the link between knock and Cyclic Combustion Variability (CCV) was studied. To do so, we proposed to characterize CCV by the crank angle at which half of the fuel is consumed: CA_{50} . As a result of the particular link found between knock and CCV, a two step strategy was developed to identify the sources of CCV. It is based on the definition of two conditional phase averaged cycles, build from the 20% fastest (respectively 20% slowest) combustion cycles. It allowed to point out characteristics in the cylinder flow field shared between the fast, respectively the slow, combustion cycles. In order to identify which one of the characteristic contributes the most to CCV, the analysis was completed with the study of the Flame Surface Density (FSD) equation, which describes the turbulent propagation of the premixed flame inside the combustion chamber. Each term in the FSD equation accounts for a particular effect (convection, curvature, planar propagation, strain), and so their analysis allowed to determine the main contributor to CCV.

The second analysis was developed to have a more detailed description of knock inside the combustion chamber. It relies on the partitioning of the combustion chamber into sections of equal angular length. This methodology has been used to characterize the end-gas distribution at the onset of auto-ignition and the imminence of auto-ignition in the end-gas. Thus the characterization of knock was not solely reduced to a single scalar value, which allowed in particular to identify critical locations in terms of knock, i.e regions with statistically a significant accumulation of end-gas and imminent auto-ignition.

Contributions and Perspectives

This thesis first contributed to further advance the development of a LES activity on spark-ignition engines. As a further step to previous studies, the present one showed that LES approaches can be applied to investigate knock in the particular case of an industrial spark-ignition engine under real operating conditions, thus providing a substantial, meaningful

and as realistic as possible computational database. Nonetheless, the present LES approach presented some deficiencies by predicting some non-realistic cycles. As possible reason to this, the approximate modelling of the spray-wall interaction (simple rebound condition) could be cited. It would be useful to apply a more realistic spray model, in which the liquid particles can rebound, slip, splash or stick on the wall depending on local conditions. This may considerably improve the prediction of the mixture stratification inside the combustion chamber, and particularly close to the walls where the auto-ignition is generally found.

In addition, this thesis contributed to an alternative method for characterizing engine knock. It was demonstrated that characterizing knock through the auto-ignition induced pressure oscillations presents some deficiencies, since the resulting knock indicator strongly depends on parameters which are external to knock: e.g the position of the pressure probe inside the combustion chamber and the method of analysis selected to post-process the pressure oscillations. As an alternative, the CKI was modified as expressed above. This study investigated the behaviour of the present CKI formulation, which was compared to the one of a usual pressure oscillations based KI indicator. It was shown that CKI and KI globally behave in a similar way in response to an advance of the spark-timing: first a rise in the percentage of knocking cycles, second an increase of their respective maximum values. In the present case, the strong correlation between CKI and KI, confirmed previous assumptions that knock (as quantified by the local pressure oscillations analysis) roughly varies in proportion to the mass of fresh gases consumed by auto-ignition. Nonetheless, the relation was not perfectly linear, and in particular the ranking between knocking cycles differed depending on the selected indicator. For this study, the maximum acceptable CKI, CKI_T , which determines the percentage of knocking cycles at a fixed operating point, was approximately fixed based on visual observations. With the perspective to improve the use of CKI as knock indicator, a methodology could be developed to properly define such a maximum acceptable CKI. However, it is recalled that changing CKI_T does not specifically modify the general trend, which is an increase of the percentage of knocking cycles in proportion to the spark-advance.

Then, this thesis contributed to explore the relation between knock and combustion phasing. In the present case, the most severe knocking cycles (as quantified by CKI) corresponded to the earliest combustion cycles. On the opposite, the latest combustion cycles were predicted as knock free. The study showed that it was possible to define a knock limited combustion phasing, independent of the spark-timing. The existence of such a limit should be investigated in other engines and operating conditions, to confirm if it could be used as an indicator characterizing the tolerance of the engine to knock. Due to the substantial level of CCV at fixed operating conditions, a small percentage of cycles can fall below the knock limiting combustion phasing, therefore imposing to take extra safety margin to guarantee knock free operation. This pointed out the need to better control CCV in order to reduce these margins, and thus running the engine closer to the optimal operating conditions in terms of efficiency. As a key parameter to reach this objective, a reduction of the cyclic variability of the flow around the spark-plug at spark-timing should be considered, since it appears to control to a large extent the overall combustion speed.

Finally, the methodology of analysis based on the partitioning of the combustion chamber showed that the use of a single value criterion such as CKI cannot precisely characterize knock in an engine cycle, since there can be multiple scenarii inside the combustion chamber leading

to a similar CKI value. In the present case, it was shown that knock results from multiple auto-ignition spots inside the cylinder, which locally consumed a more or less significant mass of end-gas depending on the following parameters:

- The flame shape which determines the size and locations of the end-gas pockets,
- The imminence of auto-ignition in these end-gas pockets,
- The local premixed flame propagation speed which can locally consume the end-gas before auto-ignition can be reached.

Thus, characterizing knock requires a detailed description of the in-cylinder conditions. In a simple statistical analysis based on the ensemble average of partitioned individual cycles, it was possible to identify critical locations, i.e regions in the combustion chamber that accumulate a large mass of end-gas and predominantly auto-ignite, leading to a significant mass of fresh gases consumed by auto-ignition. As a perspective, it would be interesting in the medium term to investigate a strategy to relate the present methodology to design parameters. This may allow to remove knock critical locations inside the combustion chamber, and possibly to further reduce safety margins which guarantee knock free conditions, but substantially reduce the engine efficiency.

Nomenclature

BDC	Bottom-dead center
CA	Crank angle
CCV	Cyclic combustion variability
CFD	Computational fluid dynamics
CFM	Coherent flame model
CHT	Conjugate heat transfer
CKI	Computational knock index
CPU	Central processing Unit
DI	Direct-injection
DNS	Direct numerical simulation
ECFM	Extended coherent flame model
EU	European union
FSD	Flame surface density
GHG	Greenhouse gas
HTC	Heat transfer coefficient
ICE	Internal combustion engine
IMEP	Indicated mean effective pressure

ISSIM	Imposed stretch spark-ignition model
KI	Knock intensity
KLSA	Knock limiting spark-advance
LES	Large-eddy simulation
MON	Motor octane number
ON	Octane number
PDF	Probability density function
PFI	Port fuel injection
PRF	Primary reference fuel
RANS	Reynolds averaged Navier-Stokes
RON	Research octane number
ROP	Reference operating point
SFC	Specific Fuel Consumption
SGS	Sub-grid scale
TDC	Top-dead center
TKI	Tabulated kinetics of ignition
TRF	Toluene reference fuel

List of Figures

1.1	Contribution of each source sector to GHG emissions (source Eurostat).	14
1.2	Evolution of the legislation in terms of CO_2 emissions (per vehicle).	14
1.3	P-V diagram of an ideal Otto cycle in comparison to an actual engine cycle.	15
1.4	Principle of downsized engines.	16
1.5	Specific Fuel Consumption map of the 1.5L TSI evo by VW. Re-printed from [35].	17
1.6	Illustration of a knock event in a spark-ignition engine.	17
1.7	Illustration of rumble in a spark-ignition engine.	18
1.8	Erosion of the piston due to knocking combustion	19
2.1	Auto-ignition delay τ_{AI} for iso-octane under various operating conditions. Re-printed from Mehl et al. [84].	27
2.2	Illustration of single-stage and two-stage auto-ignition for iso-octane in air at stoichiometric conditions and $P = 15$ atm. (a) and (b) adapted from Yoo et al. [133]. (c) re-printed from Mehl et al. [84].	28
2.3	Modes of auto-ignitive reaction front propagation identified in the $\xi - \epsilon$ diagram of Bradley. Adapted from Bradley et al. [13].	32
2.4	Visualization of auto-ignition spots in the end-gas by laser-induced fluorescence (LIF). Re-printed from Schiessl et al. [117]	34

LIST OF FIGURES

2.5	High speed images of the combustion in a normal cycle and a knocking cycle, and the impact of the auto-ignition on the in-cylinder pressure signal. Re-printed from Kawahara et al. [65].	35
2.6	Oscillations in the local in-cylinder pressure caused by a transition of auto-ignition mode from deflagration to detonation. Re-printed from Robert et al. [113].	37
2.7	Cycle to cycle variations in the local pressure signal recorded experimentally (brown) and by LES (black) at fixed operating conditions. Re-printed from Robert et al. [112].	38
3.1	Conceptual representation of the LES on the turbulent energy spectrum plotted as a function of the wave number.	44
3.2	Illustration of typical length scales in a piston engine, relatively to the scales resolved on typical LES meshes (grey square).	47
3.3	Premixed turbulent combustion diagram by Peters [100]. l_t is the integral length scale, l_f the laminar flame thickness (noted δ_L in the rest of the manuscript), u' is the turbulent velocity and S_L is the laminar flame speed. The flame structure in a spark-ignition engine can be estimated to be mostly located in the flamelet regime (Blue area). Re-printed from Richard [110].	49
3.4	Principle of the flame front filtering as in ECFM-LES. Re-printed from [110].	51
3.5	Summary of the variables transported in the fresh and burned gases.	54
3.6	Schematic of the resolved and sub-grid scale contributions in the FSD equation.	56
3.7	Illustration of the turbulence/flame interaction: only vortices whose dimension is larger than $\hat{\Delta}$ manage to wrinkle the flame front. Reprinted from [110].	58
3.8	Ignition process from spark-discharge to turbulent premixed flame propagation. Reprinted from [55].	59
3.9	Simplified scheme of the spark ignition system. Reprinted from [110].	59
3.10	Schematic representation of the model. Re-printed from [112].	63
4.1	Schematic of the RENAULT 1.2 TCe 115 engine. Only Cylinder 1 is simulated. The dotted lines delineates the computational domain.	69
4.2	Computational domain for Cylinder 1 with the combustion chamber, intake and exhaust ports, and the intake manifold.	69
4.3	Top view of <i>Cylinder</i> 1. The spark-plug is located centrally, the fuel injector is situated laterally on the intake side between the intake valves.	70
4.4	Intake and Exhaust valve lift. The overlap reaches 88 crank angle.	71
4.5	Visualization of the direct-injection 12 CA after the start of injection. The fuel is propelled against the bowl-shape piston and redirected towards the spark-plug.	72

LIST OF FIGURES

4.6	Inlet and Outlet pressure signals from 0D-1D simulation. Exhaust Valves Opening (EVO) and Closure (EVC) are highlighted as well as Intake Valves Opening (IVO) and Closure (IVC).	72
5.1	Schematic of the weak thermal coupling as implemented in CONVERGE CFD.	77
5.2	View of the solid parts of the computational domain used in the CHT calculation.	78
5.3	Cut view of the computational domain.	79
5.4	Trapped mass inside the combustion chamber right before spark-timing for Cycles 1, 2 and 3.	83
5.5	Temporal evolution of the mean in-cylinder pressure signals at ROP for the RANS simulation of combustion used in the CHT approach.	84
5.6	Top view of the combustion chamber. Indicated are the positions of the four thermocouples, set at 1.5 to 2 mm ahead of the cylinder-roof.	85
5.7	CHT vs. Experiment: Local temperature predicted/measured at each of the four thermocouples location.	85
5.8	Temperature distribution along surfaces predicted by the RANS-CHT calculation.	87
6.1	View of the LES tetrahedric mesh during the intake stroke.	91
6.2	Flow rate profile of the injected fuel.	94
6.3	Schematic of the rebound condition implemented in AVBP.	94
6.4	Target (0D-1D simulation) and actual (NSCBC) pressure signals recorded at the inlet boundary. Exhaust Valves Opening (EVO) and Closure (EVC) are highlighted as well as Intake Valves Opening (IVO) and Closure (IVC).	96
6.5	Instantaneous ν_t/ν field for Cycle 3 at four different instants. During the intake stroke, at BDC, during the compression stroke and at combustion TDC. Intake (exhaust) valves are on the left (right) respectively.	97
6.6	Total and resolved flame surface for Cycle 3.	98
6.7	Temporal evolution of the in-cylinder pressure signals at ROP, for the LES cycles compared with the 500 experimental cycles.	99
6.8	P_{max} over CAP_{max} (Matekunas diagram), for the 30 LES cycles compared with the 500 experimental cycles.	100
6.9	Range of the experimental cycles into sub-sets of 30 cycles.	101
6.10	Ratio Set_{max}/Set_{min} of the percentage of knocking cycle, as a function of the number of cycles per sub-set.	103

LIST OF FIGURES

6.11 Spark-timing sweep methodology. I = Intake stroke, C = Compression stroke, Comb = Combustion, E = Exhaust stroke. Only the combustion phases are re-computed in parallel. (Adapted from [87]).	104
6.12 <i>IMEP</i> of cycle i versus <i>IMEP</i> of cycle $i-1$	105
6.13 LES in-cylinder pressure signals for the 30 cycles at each of the five spark-timings.	106
6.14 Knock intensity predicted by LES as a function of spark-timing. 0 CA corresponds to combustion TDC.	107
6.15 Percentage of knocking cycles predicted by LES as a function of spark-timing. 0 CA corresponds to combustion TDC	107
7.1 Top view of the combustion chamber. Position of 18 numerical probes inside the combustion chamber.	113
7.2 KI (by MAPO analysis) predicted from the 18 numerical probes for Cycle 5 at ROP.	113
7.3 KI resulting from two different methods of pressure signal analysis: MAPO and KPPK.	114
7.4 Visualization of cool flame and main auto-ignition (main AI) on the space integral of the reaction rate $\int \tilde{\omega}_c^{AI} dV$, for LES Cycle 5 at ROP.	116
7.5 Space integral of the reaction rate $\int \tilde{\omega}_c^{AI} dV$ and temporal evolution of the maximum to instantaneous spatially averaged mean cylinder pressure P_{max}/P_{mean} , for LES Cycle 5 at ROP.	117
7.6 Space integral of the reaction rate $\int \tilde{\omega}_c^{AI} dV$ and temporal evolution of \tilde{c}_{AI}^{max} , for LES Cycle 5 at ROP.	117
7.7 Space integral of the reaction rate $\int \tilde{\omega}_c^{AI} dV$ before and after thresholding.	118
7.8 Space integral of the reaction rate $\int \tilde{\omega}_c^{AI} dV$ and temporal evolution of the maximum to instantaneous spatially averaged mean cylinder pressure P_{max}/P_{mean} , for LES Cycle 17 at ROP.	118
7.9 Comparison of CKI levels before and after thresholding, applied to each of the 30 LES cycles at ROP.	119
7.10 Schematic of the classification between normal (non-knocking) and knocking cycles. KI_T is the maximum acceptable KI value set by the operator.	120
7.11 Percentage of LES knocking cycles as a function of the spark-timing respectively based on KI (by MAPO analysis) and CKI, using maximum acceptable limits $KI_T = 0.159 \text{ bars}$ and $CKI_T = 0.01\%$. 0 °CA corresponds to combustion TDC.	121
7.12 Percentage of knocking cycles per ST based on CKI, using various CKI_T	122

LIST OF FIGURES

7.13	CKI (left graph) and KI by MAPO analysis (right graph) respectively for each of the 30 LES cycles for each of the five spark-timings, distributed as a function of the spark-timing. 0 °CA corresponds to combustion TDC.	122
7.14	CKI correlated to KI (by MAPO analysis). Each circle corresponds to an individual cycle (each of the 30 LES cycles for each of the five spark-timings are represented). .	123
8.1	Illustration of the CCV observed in the LES results at ROP based on the temporal evolution of (a) the in-cylinder pressure signal and (b) the fuel mass fraction	126
8.2	Estimation of CA_{50} based on the temporal evolution of the fuel mass fraction Y_F . .	127
8.3	Scatter plot of CKI as a function of CA_{50} for the 30 LES cycles at ROP. Each diamond represents one LES cycle.	128
8.4	Temporal evolution of the mean in-cylinder fresh gases temperature for the 30 simulated cycles at ROP, coloured by their respective CA_{50}	128
8.5	Scatter plot of the CA_{50} as a function of the CA_{02} for the 30 LES cycles at ROP. Each diamond represents one LES cycle. Indicated is the correlation coefficient of Bravais-Pearson $R_{(CA_{50}, CA_{02})}$	129
8.6	Correlation between CA_{02} and different global parameters. Indicated are the correlation coefficients of Bravais-Pearson $R_{X,Y}$	130
8.7	Definition of the conditionally averaged cycle C_{early} (respectively C_{late}) from the 20% earliest (respectively latest) CA_{02} cycles.	132
8.8	Illustration of the cut planes through the spark-plug MID_{XZ} and MID_{YZ} . Intake ports are on the left of the figure, exhaust ports on the right.	132
8.9	Magnitude field of the 3D resolved velocity projected in plane MID_{XZ} for the two conditionally averaged cycles taken at 6 °CA before combustion TDC (0.7 °CA before spark-timing).	133
8.10	Field of the laminar flame speed in the cut plane MID_{XZ} for the two conditionally averaged cycles taken at 6 °CA before combustion TDC (0.7 °CA before spark-timing).	134
8.11	Field of the laminar flame speed in the cut plane MID_{XY} for the two conditionally averaged cycles taken at 6 °CA before combustion TDC (0.7 °CA before spark-timing). The cross indicates the center of the spark-plug.	135
8.12	PDF of the laminar flame speed and the resolved velocity magnitude conditioned to the fresh gases ahead of the premixed flame front. PDF were built from in-cylinder conditions at 3.3 °CA after the spark-timing	136
8.13	Temporal evolution of the total flame surface during the first instants of the premixed flame propagation for the 6 earliest (respectively latest) CA_{02} cycles.	137

LIST OF FIGURES

8.14	Temporal evolution of the productive/destructive source terms in the FSD equation for the 6 fastest (respectively slowest) combustion cycles used to build C_{early} (respectively C_{late}).	139
8.15	Scatter plot of CKI as a function of CA_{50} for each of the 30 LES cycles at each of the five spark-timings. Each symbol represents one LES cycle.	140
8.16	Mean CKI (left ordinate axis) as a function of the mean CA_{50} for each of the five spark-timings. Indicated on the right ordinate axis is the gap between the maximum to minimum CA_{50} per spark-timing.	141
8.17	Scatter plot of CKI as a function of $\mathcal{Y}_F^u(t = t_{AI})$. Each symbol represents one simulated knocking cycle. Indicated is the correlation coefficient of Bravais-Pearson $R_{(CKI, \mathcal{Y}_F^u(t=t_{AI}))}$.	142
8.18	Top views of the premixed flame and auto-ignition fronts for Cycle 11 at ST = -11°CA, $C_{11}^{-9.3}$. The premixed flame front is materialized by an iso-contour $\tilde{c}_\Sigma = 0.7$ and coloured by the flame surface density, while the auto-ignition front is materialized by an iso-contour $\tilde{c}_{AI} = 0.3$, and coloured in green. 0 °CA corresponds to combustion TDC. Intake valves are on the left, exhaust valves on the right.	143
8.19	Illustration of the cyclic variability in the premixed flame shape based on two individual iso- $\mathcal{Y}_F^u(t = t_{AI})$ cycles, taken at a few crank angles before the onset of auto-ignition. Shown are iso-surfaces of $\tilde{c}_\Sigma = 0.5$. On each picture the intake is on the left and the exhaust on the right.	144
8.20	Schematic of the combustion chamber partitioning in sections of equivalent angle θ .	145
8.21	Polar representation of the distribution of \tilde{m}_i^u along the cylinder using three different partitioning. The length of the bar directly indicates the level of \tilde{m}_i^u in the section i . On the Figures the intake is on the left side and the exhaust on the right side.	146
8.22	Distribution of \tilde{m}_i^u along the cylinder using three different partitioning.	147
8.23	Scatter plot of CKI as a function of $\mathcal{Y}_F^u(t = t_{AI})$. Each symbol represents one LES knocking cycle. Highlighted in blue is the set of cycles under analysis.	148
8.24	Total mass of end-gas m^u at the onset of main auto-ignition for the six individual cycles under analysis. Cycles are listed by decreasing CKI.	149
8.25	Distribution of \tilde{m}_i^u for each of the 6 individual cycles under analysis. The bold dotted circle corresponds to $\overline{\tilde{m}_i^u}$ in the cycle.	150
8.26	Illustration of the notion of end-gas pockets based on cycle $C_{11}^{3.91\%}$. There are five pockets in this cycle, highlighted in green.	151
8.27	Distribution of \tilde{m}_i^u for the 6 individual cycles under analysis. Highlighted are the location of the first auto-ignition spots. Multiple circles on a cycle means that auto-ignition first appears simultaneously in different locations.	153

LIST OF FIGURES

8.28	CKI and mass of fresh gases consumed m_{AI_1} by the first auto-ignition spots for the six individual cycles under analysis. Cycles are plotted by decreasing CKI.	154
8.29	Distribution of \check{m}_i^u for the 6 individual cycles under analysis, coloured by the auto-ignition delay $\tau_{AI,i}$ in the sections.	155
8.30	Distribution of \check{m}_i^u for cycle $C_{11}^{3.91\%}$, coloured by (a) the auto-ignition delay $\tau_{AI,i}$ and (b) the fraction of end-gas consumed by auto-ignition $f_{AI,i}$ in the sections.	157
8.31	Distribution of \check{m}_i^u for the two smallest CKI cycles, coloured by the auto-ignition delay $\tau_{AI,i}$ (left Figures) and the fraction of end-gas consumed by auto-ignition $f_{AI,i}$ (right Figures) in the sections.	158
8.32	Distribution of \check{m}_i^u for the three intermediate CKI cycles, coloured by the main auto-ignition delay $\tau_{AI,i}$ (left Figures) and the fraction of end-gas consumed by auto-ignition $f_{AI,i}$ (right) in the sections.	160
8.33	Distribution of the ensemble average $\langle \check{m}_i^u \rangle$ coloured by its standard deviation $\sigma_{\check{m}_i^u}$	162
8.34	Statistical end-gas distribution along the cylinder with each section coloured by (a) the ensemble averaged auto-ignition delay and (b) the ensemble averaged mass fraction of end-gas consumed by auto-ignition.	163
8.35	Zoom on the direct-injection cavity.	163

LIST OF FIGURES

List of Tables

3.1	Modelling of unresolved convection terms in the spatially filtered Navier-Stokes equations. $\bar{\rho}$ is the filtered density, \tilde{u}_i is the component of the filtered velocity vector $\tilde{\mathbf{u}}$ in the direction i , \tilde{Y}_k is the filtered mass fraction of species k , e_t is the total energy, \bar{P} is the filtered pressure, ν_t is the turbulent kinematic viscosity to be modelled, \tilde{S}_{ij}^* is the trace-less symmetric part of the strain rate tensor, k_{sgs} is the SGS kinetic energy, C_p is the specific heat capacity, Pr_t and Sc_t are respectively the turbulent Prandtl and Schmidt numbers.	48
4.1	Main characteristics of the RENAULT 1.2 TCe 115 engine.	68
4.2	Operating conditions at the reference operating point.	71
5.1	Summary of the RANS models used in the simulation.	80
5.2	Convection boundary conditions imposed on the external limits of the solid domain.	81
5.3	Boundary conditions imposed on the external limits of the solid domain. . . .	82
6.1	Relaxation coefficients imposed at the inlet and outlet boundaries.	92
6.2	Incoming species mass fractions imposed for the LES at the inlet and outlet boundaries of the domain.	93
6.3	Set of parameters used for the LES.	95
6.4	Set of combustion models for the LES.	95

LIST OF TABLES

6.5 $\langle IMEP \rangle$ and $COV(IMEP)$ at ROP based on the LES and experimental samples. . . 101

6.6 $\langle CAP_{max} \rangle$ and $COV(CAP_{max})$ at ROP based on the LES and experimental samples. 102

6.7 Maximum knock intensity KI_{max} at ROP based on the LES and experimental samples.102

6.8 Percentage of knocking cycles at ROP based on the LES and experimental samples. . . 103

8.1 Notation for the six individual cycles with $5\% < \mathcal{Y}_F^u(t = t_{AI}) < 5.5\%$. Cycles are listed by decreasing CKI. 147

8.2 Proportion of the total mass of end-gas m^u contained in the largest pocket of end-gas for each of the six cycles under analysis. Cycles are listed by decreasing CKI. 151

Bibliography

- [1] P. G. Aleiferis, Y. Hardalupas, A. M. K. P. Taylor, K. Ishii, and Y. Urata. Flame chemiluminescence studies of cyclic combustion variations and air-to-fuel ratio of the reacting mixture in a lean-burn stratified-charge spark-ignition engine. *Combustion and Flame*, 136:72–90, 2004. 38, 129, 130
- [2] T. Alger, B. Mangold, C. Roberts, and J. Gingrich. The interaction of fuel anti-knock index and cooled egr on engine performance and efficiency. *SAE Int. J. Engines*, 5(3):1229–1241, 2012. 39
- [3] ASTM. *Annual Book of ASTM Standards, 05.05 - D2699 & D2700*. 2017. 26
- [4] F.A. Ayala, M.D. Gerty, and J.B. Heywood. Effects of combustion phasing, relative air-fuel ratio, compression ratio, and load on si engine efficiency. *SAE Technical Paper*, 2006. 140
- [5] F.A. Ayala, M.D. Gerty, and J.B. Heywood. Octane numbers of ethanol- and methanol-gasoline blends estimated from molar concentrations. *Energy & Fuels*, 24(12):6576–6585, 2006. 40
- [6] L. Bates, D. Bradley, G. Paczko, and N. Peters. Engine hot spots: Modes of auto-ignition and reaction propagation. *Combustion and Flame*, 166:80–85, 2016. 32
- [7] B. Bäuerle, F. Hoffmann, F. Behrendt, and J. Warnatz. Detection of hot spots in the end gas of an internal combustion engine using two-dimensional lif of formaldehyde. *25th Symposium (International) on Combustion*, pages 135–141, 1994. 33, 34
- [8] A. Bertola, J. Stadler, T. Walter, P. Wolfer, C. Gossweiler, and M. Rothe. Pressure indication during knocking conditions. *7th International AVL Symposium on Internal Combustion Diagnostics*, 2006. 36

BIBLIOGRAPHY

- [9] M. Boger, D. Veynante, H. Boughanem, and A. Trouv'e. Direct numerical simulation analysis of flame surface density concept for large eddy simulation of turbulent premixed combustion. *27th Symposium (International) on Combustion/The combustion Institute*, pages 917–925, 198. 55
- [10] P. Boudier, S. Henriot, T. Poinsot, and T. Baritaud. A model for turbulent flame ignition and propagation in spark-ignition engines. *Symposium (International) on Combustion*, 24(1):503–510, 1992. 50
- [11] D. Bradley. Autoignitions and detonations in engines and ducts. *Phil. Trans. R. Soc. A*, 370:689–714, 2012. 27, 34, 36
- [12] D. Bradley and R.A. Head. Engine auto-ignition: The relationship between octane numbers and auto-ignition delay times. *Combustion and Flame*, 147:171–184, 2006. 27
- [13] D. Bradley, C. Morley, X. J. Gu, and D. R. Emerson. Amplified pressure waves during autoignition: Relevance to cai engines. *SAE International Journal*, 2002. 32, 144, 173
- [14] G. Brecq, J. Belettre, and M. Tazerout. Experimental determination of knock in gas si engine. *SAE Int. J. of Engines*, 2001. 35, 102, 113
- [15] A. A. Burluka, K. Liu, C. G. W. Sheppard, A. J. Smallbone, and R. Wooley. The influence of simulated residual and no concentrations on knock onset for prfs and gasolines. *SAE International Journal*, 2004. 27
- [16] F. Charlette, C. Meneveau, and D. Veynante. A power-law flame wrinkling model for LES of premixed turbulent combustion part I: Non-dynamic formulation and initial tests. *Combustion and Flame*, 131(1), 2002. 58
- [17] Y. Chen and R. Raine. A study on the influence of burning rate on engine knock from empirical data and simulation. *Combustion and Flame*, 162(5), 2015. 38
- [18] S. Chevillard, O. Colin, J. Bohbot, M. Wang, E. Pomraning, and P.K. Senecal. Advanced methodology to investigate knock for downsized gasoline direct injection engine using 3D RANS simulations. *SAE Technical Paper*, 2017. 36, 115, 116, 124, 164, 168
- [19] O. Colin. *Simulations aux grandes échelles de la combustion turbulente prémélangée dans les statoréacteurs*. 2000. 95
- [20] O. Colin, A. Benkenida, and C. Angelberger. 3d modeling of mixing, ignition and combustion phenomena in highly stratified gasoline engines. *Oil & Gas Science and Technology Rev. IFP*, 58(1):47–62, 2003. 50, 80
- [21] O. Colin, F. Ducros, D. Veynante, and T. Poinsot. A thickened flame model for large eddy simulations of turbulent premixed combustion. *Physics of Fluids*, 12(7):1843–1863, 2000. 50, 52, 57
- [22] O. Colin, A. Pires da Cruz, and S. Jay. Detailed chemistry-based anti-ignition model including low temperature phenomena applied to 3-d engine calculations. *Proceedings of the Combustion Institute*, 30:2649–2656, 2005. 30, 64

BIBLIOGRAPHY

- [23] O. Colin and K. Truffin. A spark ignition model for large eddy simulation based on an fsd transport equation (ISSIM-LES). *Proceedings of the Combustion Institute*, 33(2):3097–3104, 2010. 59, 62, 80, 95
- [24] E Corti, N. Cavina, A. Cerofolini, C. Forte, G. Mancini, D. Moro, F. Ponti, and V. Ravaglioli. Transient spark advance calibration approach. *Energy Procedia*, 45:967–976, 2014. 39
- [25] E Corti and C. Forte. Combination of in-cylinder signal analysis and CFD simulation for knock detection purposes. *SAE Int. J. Engines*, 2009. 36, 112
- [26] E Corti and C. Forte. Statistical analysis of indicating parameters for knock detection purposes. *SAE Int. J. Engines*, 2009. 35, 36
- [27] P. I. Crumpton, J. A. MacKenzie, and K. W. Morton. Cell vertex algorithms for the compressible navier-stokes equations. *Journal of Computational Physics*, 109:1–15, 1993. 90
- [28] H.J. Curan, P. Gaffuri, W.J. Pitz, and C.K. Westbrook. A comprehensive modeling study of n-heptane oxidation. *Proceedings of the Combustion Institute*, 114:149–177, 1998. 29
- [29] H.J. Curan, P. Gaffuri, W.J. Pitz, and C.K. Westbrook. A comprehensive modeling study of iso-octane oxidation. *Proceedings of the Combustion Institute*, 129:253–280, 2002. 28, 29
- [30] A. D’Adamo, S. Breda, S. Iaccarino, F. Berni, S. Fontanesi, B. Zardin, and M. Borghi. Development of a RANS-based knock model to infer the knock probability in a research spark-ignition engine. *SAE Int. J. Engines*, 2017. 36
- [31] C Dahnz, K-M. Han, U. Spicher, M. Magar, R. Schiessl, and U. Maas. Investigation on pre-ignition in highly supercharged si engines. *SAE Int. J. Engines*, 2010. 18
- [32] R. Diwakar. Assessment of the ability of a multidimensional computer code to model combustion in a homogeneous-charge engine. *SAE Technical Paper*, 1984. 95
- [33] A.M. Douaud and P. Eyzat. Four octane number method for predicting the anti-knock behavior of fuels and engines. *SAE Paper*, 1978. 29
- [34] G. Edgar. Measurement of knock characteristics of gasoline in terms of a standard fuel. *Industrial & Engineering Chemistry*, 19(1):145–146, 1927. 26
- [35] F. Eichler, W. Demmelbauer-Ebner, J. Theobald, B Stiebels, H. Hoffmeyer, and M. Kreft. The new ea211 tsi evo from volkswagen. *37 Internationales Wiener Motorensymposium*, 2016. 17, 173
- [36] H.J. Emeleus. The spectra of the phosphorescent flames of carbon disulphide and ether. *Journal of the Chemical Society*, pages 2948–2951, 1926. 28
- [37] H.J. Emeleus. The light emission from the phosphorescent flames of ether, acetaldehyde, propaldehyde, and hexane. *Journal of the Chemical Society*, pages 1733–1739, 1929. 28

BIBLIOGRAPHY

- [38] B. Enaux, V. Granet, O. Vermorel, C. Lacour, C. Pera, C. Angelberger, and T. Poinsot. LES study of cycle-to-cycle variations in a spark ignition engine. *Proceedings of the Combustion Institute*, 33(2):3115–3122, 2011. 38, 94, 129, 130
- [39] S. Fontanesi, G. Cicalese, G. Cantore, and A. D’Adamo. Integrated in-cylinder/CHT analysis for the prediction of abnormal combustion occurrence in gasoline engines. 2014. 76, 86
- [40] S. Fontanesi, G. Cicalese, A. d’Adamo, and G. Cantore. A methodology to improve knock tendency prediction in high performance engines. *Energy Procedia*, 45:769–778, 2014. 76
- [41] S. Fontanesi, G. Cicalese, A. D’Adamo, and G. Pivetti. Validation of a CFD methodology for the analysis of conjugate heat transfer in a high performance si engine. 2011. 86
- [42] S. Fontanesi, G. Cicalese, and A. Tiberi. Combined in-cylinder/CHT analysis for the accurate estimation of the thermal flow field of a high performance engine for sport car applications. 2013. 86
- [43] S. Fontanesi, A. D’Adamo, S. Paltrinieri, G. Cantore, and C. Rutland. Assessment of the potential of proper orthogonal decomposition for the analysis of combustion ccv and knock tendency in a high performance engine. 2013. 78
- [44] S. Fontanesi, S. Paltrinieri, A. D’Adamo, G. Cantore, and C. Rutland. Knock tendency prediction in a high performance engine using LES and tabulated chemistry. 6(1), 2013. 29
- [45] L. Francqueville and J-B. Michel. On the effects of egr on spark-ignited gasoline combustion at high load. *SAE International Journal Engines*, 2014. 39
- [46] B.M. Gautier, D.F. Davidson, and R.K. Hanson. Shock tube determination of ignition delay times in full-blend and surrogate fuel mixtures. *Combustion and Flame*, 139:300–311, 2004. 29
- [47] M. Germano, U Piomelli, P Moin, and W.H Cabot. A dynamic subgrid-scale eddy viscosity model. *Physics of Fluids*, 3(7):1760–1765, 1991. 49
- [48] O. Gicquel, N. Darabiha, and D. Thevenin. Laminar premixed hydrogen/air counterflow flame simulations using flame prolongation of idlm with differential diffusion. *Proceedings of the Combustion Institute*, 28:1901–1908, 2000. 30
- [49] N. Gourdain, L. Gicquel, M. Montagnac, M. Vermorel, O. and Gazaix, G. Staffelbach, M. Garcia, J. Boussuge, and T. Poinsot. High performance parallel computing of flows in complex geometries - part 1: Methods. *Computational Science & Discovery*, 2, 2009. 90
- [50] N. Gourdain, L. Gicquel, M. Montagnac, M. Vermorel, O. and Gazaix, G. Staffelbach, M. Garcia, J. Boussuge, and T. Poinsot. High performance parallel computing of flows in complex geometries - part 2: Applications. *Computational Science & Discovery*, 2(1), 2009. 90

BIBLIOGRAPHY

- [51] V. Granet, O. Vermorel, C. Lacour, B. Enaux, V. Dugué, and T. Poinso. Large-eddy simulation and experimental study of cycle-to-cycle variations of stable and unstable operating points in a spark ignition engine. *Combustion and Flame*, 159:1562–1575, 2012. 39, 94, 99
- [52] X. J. Gu, D. R. Emerson, and D. Bradley. Modes of reaction front propagation from hot spots. *Combustion and Flame*, 133:63–74, 2003. 31, 32
- [53] M.P. Halstead, L.J. Kirsch, and C.P. Quinn. The auto-ignition of hydrocarbon fuels at high temperatures and pressures - fitting of a mathematical model. *Combustion and Flame*, 30:45–60, 1977. 29
- [54] Z. Han and R. D. Reitz. A temperature wall function formulation for variable-density turbulent flows with application to engine convective heat transfer modeling. *Int. J. Heat Mass Transfer*, 40(3):613–625, 1997. 80
- [55] N. Hayashi, A. Sugiura, Y. Abe, and K. Suzuki. Development of ignition technology for dilute combustion engines. *SAE International Journal*, 2017. 59, 174
- [56] A. Hettinger, A. Kulzer, and U. Spicher. Higher specific load-increasing knock risk evaluation of measures for knock reduction using multiple pressure indication. *Int. Symp. Combust. Diag. (9)*, 2010. 39
- [57] H. Hirooka, S. Mori, and R. Shimizu. Effects of high turbulence flow on knock characteristics. *SAE Int. J. Engines*, 2012. 38
- [58] C. W. Hirt, A. A. Amsden, and J. L. Cook. An arbitrary lagrangian-eulerian computing method for all flow speeds. *Journal of Computational Physics*, 131(4):371–385, 1974. 90
- [59] B. Hoepke, S. Jannsen, E. Kasseris, and W. K. Cheng. Egr effects on boosted si engine operation and knock integral correlation. *SAE Int. J. Engines*, 5(2), 2012. 39
- [60] N. Iafrate. Phd. simulation aux grandes echelles diphasiques dans les moteurs downsizés à allumage commandé. 2016. 93
- [61] S. Jay and O. Colin. A variable volume approach of tabulated detailed chemistry and its applications to multidimensional engine simulations. *Proceeding of the Combustion Institute*, 33:3065–3072, 2011. 30
- [62] J.C.P. Jones, J.M. Spelina, and J. Frey. Optimizing knock thresholds for improved knock control. *Int. J. of Engine Research*, 15:123–132, 2014. 35
- [63] S.A. Kaiser, M. Schild, and C. Schulz. Thermal stratification in an internal combustion engine due to wall heat transfer measured by laser-induced fluorescence. *Proceedings of the Combustion Institute*, pages 2911–2919, 2013. 33, 86, 152
- [64] E. Kasseris and J. Heywood. Charge cooling effects on knock limits in si di engines using gasoline/ethanol blends: Part 2-effective octane numbers. *SAE Int. J. Fuels Lubr.*, 5(2):844–854, 2012. 40

BIBLIOGRAPHY

- [65] N. Kawahara, E. Tomita, and M. Kanti Roy. Visualization of autoignited kernel and propagation of pressure wave during knocking combustion in a hydrogen spark-ignition engine. *SAE Int. J.*, 2009. 35, 36, 39, 174
- [66] N. Kawahara, E. Tomita, and Y. Sakata. Auto-ignited kernels during knocking combustion in a spark-ignition engine. *Proceedings of the Combustion Institute*, 31(2):2999–3006, 2007. 33, 34, 39
- [67] J. Klimstra. The knock severity index - a proposal for a knock classification method. *SAE Int. J. Fuels Lubr.*, 1984. 36
- [68] V. Knop, J.B. Michel, and O. Colin. On the use of a tabulation approach to model auto-ignition during flame propagation in si engines. *Applied Energy*, 88:4968–4979, 2011. 30
- [69] H. Kobayashi and H. Kawazoe. Flame instability effects on the smallest wrinkling scale and burning velocity of high-pressure turbulent premixed flames. *Proceedings of the Combustion Institute*, 28(1):275–382, 2000. 39
- [70] G. König, R. R. Maly, D. Bradley, A. K. C. Lau, and C. G. W. Sheppard. Role of exothermic centres on knock initiation and knock damage. *SAE Technical Paper*, 1990. 31
- [71] G. König and C. G. W. Sheppard. End gas autoignition and knock in a spark ignition engine. *SAE Technical Paper*, 1990. 18, 33, 36, 39
- [72] M. A. Kucheba, K. N. C. Bray, E. Ikonou, and A. D. Gosman. Calculations and measurements of the temperature field in a motored engine and their implications for knock. *SAE Technical Paper*, 1989. 33
- [73] F.-A. Lafossas, M. Castagne, J.P. Dumas, and S. Henriot. Development and validation of a knock model in spark ignition engines using a CFD code. *SAE Technical Paper*, 2002. 29
- [74] O. Laget, B. Reveille, L. Martinez, Truffin K., C Habchi, and C. Angelberger. LES calculations of a four stroke engine. *SAE Technical Paper*, 2011. 68
- [75] L. Landry, F. Halter, F. Foucher, E. Samson, and C. Mounaïm-Rousselle. Effect of pressure and dilution on flame front displacement in boosted spark-ignition engine combustion. *SAE Int. J. Fuels Lubr.*, 1(1), 2009. 39
- [76] B. E. Launder and D. B. Spalding. The numerical computation of turbulent flows. *Computer Methods in Applied Mechanics and Engineering*, 3(2):269–289, 1974. 80
- [77] P.D. Lax and B. Wendroff. Difference schemes for hyperbolic equations with high order accuracy. *Communications on Pure and Applied Mathematics*, pages 381–398, 1964. 94
- [78] G. Lecocq, S. Richard, J-B. Michel, and L. Vervisch. A new LES model coupling flame surface density and tabulated kinetics approaches to investigate knock and pre-ignition in piston engines. *Proceedings of the Combustion Institute*, 33(2):3105–3114, 2011. 30

BIBLIOGRAPHY

- [79] M. Leguille, F. Ravet, J. Le Moine, E. Pomraning, K. Richards, and P. K. Senecal. Coupled fluid-solid simulation for the prediction of gas-exposed surface temperature distribution in a si engine. *SAE Technical Paper*, 2011. 21, 76
- [80] J.C Livengood and P.C Wu. Correlation of autoignition phenomena in internal combustion engines and rapid compression machines. *Proceedings of the Combustion Institute*, 5:347–356, 1955. 29
- [81] G. M. Makhviladze and D. I Rogatykh. Non uniformities in initial temperature and concentration as a cause of explosive chemical reactions in combustible gases. *Combustion and Flame*, 87:347–356, 1991. 32
- [82] A. Manz. *Modeling of End-Gas Autoignition for Knock Prediction in Gasoline Engine*. Logos Verlag Berlin, 2016. 38
- [83] M. Mehl, J.Y. Chen, W.J. Pitz, Sarathy S.M., and C.K. Westbrook. Application toward a reduced surrogate mechanism for CFD engine modeling. *Energy & Fuels*, 25:5215–5223, 2011. 29
- [84] M. Mehl, W.J. Pitz, C.K. Westbrook, and H.J. Curran. Kinetic modeling of gasoline surrogate components and mixtures under engine conditions. *Proceedings of the Combustion Institute*, 33:193–200, 2011. 27, 28, 29, 173
- [85] M. Metghalchi and J.C. Keck. Burning velocities of mixtures of air with methanol, isooctane and indolene at high pressure and temperature. *Combustion and Flame*, 48:191–210, 1982. 52
- [86] C. D. Miller. Roles of detonation waves and autoignitions in si engines, knock as shown by photographs taken at 40,000 and 200,000 frames per second. *SAE Q. Trans.*, 1:99–143, 19477. 18
- [87] A. Misdariis. Phd, schémas cinétiques réduits et couplage thermique pour les simulations aux grandes échelles du cliquetis dans les moteurs à piston. 2015. 20, 104, 167, 176
- [88] A. Misdariis, A. Robert, O. Vermorel, S. Richard, and T Poinso. Numerical methods and turbulence modeling for LES of piston engines: Impact on flow motion and combustion. *Oil & Gas Science and Technology - Rev IFP Energies Nouvelles*, 69(1):83–105, 2012. 49, 94
- [89] A. Misdariis, O. Vermorel, and T. Poinso. A methodology based on reduced schemes to compute autoignition and propagation in internal combustion engines. *Proceedings of the Combustion Institute*, pages 4304–4312, 2014. 29
- [90] A. Misdariis, O. Vermorel, and T. Poinso. LES of knocking in engines using dual heat transfer and two-step reduced schemes. *Combustion and Flame*, 162(11):4304–4312, 2015. 77, 80
- [91] V. Moureau, G. Lartigue, Y. Sommerer, C. Angelberger, O. Colin, and T. Poinso. Numerical methods for unsteady compressible multi-component reacting flows on fixed and moving grids. *Journal of Computational Physics*, 202(2):710–736, 2005. 90

BIBLIOGRAPHY

- [92] F. Nicoud, H.B. Toda, O Crabit, G. Balarac, S. Bose, and J. Lee. Using singular values to build a subgrid-scale model for large eddy simulations. *Physics of Fluids, American Institute of Physics*, 23(8):85–106, 2011. 49
- [93] A. K. Oppenheim. Dynamic features of combustion. *Phil. Trans. R. Soc. Lond., A* 315:451–508, 1985. 31
- [94] N. Ozdor, M. Dulger, and E. Sher. Cyclic variability in spark ignition engines, A literature survey. *SAE Technical Paper*, 1994. 129
- [95] J. Pan and C. G. W. Sheppard. A theoretical and experimental study of the modes of end gas autoignition leading to knock in s.i. engines. *SAE Technical Paper*, 1994. 31, 32
- [96] J. Pan, C. G. W. Sheppard, A. Tindall, M. Berzins, S. V. Pennington, and J. M. Ware. End gas inhomogeneity, autoignition and knock. *SAE Technical Paper*, 1998. 33, 36, 112
- [97] C. Patil, S. Varade, and S. Wadkar. A review of engine downsizing and its effects. *International Journal of Current Engineering and Technology*, 2017. 16
- [98] C. Pera, V. Knop, S. Chevillard, and J. Reveillon. Effects of residual burnt gas heterogeneity on cyclic variability in lean-burn si engines. *Flow Turbulence Combustion*, 92:837–863, 2014. 38, 130
- [99] C. Pera, V. Knop, and J. Reveillon. Influence of flow and ignition fluctuations on cycle-to-cycle variations in early flame kernel growth. *Proceedings of the Combustion Institute*, 35:2897–2905, 2015. 38, 130
- [100] N. Peters. The turbulent burning velocity for large-scale and small-scale turbulence. *J. Fluid. Mech.*, 384:107–132, 1999. 49, 174
- [101] Norbert Peters. *Turbulent Combustion*. Cambridge University Press, 2000. 50
- [102] B. Peterson, D. L. Reuss, and V. Sick. On the ignition and flame development in a spray-guided direct-injection spark-ignition engine. *Combustion and Flame*, 161(1):240–255, 2014. 129, 130
- [103] A. Pires da Cruz. Three-dimensional modeling of self-ignition in hcci and conventional diesel engines. *Combustion Science Technology*, 176:867–887, 2004. 30
- [104] S. Pischinger, M. Günter, and O Budak. Abnormal combustion phenomena with different fuels in a spark ignition engine with direct injection. *Combustion and Flame*, 2017. 18
- [105] T. Poinso and D. Veynante. *Theoretical and Numerical Combustion, Third Edition*. 2012. 44, 45
- [106] T.J Poinso and S.K Lele. Boundary conditions for direct simulations of compressible viscous flows. *Journal of Computational Physics*, 101:104–129, 1992. 92

BIBLIOGRAPHY

- [107] M. Pöschl and T. Sattelmayer. Influence of temperature inhomogeneities on knocking combustion. *Combustion and Flame*, 2008. 28, 33, 34, 36, 37, 38, 112, 116
- [108] M. Ribaucour, R. Minetti, L.R. Sochet, H.J. Curran, W.J. Pitz, and C.K. Westbrook. Ignition of isomers of pentane: An experimental and kinetic modeling study. *Proceedings of the Combustion Institute*, 28:1671–1678, 2000. 28
- [109] H. R. Ricardo. *The Internal-Combustion Engine, Vol II*. Blackie & Son Limited, 1923. 26
- [110] S. Richard. *PhD Manuscript. Simulation aux grandes échelles de la combustion dans les moteurs à allumage commandé*. 2005. 49, 50, 51, 57, 58, 59, 174
- [111] S. Richard, O. Colin, O. Vermorel, A. Benkenida, C. Angelberge, and D. Veynante. Towards large eddy simulation of combustion in spark ignition engines. *Proceedings of the Combustion Institute*, 31:3059–3066, 2007. 55
- [112] A. Robert, S. Richard, O. Colin, L. Martinez, and L. de Francqueville. LES prediction and analysis of knocking combustion in a spark ignition engine. *Proceedings of the Combustion Institute*, 35(3):2941–2948, 2015. 30, 36, 38, 39, 62, 63, 95, 104, 105, 123, 152, 174
- [113] A. Robert, S. Richard, O. Colin, and T. Poinso. LES study of deflagration to detonation mechanisms in a downsized spark ignition engine. *Combustion and Flame*, 162(7):2788–2807, 2015. 30, 32, 36, 37, 142, 174
- [114] A. Robert, K. Truffin, N. Iafrate, S. Jay, O. Colin, and C. Angelberger. LES analysis of knock in a direct injection spark ignition engine. *To be published*, 2016. 53
- [115] Anthony Robert. *PhD. Simulation aux Grandes Échelles des combustions anormales dans les moteurs downsizés à allumage commandé*. 2014. 20, 115, 167
- [116] M. Rudgyard and T. Schonfeld. Steady and unsteady flow simulations using the hybrid flow solver AVBP. *AIAA*, 37(11):1378–1385, 1999. 20
- [117] R. Schiessl and U. Maas. Analysis of endgas temperature fluctuations in a si engine by laser-induced fluorescence. *Combustion and Flame*, 2002. 33, 34, 173
- [118] S. Shih, E. Itano, J. Xin, M. Kawamoto, and Y. Maeda. Engine knock toughness improvement through water jacket optimization. *SAE International Journal Fuels Lubricant*, 2003. 39
- [119] J. Smagorinsky. General circulation experiments with the primitive equations: 1. the basic experiment. *Monthly Weather Review*, 91(3):99–164, 1963. 49
- [120] D.B. Spalding. The combustion of liquid fuels. *In Symposium (international) on combustion*, 4:847–864, Elsevier, 1953. 93
- [121] R. Stein, D. Polovina, K. Roth, and M. et al. Foster. Effect of heat of vaporization, chemical octane, and sensitivity on knock limit from ethanol-gasoline blends. *SAE Int. J. Fuels Lubr.*, 5(2):823–843, 2012. 40

BIBLIOGRAPHY

- [122] K. Tanoue, T. Jimoto, T. Kimura, M. Yamamoto, and J. Hashimoto. Effect of initial temperature and fuel properties on knock characteristics in a rapid compression and expansion machine. *Proceedings of the Combustion Institute*, pages 1–9, 2016. 36, 37
- [123] H.B. Toda, O Crabit, G. Balarac, S. Bose, J. Lee, H. Choi, and F. Nicoud. A subgrid-scale model based on singular values for LES in complex geometries. *Center for Turbulence Research, NASA Ames/Stanford Univ.*, pages 193–202, 2010. 49
- [124] K. Truffin, C. Angelberger, S. Richard, and C. Pera. Using large-eddy simulation and multivariate analysis to understand the sources of combustion cyclic variability in a spark-ignition engine. *Combustion and Flame*, 2015. 129, 130
- [125] K. Truffin and O. Colin. Auto-ignition model based on tabulated detailed kinetics and presumed temperature pdf - application to internal combustion engine controlled by thermal stratifications. *International Journal of Heat and Mass Transfer*, 54:4885–4894, 2011. 33
- [126] O. Vermorel, S. Richard, O. Colin, C. Angelberger, A. Benkenida, and D. Veynante. Towards the understanding of cyclic variability in a spark ignited engine using multi-cycle LES. *Combustion and Flame*, 156(8):1525–1541, 2009. 50, 95, 129, 130
- [127] D. Veynante and T. Poinso. Reynolds average and large-eddy simulation modeling for turbulent combustion. *New Tools in Turbulence Modeling*, 1997. 55
- [128] C.K. Westbrook. Chemical kinetics of hydrocarbon ignition in practical combustion systems. *Proceedings of the Combustion Institute*, 28:1563–1577, 2000. 28
- [129] C.K. Westbrook and F.L. Dryer. Chemical kinetic modeling of hydrocarbon combustion. *Progress in Energy and Combustion Science*, 10:1–57, 1984. 28
- [130] E. Winklhofer, A. Hirsh, P. Kapus, M. Kortschak, and H. Philipp. Tc gdi engines at very high power density - irregular combustion and thermal risk. *SAE Technical Paper*, 2009. 145
- [131] R. Worret, S. Bernhardt, F. Schwartz, and U. Spicher. Application of different cylinder pressure based knock detection methods in spark ignition engines. *SAE Int. J. Fuels Lubricant*, 2002. 35, 36, 113, 114
- [132] V. Yakhot, S. A. Orszag, S. Thangam, T. B. Gatski, and C. G. Speziale. Development of turbulence models for shear flows by a double expansion technique. *Physics of Fluids A: Fluid Dynamics*, 4(7):1510–1520, 1992. 80
- [133] C. S. Yoo, Z. Luo, T. Lu, H. Kim, and J. H. Chen. A DNS study of ignition characteristics of a lean iso-octane/air mixture under hcci and saci conditions. *Proceedings of the Combustion Institute*, 34(2):2985–2993, 2013. 28, 173
- [134] J-M. Zaccardi and D. Escudié. Overview of the main mechanisms triggering low-speed pre-ignition in spark-ignition engines. *Int. J. of Energy Research*, 15, 2014. 18

BIBLIOGRAPHY

- [135] J. Zador, C.A. Taatjes, and R.X. Fernandes. Kinetics of elementary reactions in low-temperature auto-ignition chemistry. *Progress in Energy and Combustion Science*, 37:371–421, 2011. 28
- [136] Ya. B. Zel'dovich. Regime classification of an exothermic reaction with non-uniform initial conditions. *Combustion and Flame*, 39, 1980. 31, 37, 144

Titre: Étude du cliquetis dans un moteur industriel à allumage commandé par Simulation aux Grandes Échelles

Mots clés: cliquetis, auto-inflammation, variabilités cycliques de combustion, simulation aux grandes échelles.

Résumé: Les préoccupations environnementales actuelles ont conduit les constructeurs automobiles à proposer de nouvelles technologies dans le but de réduire les émissions de CO₂. Parmi ces technologies, le downsizing appliqué aux moteurs turbocompressés à allumage commandé est une des solutions privilégiées, car permettant d'atteindre des points de fonctionnement fortement chargés, avec un meilleur rendement thermique. Cependant, les fortes charges favorisent l'apparition de cliquetis, un phénomène potentiellement dommageable pour le moteur et qui l'empêche d'exploiter tout son potentiel. Du fait des variabilités cycliques de combustion dans le moteur, le cliquetis, qui dépend des conditions locales dans la chambre de combustion, peut apparaître uniquement sur quelques cycles, à différents endroits et instants. Dans cette thèse, une approche par Simulation aux Grandes Échelles (SGE) a été choisie, dans le but d'étudier et d'améliorer notre compréhension du cliquetis. L'étude se base sur la SGE d'un moteur industriel, le RENAULT 1.2 TCe 115. Un premier ensemble de 30 cycles a été simulé sur un point de fonctionnement de référence, correspondant à un point cliquetant dans la base de données banc d'essais

fournie par RENAULT. Les résultats de simulation ont été comparés aux résultats expérimentaux, aussi bien en termes de variabilités cycliques de combustion que de cliquetis. A la suite, un balayage d'avance à l'allumage a été simulé pour étendre la base de données LES à des points plus faiblement et plus fortement cliquetants. La base de données résultante se compose de 150 cycles de combustion, utilisés pour développer des méthodologies et outils, dans le but de mieux caractériser le cliquetis et d'approfondir sa compréhension. L'accès numérique à toute grandeur dans la chambre de combustion, combiné à la description séparée dans cette simulation entre la flamme de pré-mélange initiée par la bougie et l'auto-inflammation dans les gaz frais, ont permis de caractériser le cliquetis en se focalisant sur son origine : l'auto-inflammation. A la suite, les méthodologies et outils développés ont soutenu une analyse détaillée des mécanismes qui contrôlent l'apparition du cliquetis. En particulier, le lien entre le cliquetis et les variabilités cycliques de combustion a été exploré. Les résultats mettent notamment en évidence l'impact des variabilités cycliques, aussi bien de la vitesse de propagation que de la forme de la flamme de pré-mélange, sur le cliquetis.

Title: Investigating knock in an industrial spark-ignition engine by Large-Eddy Simulation

Keywords: knock, auto-ignition, cyclic combustion variability, large-eddy simulation.

Abstract: The rising concerns about the environment have led car manufacturers to come up with new engine technologies, in order to reduce the impact of internal combustion engines on CO₂ emissions. In this context, downsizing of turbocharged spark-ignition engines has become a commonly used technology, the advantage of which is to operate the engine under thermally more efficient high loads. However, these high loads favour the appearance of potentially damaging knock phenomena, which prevent the engine to fully exploit its potential. Because of cyclic combustion variability (CCV) in the engine, knock, which depends on the local conditions inside the combustion chamber, can appear at different locations and timings and not in all engine cycles. In this thesis, a Large-Eddy Simulation (LES) approach was selected to investigate and further improve our understanding of the appearance of knock. The study is based on the LES of a production engine, the RENAULT 1.2 TCe 115. For this engine, a set of 30 cycles was initially simulated at a single operating point,

corresponding to a knocking point in the test bench database from RENAULT. The results were compared to experimental findings, both in terms of CCV and knock. Subsequently, a spark-timing sweep was simulated in order to enlarge the LES database to also include weaker and stronger knock levels. The resulting LES, which consists of 150 combustion cycles, was used to develop methodologies and tools with the objective to better characterize and understand knock. The computational access to any quantity inside the combustion chamber, together with the separate description with the present LES approach between the spark-triggered premixed flame propagation and auto-ignition, were exploited to characterize knock focusing on its source: auto-ignition in the fresh gases. Then, the developed methodologies and tools supported a detailed analysis of the mechanisms that control the knock onset. In particular, its link with CCV was explored. The results point out the impact of the cyclic variability in the premixed flame propagation speed and shape on knock.

